

## Mapping the reaction landscape for the C1 chemistry

Khramenkova, E.

**DOI**

[10.4233/uuid:f37f4e0c-4869-434a-ba93-24db7662eabb](https://doi.org/10.4233/uuid:f37f4e0c-4869-434a-ba93-24db7662eabb)

**Publication date**

2022

**Document Version**

Final published version

**Citation (APA)**

Khramenkova, E. (2022). *Mapping the reaction landscape for the C1 chemistry*. [Dissertation (TU Delft), Delft University of Technology]. <https://doi.org/10.4233/uuid:f37f4e0c-4869-434a-ba93-24db7662eabb>

**Important note**

To cite this publication, please use the final published version (if applicable). Please check the document version above.

**Copyright**

Other than for strictly personal use, it is not permitted to download, forward or distribute the text or part of it, without the consent of the author(s) and/or copyright holder(s), unless the work is under an open content license such as Creative Commons.

**Takedown policy**

Please contact us and provide details if you believe this document breaches copyrights. We will remove access to the work immediately and investigate your claim.

# Mapping the reaction landscape for the C1 chemistry

**Dissertation**

for the purpose of obtaining the degree of doctor  
at Delft University of Technology  
by the authority of the Rector Magnificus prof.dr.ir. T.H.J.J. van der Hagen  
chair of the Board for Doctorates  
to be defended publicly on  
Tuesday 20 December 2022 at 10:00 o'clock

by

**Elena Viktorovna KHRAMENKOVA**

Master of Science in Biotechnology  
ITMO University, Russia  
born in Bratsk, Russia

This dissertation has been approved by the promotor:

promotor: prof. dr. E.A. Pidko

copromotor: dr. G. Li

**Composition of the doctoral committee:**

Rector Magnificus

chairperson

Prof. dr. E.A. Pidko

Delft University of Technology, promotor

Dr. G. Li

Wageningen University & Research, copromotor

**Independent members:**

Dr. S. Grecea

University of Amsterdam

Prof. dr. ir. V. Van Speybroeck

Ghent University, Belgium

Prof. dr. ir. A. Urakawa

Delft University of Technology

Prof. dr. ir. T.J.H. Vlugt

Delft University of Technology

Prof. dr. R.A. van Santen

Eindhoven University of Technology

The work described in this thesis was carried out in the Inorganic Systems Engineering group and the Catalysis Engineering section, Faculty of Applied Sciences, Delft University of Technology. The research was financed by the European Research Council (ERC) under the European Union's Horizon 2020 Research and Innovation Program (grant agreement No. 725686). The use of supercomputer facilities was sponsored by NWO Domain Science.



European Research Council

Established by the European Commission

Printed by: Proefschrift specialist

Copyright © 2022 by E.V. Khramenkova

An electronic version of this dissertation is available at the TU Delft repository

**To my family**



---

---

# Contents

---

---

<b>Chapter 1</b>	<i>Operando</i> computational characterization and modelling in heterogeneous catalysis	<b>2</b>
<b>Chapter 2</b>	Global optimization of extraframework ensembles in zeolites: structural analysis of extraframework aluminum species in MOR and MFI zeolites	<b>36</b>
<b>Chapter 3</b>	Unraveling nature of extraframework catalytic ensembles in zeolites: flexibility and dynamics of the copper-oxo trimers in mordenite	<b>60</b>
<b>Chapter 4</b>	High stability of methanol to aromatic conversion over bimetallic Ca,Ga-modified ZSM-5	<b>86</b>
<b>Chapter 5</b>	Impact of metal ion concentration on the formation of active CuAl-oxo clusters in mordenite for oxidative activation of methane	<b>108</b>
<b>Chapter 6</b>	Solvent-mediated outer-sphere CO <sub>2</sub> electroreduction mechanism over Ag111 surface	<b>134</b>
<b>Summary</b>		<b>157</b>
<b>Samenvatting</b>		<b>161</b>
<b>Acknowledgements</b>		<b>165</b>
<b>List of publications and presentations</b>		<b>167</b>
<b>Curriculum Vitae</b>		<b>170</b>



---

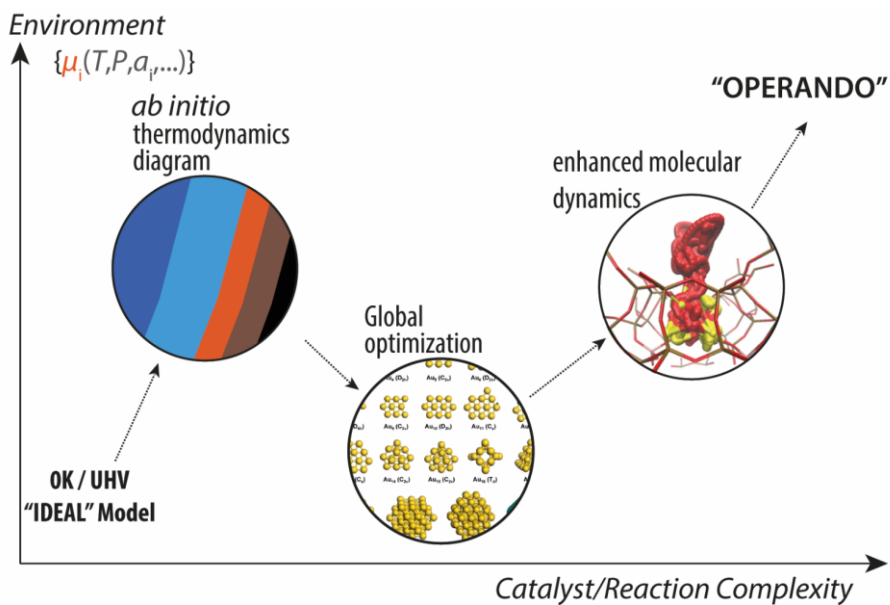
---

# Chapter 1

---

---

## *Operando* computational characterization and modelling in heterogeneous catalysis



## Summary

---

A recent trend in heterogeneous catalysis is to mimic operational conditions by performing experimental and theoretical investigations in *operando* regimes. In this way, the catalytic system is viewed as a dynamic object, where the active site represents an ensemble of states, capable of adapting various configurations possible within a defined temperature and pressure range. To move from the conventional description of the catalytic system in computational heterogeneous catalysis, where only a limited number of states are accounted for, novel theory methods, used exclusively or in combination with the experiment, can reach the complexity of the realistic catalytic process. Mingled with experimental measurements, the theoretical models can fit the spectral data utilizing the machine learning algorithms to validate the proposed reaction intermediates and pathways responsible for catalytic activity. To establish an ensemble of the lowest-lying configurations, the methods such as global optimization and *ab initio* thermodynamics analysis are often used jointly, whereas enhanced molecular dynamics can solely reveal the dynamics of the system under operating conditions. Employing these methods provides the relevant structures or reaction mechanisms characteristic of a particular chemical environment.

This chapter is based on the following book chapter:

Khramenkova E. V., Meeprasert J., Uslamin E. A., Pidko E. A.  
*Operando Methods in Catalysis and Material Science* (Wiley-VCH Verlag), *submitted*

## **1.1. Introduction: “bridging the gap” between macro- and micro-scales**

Gaining reliable information at the atomic or nanoscale levels under operating conditions is crucial for understanding the correlations between the structure of the catalyst and its catalytic behavior. Heterogeneous reactions are known for the complications related to the identification of active sites. Their complex multicomponent nature enables a variety of reaction pathways that can be simultaneously observed within a system maintaining spatially and structurally diverse active sites. The idea of identifying the structure of the active site under the reaction conditions is important for the development of new catalytic systems and can be pursued via both empirical and theory-driven approaches. The former includes high-throughput approaches that generate abundant data on the exploration of the materials space and, specifically, the catalyst reactivity and performance. The high-throughput catalytic data, which is conventionally most often employed for catalyst discovery and process optimization, can identify the patterns connecting the performance of the catalyst to its composition and the reaction conditions. With machine-learning algorithms for data analysis, information on the beneficial composition and reaction regimes can be gathered. However, it merely provides insights into the electronic/geometrical features of the active sites. The “evolutionary” approach, applied within this strategy, guides the search for successful trials, although might skip the areas of potential activity. This macro-scale information constructs the empirical descriptors between a macroscale parameter (conditions/composition) and selectivity/activity, thus, any generalizations beyond input data are limited. In contrast, the theory-driven approach studies the underlying fundamental characteristics of the system to predict and explain its catalytic outcome based on the models simplifying the real experiment. This reflects an overall shift towards computational modelling and data analysis that applies the generation and processing of the macro- and microscale data prior to the experiments. Today’s efforts in modelling catalysis are devoted to overcoming the inconsistencies between the oversimplified *in vacuo* (UHV) and *operando* modelling techniques by capturing the realistic dynamics and condition-dependencies of the catalyst system.<sup>1</sup>

The two approaches are not contradictory but rather complementary. “Bridging the gap” between high-throughput experimentation and theory defines the interconnection between the macroscale parameters (*i.e.* temperature, pressure, concentrations) and electronic/geometric transformations (confinement, oxidation state, bandgap, coordination number). This problem can be tackled experimentally, with the use of the recent spectroscopic developments of the *operando/in-situ* modelling techniques, that allow monitoring of the catalytic system under realistic conditions. The spectroscopic characterization often suffers from a lack of certainty and heavily relies on researchers’ chemical intuition about possible reaction mechanisms in the system. First principle calculations can provide a necessary ingredient for investigating the catalyst performance

by giving its atomistic description. The toolbox of computational chemistry deals with this multiscale problem by applying advanced modelling techniques that can relate the electronic transformations to a certain state, in which the system is present. The experimental and modelling techniques can be used as independent investigation methods or in alliance with each other. An example representing the combination of experimental and computational data is merging the spectroscopic data with the microkinetic model to gain a deeper understanding of the reaction mechanism and the nature of active sites. Nevertheless, the problem under investigation defines which extensions are crucial and which methodology is to be applied.

## 1.2. The interplay of theory and experiment

Understanding the nature of the active site and the mechanism, by which it promotes the catalytic reaction is the key challenge for modern catalysis science. There is growing evidence in the literature on the crucial role of dynamic phenomena in heterogeneous catalysis. When exposed to the reaction conditions, the active sites on the surface evolve and reconstruct in response to the external stimuli, therefore, altering their chemical reactivity and catalytic behavior. The change in the composition and geometry of the reactive ensembles on the surface can accompany processes taking place at different time and length scales. Surface reconstructions can play a crucial role in catalyst activation and deactivation processes. More recently, evidence has been presented that the structural dynamics of the active site can play a crucial role in providing the most favorable reaction path for the catalytic cycle. The dynamic behavior of the active sites can be studied under reactive conditions employing *operando* spectroscopy and imaging methods. *Operando* spectroscopy techniques provide information about the structural changes occurring during the catalytic reaction. These effects are critically important for the understanding of the actual mechanisms in heterogeneous catalysis.<sup>2</sup> Despite significant development in *operando* techniques, extracting the molecular-level details on the nature of the active sites and the reaction mechanism directly from the experiment is still a challenge. This is largely associated with the problem of the unbiased interpretation of the experimental data, which can be addressed by combining the experiment with theory. In this section, we first provide a brief overview of the modern *operando* techniques and their capabilities to follow the dynamics of the active sites. We then discuss the potential of theory to gain a better understanding of the *operando/in-situ* measurements. When experimental and theory-driven approaches are combined, they could validate the theoretical models and bring to light the atomistic details of the reaction mechanism, which are crucial for further rational design and optimization of catalyst systems.

The term *in-situ* corresponds to monitoring a catalyst under the reaction conditions, while *operando* implies the use of a combination of physical-chemical techniques to follow the catalytic activity and the structural changes of the catalyst simultaneously. A

combination of *operando* and *in-situ* techniques is applied to follow the state of the catalyst during different stages of preparation and activation and to trace its behavior under reactive conditions and deactivation. These effects are well illustrated by the supported metal nanoparticles changing their size, shape and oxidation state.<sup>3,4</sup> Generally, the structural changes can be induced by multiple factors: non-catalytic chemical reactions between the catalytic surface and the reactants, changes in the chemical potential of reactant molecules under different reaction conditions, local heat dissipation effects, phase transformations and the surface etching in liquid medium.<sup>5-9</sup> Modern *operando* methods based on different physical principles target different aspects of the catalytic process. These methods include high-resolution transmission environmental electron microscopy (HRTEM), vibrational (IR) and Raman spectroscopy and a number of X-ray diffraction (XRD, XRD, PDF) X-ray emission (XES, RIXS) and X-ray absorption techniques (NEXAFS, EXAFS). Given the large scope of the field of *operando* characterization of heterogeneous catalysis, we refer the reader interested in the details and capabilities of the characterization techniques to the following review articles.<sup>10-14</sup>

A comprehensive understanding of a dynamic catalytic system can be gained from a combination of different techniques. Thus, the XAS techniques play an important role in catalytic research and are often used to characterize the local geometry and electronic structure of the active species. Excited by X-rays, the photoelectrons are moved to the unoccupied localized and delocalized states where different transitions and scattering pathways provide element-specific information on the local atomic and electronic structure of the material. While XAS techniques are mostly used to probe the local configuration of metal centers, vibrational spectroscopy applied under *operando* conditions can provide information about the structure of the adsorbate species on the catalyst surface. Combining these complementary spectroscopic methods can provide information on the complex molecular mechanisms underlying the catalytic reaction.<sup>15</sup> It is worth noting however that the *operando/in-situ* studies often suffer from either an intrinsic ensemble-averaging or from the extrapolation of the local effects to the overall catalytic system. For instance, TEM-based methods provide a detailed structural picture of the local particles which is not always representative of the whole entity. An ensemble-averaging spectroscopy and diffraction techniques, namely XAS and XRD and in some cases NMR and EPR techniques, can also provide incorrect structural data due to the high heterogeneity of the real catalyst sample.<sup>16</sup> Overall, the interpretation of spectral features is not always a straightforward task. It often relies on simple fingerprinting which is essentially a comparison of the target spectra with the spectra of reference material. Employing effective computational methods for the validation of experimental data is, therefore, crucial for unbiased data analysis protocols. The development of the modelling techniques such as time-dependent DFT, Bethe-Salpeter method and full scattering formalism allowed the fitting of the parameters and interpreting of the experimentally

obtained spectra using theoretical.<sup>17</sup> The employment of the machine learning algorithms enables the automatic spectra matching, and regression of structure parameters.<sup>18</sup>

The examples of dynamics of the various catalytic systems attributed to their mobile active centers are numerous, described in both theory and experiments. Several excellent reviews published recently have been devoted to this topic.<sup>19,20</sup> Below we will illustrate the phenomenon of active-site dynamics revealed by *operando/in-situ* techniques and rationalized through molecular modelling by considering several relevant examples from the recent literature.

One of the notorious examples is zeolite catalysts modified with transition metals.<sup>21,22</sup> These materials often demonstrate a wide variety of co-existing TM species with different stoichiometry, oxidation states and coordination. For instance, Cu-containing zeolites utilized as a catalyst for the selective reduction of NO<sub>x</sub> by NH<sub>3</sub> (SCR)<sup>23,24</sup> may contain various Cu species with distinct chemical reactivity and catalytic behavior. *Ex-situ* electron paramagnetic resonance spectroscopy study supported by previous XAS and UV-vis results provided critical information about the oxidation state and local environment of Cu species in Cu-modified CHA zeolite. Although this zeolite framework possesses only one crystallographically independent tetrahedral site (T-site), 8 different types of Cu species were detected. These included isolated Cu<sup>+</sup> and Cu<sup>2+</sup>-OH<sup>-</sup> species as well as different oxygen-bridged Cu<sub>x</sub>O<sub>y</sub> clusters. Furthermore, a number of EPR-silent tetrahedral Cu<sup>2+</sup> species have been also detected.<sup>25</sup> The speciation and the behavior of the intrazeolite transition metal complexes become more complex as the catalyst is exposed to the reaction conditions. The initial experimental evidence of the highly mobile and dynamic nature of the Cu sites in Cu/SSZ-13 under the varied catalyst activation and the SCR reaction conditions has been provided by Gao et al.<sup>26</sup> It was found that the intrazeolite Cu ions rearrange in the zeolite pores during the high-temperature catalyst activation. The dehydration of the zeolite in dry N<sub>2</sub> resulted in the mobilization of the cations in the deposited oxidic clusters, which at the elevated temperature gives rise to their migration and deposition at the exchange sites neighboring lattice aluminum atoms. Importantly, such an immobilization of the cations is accompanied by a sharp decline in the catalytic performance. The authors proposed that at low temperatures, the metastable dimeric Cu sites are responsible for the high catalytic activity in the zeolite materials with a low Cu loading. However, these Cu dimers dissociate at 250–350 °C to form much less reactive isolated Cu<sup>2+</sup> sites. It was proposed that such dimeric sites can be stabilized by increasing the Cu loading in the zeolite.

The spectroscopic information about the different species in heterogeneous catalysts could be rationalized and interpreted at the atomistic level through the aid of computational modelling. The spectroscopic characterization and computational modelling synergy can be achieved through the direct theoretical prediction of the diverse predicted spectral characteristics for various active site candidates<sup>27,28</sup> or through detailed

mechanistic studies and the resulting property-activity relations.<sup>29-31</sup> In this way, the computational chemistry methods come into play for the development of a molecular view on the evolution of the active sites under reactive conditions, their identification and investigation of the associated reaction mechanisms.<sup>32</sup> An excellent example of the synergy between theory and experiment in demonstrating the crucial role of Cu mobility in the SCR process has been presented by Paolucci et al.<sup>33</sup> The authors followed the evolution of the state of Cu ions in the zeolite catalyst during the catalyst activation and the SCR process by XANES complemented by DFT calculations. During the reaction, the authors observed transient oxidation of the isolated Cu(I) sites to form multinuclear Cu(II) clusters. The observed kinetics suggested a pseudo-bimolecular reaction between two-fold coordinated Cu (Cu(I)(NH<sub>3</sub>)<sub>2</sub>) moieties and O<sub>2</sub>, which was further rationalized by DFT calculations. *Ab initio* molecular dynamics (aiMD) simulations showed that during the SCR reaction, the solvation by ammonia mobilizes the Cu<sup>+</sup> sites originally stabilized at the zeolitic cation sites. The resulting Cu(I)(NH<sub>3</sub>)<sub>2</sub> species diffuse through the zeolite channels to meet another Cu(I)(NH<sub>3</sub>)<sub>2</sub> structure and the subsequent highly exothermic oxidation of such neighboring Cu(I)(NH<sub>3</sub>)<sub>2</sub> species yields Cu (II) dimers. The cationic mobility and the possibility to change the nuclearity of the catalytic Cu species during the SCR catalytic cycle have been proposed to be one of the key factors behind the unique catalytic properties of the Cu-modified zeolite catalysts.

To summarize, great progress has been made in the last decades in gathering the data from *operando* spectroscopic techniques and linking these observations with the theory of heterogeneous catalysts. Similar to the experiments, the theory moves from the UHV conditions and progresses into *operando* conditions, where the system is studied under experimentally relevant temperature and pressure. However, when implemented, theory-driven studies conventionally rely on the theoretical models and mechanisms solely based on the chemical intuition of a researcher. To account for considerably more candidates – systems' states – one has to implement the modelling approaches that effectively scan the potential energy surface (PES) for various accessible local and global minima. These approaches employ new strategies for more effective PES sampling utilizing conventional electronic structure methods calculations of various precision. Below we evaluate in detail the new computational advances and the electronic structure methods they are based on. Here a focus is made on the global optimization methods and enhanced molecular dynamics that were found to go beyond one's chemical intuition.

### **1.3. Computational methods in catalysis**

#### **1.3.1. *Ab initio* methods**

The accurate predictions of the geometrical configurations and electronic structures became possible with the development of computer hardware and various computational methods. In the zeolites framework, the elementary reaction takes place at a timescale of

$10^{-6}$  s, while the corresponding electronic motion that governs the process has a timescale of  $10^{-16}$  s. Many reactions requiring high accuracy can be nowadays studied by performing electronic structure calculations, therefore, giving the right description of the electronic structure is the key.

The electronic structure can be predicted using the quantum chemical methods including the density functional theory (DFT),<sup>34</sup> semiempirical methods<sup>35</sup> and *ab initio* quantum chemical methods.<sup>36</sup> In *ab initio* methods, the energy of a chemical system is described by the many-body Schrödinger equation as  $\hat{H}\psi = E\psi$ , where  $\hat{H}$  is the Hamiltonian operator,  $E$  is the energy of the chemical system and  $\psi$  is the many-body wave function.<sup>37</sup> The latter is an analytical description of the quantum state of a chemical system, which includes the coordinates and spin state of each particle within the system, making the exact analytical solutions of the Schrödinger equation only feasible for systems with only particle. The many-body problem was reduced via multiple approximations such as the Born-Oppenheimer, narrowing down the many-body problem to the only-electrons problem. However, the exact solution exists only for the one-electron hydrogen equation.<sup>38</sup>

To solve the problem of interacting electrons another simplification was made which is known as the Hartree-Fock approximation.<sup>39</sup> It postulates that electrons do not interact directly with each other and each electron is moving in the field generated by the nuclei and other  $N-1$  electrons. With this approximation in place, the electronic positions are no longer coupled and the Schrödinger equation may be solved. This approximation does not account for the correlation of the electronic motion, causing an overestimation of the system's energy better known as the correlation energy. The improvement in the correlated motion was introduced in post-Hartree-Fock methods such as Configuration Interaction (CI) and Møller-Plesset perturbation theory (MPn). These methods are able to accurately describe chemical systems but are extremely computationally expensive for conducting explicit studies on a set of relevant reactions.<sup>40</sup> Therefore, these methods cannot realistically be employed in the genetic algorithm or enhanced molecular dynamics where many electronic structure calculations are necessary. DFT is a quantum mechanical method that is better suited for numerous yet accurate calculations.

In density functional theory,<sup>41</sup> the electronic structure of a system is described by the probability distribution of the electrons around nuclei. It is more commonly referred to as the electron density function, instead of the wave function. The electron density function is a function of positions of three spatial coordinates, while the many-body wave function depends on the coordinates and spin states of all electrons. The approximate solution of the Schrödinger equation proposed by Kohn and Sham using the electron distribution:  $E[\rho] = T[\rho] + E_{\text{EXT}}[\rho] + V[\rho] + E_{\text{XC}}[\rho]$ , where  $E$  is the energy of the system,  $T$  describes the kinetic energy of the electrons,  $E_{\text{EXT}}$  is the interaction energy between the electron and the external potential,  $V$  is the potential energy of the repulsion interactions

between electrons and  $E_{XC}$  is known as the exchange-correlation energy. The exchange-correlation energy represents the difference between the system of non-interacting electrons and the real one. The numerous approximations of the exchange-correlation functional gave rise to the development of different DFT methods including the Local Density Approximation (LDA),<sup>42</sup> Generalized Gradient Approximation (GGA),<sup>43</sup> meta-GGA,<sup>44,45</sup> and Hybrid methods.<sup>46</sup> The problem associated with the conventional density functional is the lack of description of the long-range dispersion interactions which results in strongly underestimated adsorption energies and reaction barriers. To circumvent these problems, the DFT-D approach has been developed which includes a semiempirical damped-potential term.<sup>47</sup>

### 1.3.2. Semiempirical methods

The semiempirical methods provide the balance between the electronic density methods and the force field methods, giving the accuracy of the former and the computational costs of the latter. Some of the semiempirical methods are based on Hartree-Fock formalism but include empirical parameters to approximate certain electronic interactions. One of the widely used methods is GFN- $x$ TB developed by Stephan Grimme.<sup>48-50</sup> The special focus of these methods is on predicting geometries, vibrational frequencies and non-covalent interactions for large chemical systems containing thousands of atoms. Initially, these methods were not suitable for solid calculations under periodic boundary conditions but it has now become also possible. The term ‘extended’ in the name  $x$ TB implies that the parameters are available for almost all the periodic table of elements, up to radon.

Currently, GFN- $x$ TB methods are represented by three unique calculators: GFN0, GFN1 and GFN2, which utilize the same theory and differ in the complexity with which it is implemented. They are based on the density functional tight-binding (DFTB) theory which aims to improve upon the LDA approximation of classical DFT. In the DFTB method, the total energy of the system can be defined as follows:

$$E[\rho] = E^{(0)}[\rho_0] + E^{(1)}[\rho_0, \delta\rho] + E^{(2)}[\rho_0, (\delta\rho)^2] + E^{(3)}[\rho_0, (\delta\rho)^3] + \dots \quad (E1.1)$$

where the electron density is described by density deviations ( $\delta\rho$ ) with respect to the neutral atomic reference density ( $\rho_0$ ). GFN1- $x$ TB – the first version of these methods – utilizes the second order with some terms up to the third order, using the same approximation for the Hamiltonian and electrostatic energy as DFTB. Instead of relying on an atom pair-wise parametrization, element-specific empirical fitting is used. The biggest drawback related to the GFN1- $x$ TB method is the spherically symmetric description of the atom pair-wise electrostatic interactions. To account for this deficiency, the GFN2- $x$ TB method has been developed with a multipole electrostatic treatment up to quadrupole terms. GFN2- $x$ TB has the same parametrization as the GFN1, employs the latest D4 dispersion model and does not have pair parameters.<sup>51</sup>

### 1.3.3. Classical methods

A large ensemble of atoms is generally studied in the framework of classical force field methods, where the interactions between atoms are governed by a certain potential. These simulations are good at describing the adsorption and diffusion behavior when no bond-breaking or making processes occur in the reaction. To model these effects a great number of force fields were designed, where the functional form and the parameters are specified to calculate the potential energy of the system. The parameters are generally divided from *ab initio* calculations or by fitting to experimental data. Within the certain force field, the molecules are defined as the set of atoms that are held together by, for instance, harmonic forces and the chosen type of the force field replaces the true potential with a simplified model in a simulated region. The force field of choice and its functional form should be simple enough to be evaluated quickly but sufficiently detailed to calculate the properties of interest. A relatively good and simple approximation for many systems gives the Lennard-Jones potential. Lennard-Jones' potential describes the energy of interactions between two non-bonding atoms or molecules based on their distance of separation. The commonly used expression for the Lennard-Jones potential can be defined as the following:

$$V_{LJ}(r) = 4\epsilon \left[ \left( \frac{\sigma}{r} \right)^{12} - \left( \frac{\sigma}{r} \right)^6 \right] \quad (\text{E1.2})$$

The equational form of Lennard-Jones potential (E1.2) contains a short-range repulsion  $r^{-12}$  term represented with Pauli repulsion and describes the electrons overlapping, whereas  $r^{-6}$  is a long-range attraction term describing attraction at such long-range interactions as Van der Waals and dispersion forces. Hence, the behavior at short distances is governed by the repulsive term and the behavior at short distances is governed by the attractive term. The depth of the potential well  $\epsilon$  defines how strongly atoms attract each other, and the distance at which the intermolecular potential between two atoms equals zero is defined as  $\sigma$ . The approximations to define the distance and energy parameters for interatomic interactions are based on mixing rules.<sup>52</sup>

### 1.3.4. Employing different methods for the PES exploration

The available computational chemistry toolbox includes a wide variety of methods that can be classified according to their accuracy and dimensions. The exploration of the PES using global optimization techniques or enhanced molecular dynamics can be carried out using some low-cost interatomic potentials (force fields) within the framework of classical mechanics allowing to study of the behavior of the chemical systems containing thousands of atoms.<sup>53</sup> The corresponding methods are usually empirical and do not consider explicitly the electrons in the system. The possibility to treat extended systems with such methods is achieved at the expense of a substantial loss of generality and accuracy. With this approach, large nanoparticles can be described, as they mimic the

solid state to a large extent.<sup>54,55</sup> Amongst the atomistic potentials that are used for the optimization of nanoalloys, Gupta many-body potential has been extensively used.<sup>56,57</sup> However, with the improvement of the computational power, first-principles methods became more actively utilized for Genetic Algorithm (GA) and Molecular Dynamics (MD) studies.<sup>58</sup> These methods provide the quantum mechanical description of a chemical system. Such methods are particularly important for processes that involve bond breaking or making, which include, of course, the dynamic evolution of the catalytic ensembles and their transformations under the conditions of the catalytic reactions. When full *ab initio* DFT methods are still too demanding for the comprehensive exploration of the vast configurational space, the accelerated semiempirical methodologies come into play.<sup>48,59</sup> They provide a good compromise between the generality, accuracy and speed required for the PES exploration techniques. Another approach is to use the semiempirical or purely empirical methods for the exhaustive search followed by a further structure refinement at the higher level of theory.<sup>60</sup>

#### **1.4. Global optimization methods**

One way to tackle the structural complexity of the active sites in a rational way is to carry out an exhaustive exploration of the underlying PES – a hyperspace in the 3N-dimensional space – relating the energy and distribution and location of atoms constituting the chemical system. Global and local optimization algorithms are designed to address this problem. Global optimization (GO) algorithms have an advantage over local optimization, where the latter can only provide information over a particular point and its neighboring area. Scanning the PES with global optimization algorithms is carried out using heuristic methods, that search the breadth of an E(X) function, where X is a 3N-dimensional vector of atomic coordinates. As the PES exploration aims to visit the local minima basins, the GO methods try to locate the minimum X by minimizing the following function:

$$E(X) = \min[E(X)] \tag{E1.3}$$

The overall idea behind the GO is to find a global minimum (GM) on the PES in an efficient way by minimizing the computational costs required.<sup>61</sup> To solve a global optimization problem related to a certain catalytic system, an issue regarding the amount of computational resources required for searching a GM for a given cluster has to be adequately addressed. For an N-atom system 3N+1 – dimensional PES has to be explored. The complications arise with increasing the system size, where the number of stable structures exponentially rises with the number of atoms. Therefore the computational methods have to provide a good compromise between the amount of the computational sources and the adequacy of the proposed catalytic model. The use of additional information on the system bonding or preferable coordination in biased GO methods can

drastically accelerate the global PES exploration.<sup>60</sup> However, defining structural motifs prior to GO might result in erroneous structures, making the unbiased GO methods for the exploration of the PES more desirable.

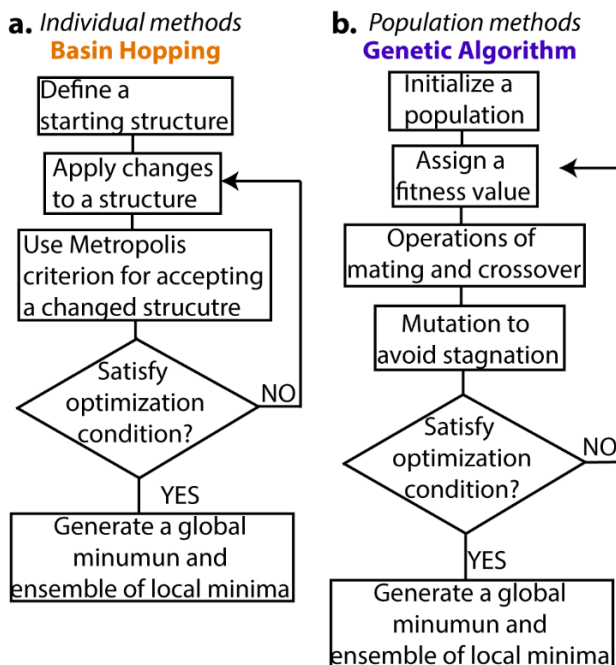


**Figure 1.1** Comparison of different GO methods. **(a)** Individually-based Basin Hopping (BH), and **(b)** population-based Genetic Algorithm. Reproduced with permission from ref (62).

A general workflow of a representative individually-based algorithm is schematically illustrated in **Figure 1.1a**, exemplifying the basin-hopping algorithm. The procedure starts with the generation of the starting configuration. Then it gets restructured using a selected procedure. The system makes a decision based on the Metropolis criterion if a new configuration is accepted or not. If not, the new configuration is rejected and the current one gets transformed again.

The individually-based methods are distinguished by the way they generate new structures  $x^{i+1}$  from the current one  $x^i$ . In the basin-hopping algorithm, random atomic displacements from their original positions are employed (Cartesian displacement operator, geometric center displacement operator), twist operator that generates structural alterations by rotating a set of atoms around a certain axis, exchange operator that exchanges the pairs of atoms between two chemical species, etc.<sup>63</sup> In the Monte-Carlo minimization algorithm, a random change in randomly selected dihedral angles was implemented.<sup>64</sup> The MD codes are known to solve the Newtonian, Langevin, or Brownian equations of motion, collect information on the dynamics of the system and move the

structure from one minimum to another. Temperature plays an important role in governing both MC and MD methods. These algorithms were called equivalent to crystallizing the system at a slow rate from meted state.<sup>65</sup> The simulated annealing method is based on the variation of the MD - and MC-based algorithms, in which the system is heated up to a high temperature to enable a broad exploration of the PES, followed by the temperature decrease to generate new configurations. In the individually-based algorithms, the choice of the starting configuration is critical, because if it is chosen incorrectly, an irrelevant region of the PES would be explored.<sup>65</sup>

In contrast to the individual GO methods, population-based algorithms operate with a population, collection of different structural solutions, which is evolving through perturbation operations and updating mechanisms. The algorithm conceptually mimics the evolution or animal behavior with the most popular examples being the genetic algorithm (GA),<sup>66</sup> artificial bee colony (ABC),<sup>67,68</sup> particle swarm optimization (PSO),<sup>69</sup> and differential evolution (DE).<sup>70</sup> **Figure 1.1b** illustrates the workflow for the population-based algorithms, which include the following primary steps, namely, the generation of the population of clusters followed by an update of the population pool by applying the specific operators on an individual cluster in the population until convergence criteria are met. Compared to the individually-based methods, evolutionary algorithms depend much less on the choice of the initial configuration. As a result, in these methods, random initial structures can be used. Population-based GO algorithms can be effectively used to locate the GM or their low-energy isomers that correspond to the configurations formed in the experiment and reflect the equilibrium in the low-temperature limit.<sup>71</sup> Population-based GO methods have successfully been applied to optimizing the structures of nanoparticles and clusters: MgO-supported Pd, Au and AuPd,<sup>72</sup> Ir and Ir-rich PdIr clusters,<sup>68</sup> identification of the catalytically relevant stable surfaces, 2D nanostructures of boron-carbon compounds,<sup>73</sup> single-layer and bilayer materials of C, Si, Ge, Sn and Pd.<sup>74</sup> In the next section, we will illustrate the power and capabilities of the popular population and individual-based GO methods with relevant recent heterogeneous catalysis examples.

#### **1.4.1. Individual-based algorithms**

A representative individually-based GO method, the Basin Hopping algorithm (**Figure 1.1a**), is the Monte Carlo (MC) method, in which the system jumps between the minima by performing random hopping transformations and local minimization of the candidates. The algorithm explores the PES using Monte Carlo sampling of the local minima by applying random atomic displacements and the Metropolis criterion.<sup>63</sup> The algorithm starts with geometry optimization of the initial configuration followed by the Markovian process. The applied structural changes depend on the nature of the system and can include such operations as random changes or the exchange of atoms. If the structural alterations were sufficient for overcoming a nearby transition state, the algorithm moves to another minimum. In this way, the proximity of the starting

configuration is explored, which contrasts with the GA method, which samples more distant PES regions via crossover operation.<sup>65</sup> The selection of the low-lying structures is based on the Metropolis MC criterion, which accepts a new structure if a random number between 0 and 1 is less than the Boltzmann factor ( $e^{-\Delta E/kT}$ , where  $T$  is the temperature and  $\Delta E$  is the energy difference between an isomer and initial local minima). These MC moves are repeated for a given number of steps, and the global minimum is assumed to be the lowest-lying isomer. The main disadvantage of the BH approach is that random changes can be insufficient to escape from a significantly deep energy basin and can also give rise to the slow convergence of the search.<sup>57</sup>

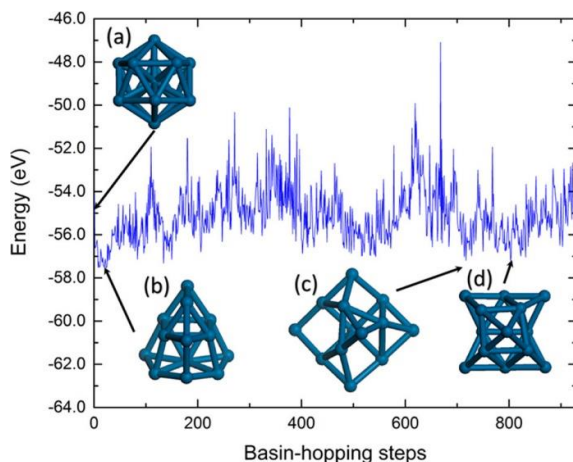


**Figure 1.2** DFT-based BH for  $\text{Pt}_{13}$  with the starting configuration (a) and generated low-lying structures (b, c, d). Reproduced with permission from ref (75).

These issues are addressed by modifying and extending the BH procedure with other GO methods. For example, the parallel excitable walkers (PAW) extension of the BH allows the sampling simultaneously different PES regions by running several BH optimizations in parallel. To prevent “walkers” from sampling the same region, they dynamically repel each other and their movements across distinct regions are of the order of the parameter space.<sup>76</sup> For geometrically different structures, the Metropolis MC selection criterion is used. Another way to overcome the slow convergence and the minima trapping is based on the incorporation of GA strategies into the standard BH method. Huang et al.<sup>57</sup> employed the BH-GA combined algorithm to carry out the GO of PtCo clusters. They combined the BH elements such as the random shift of coordinates, local optimization by the steepest descent algorithm, and the operations of crossover and mutation from the GA. A similar approach was employed by Paz-Borbón et al, who increased the efficiency of the DFT-based BH optimization of bimetallic nanoparticles by enabling low-energy permutations of the different metal compounds through the atom-exchange “swap” routine implemented in the BH algorithm.<sup>77</sup>

DFT- and empirical potentials-based BH algorithm was used to identify the most stable bimetallic Pt-Cu species supported on CeO<sub>2</sub>(111) surface. Simulations revealed a strong preference for the bimetallic species to form pseudo-planar configurations on the oxide surface. This tendency was rationalized by the formation of strong bonds between the metallic atoms and oxygen atoms of the surface. Fung et al employed a plane-wave BH to identify structures of the stable Pt<sub>13</sub> clusters (**Figure 1.2**). Even for such a small system, the identification of all GMs required about 1000 simulation steps.

The main problem of the ordinary Monte Carlo algorithm is that they tend to revisit many times the neighboring configurations.<sup>78</sup> To overcome this, a flooding algorithm has been proposed. If a basin was visited during the simulations, the potential is increased to reduce the chances of accepting the configuration from the same region. This approach is complicated by the difficulty of determining the shape of the basin that has to be flooded. Thus to effectively climb out of the wrong funnels, a standard Markovian-based MC process was abandoned. In the Minima Hopping (MH) algorithm, a feedback mechanism that accounts for the whole simulation history and enforces the exploration of new regions is introduced.

MD-based simulations are also employed in the individually based algorithms where Newton's equations of motion are solved to generate a trajectory of atomic positions. Compared to the MC approach, where no time scale is involved and the configurations are selected randomly, MD methods explicitly simulate time evolution.<sup>79</sup> It results in a trajectory that shows how the position and velocities of the particles in the system vary with time. MD can realistically describe the molecular motion that involves large structural alterations and conformations changes. Hence, MD methods can investigate the evolution and dynamic behavior of important intermediates and reactive ensembles that are relevant under the conditions of catalytic conversion.

As long as no bonds are broken or formed in the process, the MD simulations can rely on the definition of classical interatomic potentials, which define the energy of the system and the forces that arise via individual terms for the bond stretching, angles bending, van der Waals and electrostatic interactions. To account for the electronic properties and, related, changes in the electronic structure during chemical transformations, the electronic Schrödinger equation has to be solved in the aiMD approach. AiMD allows direct monitoring of the evolution of the chemical system over different states, accounting for the cleavage of the bonds. The idea behind the aiMD is to combine finite temperature dynamics with forces acting on the nuclei from the electronic structure calculations computed "on the fly" as the trajectory is being generated.<sup>80</sup> Another important aspect is that aiMD takes the solvent effect into account explicitly and is general enough for simulating large multicomponent systems. However, while being reliable in terms of the electronic structure and geometry predictions, this computationally demanding technique requires a lot of resources to simulate high-energy rare events. The

key limitations of the conventional aiMD methods are the exponentially low probability of overcoming a high activation barrier at relatively low temperatures and the high probability of being trapped in high-entropy regions when the temperature is high.<sup>81</sup> Several highly efficient and successful computational strategies have been developed to enhance sampling in the MD simulations, which will be briefly discussed below.

MD-based sampling techniques are often employed for extracting physically meaningful conformations. A lot of methods have been designed to perform MD-based conformational searches.<sup>82,83</sup> A good efficiency has been achieved for small organic molecules, assuming that all the conformations can be identified as a combination of the dihedral angles and a small number of conformations of small rings. However, these methods do not account for the more complex interactions, including intramolecular nonbonded interactions and the confinement effect. A version of the conformational search is a low-frequency mode-following method. As proposed by Paul Labute, the low-lying conformations can be found by perturbing the system on each iteration along the low-frequency mode direction.<sup>84</sup>

Another extension of the MD for studying rare events is metadynamics.<sup>85</sup> The metadynamics uses an adaptive biasing potential along the simulations to escape local minima and jump over the high energy barriers as a function of one or several CVs. Ideally, this bias potential has to be equal to the free energy inverted in sign to achieve uniform sampling. The total potential consists of the original potential  $V_0(x)$  and a history-dependent biasing potential  $\Delta V(x, t)$ :

$$V(x) = V_0(x) + \Delta V(x, t) \quad (\text{E1.4})$$

where  $x$  is a configurational variable. This biasing potential is accumulated from the Gaussian functions with the predefined parameters and centered on the points of the CV.<sup>86</sup> As the simulations proceed, the minima of the Free Energy Surface (FES) are getting filled with the optimal biasing potential. The use of the history-dependent bias allows for marking the areas of the CV that might have been visited before and avoiding them.

The thermodynamic integration method, sometimes also referred to as the blue moon sampling, prompts the barriers crossing by freezing the reaction coordinate in a number of windows and calculating the mean force at each state. In this way, several selected local configurations are explored and for each of them, the mean force is computed. These local mean forces are then used to reconstruct the FES via numerical integration. For a point  $x$  in the configurational space of the collective variable, the free energy difference is expressed as:

$$F(x) - F(x_0) = \int_{x_0}^x \left( \frac{\partial F}{\partial x} \right) dx \quad (\text{E1.5})$$

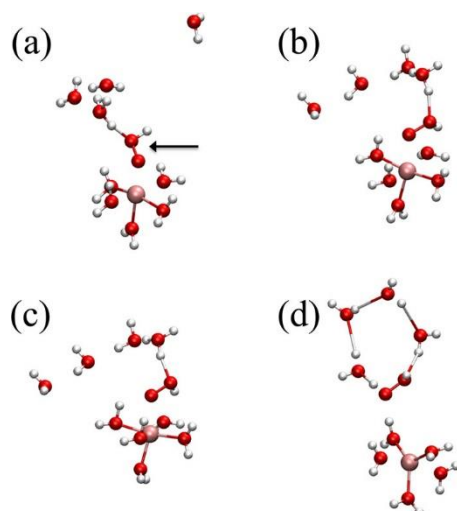


**Figure 1.3** Representative snapshots from the constrained aiMD of the second stage of H<sub>2</sub>O oxidation over a water-solvated Fe-oxo complex. Simulations reveal the reaction of the oxo ligand with H<sub>2</sub>O results in (a) the formation of the Fe-bound H-O-O<sup>-</sup> ion Fe center with a second H<sup>+</sup> released to the solvent, which is (b) stabilized by the formation of a short open chain of H<sub>2</sub>O molecules. Subsequent closure of the chain (c) is accompanied by the re-orientation of one of the water molecules with its O-H-bond toward the peroxo ion. The subsequent (d) concerted proton transfer within the solvation cluster results in the H<sub>2</sub>O<sub>2</sub> product formation. Reproduced with permission from ref (87).

This method does not require tuning the parameters, and its statistical error can be improved by either extending the simulation time or introducing more states on the reaction path. Although the kinetic end entropic outcome of the metadynamics-based methods is not always straightforward, it is the method of choice when high dimensional FES is explored with multiple CVs. The thermodynamic integration is more straightforward, but its utility is normally limited to the simple reaction described by a single CV.

For example, this method was successfully used by Cheng and co-workers to study the electrochemical reduction of CO<sub>2</sub> to CO and formates on the Cu surface.<sup>88</sup> The combination of the aiMD and thermodynamic integration was used to study the dynamic effects of solvents in the conversion of H<sub>2</sub>O into H<sub>2</sub>O<sub>2</sub> over Fe(IV)-oxo (ferryl) complexes (**Figure 1.3**). The simulation revealed that the reaction proceeds in two steps, namely, the solvent-assisted formation of the H-O-O<sup>-</sup> species at the Fe center followed by a very fast reprotonation of the intermediate by the solvent. The representative snapshots of the simulation shown in **Figure 1.3** highlight the highly dynamic nature and varied coordination environment of the solvated Fe complex during the catalytic reaction.

Usually, the biggest challenge in the application of these advanced sampling techniques to realistic catalytic systems is to find suitable collective variables that drive the transition from one energy basin to another. It is assumed that microscopic variables change fast and they can instantaneously get equilibrated. However, each step uses molecular dynamics for equilibration, which is not always efficient at escaping the metastable states.<sup>89</sup> And if some important CVs are missing, the simulations can suffer from insufficient sampling and lead to slow convergence. The task of choosing CVs is far from trivial. There are several criteria that a suitable CV has to meet: a clear distinction between the local minima; a description of the relevant events occurring in the system; the number of them should not be too large. Popular CVs, that is, for example, supported by the PLUMED package, include the absolute position of an atom or a group of atoms, the distance between atoms, angle, torsion, minimum distance, coordination number, number of intra-protein hydrogen bonds, the radius of gyration, dipole moment and others.<sup>90</sup> Apart from the CV-based algorithms, some methods do not require the specification of predefined CVs.

#### 1.4.2. Population-based methods

The population-based methods offer an advantage over the individually-based methods discussed above in being independent of the initial configuration. Such methods are commonly considered to be more effective in generating configurations from different regions of PES. A genetic algorithm (GA) is one of the most widely known and used population-based GO methods that follow the principles of natural selection and evolution. A more detailed description of the method can be found<sup>91,92</sup> and the workflow of the method is illustrated in **Figure 1.1b**. This algorithm learns the features of “good” structural solutions and keeps improving them throughout the continuous change of the structure. Note, that the level of “goodness” is defined by the energy of the structure computed at a particular level of theory. The general workflow for finding the overall best solution can be described as the sequence of operations such as fitness assignment, crossover, mutation and selection. The algorithm starts with the generation of the population pool, which size is defined by the available computational resources. In the first step, geometry optimization is carried out for all starting configurations at an appropriate level of theory. Then each configuration gets assigned its fitness value which is a function of its relative energy. Both absolute and dynamic fitness can be used, where the former compares the fitness values between the generation, while the latter scales the fitnesses of all individuals relative to the worst and best candidates. The dynamic scaling uses the normalized value of the energy of each structure in the population pool:

$$\rho_i = \frac{U_i - U_{\min}}{U_{\max} - U_{\min}} \quad (\text{E1.6})$$

where  $U_{\max}$  and  $U_{\min}$  are the maximum and minimum energy in the current population. The fitness can be represented by different functions. The most used fitness functions are

the exponential, linear and hyperbolic tangent.<sup>66</sup> The choice of the fitness function controls how significantly the fitness decreases with the energy increase. The new structures are generated following the procedures of mating and crossover applied to the previous generation. To produce new configurations in the crossover operation, an offspring and a few parent structures are chosen amongst selected configurations, which are then combined using the roulette wheel or the tournament selection for mating. In the roulette wheel approach, the cluster is chosen randomly and its fitness value is compared to a random number between 0 and 1. To be accepted for a genetic operation, the fitness value has to be greater than a random value. In the tournament approach, the parents are the two structures with the highest fitness score selected from a “tournament” pool, which is generated from randomly selected structures. The subsequent crossover operations include one-point and two-point crossover. For the former, the parent strings are cut at the same position and offspring is generated by adding complementary genes. In the latter, two-point crossover, the offspring are generated from the parent string that is cut at two different positions. A sufficient diversification of the generated population is ensured by the mutation operations, which keeps the population from stagnation. The mutations are performed on the offspring with a certain probability and they include such operations on the atoms as relocation, rotation, exchange etc.<sup>62</sup> In the selection step, the produced offspring with the highest fitness value is selected for the next iteration, which includes only the structures with the lowest energy, whereas the other structures are discarded.

A genetic algorithm has been very successfully utilized for unravelling structures of nano-sized metallic clusters. A relevant example of the use of DFT-PAW-PBE-based GA in heterogeneous catalysis is the computational study by Liu and co-workers on CO oxidation by gold nanoparticles (**Figure 1.4**).<sup>93</sup> The idea behind this is to provide insight relevant to the design of more active Au catalysts for CO oxidation by studying the relationships between the adsorption energies of O<sub>2</sub> and CO and the reaction barriers. Initially, the global minima of small Au<sub>n</sub> (n = 3–16, 20) configurations were obtained with the GA, while the larger species (n = 38, 55, 79) were constructed using the Wulff theorem based on the energies of the extended surfaces. It was shown that the structures having less than 13 atoms adopt a planar or two-dimensional configuration, while the larger ones adopt a three-dimensional configuration. Next, it was shown that the reaction barriers relevant to the CO oxidation scale linearly with CO and O<sub>2</sub> adsorption energies, where different scaling relationships were formulated for each class. In general, the planar Au clusters required stronger adsorption of O<sub>2</sub> than three-dimensional structures, with the most optimal performance achieved for the planar Au<sub>9</sub> and three-dimensional Au<sub>79</sub>. Authors indicate that the catalytic performance can be further improved by, for instance, introducing alloying elements, because the Sabatier optimum was not achieved with pure Au particles.

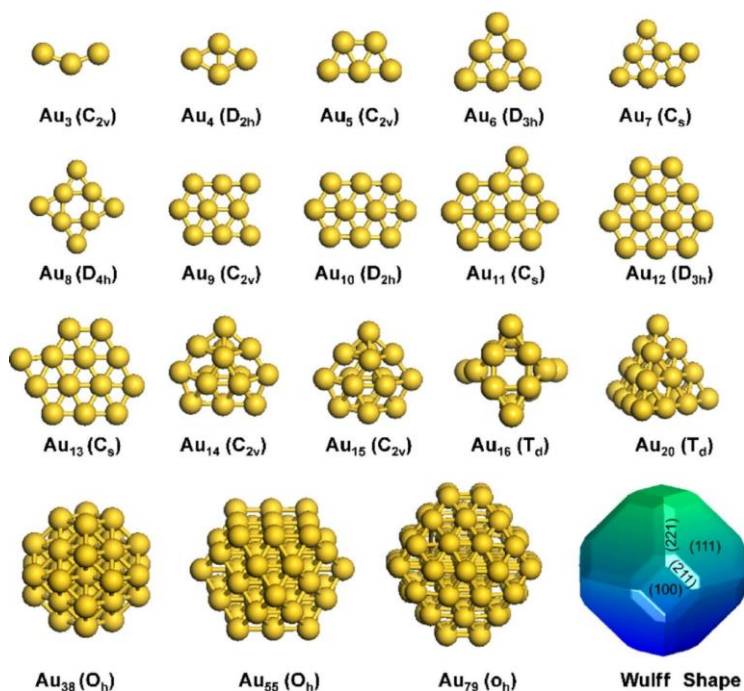


**Figure 1.4** The most stable configurations and symmetries of  $Au_n$  ( $n = 3-16$  and  $20$ ) clusters generated using GA. The clusters with 13 atoms have a two-dimensional structure, while more atoms in the structure result in three-dimensional configurations. Reproduced with permission from ref (93).

GA is a powerful tool to reduce the incompleteness of the local structural analysis in such tasks as the search for comprehensive energy scaling relationships and the development of transferable reactivity descriptors. Liu et al carried out a thorough computational study on surface reconstruction and segregation effects during  $CO_2$  hydrogenation over CoCu alloys.<sup>94</sup> The authors found that the formation of strongly-bound surface intermediates such as  $*CO$ ,  $*COOH$  and  $HCOO^*$  in the course of the reaction induces substantial restructurings and segregation of the reactive surfaces. GA was used to predict the lowest-energy surface configurations. It was proposed that the preference for the segregation of the alloy surfaces can be predicted from the adsorption preference of a given intermediate, defined as the binding energy difference. Importantly, the computational analysis of the reaction mechanism revealed that surface segregation can give rise to the enhanced stability of some of the key reactive intermediates, such as the activated surface carboxylate in this case. Computational analysis predicted that the Co-segregated surfaces should exhibit higher activity in  $CO_2$  conversion, which however comes at the expense of the decreased selectivity to the target  $CH_3OH$  product. The authors emphasized the rather misleading picture obtained by the model in vacuum calculations and advocated for the importance of the *operando* computational modelling

to understand and predict the complex dynamic surface phenomena taking place under the actual reaction conditions and often playing the defining role in the behavior and performance of the catalyst system.

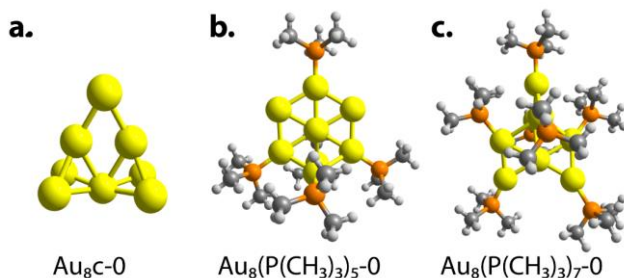


**Figure 1.5** Global minima of  $Au_8^{2+}$  and  $Au_8L_n^{2+}$  generated using NWPEsSe algorithm. (a)  $Au_8C-0$  cluster, (b)  $Au_8(P(CH_3)_3)_5-0$  cluster, (c)  $Au_8(P(CH_3)_3)_7-0$  cluster. The figure is reproduced from ref (68).

Artificial bee Colony (ABC) is a swarm intelligence population-based method, which was inspired by the behavior of bee colonies, where differently-specialized bees are looking for the best nectar.<sup>95</sup> This algorithm has been successfully utilized in various optimization problems as well as for predicting protein structures and nanoparticle configurations.<sup>96,97</sup> In the ABC algorithm, three kinds of bees are present: employed, onlooker and scout bees.<sup>98</sup> The employed bees are looking for new better solutions in the neighborhood of the current one using the expression:

$$v_{km} = x_{km} + \phi_{km}(x_{km} - x_{lm}) \quad (E1.7)$$

where  $m$  and  $l$  are random indexes, and  $\phi_{km}$  is a random number in  $[-1,1]$ . The onlookers bees are looking for new solutions in a probabilistic manner utilizing the following equations:

$$p_k = \frac{fit_k}{\sum_{n=1}^{SN} fit_n} \quad (E1.8)$$

where  $fit_k$  is the fitness value of the solution  $k$  and  $SN$  is the number of solutions.<sup>99</sup> The scout bees check if there are structures that were not updated in the predetermined number of trials, then it gets discarded and replaced with a new solution, generated according to:

$$x_{km} = x_m^{min} + rand(0,1)(x_m^{max} - x_m^{min}) \quad (E1.9)$$

where  $k$  equals the number of solutions and  $m$  is the number of parameters. The Northwest Potential Energy Search Engine (NWPEsSe) method is an extension of the ABC methodology, which allows dealing with structures containing more than 1300 atoms.<sup>68</sup> In NWPEsSe, each cycle uses only one employed, onlooker and scout bees and the generated structures do not replace other configurations but append to the population.

**Figure 1.5** shows the most stable gold clusters stabilized by phosphine ligands predicted

by the NWPEsSe algorithm. For bare golden clusters, the Au<sub>8</sub>c-0 isomer (**Figure 1.5a**) is the most stable configuration while the ligated by 5 P(CH<sub>3</sub>)<sub>3</sub> (**Figure 1.5b**) and 7 P(CH<sub>3</sub>)<sub>3</sub> (**Figure 1.5c**) clusters have a different GM as their cores which points out that the ligation can drastically influence the electronic stabilization.

Both individual- and population-based methods can be successfully applied to sample the PES of complex catalytic systems. In this way, robust solutions can be generated that are difficult to predict based solely on chemical intuition. In some methods, such as GO algorithms, a single global minimum structure with the highest stability is produced. However, in the last decade, there was growing evidence that in many cases the highest catalytic activity comes from structures with lower stability. In the next paragraph, the catalytic role of the global minima structure and other low-energy isomers obtained in GO methods will be discussed.

### 1.4.3. GM vs metastable states: what to choose?

Until recently, computational studies reduced the catalytic systems to stationary models and put the main emphasis on finding the global minima - assumed to be the active sites - from the GO methods. It has been often assumed that this structure or interface is maintained under reactive conditions. In reality, the catalytic systems undergo restructuring due to the heat, electrochemical potential, and pressure of the reactants and products. Thus a catalytic interface has to be studied in a view of evolving statistical ensemble, where every structure has its contribution to the catalytic activity.<sup>19</sup> Sun et al. showed that the GO algorithms produce the GMs that can alone give a misleading picture of the catalyst's reactivity, underestimating the catalytic role of the metastable sites. The dynamics and migration of these sites over small isomerization barriers complicate establishing the interdependence between the occurrence of the active sites, their structure and activity.

For example, metastable configurations of H-covered Pt<sub>13</sub> clusters have been shown to play a key role in the hydrogen evolution reaction (HER) and catalytic methane activation. Computational analysis revealed that the HER activity of different H-covered Pt<sub>13</sub> configurations correlates inversely with their relative stability. The second-most stable nanoparticle configuration (Pt<sub>13</sub>H<sub>26</sub>GM2) was found to be a million times more active than the GM structure (Pt<sub>13</sub>H<sub>26</sub>GM0) (**Figure 1.6** left). To account for both activity and stability, the weighted exchange current densities were evaluated. The right part of **Figure 1.6** shows that the free energy of the Pt<sub>13</sub>H<sub>26</sub>GM2 is too high to give a substantial contribution at room temperature and Pt<sub>13</sub>H<sub>26</sub>GM1 provides a smaller enhancement though but a higher occurrence probability. Similarly, the activity of Pt nanoparticles in methane activation is also governed by the minor metastable isomers. The calculated rate constants for methane activation were normalized with the corresponding Boltzmann distribution to account for the relative population of different H-covered Pt<sub>13</sub> configurations. It was demonstrated that the catalytic reaction is dominated by the

metastable isomer  $\text{Pt}_{13}\text{H}_{26}\text{GM1}$ , which intrinsic reactivity is 580 more active than the most stable configuration of the GM0. Even when corrected by its occurrence probability, this structure remains 30 times more active than the GM0.

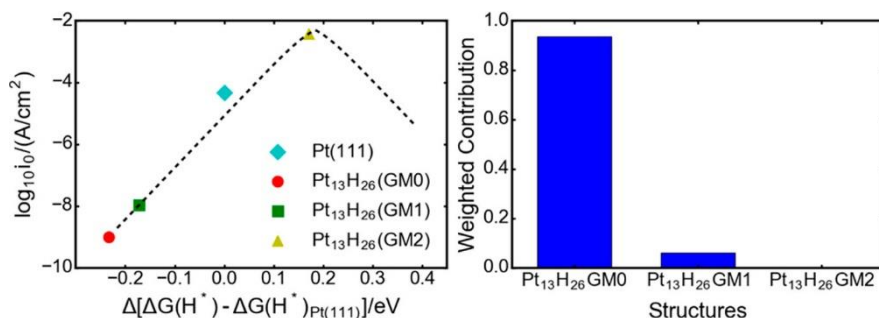


**Figure 1.6** The activity of the three most stable global minima configurations of the  $\text{Pt}_{12}\text{H}_{26}$  in the HER. Left: the exchange current densities vs adsorption free energies of hydrogen. Right: The normalized contribution of different global minima structures in the HER rate. Reproduced with permission from ref (100).

The population-based GO methods provide a very diverse functionality in the screening of the PES and deriving the ensemble of configurations, but they have common disadvantages of being limited by the harmonic approximation and lacking temperature effects.<sup>101</sup> Therefore, identified energetically stable configurations are commonly attributed to low-temperature conditions. On the other hand, the individually-based GO methods can provide very interesting and important insights into the reaction mechanisms under the catalyst operation conditions, but they are not suitable for a large-scale exploration of alternative reaction mechanisms under varying reaction conditions. Due to the extremely high computational demands and complexity of the underlying techniques, they are normally limited to a selected catalytic step and focus on a very narrow pre-defined range of reaction conditions. To get an insight into the condition-dependencies of active site speciation and reaction mechanisms with these methods, separate integration needs to be done for each point in the highly complex multidimensional condition space. To understand how the variations of reaction conditions may influence the stability/preferred configuration of the reactive ensembles and/or the progress of the catalytic reaction, alternative methodology such as *ab initio* thermodynamics can be utilized.

### 1.5. *Ab initio* thermodynamics analysis

The GO methods are powerful tools to screen the vast chemistry space of the surface intermediates and determine the intrinsically most stable configurations of the catalytic ensembles. The main limitation of these methodologies is that most implementations

target the global search for the minima on the potential energy surface representing the idealistic 0K/UHV catalyst model. The transition to the *operando* model of the catalyst surfaces requires that the structural search and stability assessment is expanded with additional degrees of freedom due to the conditions space that encompasses the effects of finite temperature, pressure and the reactive environment.<sup>101</sup> One of the most powerful and practical approaches to account for these effects is the *ab initio* thermodynamics analysis (aiTA) originally introduced by Reuter.<sup>102–104</sup>

This method assumes the exact match of the minima on the potential and free energy surfaces. The condition-dependent free energies of the candidate structures are obtained by applying free energy corrections computed from statistical thermodynamics to the electronic energies obtained from DFT calculations. The fundamental approximations and main principles of the method are summarized below. Considering the simple model of gas-solid heterogeneous catalytic systems, we can divide the system into three parts, namely, the gas phase, the bulk solid phase and the exposed surface. Assuming three parts are homogeneous and in equilibrium with each other, we can express the surface free energy as:

$$\gamma(T, p_i) = \frac{1}{A} [G(T, p_i, N_i, N_j) - N_i \mu_i - N_j \mu_j] \quad (\text{E1.10})$$

where  $\gamma$  is the surface free energy,  $A$  is the surface area,  $G$  is the Gibbs free energy of a particular surface configuration containing  $N_i$  species  $i$  and  $N_j$  species  $j$ , and  $\mu_i$  and  $\mu_j$  are the chemical potentials of the corresponding reservoirs of species  $i$  and  $j$ . Note, that species  $i$  are present in the gas phase.

To compare the stabilities of different candidate configurations, it is more convenient to compare with a reference surface configuration which usually is the clean surface, as shown in (E1.11).

$$\gamma(T, p_i) - \gamma_0(T, p_0) = \frac{1}{A} [G(T, p_i, N_i, N_j) - G_0(T, p_i, N'_i, N'_j) - \Delta N_i \mu_i - \Delta N_j \mu_j] \quad (\text{E1.11})$$

where  $\gamma_0$  and  $G_0$  are the surface free energy and Gibbs free energy of the reference surface configuration, respectively. For the Gibbs free energy, it can be approximated from the total DFT energies via equation (E1.12):

$$G = E^{\text{total}} + F^{\text{vib}} + F^{\text{conf}} + pV \quad (\text{E1.12})$$

where  $E^{\text{total}}$  is the total DFT energies,  $F^{\text{vib}}$  is the vibrational free energy,  $F^{\text{conf}}$  is the configuration free energy, and  $V$  is the volume. In most cases, only the  $E^{\text{total}}$  is considered because the differences in other terms are assumed to be minor. For example, in the solid state below 1000 K, the change of  $F^{\text{vib}}$  and  $F^{\text{conf}}$  does not exceed  $10 \text{ meV}/\text{\AA}^2$  and  $3 \text{ meV}/\text{\AA}^2$ , respectively. With these approximations, therefore, we can express that

$$\Delta E^{\text{tot}} = E^{\text{tot}}(N_i, N_j) - E_0^{\text{tot}}(N'_i, N'_j) - \Delta N_i E^{\text{tot}}(i) - \Delta N_j E^{\text{tot}}(j) \quad (\text{E1.13})$$

where the terms on the right-hand side are the DFT total energies for the investigated surface configuration, reference surface configuration, and the reservoirs of components gas-phase species  $i$  and metal-phase species  $j$ , respectively. The last two terms allow us to compare the stability of configurations with different numbers of species. The chemical potential can be calculated from  $\Delta\mu_i = \Delta\mu_i(T, p_i)$  where  $\Delta\mu_i = \mu_i - E^{\text{tot}}(i)$  and  $E^{\text{tot}}(i)$  is the total DFT energies of the isolated gas-phase species  $i$ . Otherwise, these values can also be found in thermodynamic tables.<sup>105</sup> The  $\mu_j$ , which is the chemical potential of surface species, can be evaluated from the excess surface free energy with regard to the reference configuration.

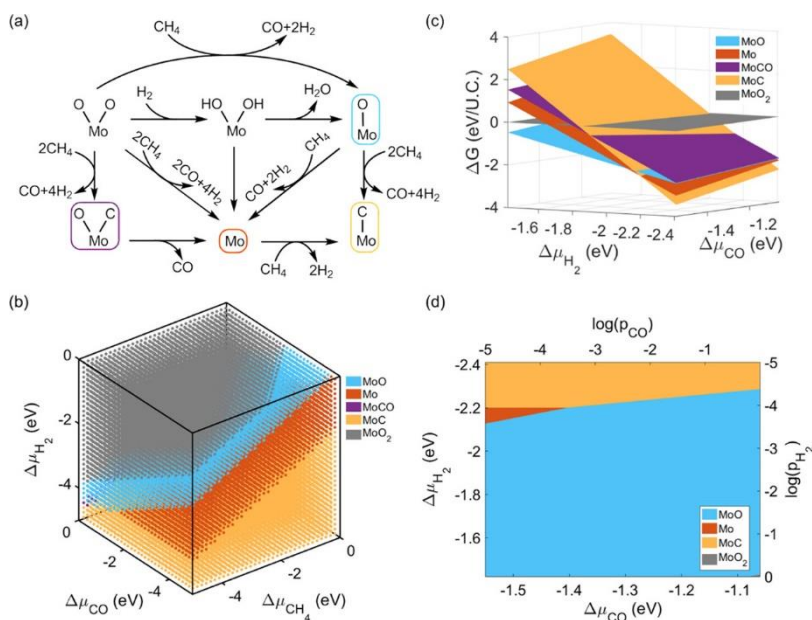


**Figure 1.7** (a) The simplified reduction and carburization pathways of  $[\text{MoO}_2]^{2+}$  cations in ZSM-5 zeolite with  $\text{CH}_4$  during the MDA reaction. (b) aiTA-computed phase diagram for the intrazeolite  $\text{MoO}_x\text{C}_y$  species depicting the most stable active site composition at different chemical potentials of  $\mu_{\text{CH}_4}$ ,  $\mu_{\text{CO}}$ , and  $\mu_{\text{H}_2}$  derived from the respective (c) condition-dependent Gibbs free energy diagrams. *Operando* computational characterization of the reactive sites follows from (d) the projection of the most stable species at a fixed  $\mu_{\text{CH}_4}$  corresponding to the MDA catalytic conditions ( $p_{\text{CH}_4} = 0.95$  atm and  $T = 1000$  K). Reproduced with permission from ref (108).

The aiTA is widely used for *operando* computational characterization of the reactive ensembles on the surfaces<sup>106</sup> and in the pores of solid catalysts.<sup>21</sup> This approach enables the identification of the structure and morphologies of clusters, surface structural motifs, catalyst composition and their evolution under varying reaction conditions.<sup>107</sup>

A representative example of the aiTA is the identification of the structure of molybdenum (oxy) carbide clusters formed at the different stages of operation in the Mo/ZSM-5 zeolite methane dehydroaromatization (MDA) catalyst.<sup>108</sup> The very high operating temperature and high rate of catalyst deactivation in this process are the key hurdles in the experimental identification of the active site and the reaction mechanism.<sup>109</sup> The possible reduction paths for the oxidic  $[\text{MoO}_2]^{2+}$  and  $[\text{Mo}_2\text{O}_5]^{2+}$  precursor species inside the ZSM-5 pores were studied by periodic DFT calculations, while the aiTA method was employed to assess the condition-dependent stabilities of the reduced active configurations. **Figure 1.7b** presents a projection of the condition-dependent formation Gibbs free energies showing the most stable  $[\text{MoO}_x\text{C}_y]^{2+}$  species as a function of temperature and composition of the reactive gaseous phase expressed as chemical potentials  $\mu_{\text{CH}_4}$ ,  $\mu_{\text{CO}}$  and  $\mu_{\text{H}_2}$ . Counterintuitively, the results showed that the initial  $[\text{MoO}_2]^{2+}$  species are destabilized at a lower  $p_{\text{H}_2}$ , where the partially reduced  $[\text{MoO}]^{2+}$  and carburized  $[\text{MoC}]^{2+}$  cations become favored. A similar analysis for the alternative binuclear  $[\text{Mo}_2\text{O}_5]^{2+}$  sites further confirmed the importance of  $p_{\text{H}_2}$  for the stability of the carburized binuclear clusters. The computational analysis revealed that the partially reduced Mo-oxo and carburized Mo carbide intrazeolite cations are predominantly formed during the MDA activation period. The complementary reactivity analysis further pointed to the higher reactivity of the Mo carbide species than their oxygenated counterparts.

The implicit solvent models (e.g. PCM, SMD, etc) can account for the effect of the medium if the solvent does not actively participate in the chemical reaction.<sup>110–112</sup> Nevertheless, complex non-ideal condition dependencies are still not present in most of the computational techniques. These dependencies include the effect of temperature on the solubility of the gaseous reactants, their concentrations and non-ideal activity coefficients and the variations in their partial pressures<sup>113</sup> More advanced solvent schemes, such as COSMO-RS<sup>114,115</sup> or 3D-RISM<sup>116,117</sup>, can account for these factors. Using the COSMO-RS approach, condition-dependent deactivation routes in homogeneous catalytic systems have been revealed.<sup>118,119</sup> Despite these findings, the implementation of a “solvent-corrected” aiTA methodology that describes the liquid-solid interface has not been addressed yet. Additionally to that, a methodology describing the varied concentrations of the non-gaseous species has not been reported so far.

The aiTA methodology enables assessing the relative stabilities and equilibrium population of a given set of configurations under the reaction conditions. This represents aiTA approach as the basic tool for the *operando* computational characterization of heterogeneous catalyst models that allows the modelling structure and composition of the catalyst surface exposed to a reactive environment. The key limitations of this approach are related to (E1.10) the quality and scope of the candidate configurations included in the analysis and (E1.11) the assumption of chemical equilibrium established between all

components in the system. The former limitation can be addressed by combining the aiTA approach with an exhaustive configurational sample using e.g. GO methods.

## 1.6. Scope of the thesis

---

The main aim of this thesis is to develop and implement new *operando* modelling strategies for such complex catalytic systems as cation-modified zeolites and multiphase (electro) catalytic surfaces. Here, we have particularly investigated the methodologies to find the configurations of the reactive extraframework species that are relevant under the reaction conditions and probe their role in the catalytic transformations. The expert-bias-free global optimization approach and the enhanced molecular dynamics techniques in combination with the *ab initio* thermodynamics approach were utilized for gaining an insight into the structure and reactivity of the catalytically active moieties in several industrially-relevant heterogeneous catalyst systems.

**Chapter 2** presents an expert-bias-free discovery of the structural solutions for the Al-oxo stoichiometries in different zeolites topologies. The extraframework Al-oxo species of various nature confined in the cavities of mordenite and ZSM-5 were predicted utilizing the computational power of the genetic algorithm with the semiempirical calculator. The analysis of the possible occurrence of generated global minima Al-oxo stoichiometries has shown the preference for the formation of mononuclear and binuclear species under relevant catalytic conditions.

**Chapter 3** presents a computational investigation of the dynamic behavior of the reactive catalytic species in a reactive environment. To study the nature of the dynamic extraframework copper clusters in mordenite, we have developed a novel workflow, that brings a more reasonable description of the systems with complicated electronic structures. Herein, the power of the *ab initio* molecular dynamics with enhanced sampling and unsupervised machine learning algorithms were combined to enable the expert-bias-free identification of the structurally distinct configurations of the active site. The role of the metastable states and the reactive ensembles for the catalytic reactivity under realistic experimental conditions is evaluated by a model reaction of selective methane oxidation.

**Chapter 4** is a joint experimental-theoretical study that establishes the connection between the nature of the active site formed under *operando* conditions and catalysts' reactivity and stability. In the methanol-to-hydrocarbons reaction, the addition of the Ca species to the oxygenated Ga site in the ZSM-5 structure was found to moderate the activity of the catalyst and prolong the catalyst's lifetime. A genetic algorithm combined with the *ab initio* thermodynamics analysis has given an interpretation of these effects, which originate from the lower dehydrogenation activity of the highly hydrated bimetallic Ca-Ga sites.

**Chapter 5** utilizes the workflow designed in **Chapter 3** and *ab initio* thermodynamics analysis for investigating the concentrations dependencies in methane to methanol process over Cu-oxo in mordenite. The structural nature of the thermodynamical favorability of the bimetallic CuAl-oxo species formation in zeolite was discussed. Evaluating the formation of the bimetallic Cu-Al sites as the defects gave an interpretation of the experimentally observed increase in the catalytic activity of the Cu/MOR at certain concentrations of copper.

**Chapter 6** is devoted to the investigation of the role of the complex reaction environment on the reactivity of the heterogeneous catalyst with the electrochemical CO<sub>2</sub> reduction over Ag surfaces as the representative example. Here a multiscale modelling approach is employed to understand the state of the catalytic surfaces and provide insight into the possible reaction channels under the reaction conditions. The presence of electrolytes and the various cations in it has been shown to influence the accessibility of the CO<sub>2</sub> molecules to the silver surface, governing the outcome of the catalytic process. Based on these findings, an alternative outer-sphere reaction mechanism for CO<sub>2</sub> reduction has been proposed.

## 1.7. References

1. Medford, A. J., Kunz, M. R., Ewing, S. M., Borders, T. & Fushimi, R. Extracting Knowledge from Data through Catalysis Informatics. *ACS Catal.* **8**, 7403–7429 (2018).
2. Reuter, K. *Operando Research in Heterogeneous Catalysis. Springer Series in Chemical Physics* vol. 114 (Springer, 2017).
3. Luo, L., Engelhard, M. H., Shao, Y. & Wang, C. Revealing the Dynamics of Platinum Nanoparticle Catalysts on Carbon in Oxygen and Water Using Environmental TEM. *ACS Catal.* **7**, 7658–7664 (2017).
4. Wen, Y. N. & Zhang, J. M. Surface energy calculation of the bcc metals by using the MAEAM. *Comput. Mater. Sci.* **42**, 281–285 (2008).
5. Prieto, G., Zečević, J., Friedrich, H., De Jong, K. P. & De Jongh, P. E. Towards stable catalysts by controlling collective properties of supported metal nanoparticles. *Nat. Mater.* **12**, 34–39 (2013).
6. Meijerink, M. J., De Jong, K. P. & Zečević, J. Growth of Supported Gold Nanoparticles in Aqueous Phase Studied by in Situ Transmission Electron Microscopy. *J. Phys. Chem. C* **124**, 2202–2212 (2020).
7. Ano, T. *et al.* Probing the temperature of supported platinum nanoparticles under microwave irradiation by in situ and *operando* XAFS. *Commun. Chem.* **3**, 1–11 (2020).
8. Arulmozhi, N., Hersbach, T. J. P. & Koper, M. T. M. Nanoscale morphological evolution of monocrystalline Pt surfaces during cathodic corrosion. *Proc. Natl. Acad. Sci. U. S. A.* **117**, 32267–32277 (2020).
9. Jiang, K. *et al.* Effects of Surface Roughness on the Electrochemical Reduction of CO<sub>2</sub> over Cu. *ACS Energy Lett.* **5**, 1206–1214 (2020).
10. Chee, S. W., Lunkenbein, T., Schlogl, R. & Roldan Cuenya, B. In situ and *operando* electron microscopy in heterogeneous catalysis-insights into multi-scale chemical dynamics. *J. Phys. Condens. Matter* **33**, 153001 (2021).
11. Lamberti, C., Zecchina, A., Groppo, E. & Bordiga, S. Probing the surfaces of heterogeneous catalysts by in situ IR spectroscopy. *Chem. Soc. Rev.* **39**, 4951–5001 (2010).
12. Singh, J., Lamberti, C. & Bokhoven, J. A. V. Advanced X-ray absorption and emission spectroscopy:

- In situ catalytic studies. *Chem. Soc. Rev.* **39**, 4754–4766 (2010).
13. Beale, A. M., Van Der Eerden, A. M. J., Kervinen, K., Newton, M. A. & Weckhuysen, B. M. Adding a third dimension to *operando* spectroscopy: A combined UV-Vis, Raman and XAFS setup to study heterogeneous catalysts under working conditions. *Chem. Commun.* **24**, 3015–3017 (2005).
  14. Bentrup, U. Combining in situ characterization methods in one set-up: Looking with more eyes into the intricate chemistry of the synthesis and working of heterogeneous catalysts. *Chem. Soc. Rev.* **39**, 4718–4730 (2010).
  15. Lukashuk, L. & Foettinger, K. *In situ* and *operando* spectroscopy: A powerful approach towards understanding catalysts. *Johnson Matthey Technol. Rev.* **62**, 316–331 (2018).
  16. Bergmann, A. & Roldan Cuenya, B. *Operando* Insights into Nanoparticle Transformations during Catalysis. *ACS Catal.* **9**, 10020–10043 (2019).
  17. Chandrasekaran, P. *et al.* Prediction of high-valent iron K-edge absorption spectra by time-dependent Density Functional Theory. *Dalt. Trans.* **40**, 11070–11079 (2011).
  18. Timoshenko, J. & Roldan Cuenya, B. *In Situ / Operando* Electrocatalyst Characterization by X-ray Absorption Spectroscopy. *Chem. Rev.* **121**, 882–961 (2021).
  19. Zhang, Z., Zandkarimi, B. & Alexandrova, A. N. Ensembles of Metastable States Govern Heterogeneous Catalysis on Dynamic Interfaces. *Acc. Chem. Res.* **53**, 447–458 (2020).
  20. Frenkel, A. I. *et al.* Critical review: Effects of complex interactions on structure and dynamics of supported metal catalysts. *J. Vac. Sci. Technol. A Vacuum, Surfaces, Film.* **32**, 020801 (2014).
  21. Li, G. & Pidko, E. A. The Nature and Catalytic Function of Cation Sites in Zeolites: a Computational Perspective. *ChemCatChem* **11**, 134–156 (2019).
  22. Kosinov, N., Liu, C., Hensen, E. J. M. & Pidko, E. A. Engineering of Transition Metal Catalysts Confined in Zeolites. *Chem. Mater.* **30**, 3177–3198 (2018).
  23. Xu, J., Qin, Y., Wang, H., Guo, F. & Xie, J. Recent advances in copper-based zeolite catalysts with low-temperature activity for the selective catalytic reduction of NO: X with hydrocarbons. *New J. Chem.* **44**, 817–831 (2020).
  24. Paolucci, C. *et al.* Isolation of the copper redox steps in the standard selective catalytic reduction on Cu-SSZ-13. *Angew. Chem. Int. Ed.* **53**, 11828–11833 (2014).
  25. Godiksen, A. *et al.* Coordination environment of copper sites in Cu-CHA zeolite investigated by electron paramagnetic resonance. *J. Phys. Chem. C* **118**, 23126–23138 (2014).
  26. Gao, F. *et al.* Understanding ammonia selective catalytic reduction kinetics over Cu/SSZ-13 from motion of the Cu ions. *J. Catal.* **319**, 1–14 (2014).
  27. Artiglia, L. *et al.* In Situ X-ray Photoelectron Spectroscopy Detects Multiple Active Sites Involved in the Selective Anaerobic Oxidation of Methane in Copper-Exchanged Zeolites. *ACS Catal.* **9**, 6728–6737 (2019).
  28. Kolganov, A. A., Gabrienko, A. A., Chernyshov, I. Y., Stepanov, A. G. & Pidko, E. A. The accuracy challenge of the DFT-based molecular assignment of <sup>13</sup>C MAS NMR characterization of surface intermediates in zeolite catalysis. *Phys. Chem. Chem. Phys.* **22**, 24004–24013 (2020).
  29. Sushkevich, V. L., Palagin, D. & van Bokhoven, J. A. The Effect of the Active-Site Structure on the Activity of Copper Mordenite in the Aerobic and Anaerobic Conversion of Methane into Methanol. *Angew. Chem. Int. Ed.* **57**, 8906–8910 (2018).
  30. Li, G. *et al.* Stability and reactivity of copper oxo-clusters in ZSM-5 zeolite for selective methane oxidation to methanol. *J. Catal.* **338**, 305–312 (2016).
  31. Li, G., Pidko, E. A. & Hensen, E. J. M. Synergy between Lewis acid sites and hydroxyl groups for the isomerization of glucose to fructose over Sn-containing zeolites: A theoretical perspective. *Catal. Sci. Technol.* **4**, 2241–2250 (2014).
  32. Sharapa, D. I., Doronkin, D. E., Studt, F., Grunwaldt, J. D. & Behrens, S. Moving Frontiers in Transition Metal Catalysis: Synthesis, Characterization and Modeling. *Adv. Mater.* **31**, 1807381 (2019).
  33. Paolucci, C. *et al.* Dynamic multinuclear sites formed by mobilized copper ions in NO<sub>x</sub> selective catalytic reduction. *Science* **357**, 898–903 (2017).
  34. Schleder, G. R., Padilha, A. C. M., Acosta, C. M., Costa, M. & Fazzio, A. From DFT to machine

- learning: Recent approaches to materials science - A review. *J. Phys. Mater.* **2**, 32001 (2019).
35. Thiel, W. Semiempirical quantum–chemical methods. *Wiley Interdiscip. Rev. Comput. Mol. Sci.* **4**, 145–157 (2014).
  36. Friesner, R. A. & Guallar, V. *Ab initio* quantum chemical and mixed quantum mechanics/molecular mechanics (QM/MM) methods for studying enzymatic catalysis. *Annu. Rev. Phys. Chem.* **56**, 389–427 (2005).
  37. Berezin, F. A. & Shubin, M. *The Schrödinger Equation*. vol. 66 (Springer Science & Business Media, 2012).
  38. Desgranges, C. & Delhommelle, J. *A Mole of Chemistry: An Historical and Conceptual Approach to Fundamental Ideas in Chemistry*. (CRC Press, 2020).
  39. Hartree, D. R. The Wave Mechanics of an Atom with a Non-Coulomb Central Field Part I Theory and Methods. in *Mathematical Proceedings of the Cambridge Philosophical Society* vol. 24 89–110 (Cambridge University Press, 1928).
  40. Pidko, E. A. & Hensen, E. J. M. Computational Chemistry of Zeolite Catalysis. in *Zeolites and Zeolite-like Materials* 111–135 (Elsevier, 2016).
  41. Nityananda, R., Hohenberg, P. & Kohn, W. Inhomogeneous electron gas. *Resonance* **22**, 809–811 (2017).
  42. Von Barth, U. & Hedin, L. A local exchange-correlation potential for the spin polarized case. I. *J. Phys. C Solid State Phys.* **5**, 1629–1642 (1972).
  43. Langreth, D. C. & Perdew, J. P. Theory of nonuniform electronic systems. I. Analysis of the gradient approximation and a generalization that works. *Phys. Rev. B* **21**, 5469–5493 (1980).
  44. Tao, J., Perdew, J. P., Staroverov, V. N. & Scuseria, G. E. Climbing the density functional ladder: Nonempirical meta–generalized gradient approximation designed for molecules and solids. *Phys. Rev. Lett.* **91**, 146401 (2003).
  45. Perdew, J. P., Ruzsinszky, A., Csonka, G. I., Constantin, L. A. & Sun, J. Workhorse semilocal density functional for condensed matter physics and quantum chemistry. *Phys. Rev. Lett.* **103**, 26403 (2009).
  46. Becke, A. D. A new mixing of Hartree-Fock and local density-functional theories. *J. Chem. Phys.* **98**, 1372–1377 (1993).
  47. Grimme, S., Antony, J., Ehrlich, S. & Krieg, H. A consistent and accurate *ab initio* parametrization of density functional dispersion correction (DFT-D) for the 94 elements H-Pu. *J. Chem. Phys.* **132**, 154104 (2010).
  48. Grimme, S., Bannwarth, C. & Shushkov, P. A Robust and Accurate Tight-Binding Quantum Chemical Method for Structures, Vibrational Frequencies, and Noncovalent Interactions of Large Molecular Systems Parametrized for All spd-Block Elements ( $Z = 1-86$ ). *J. Chem. Theory Comput.* **13**, 1989–2009 (2017).
  49. Bannwarth, C., Ehlert, S. & Grimme, S. GFN2-xTB - An Accurate and Broadly Parametrized Self-Consistent Tight-Binding Quantum Chemical Method with Multipole Electrostatics and Density-Dependent Dispersion Contributions. *J. Chem. Theory Comput.* **15**, 1652–1671 (2019).
  50. Pracht, P., Caldeweyher, E., Ehlert, S. & Grimme, S. A Robust Non-Self-Consistent Tight-Binding Quantum Chemistry Method for large Molecules. *ChemRxiv* preprint10.26434/chemrxiv.8326202.v1 (2019).
  51. Bannwarth, C. *et al.* Extended tight-binding quantum chemistry methods. *Wiley Interdiscip. Rev. Comput. Mol. Sci.* **11**, e1493 (2021).
  52. Von Solms, N., Koo, K. Y. & Chiew, Y. C. Mixing rules for binary Lennard-Jones chains: Theory and Monte Carlo simulation. *Fluid Phase Equilib.* **180**, 71–85 (2001).
  53. Ivanov, M. V., Talipov, M. R. & Timerghazin, Q. K. Genetic algorithm optimization of point charges in force field development: Challenges and insights. *J. Phys. Chem. A* **119**, 1422–1434 (2015).
  54. Jones, J. E. On the determination of molecular fields. —II. From the equation of state of a gas. *Proc. R. Soc. London* **106**, 463–477 (1924).
  55. Cleri, F. & Rosato, V. Tight-binding potentials for transition metals and alloys. *Phys. Rev. B* **48**, 22–33 (1993).
  56. Yang, Y. H. *et al.* Spark-based improved Basin-Hopping Monte Carlo algorithm for structural

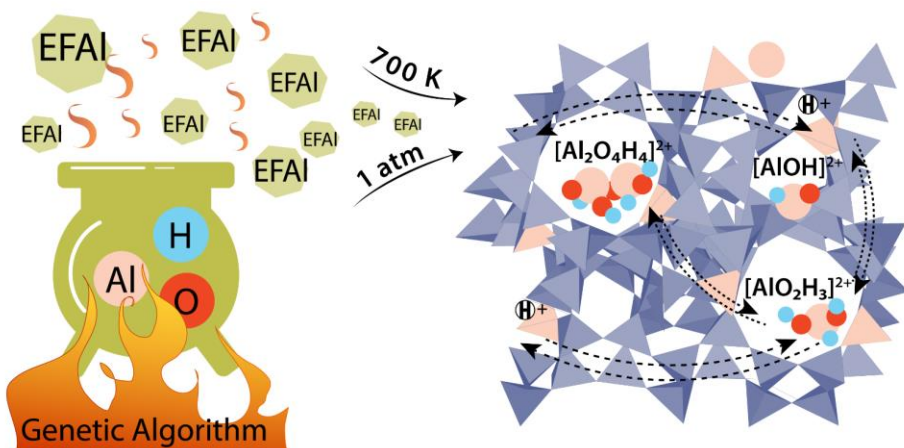
- optimization of alloy clusters. *Phys. Lett. Sect. A Gen. At. Solid State Phys.* **383**, 464–470 (2019).
57. Huang, R., Bi, J. X., Li, L. & Wen, Y. H. Basin Hopping Genetic Algorithm for Global Optimization of PtCo Clusters. *J. Chem. Inf. Model.* **60**, 2219–2228 (2020).
  58. Alexandrova, A. N. & Boldyrev, A. I. Search for the  $\text{Li}_n^{0+1/-1}$  ( $n = 5-7$ ) lowest-energy structures using the ab initio Gradient Embedded Genetic Algorithm (gega). Elucidation of the chemical bonding in the lithium clusters. *J. Chem. Theory Comput.* **1**, 566–580 (2005).
  59. Bannwarth, C., Ehlert, S. & Grimme, S. GFN2-xTB - An Accurate and Broadly Parametrized Self-Consistent Tight-Binding Quantum Chemical Method with Multipole Electrostatics and Density-Dependent Dispersion Contributions. *J. Chem. Theory Comput.* **15**, 1652–1671 (2019).
  60. Jäger, M., Schäfer, R. & Johnston, R. L. First principles global optimization of metal clusters and nanoalloys. *Adv. Phys. X* **3**, 1077–1108 (2018).
  61. Hartke, B. Global optimization. *Wiley Interdiscip. Rev. Comput. Mol. Sci.* **1**, 879–887 (2011).
  62. Zhang, J. & Glezakou, V. A. Global optimization of chemical cluster structures: Methods, applications, and challenges. *Int. J. Quantum Chem.* **121**, e26553 (2021).
  63. Rondina, G. G. & Da Silva, J. L. F. Revised basin-hopping monte carlo algorithm for structure optimization of clusters and nanoparticles. *J. Chem. Inf. Model.* **53**, 2282–2298 (2013).
  64. Li, Z. & Scheraga, H. A. Monte Carlo-minimization approach to the multiple-minima problem in protein folding. *Proc. Natl. Acad. Sci. U. S. A.* **84**, 6611–6615 (1987).
  65. Heiles, S. & Johnston, R. L. Global optimization of clusters using electronic structure methods. *Int. J. Quantum Chem.* **113**, 2091–2109 (2013).
  66. Johnston, R. L. Evolving better nanoparticles: Genetic algorithms for optimising cluster geometries. *J. Chem. Soc. Dalton Trans.* **3**, 4193–4207 (2003).
  67. Zhang, J. & Dolg, M. Global optimization of clusters of rigid molecules using the artificial bee colony algorithm. *Phys. Chem. Chem. Phys.* **18**, 3003–3010 (2016).
  68. Zhang, J., Glezakou, V. A., Rousseau, R. & Nguyen, M. T. NWPEsSe: An Adaptive-Learning Global Optimization Algorithm for Nanosized Cluster Systems. *J. Chem. Theory Comput.* **16**, 3947–3958 (2020).
  69. Call, S. T., Zubarev, D. Y. & Boldyrev, A. I. Global minimum structure searches via particle swarm optimization. *J. Comput. Chem.* **28**, 1177–1186 (2007).
  70. Storn, R. & Price, K. Differential Evolution – A Simple and Efficient Heuristic for Global Optimization over Continuous Spaces. *J. Glob. Optim.* **11**, 341–359 (1997).
  71. Ferrando, R. Determining the equilibrium structures of nanoalloys by computational methods. *J. Nanopart. Res.* **20**, 1–13 (2018).
  72. Hussein, H. A., Davis, J. B. A. & Johnston, R. L. DFT global optimisation of gas-phase and MgO-supported sub-nanometre AuPd clusters. *Phys. Chem. Chem. Phys.* **18**, 26133–26143 (2016).
  73. Luo, X. *et al.* Predicting two-dimensional boron-carbon compounds by the global optimization method. *J. Am. Chem. Soc.* **133**, 16285–16290 (2011).
  74. Luo, W., Ma, Y., Gong, X. & Xiang, H. Prediction of silicon-based layered structures for optoelectronic applications. *J. Am. Chem. Soc.* **136**, 15992–15997 (2014).
  75. Fung, V. & Jiang, D. E. Exploring Structural Diversity and Fluxionality of  $\text{Pt}_n$  ( $n = 10-13$ ) Clusters from First-Principles. *J. Phys. Chem. C* **121**, 10796–10802 (2017).
  76. Rossi, G. & Ferrando, R. Global optimization by excitable walkers. *Chem. Phys. Lett.* **423**, 17–22 (2006).
  77. Paz-Borbón, L. O. *et al.*  $\text{CeO}_2(111)$  electronic reducibility tuned by ultra-small supported bimetallic Pt-Cu clusters. *Phys. Chem. Chem. Phys.* **21**, 15286–15296 (2019).
  78. Goedecker, S. Minima hopping: An efficient search method for the global minimum of the potential energy surface of complex molecular systems. *J. Chem. Phys.* **120**, 9911–9917 (2004).
  79. Pidko, E. A. & Van Santen, R. A. Computational approach in zeolite science. in *Zeolite Characterization and Catalysis: A Tutorial* 223–250 (Springer Netherlands, 2010).
  80. Tuckerman, M. E. *Ab initio* molecular dynamics: Basic concepts, current trends and novel applications. *J. Phys. Condens. Matter* **14**, R1297 (2002).

81. Ma, S. & Liu, Z. P. Machine Learning for Atomic Simulation and Activity Prediction in Heterogeneous Catalysis: Current Status and Future. *ACS Catal.* **10**, 13213–13226 (2020).
82. Klebe, G. & Mietzner, T. A fast and efficient method to generate biologically relevant conformations. *J. Comput. Aided. Mol. Des.* **8**, 583–606 (1994).
83. Boström, J., Greenwood, J. R. & Gottfries, J. Assessing the performance of OMEGA with respect to retrieving bioactive conformations. *J. Mol. Graph. Model.* **21**, 449–462 (2003).
84. Labute, P. LowModeMD – Implicit low-mode velocity filtering applied to conformational search of macrocycles and protein loops. *J. Chem. Inf. Model.* **50**, 792–800 (2010).
85. Sutto, L., Marsili, S. & Gervasio, F. L. New advances in metadynamics. *Wiley Interdiscip. Rev. Comput. Mol. Sci.* **2**, 771–779 (2012).
86. Abrams, C. & Bussi, G. Enhanced sampling in molecular dynamics using metadynamics, replica-exchange, and temperature-acceleration. *Entropy* **16**, 163–199 (2014).
87. Bernasconi, L., Kazaryan, A., Belanzoni, P. & Baerends, E. J. Catalytic Oxidation of Water with High-Spin Iron(IV)-Oxo Species: Role of the Water Solvent. *ACS Catal.* **7**, 4018–4025 (2017).
88. Cheng, T., Xiao, H. & Goddard, W. A. Reaction Mechanisms for the Electrochemical Reduction of CO<sub>2</sub> to CO and Formate on the Cu(100) Surface at 298 K from Quantum Mechanics Free Energy Calculations with Explicit Water. *J. Am. Chem. Soc.* **138**, 13802–13805 (2016).
89. Zhu, Q., Oganov, A. R. & Lyakhov, A. O. Evolutionary metadynamics: A novel method to predict crystal structures. *CrystEngComm* **14**, 3596–3601 (2012).
90. Bonomi, M. *et al.* PLUMED: A portable plugin for free-energy calculations with molecular dynamics. *Comput. Phys. Commun.* **180**, 1961–1972 (2009).
91. Hussein, H. A. & Johnston, R. L. The DFT-genetic algorithm approach for global optimization of subnanometer bimetallic clusters. in *Frontiers of Nanoscience* vol. 12 145–169 (Elsevier, 2018).
92. Jennings, P. C., Lysgaard, S., Hummelshøj, J. S., Vegge, T. & Bligaard, T. Genetic algorithms for computational materials discovery accelerated by machine learning. *Npj Comput. Mater.* **5**, 46 (2019).
93. Liu, J. X., Filot, I. A. W., Su, Y., Zijlstra, B. & Hensen, E. J. M. Optimum Particle Size for Gold-Catalyzed CO Oxidation. *J. Phys. Chem. C* **122**, 8327–8340 (2018).
94. Liu, S. *et al.* Adsorption Preference Determines Segregation Direction: A Shortcut to More Realistic Surface Models of Alloy Catalysts. *ACS Catal.* **9**, 5011–5018 (2019).
95. Karaboga, D. & Akay, B. A comparative study of Artificial Bee Colony algorithm. *Appl. Math. Comput.* **214**, 108–132 (2009).
96. Bahamish, H. A. A., Abdullah, R. & Salam, R. A. Protein tertiary structure prediction using artificial bee colony algorithm. in *Proceedings - 2009 3rd Asia International Conference on Modelling and Simulation, AMS 2009* 258–263 (IEEE, 2009).
97. Li, B., Chiong, R. & Lin, M. A balance-evolution artificial bee colony algorithm for protein structure optimization based on a three-dimensional AB off-lattice model. *Comput. Biol. Chem.* **54**, 1–12 (2015).
98. Zhang, J. & Dolg, M. ABCluster: The artificial bee colony algorithm for cluster global optimization. *Phys. Chem. Chem. Phys.* **17**, 24173–24181 (2015).
99. Ozturk, C., Hancer, E. & Karaboga, D. Dynamic clustering with improved binary artificial bee colony algorithm. *Appl. Soft Comput. J.* **28**, 69–80 (2015).
100. Sun, G. & Sautet, P. Metastable Structures in Cluster Catalysis from First-Principles: Structural Ensemble in Reaction Conditions and Metastability Triggered Reactivity. *J. Am. Chem. Soc.* **140**, 2812–2820 (2018).
101. Grajciar, L. *et al.* Towards *operando* computational modeling in heterogeneous catalysis. *Chem. Soc. Rev.* **47**, 8307–8348 (2018).
102. Reuter, K. & Scheffler, M. Composition and structure of the RuO<sub>2</sub>(110) surface in an O<sub>2</sub> and CO environment: Implications for the catalytic formation of CO<sub>2</sub>. *Phys. Rev. B - Condens. Matter Mater. Phys.* **68**, 45407 (2003).
103. Reuter, K. *Ab initio* thermodynamics and first-principles microkinetics for surface catalysis. *Springer Ser. Chem. Phys.* **114**, 541–563 (2017).

104. Reuter, K., Stampf, C. & Scheffler, M. *Ab Initio* Atomistic Thermodynamics and Statistical Mechanics of Surface Properties and Functions. in *Handbook of Materials Modeling* 149–194 (Springer Netherlands, 2005).
105. Tables, J. T. JANAF Thermochemical. ‘DR Stull and H. Prophet, project directors, Natl.’ *Nat. Stand. Ref. Data Ser., Nat. Bur. Stds.(US)* vol. 1141 (1971).
106. Xu, H. & Cheng, D. First-principles-aided thermodynamic modeling of transition-metal heterogeneous catalysts: A review. *Green Energy Environ.* **5**, 286–302 (2020).
107. Bruix, A., Margraf, J. T., Andersen, M. & Reuter, K. First-principles-based multiscale modelling of heterogeneous catalysis. *Nat. Catal.* **2**, 659–670 (2019).
108. Li, G., Vollmer, I., Liu, C., Gascon, J. & Pidko, E. A. Structure and Reactivity of the Mo/ZSM-5 Dehydroaromatization Catalyst: An *Operando* Computational Study. *ACS Catal.* **9**, 8731–8737 (2019).
109. Kosinov, N. & Hensen, E. J. M. Reactivity, Selectivity, and Stability of Zeolite-Based Catalysts for Methane Dehydroaromatization. *Adv. Mater.* **32**, 2002565 (2020).
110. Jalan, A., Ashcraft, R. W., West, R. H. & Green, W. H. Predicting solvation energies for kinetic modeling. *Annu. Reports Prog. Chem. - Sect. C* **106**, 211–258 (2010).
111. Tomasi, J., Mennucci, B. & Cammi, R. Quantum mechanical continuum solvation models. *Chem. Rev.* **105**, 2999–3093 (2005).
112. Cramer, C. J. & Truhlar, D. G. Implicit Solvation Models: Equilibria, Structure, Spectra, and Dynamics. *Chem. Rev.* **99**, 2161–2200 (1999).
113. Vogiatzis, K. D. *et al.* Computational Approach to Molecular Catalysis by 3d Transition Metals: Challenges and Opportunities. *Chem. Rev.* **119**, 2453–2523 (2019).
114. Eckert, F. & Klamt, A. Fast Solvent Screening via Quantum Chemistry: COSMO-RS Approach. *AIChE J.* **48**, 369–385 (2002).
115. Klamt, A. The COSMO and COSMO-RS solvation models. *Wiley Interdiscip. Rev. Comput. Mol. Sci.* **8**, e1338 (2018).
116. Sato, H. A modern solvation theory: Quantum chemistry and statistical chemistry. *Phys. Chem. Chem. Phys.* **15**, 7450–7465 (2013).
117. Kovalenko, A. Molecular theory of solvation: Methodology summary and illustrations. *Condens. Matter Phys.* **18**, 32601 (2015).
118. Liu, C., van Putten, R., Kulyaev, P. O., Filonenko, G. A. & Pidko, E. A. Computational insights into the catalytic role of the base promoters in ester hydrogenation with homogeneous non-pincer-based Mn-P,N catalyst. *J. Catal.* **363**, 136–143 (2018).
119. Kulyaev, P. O. & Pidko, E. A. *Operando* Modeling of Multicomponent Reactive Solutions in Homogeneous Catalysis: from Non-standard Free Energies to Reaction Network Control. *ChemCatChem* **12**, 795–802 (2020).



### Global optimization of extraframework ensembles in zeolites: structural analysis of extraframework aluminum species in MOR and MFI zeolites



## Summary

---

Metal-modified zeolites are versatile catalytic materials with a wide range of industrial applications. Their catalytic behavior is determined by the nature of the externally introduced cationic species, i.e., its geometry, chemical composition, and location within the zeolite pores. Superior catalyst designs can be unlocked by understanding the confinement effect and spatial limitations of the zeolite framework and its influence on the geometry and location of such cationic active sites. In this study, we employ the genetic algorithm (GA) global optimization method to investigate extraframework aluminum species and their structural variations in different zeolite matrices. We focus on the extraframework aluminum (EFAl) as a model system because they greatly influence the product selectivity and catalytic stability in several zeolite-catalyzed processes. Specifically, the GA was used to investigate the configurational possibilities of EFAl within the mordenite (MOR) and ZSM-5 frameworks. The  $\chi$ TB semi-empirical method within the GA was employed for an automated sampling of the EFAl-Zeolite space. Further, geometry refinement at the density functional theory (DFT) level of theory allowed us to improve the most stable configurations obtained from the GA and elaborate on the limitations of the  $\chi$ TB method. A subsequent *ab initio* thermodynamics analysis (aiTA) was opted to predict the most favorable EFAl structure(s) under the catalytically relevant *operando* conditions.

This chapter is based on the following publication:

Khramenkova E. V., Venkatraman H., Soethout V., Pidko E. A.  
*Phys. Chem. Chem. Phys.* **24**, 27047–27054 (2022).

## **2.1. Introduction**

The development of advanced predictive models in heterogeneous catalysis requires a deep insight into the molecular-level structure of the active sites, their catalytic mechanism and evolution under the operating conditions.<sup>1,2</sup> The structural complexity and heterogeneity of common solid catalysts are major challenges in constructing representative active site models, which are conventionally done using a combination of various indirect characterization data and chemical intuition of the researchers.<sup>3</sup> Global optimization techniques provide a practical approach to reducing the expert bias in addressing the active site structure in heterogeneous catalysts.<sup>4</sup>

One of the most popular global optimization (GO) techniques is the genetic algorithm (GA) which allows scanning the potential energy surface (PES) of a given system and predicting the most stable structures via an evolutionary algorithm.<sup>3</sup> The underlying principles of the algorithm are based on learning the “good” features of the possible structural moieties and improving them throughout the continuous structures’ alterations. In this manner, a pool of advanced solutions can be identified which is otherwise challenging to guess based on chemical intuition and spectroscopic data only.<sup>5,6</sup> GO algorithms have been successfully used to tackle the structural problem of the active sites in heterogeneous catalysis including oxides,<sup>7,8</sup> supported metal nanoparticles,<sup>9</sup> electrocatalytic interfaces,<sup>10</sup> and, since quite recently, also for the zeolite-based catalysts.<sup>11,12</sup>

Zeolites are porous, crystalline aluminosilicates, whose reactivity and catalytic behavior can be widely adjusted by modifying them with extraframework (EF) metal-containing species.<sup>13,14</sup> The structural and catalytic properties of such EF species depend on the chemical composition (lattice Si/Al ratio), presence of the heteroatoms, and topological properties of the confining zeolite matrix.<sup>15</sup> As the spectrum of plausible variations in features is large, it is important to understand the role of zeolite topology and the nature of the extraframework aluminum (EFAI) species, that largely influence the activity of zeolites.

The extraframework aluminum species situated in zeolites hold an important position in zeolite chemistry and catalysis. The formation of Lewis acidic EFAI in the zeolite pores during the synthesis or post-synthetic activation modulates the acidity, catalytic reactivity, and long-term stability of zeolite-based catalysts.<sup>16,17</sup> The formation of EFAI often results in releasing the aluminum from the framework in procedures of high-temperature steaming, calcination or acid/base leaching.<sup>18</sup> The structures of the EFAI are not completely known, however, some authors quote the condensed and uncondensed species. The former are phases of  $\text{Al}_2\text{O}_3$ , that are formed at the external surfaces of zeolites, while the latter are aluminum and oxoaluminum cations such as  $\text{AlO}^+$ ,  $\text{AlOH}^{2+}$ ,  $\text{Al}^{3+}$ .<sup>19</sup> The formation of these mononuclear species has been proposed based on the

results of NMR spectroscopy and DFT calculations, which, until recently, have been mostly considering small mononuclear EF aluminum.<sup>16,20</sup> It has also been demonstrated that the strength of the BAS can be enhanced in the presence of  $\text{AlOH}^{2+}$ . However, the DFT calculations combined with *ab initio* thermodynamic analysis (aiTA) have shown that under the conditions of zeolite activation, the formation of the multinuclear  $\text{Al}_3\text{O}_4\text{H}_3^{4+}$  species inside FAU can be observed.<sup>16</sup> A driving force for the formation of the EFAl complexes with high nuclearity was stated to be the high basicity of terminal O-containing groups and the unsaturation of Al centers in these complexes. The experimental observation of the multinuclear species was demonstrated by Zheng et al. using the combined  $^{31}\text{P}$  solid-state NMR and 1,2-bis(dimethylphosphine) ethane probe molecule method.<sup>21</sup>

The EFAl species are speculated to reduce the effective pore size within the zeolitic framework leading to better stabilization of intermediates and transition states during the catalytic processes.<sup>22</sup> Another proposal states that EFAl species polarize the BAS in their vicinity which in turn increases the reactivity of the BAS.<sup>23,24</sup> Although several insights were gained through earlier spectroscopic and theoretical studies of EFAl moieties, their exact geometry remains elusive. The spectroscopic characterization of EFAl yields a general understanding of the coordination environment but provides limited information on the structural changes induced by the reactive conditions which are essential to discern the catalytic role of these species.<sup>3</sup>

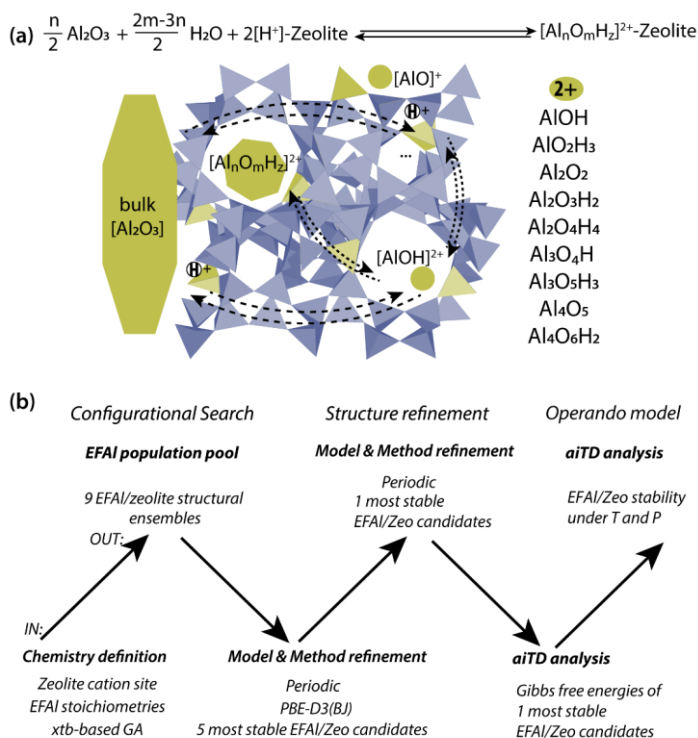
Herein, we present a computational study aimed at addressing the EFAl structures in zeolites (**Scheme 2.1a**). The computational workflow implemented to achieve this is schematically illustrated in **Scheme 2.1b**. For a given selection of EFAl stoichiometries encapsulated in MOR or ZSM-5 zeolite, an exhaustive scanning of PES was carried out using the GA based on  $x\text{TB}$  semiempirical calculations. The structures produced at the end of the GA configurational search were further refined by fully periodic DFT calculations. Subsequently, the stabilities of the structurally refined stoichiometries under catalytically relevant conditions were evaluated in the framework of aiTA. The workflow implemented in this chapter provides a bias-free approach for structural analysis of extraframework species in zeolites and allows finding configurations that could not be previously anticipated.

## 2.2. Computational details

### 2.2.1. Configurational search

A genetic algorithm (GA) was used to exhaustively explore the configurational space formed by the isomeric structures of 9 different EFAl stoichiometries, individually. **Figure 2.1** presents the cluster models of the zeolites utilized in the GA search, which are

highlighted as a part of their respective periodic structures. Such structural models were used earlier as they resemble the model catalysts of EFAl-containing zeolites prepared in impregnation or ion exchange processes. By selecting a side pocket of MOR and  $\gamma$ -site of the ZSM-5 as the cation sites accommodating EFAL, a uniform confinement effect was created across EFAl in respective frameworks.<sup>25,26</sup>



**Scheme 2.1 (a)** The model definition for the interconversion of EFAl species in a zeolite matrix with a list of stoichiometries included in the current stability analysis of molecular intrazeolite EFAl with a reference to separate phases of bulk  $\text{Al}_2\text{O}_3$  and acidic zeolite matrix ( $2[\text{H}^+]\text{-Zeolite}$ ). The structure prediction and stability evaluation of the EFAl-zeolites followed a hierarchical approach **(b)** involving the initial configurational search using a semiempirical (xtb)-based configurational search followed by a structural refinement using a full periodic DFT modelling and subsequent aiTA to evaluate the stability of the obtained extraframework ensembles under the catalytically-relevant conditions.

The models assumed the defect-free zeolite lattice and uniform confinement environment to facilitate analysis and structural exploration. Detailed information on the pore size and zeolitic topologies can be found in **Appendix A2**. The choice of the EFAl stoichiometries considered in this chapter (**Scheme 2.1a**) was inspired by the evidence from previous findings on the formation of mononuclear species:  $\text{AlOH}^{2+}$ ,  $\text{AlO}_2\text{H}_3^{2+}$ ,

binuclear species:  $\text{Al}_2\text{O}_2^{2+}$ ,  $\text{Al}_2\text{O}_3\text{H}_2^{2+}$ ,  $\text{Al}_2\text{O}_4\text{H}_4^{2+}$  and the spontaneous formation of multinuclear EF aluminum such as  $\text{Al}_3\text{O}_4\text{H}^{2+}$ ,  $\text{Al}_3\text{O}_5\text{H}_3^{2+}$ ,  $\text{Al}_4\text{O}_5^{2+}$  and  $\text{Al}_4\text{O}_6\text{H}_2^{2+}$ .<sup>20,27–30</sup> Note that these stoichiometries correspond to complete ensembles. These ensembles within zeolites can be represented as a single species with a +2 overall charge as well as by a combination of species having the same total charge (e.g. a +1 EFAl cation and a zeolite BAS or a neutral EFAl and two BAS). The cationic charge of the EF ensemble was compensated by two negatively charged  $\text{AlO}_2^-$  lattice units.

The configuration exploration was carried out using the version of GA developed by Vilhelmsen and Hammer.<sup>31</sup> The operations of fitness assignment, crossover, mutation, and selection were executed in the GA using the Atomic Simulation Environment (ASE) with the semi-empirical tight-binding calculator GFN1 –  $x\text{TB}$ .<sup>31–34</sup> The mutation probability of the GA was chosen as 30 %, and the population size at the end of each generation was set to consist of 20 structures. During the GA search, only the positions of the extraframework species were allowed to change, while the coordinates of the cluster model atoms were kept frozen. The parameters of the maximum energy difference, the maximum difference in interatomic difference and the maximum interatomic distances were set to 0.02 eV, 0.7 Å, and 0.015 Å, respectively. Convergence was assumed to be reached when the last 5 consecutive generations of the population pool were identical.

### 2.2.2. Structure refinement

Since the GFN- $x\text{TB}$  methods proved to be reliable for the geometries and frequencies calculations, but not the energies, GFN1- $x\text{TB}$  optimized configurations were further refined at the DFT level using more realistic periodic zeolite models. The structural refinement was carried out at the PBE-D3(BJ) level of theory.<sup>35</sup> The final pool of each GA run was examined and five lowest-energies configurations were extracted for the structural refinement. The compromise choice of 5 lowest-lying candidates is motivated by our preliminary cluster calculations on mononuclear EFAl species in MOR (see **Appendix A2**), showing that such a choice allows finding the minimum-energy considerations, whilst providing a good compromise between the accuracy and computational costs. For the structure refinement using periodic DFT (pDFT) calculations, the configurations obtained with the  $x\text{TB}$  GA on cluster models were directly transferred into the respective positions of the fully periodic zeolite models.

pDFT calculations were executed using Vienna *Ab Initio* Simulation Package (VASP)<sup>36</sup> with the generalized gradient approximation PBE functional and Grimme's semiempirical dispersion correction method D3 (BJ).<sup>37–39</sup> A plane wave (PW) basis set with cut-off energy of 400 eV was used in combination with the projected augmented wave (PAW)<sup>40</sup> method. Brillouin zone sampling was restricted to the  $\Gamma$  point. Convergence was assumed to be reached when the forces on the atoms were below 0.05

eV/ Å. The ZSM-5 unit cell was optimized, and the following lattice parameters were used:  $a = 20.24$ ,  $b = 20.01$  and  $c = 13.44$  Å. A supercell of MOR was constructed by a doubling monoclinic primitive cell along the  $c$  axis and with the lattice parameters of  $a = b = 13.65$ ,  $c = 15.02$  Å and  $\alpha = \beta = 90.0^\circ$  and  $\gamma = 97.2^\circ$ . Bulk  $\alpha$ -Al<sub>2</sub>O<sub>3</sub> with optimized unit cell parameters as  $a = b = 7.72$ ,  $c = 12.96$  and  $\alpha = \beta = 90.0^\circ$  and  $\gamma = 120.0^\circ$  was modelled to be used as the reference state for the EFAl aiTA calculations. Brillouin zone sampling was performed using a  $3 \times 3 \times 1$  mesh. For comparison, a thermodynamic analysis involving a less stable bulk Al(OH)<sub>3</sub> phase as a reference has been carried out with the results summarized in section A2.3. of Appendix A2.

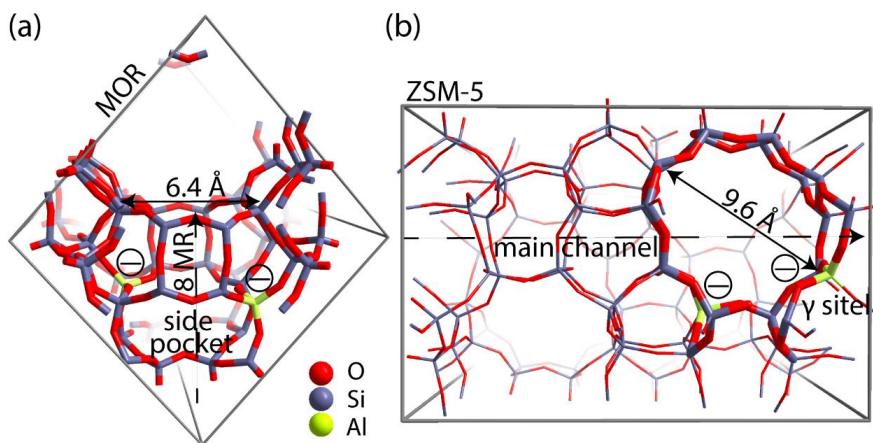


**Figure 2.1** (a) the location of the cluster model utilized in the genetic algorithm for the cationic sites global minima search incorporated in the periodic model of the mordenite; (b) the location of the cluster model utilized in the genetic algorithm for the cationic sites global minima search incorporated in the periodic model of the ZSM.

### 2.2.3. *Ab initio* thermodynamics analysis

The relative stabilities of the EFAl species in zeolite pores at the catalytically relevant conditions were next assessed in the framework of aiTA method.<sup>41–43</sup> The following equilibrium was considered for the stability assessment:



The reaction free energy is defined as:

$$\Delta G_{\text{rxn}}(T, p) = G_{\text{Al}_n\text{O}_m\text{H}_z/\text{zeolite}}^{\text{S}} - \frac{n}{2}G_{\text{Al}_2\text{O}_3}^{\text{S}} - G_{2\text{H}/\text{zeolite}}^{\text{S}} - \frac{2m-3n}{2}H_{\text{H}_2\text{O}}^{\text{g}} \quad (\text{E2.2})$$

where  $G_{\text{Al}_n\text{O}_m\text{H}_z/\text{zeolite}}^{\text{S}}$ ,  $G_{\text{Al}_2\text{O}_3}^{\text{S}}$  and  $G_{2\text{H}/\text{zeolite}}^{\text{S}}$  are the Gibbs free energies of the EFAl-containing zeolite model, bulk Al<sub>2</sub>O<sub>3</sub> and parent EFAl-free acidic zeolite matrix

(2H/zeolite). The bulk, 2H/zeolite and  $\text{Al}_n\text{O}_m\text{H}_z/\text{zeolite}$  are the DFT-approximated energies of the aluminum oxide, the respective zeolite framework with two hydrogens and the frameworks with situated EFAls. The PV-contributions entropy of the solids could be neglected and the expression for the Gibbs free energy can be written as:

$$\Delta G_{\text{rxn}}(T, p) = E_{\text{Al}_n\text{O}_m\text{H}_z/\text{zeolite}}^{\text{S}} - \frac{n}{2} E_{\text{Al}_2\text{O}_3}^{\text{S}} - E_{2\text{H}/\text{zeolite}}^{\text{S}} - \frac{2m-3n}{2} \mu_{\text{H}_2\text{O}}^{\text{g}} \quad (\text{E2.3})$$

where  $E_{\text{Al}_n\text{O}_m\text{H}_z/\text{zeolite}}^{\text{S}}$  and  $E_{2\text{H}/\text{zeolite}}^{\text{S}}$  are the pDFT-energies of the given EFAl-zeolite and the parent H-zeolite structures, respectively. The condition dependencies of the reaction free energy are explicitly accounted for with the  $\mu_{\text{H}_2\text{O}}^{\text{g}}$  defined as:

$$\mu_{\text{H}_2\text{O}}^{\text{g}}(T, p) = E_{\text{H}_2\text{O}} + \Delta\mu_{\text{H}_2\text{O}}(T, p) \quad (\text{E2.4})$$

$$\Delta\mu_{\text{H}_2\text{O}}^{\text{g}}(T, p) = H_{\text{H}_2\text{O}}(T, p^\circ) - H_{\text{H}_2\text{O}}(0 \text{ K}, p^\circ) - T \left( S_{\text{H}_2\text{O}}(T, p^\circ) - S_{\text{H}_2\text{O}}(0 \text{ K}, p^\circ) \right) + RT \ln \left( \frac{p_{\text{H}_2\text{O}}}{p_{\text{H}_2\text{O}}^\circ} \right) \quad (\text{E2.5})$$

Thermodynamic tables were used to calculate the values of entropy and enthalpy at standard pressure (1 bar) and different temperatures.<sup>44</sup> Incorporating eq.E2.4 and E2.5 in eq.E2.3 gives the change in the Gibbs free energy of formation of the EFAls stoichiometries. This methodology has been successfully employed earlier on a wide range of solid systems including zeolite catalysts.<sup>12,41,45</sup>

### 2.3. Results and discussion

**Figure 2.2** summarizes the most stable EFAl geometries among the five DFT-optimized configurations (**Figures A2.5** and **A2.6**) that were initially extracted from the bias-free  $\chi\text{TB}$ -based GA configurational search (**Figures A2.3** and **A2.4**). The pDFT refinement of the  $\chi\text{TB}$  semi-empirically optimized structural isomers results in their substantial geometrical alterations. The presence of the artefacts in  $\chi\text{TB}$  predictions has been previously shown by Vicent-Luna in a form of undesirable structural distortions of geometries with lower symmetry after the optimization.<sup>46</sup> This could be attributed to the key approximation within the GFN1 representing the noncovalent interactions via the atom pair-wise electrostatic interactions described as spherically symmetric and monopole-types.<sup>47</sup> Nevertheless, we find that the  $\chi\text{TB}$ -driven GA search provides a robust and efficient way to explore the configurational space of the intrazeolite extrametwork species to obtain a good structural guess for the subsequent pDFT refinement. Below we predominantly discuss the pDFT refined data, while the  $\chi\text{TB}$ -derived predecessor structures will only briefly be discussed where appropriate.

The global minima geometries summarized in **Figure 2.2** indicate that, apart from the little distortions in the coordinational environment caused by the formation of the hydrogen bonds, similar EFAl geometries are found for particular stoichiometries in MOR and ZSM-5 zeolites. This stands for a majority of stoichiometries, except for the multinuclear  $\text{Al}_3\text{O}_5\text{H}_3$  and  $\text{Al}_4\text{O}_6\text{H}_2$  complexes, where structurally distinct features are promoted by the different confinement spaces.

For the smallest AIOH stoichiometry, a single stable EFAl type is revealed by pDFT represented by an  $\text{AlOH}^{2+}$  cation coordinated directly to the lattice basic oxygen ions of one of the framework  $\text{AlO}_2^-$  anions with the second one providing the indirect charge-compensation of the cationic EFAl (**Figure 2.2a**). The GA structural exploration has also revealed alternative configurations for the mordenite-confined AIOH represented by an  $\text{Al}=\text{O}^+$  and an adjacent Brønsted acid site (**Figure A2.3c**), additionally stabilized within the narrower confinement space of the MOR side-pocket. Such configurations have been discussed in the previous EFAl literature.<sup>19,48</sup> However, they were found unstable or underwent restructuring into the charge-alternative states during the pDFT refinement. Similarly, a single stable configuration is found for another mononuclear stoichiometry –  $\text{AlO}_2\text{H}_3$ , represented by a tetrahedral  $\text{Al}(\text{OH})_2^+$  EFAl cation coordinated to one lattice  $\text{AlO}_2^-$  anion with the second one charge-compensated by the  $\text{H}^+$  BAS site (**Figure 2.2b**).

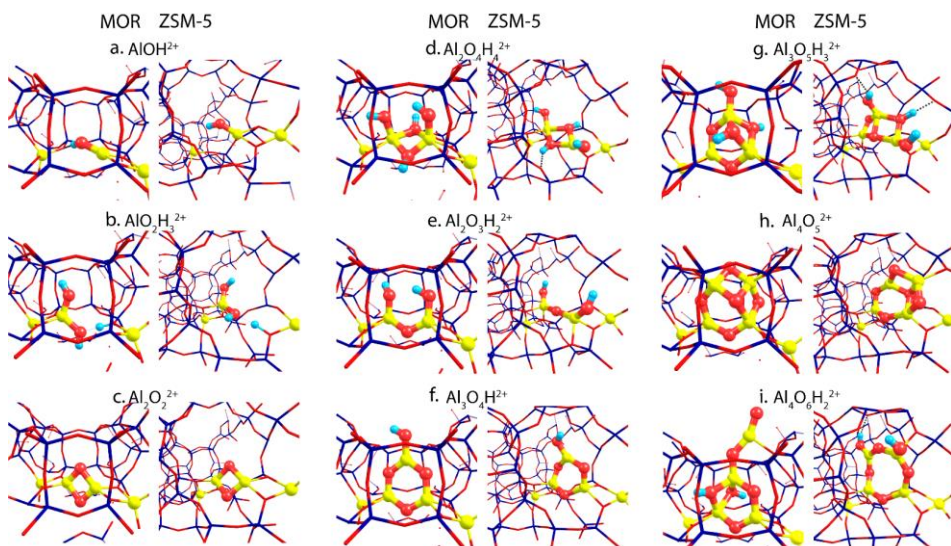


**Figure 2.2** The global minima structures of various EFAl stoichiometries produced in GA runs and subsequently optimized in the MOR and ZSM-5 zeolite frameworks.

Binuclear stoichiometries include  $\text{Al}_2\text{O}_2$  and more hydrated/hydroxylated complexes such as  $\text{Al}_2\text{O}_4\text{H}_4$  and  $\text{Al}_2\text{O}_3\text{H}_2$ . For both zeolites, the former species adopts a symmetrical diamond-shape binuclear  $\text{Al}(\mu\text{-O})_2\text{Al}^{2+}$  configuration (**Figure 2.2c**). This geometry is

portrayed as the most stable among all DFT-optimized structures, whereas some of their *x*TB-optimized predecessors reveal the presence of a linear isomer  $\text{OAl}(\mu\text{-O})\text{Al}$  which has one bridging oxygen and one terminal oxygen (**Figure A2.4a**), similar to the structure proposed earlier for EF-Ga species.<sup>49</sup> In **Figures 2d** and **2e**,  $\text{Al}_2\text{O}_4\text{H}_4$  and  $\text{Al}_2\text{O}_3\text{H}_2$  geometries respectively form symmetrical complexes that have minor distinctions in the hydrogen bond arrangements and proximity to the Al framework sites, affecting their effectivity of compensating the framework's negative charge.

More complex trinuclear species such as  $\text{Al}_3\text{O}_4\text{H}$  and  $\text{Al}_3\text{O}_5\text{H}_3$  display more possibilities of structural arrangements. In **Figure 2.2f**,  $\text{Al}_3\text{O}_4\text{H}$  stoichiometries exhibit a formation of a 6-membered ring with a coordinated OH-group, that is slightly distorted in the ZSM-5 due to the formation of the hydrogen bonds between the OH group and the framework. The optimization of the  $\text{Al}_3\text{O}_5\text{H}_3$  complexes gives a ring-shaped  $\text{Al}_3\text{O}_3\text{H}$  core moiety in MOR and an envelope-like  $\text{Al}_3\text{O}_3\text{H}$  core structure in ZSM-5, that also coordinates two additional OH-groups of the structure. (**Figure 2.2g**).

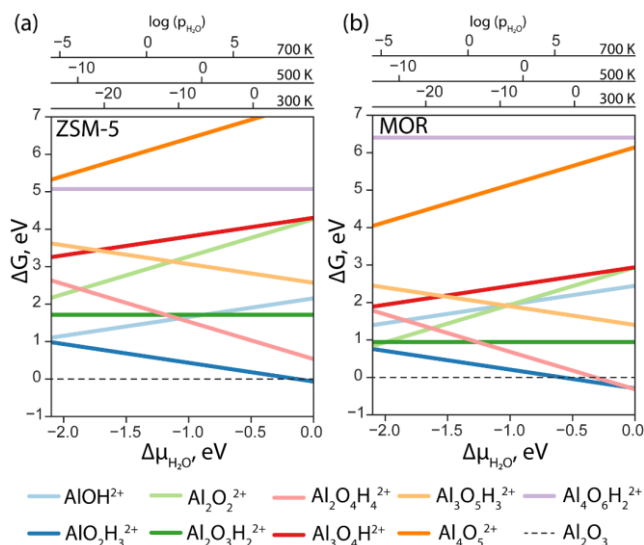


**Figure 2.3** The Gibbs free energy diagram of the EFAl species confined in ZSM-5 (**a**) and in MOR (**b**) was calculated with respect to the  $\alpha\text{-Al}_2\text{O}_3$  phase as a function of water chemical potential.

**Figure 2.2h** and **2.2i** show the EFAl moieties with the highest number of aluminum atoms considered in this study. A more hydrated  $\text{Al}_4\text{O}_6\text{H}_2$  (**2.2i**) species in mordenite accommodates a ring-shaped  $\text{Al}_3\text{O}_3\text{H}$  moiety in with bound OH-group at the same time expelling  $\text{AlO}_2$  species out of the pocket. Its ZSM-5 counterpart, on the other hand, could accommodate an 8-membered EFAl ring with two coordinated OH-groups. Another stable configuration of the  $\text{Al}_4\text{O}_6\text{H}_2$  is a 6-membered EFAl with OH-group and expelled  $\text{AlO}_2\text{H}$  species as shown in **Figure A2.6i**. For the  $\text{Al}_4\text{O}_5$  stoichiometry in **Figure 2.2h**,

the most stable isomers adapt envelope-like  $\text{Al}_3\text{O}_3$  geometries linked to an  $\text{AlO}_2$  moiety species in both zeolite frameworks. However, a more structurally diverse picture could be seen in a detailed 5-structures analysis. In **Figure A2.5h**,  $\text{Al}_4\text{O}_5$  geometry, when hosted in mordenite, tends to adapt in some cases coordination resembling the one from  $\text{Al}_4\text{O}_6\text{H}_2$  with an  $\text{AlO}_2$  species dislodged from the side pocket. Observed accommodation of the smaller species in the side pocket of MOR than in the ZSM-5 can be explained by stronger confinement and limited pore size in mordenite.

With the results of DFT optimization being sufficiently elaborated, the respective stabilities of the structures under *operando* conditions could be compared. In **Figure 2.3**, the *ab initio* thermodynamics analysis shows the Gibbs free energies of the formation of different stoichiometries as a function of water chemical potential ( $\Delta\mu_{\text{H}_2\text{O}}$ ). The values of the Gibbs free energies are computed using equation E2.3 and the  $\Delta\mu_{\text{H}_2\text{O}}$  is derived from E2.5. The logarithmic pressure scales above the diagram represent the pressures required for the high (700 K and 500 K) – and moderate (300 K) – temperature processes.

The computed results reveal a general trend of the thermodynamic preference for the formation of mononuclear and binuclear cationic EFAl species in both zeolite topologies at high water chemical potentials, which is in line with the experimental findings.<sup>16,19,28</sup> At low water chemical potential, the formation of a separate bulk aluminum oxide and zeolite BAS is predicted for the current highly stable  $\alpha\text{-Al}_2\text{O}_3$  reference structure. The cationic EFAl species are better stabilized when confined within the mordenite side pocket, as is evident from generally lower relative free energies predicted for all EFAl stoichiometries compared to those in the MFI. The largest cation  $\text{Al}_4\text{O}_6\text{H}_2^{2+}$  deviates from this trend, which because of its size cannot be accommodated within the narrow MOR side pocket resulting in the expulsion of quite an unstable O-Al=O moiety into the main channel.

The thermodynamics of EFAl speciation is highly condition-dependent. At low chemical water potentials ( $\Delta\mu_{\text{H}_2\text{O}} < -1.0$  eV), the formation of bulk  $\alpha\text{-Al}_2\text{O}_3$  oxide is preferred over the molecular cationic EFAl species indicating the limited possibility of the redispersion of Al upon the calcination zeolite activation procedures. Nevertheless, in MOR zeolite,  $\text{AlO}_2\text{H}_3$ ,  $\text{Al}_2\text{O}_3\text{H}_2$ ,  $\text{Al}_2\text{O}_2$  and  $\text{Al}_2\text{O}_4\text{H}_4$  EFAl species can be found within 1 eV from the reference value, whereas they are an additional 1 eV less stable in ZSM-5. The mononuclear  $\text{AlO}_2\text{H}_3$  and binuclear  $\text{Al}_2\text{O}_4\text{H}_4$  species are thermodynamically favored at high  $\Delta\mu_{\text{H}_2\text{O}}$ , indicating that such isolated cationic sites can potentially be formed upon e.g. steaming or ion exchange and further stabilized kinetically in the activated material. The formation of EFAl species with a higher degree of nuclearity (tri- and four-nuclear) is strongly thermodynamically unfavorable under all conditions, which is in sharp contrast to the situation previously discussed for low-silica faujasite, where trinuclear

multiple-charged EFAl confined in small sodalite cages were among the most stable species.<sup>16</sup>

The predicted EFAl stabilities depend on the specific choice of the bulk Al reference phase. We have also considered a fully hydrated  $\text{Al}(\text{OH})_3$  as a bulk reference state in aiTA (see **Figure A2.7** in **Appendix A2**). Because of the hydrated nature of the reference structure, the less hydrated multinuclear aggregates appear more stable at low  $\Delta\mu_{\text{H}_2\text{O}}$  in this case. Nevertheless, the preferential formation of mono- and binuclear cationic species at higher  $\Delta\mu_{\text{H}_2\text{O}}$  values relevant to the conditions of e.g. steam-calcination, remains unchanged by the choice of the bulk Al reference.

Our results point to a preference for the increased hydration of EFAl at higher  $\Delta\mu_{\text{H}_2\text{O}}$ , however, we should also stress that the higher degrees of hydration could destabilize the EFAl/zeolite systems as water holds the potential to cleave Al-O-(H)-bonds,<sup>50</sup> which could potentially manifest itself for stoichiometries with formal  $\text{H}_2\text{O}$  contents above those considered in this study. The outcome of the GA search and following aiTA procedure vividly indicated that a smaller pore size in mordenite offers a tighter confinement effect and better stabilization of the cationic species up to a certain size. The relative stability of the EFAl species when compared to the  $\alpha\text{-Al}_2\text{O}_3$  reference phase indicated a more pronounced stabilization of the mononuclear and binuclear species and the destabilization of the larger agglomerates due to the localized and disperse nature of the lattice negative charge and unfavorable confinement in MOR and ZSM-5. This explains the differences in EFAl speciation predicted for low-silica cage-type faujasite zeolites and suggests a different promoting effect of these species in the different zeolite topologies.

## 2.4. Conclusions

In this chapter, we applied the semiempirical-based GA to investigate the structural uncertainty surrounding the EFAl species confined within zeolites. The catalytic importance of these extraframework species motivated us to research the configurations of different EFAl nuclearities in two zeolitic frameworks: MOR and ZSM-5. Varying the stoichiometry of the EFAl accounts for the different concentrations of aluminum. For this purpose, the number of aluminum atoms ranging from 1 to 4 was considered in our study. Different zeolite topologies impose a distinct confinement effect on the anchored extraframework species. Here, we have shown that, within a chosen level of theory, the  $x\text{TB}$ -based GA method is effective for the structural exploration of complex EFAl species in zeolites by considering 9 different stoichiometries in MOR and ZSM-5. However, structural and energy refinement at the DFT level is necessary to form a basis for accurate and reliable structural evaluation and stability analysis.

The low-nuclearity EFAl structures are coherent with the findings reported by previous literature, thereby validating the proposed computational workflow. In addition, more complex multinuclear EFAl configurations were investigated and included in a stability analysis. To analyse EFAl stability under *operando* catalytically-relevant conditions, the relative energetics of the pDFT-refined low-lying structures was estimated by embedding them in the *ab initio* thermodynamics analysis. It was shown that both ZSM-5 and MOR topologies favor the formation of the cationic mononuclear EFAl in the presence of water / water vapors. Specifically, the vicinal Brønsted acid site and mononuclear  $\text{Al}(\text{OH})_2^+$  cation representing the  $\text{AlO}_2\text{H}_3$  EFAl stoichiometry were found to be the most thermodynamically stable at high  $\Delta\mu_{\text{H}_2\text{O}}$  in both zeolite frameworks. However, at low water chemical potential values, the formation of bulk  $\text{Al}_2\text{O}_3$  is more thermodynamically favorable. This can be attributed to the restricted confinement space in MOR and ZSM-5 channels. Our calculations suggest a generally better stabilization of a majority of the EFAl species in MOR zeolite.

Thus, we show that GA-based global optimization in combination with pDFT structural refinement and *ab initio* thermodynamics analysis provides an efficient computational workflow for expert-bias-free structural prediction on intrazeolite extraframework ensembles and evaluating their stabilities under catalytically-relevant conditions. By using the catalytically important EFAl species embedded in MOR and ZSM-5 frameworks, we demonstrate that our proposed approach can be a powerful tool to address the structural conundrum of extraframework speciation in zeolite-based catalysts.

## 2.5. References

1. Beznis, N. V., Weckhuysen, B. M. & Bitter, J. H. Cu-ZSM-5 zeolites for the formation of methanol from methane and oxygen: Probing the active sites and spectator species. *Catal. Letters* **138**, 14–22 (2010).
2. Vogt, C. & Weckhuysen, B. M. The concept of active site in heterogeneous catalysis. *Nat. Rev. Chem.* **6**, 89–111 (2022).
3. Grajciar, L. *et al.* Towards *operando* computational modeling in heterogeneous catalysis. *Chem. Soc. Rev.* **47**, 8307–8348 (2018).
4. Peterson, A. A. Global optimization of adsorbate-surface structures while preserving molecular identity. *Top. Catal.* **57**, 40–53 (2014).
5. Chakraborti, N. Genetic algorithms in materials design and processing. *Int. Mater. Rev.* **49**, 246–260 (2004).
6. Leardi, R. Genetic algorithms in chemistry. *J. Chromatogr. A* **1158**, 226–233 (2007).
7. Roberts, C. & Johnston, R. L. Investigation of the structures of MgO clusters using a genetic algorithm. *Phys. Chem. Chem. Phys.* **3**, 5024–5034 (2001).
8. Lee, M. H., Xu, J. & Xie, W. Exploring the Stability of Single-Atom Catalysts Using the Density Functional Theory-Based Global Optimization Method:  $\text{H}_2$  Formation on  $\text{VO}_x/\gamma\text{-Al}_2\text{O}_3(100)$ . *J. Phys. Chem. C* **126**, 6973–6981 (2022).
9. Sun, G., Alexandrova, A. N. & Sautet, P.  $\text{Pt}_8$  cluster on alumina under a pressure of hydrogen:

- Support-dependent reconstruction from first-principles global optimization. *J. Chem. Phys.* **151**, 194703 (2019).
10. Zhang, Z., Wei, Z., Sautet, P. & Alexandrova, A. N. Hydrogen-Induced Restructuring of a Cu(100) Electrode in Electroreduction Conditions. *J. Am. Chem. Soc.* **144**, 19284–19293 (2022).
  11. Hou, D., Grajciar, L., Nachtigall, P. & Heard, C. J. Origin of the Unusual Stability of Zeolite-Encapsulated Sub-Nanometer Platinum. *ACS Catal.* **10**, 11057–11068 (2020).
  12. Liu, C. *et al.* High Stability of Methanol to Aromatic Conversion over Bimetallic Ca,Ga-Modified ZSM-5. *ACS Catal.* **12**, 3189–3200 (2022).
  13. Li, G. & Pidko, E. A. The Nature and Catalytic Function of Cation Sites in Zeolites: a Computational Perspective. *ChemCatChem* **11**, 134–156 (2019).
  14. Kosinov, N., Liu, C., Hensen, E. J. M. & Pidko, E. A. Engineering of Transition Metal Catalysts Confined in Zeolites. *Chem. Mater.* **30**, 3177–3198 (2018).
  15. Tao, Y., Kanoh, H., Abrams, L. & Kaneko, K. Mesopore-modified zeolites: Preparation, characterization, and applications. *Chem. Rev.* **106**, 896–910 (2006).
  16. Liu, C., Li, G., Hensen, E. J. M. & Pidko, E. A. Nature and Catalytic Role of Extraframework Aluminum in Faujasite Zeolite: A Theoretical Perspective. *ACS Catal.* **5**, 7024–7033 (2015).
  17. Le, T. T., Chawla, A. & Rimer, J. D. Impact of acid site speciation and spatial gradients on zeolite catalysis. *J. Catal.* **391**, 56–68 (2020).
  18. Ravi, M., Sushkevich, V. L. & van Bokhoven, J. A. Towards a better understanding of Lewis acidic aluminium in zeolites. *Nat. Mater.* **19**, 1047–1056 (2020).
  19. Bhering, D. L., Ramírez-Solís, A. & Mota, C. J. A. A density functional theory based approach to extraframework aluminum species in zeolites. *J. Phys. Chem. B* **107**, 4342–4347 (2003).
  20. Yi, X. *et al.* Origin and Structural Characteristics of Tri-coordinated Extra-framework Aluminum Species in Dealuminated Zeolites. *J. Am. Chem. Soc.* **140**, 10764–10774 (2018).
  21. Zheng, A., Xiao, Y., Liu, Z., Li, G. & Chen, W. Observation of Multinuclear Extra-framework Aluminum Species in Dealuminated Zeolite Catalysts. *Res. Sq.* preprint10.21203/rs.3.rs-50498/v1 (2020).
  22. Gounder, R., Jones, A. J., Carr, R. T. & Iglesia, E. Solvation and acid strength effects on catalysis by faujasite zeolites. *J. Catal.* **286**, 214–223 (2012).
  23. Jiao, J. *et al.* Characterization of framework and extra-framework aluminum species in non-hydrated zeolites Y by <sup>27</sup>Al spin-echo, high-speed MAS, and MQMAS NMR spectroscopy at B<sub>0</sub> = 9.4 to 17.6 T. *Phys. Chem. Chem. Phys.* **7**, 3221–3226 (2005).
  24. Jiao, J., Ray, S. S., Wang, W., Weitkamp, J. & Hunger, M. Effect of dehydration on the local structure of framework silicon atoms in zeolites Y investigated by solid-state NMR spectroscopy. *Z. fur Anorg. Allg. Chem.* **631**, 484–490 (2005).
  25. Issa, H., Toufaily, J., Hamieh, T., Sachse, A. & Pinard, L. Pyridine assisted desilication of mordenite. *Appl. Catal. A Gen.* **583**, 117139 (2019).
  26. Holzinger, J., Beato, P., Lundegaard, L. F. & Skibsted, J. Distribution of Aluminum over the Tetrahedral Sites in ZSM-5 Zeolites and Their Evolution after Steam Treatment. *J. Phys. Chem. C* **122**, 15595–15613 (2018).
  27. Liu, C., Tranca, I., Van Santen, R. A., Hensen, E. J. M. & Pidko, E. A. Scaling Relations for Acidity and Reactivity of Zeolites. *J. Phys. Chem. C* **121**, 23520–23530 (2017).
  28. Li, S. *et al.* Brønsted/Lewis acid synergy in dealuminated HY zeolite: A combined solid-state NMR and theoretical calculation study. *J. Am. Chem. Soc.* **129**, 11161–11171 (2007).
  29. Liu, C., Li, G., Hensen, E. J. M. & Pidko, E. A. Relationship between acidity and catalytic reactivity of faujasite zeolite: A periodic DFT study. *J. Catal.* **344**, 570–577 (2016).
  30. Gola, A. *et al.* Effect of leaching agent in the dealumination of stabilized Y zeolites. *Microporous Mesoporous Mater.* **40**, 73–83 (2000).
  31. Vilhelmsen, L. B. & Hammer, B. A genetic algorithm for first principles global structure optimization of supported nano structures. *J. Chem. Phys.* **141**, 044711 (2014).

32. Grimme, S., Bannwarth, C. & Shushkov, P. A Robust and Accurate Tight-Binding Quantum Chemical Method for Structures, Vibrational Frequencies, and Noncovalent Interactions of Large Molecular Systems Parametrized for All spd-Block Elements ( $Z = 1-86$ ). *J. Chem. Theory Comput.* **13**, 1989–2009 (2017).
33. Bannwarth, C., Ehlert, S. & Grimme, S. GFN2-xTB - An Accurate and Broadly Parametrized Self-Consistent Tight-Binding Quantum Chemical Method with Multipole Electrostatics and Density-Dependent Dispersion Contributions. *J. Chem. Theory Comput.* **15**, 1652–1671 (2019).
34. Pracht, P., Caldeweyher, E., Ehlert, S. & Grimme, S. A Robust Non-Self-Consistent Tight-Binding Quantum Chemistry Method for large Molecules. *ChemRxiv preprint*10.26434/chemrxiv.8326202.v1 (2019).
35. Menzel, J. P. *et al.* Efficient workflow for the investigation of the catalytic cycle of water oxidation catalysts: Combining GFN-xTB and density functional theory. *J. Comput. Chem.* **42**, 1885–1894 (2021).
36. Kresse, G. & Hafner, J. *Ab initio* molecular dynamics for open-shell transition metals. *Phys. Rev. B* **48**, 13115–13118 (1993).
37. Perdew, J. P., Burke, K. & Ernzerhof, M. Generalized gradient approximation made simple. *Phys. Rev. Lett.* **77**, 3865–3868 (1996).
38. Grimme, S., Antony, J., Ehrlich, S. & Krieg, H. A consistent and accurate *ab initio* parametrization of density functional dispersion correction (DFT-D) for the 94 elements H-Pu. *J. Chem. Phys.* **132**, 154104 (2010).
39. Grimme, S., Ehrlich, S. & Goerigk, L. Effect of the damping function in dispersion corrected density functional theory. *J. Comput. Chem.* **32**, 1456–1465 (2011).
40. Blöchl, P. E. Projector augmented-wave method. *Phys. Rev. B* **50**, 17953–17979 (1994).
41. Li, G. *et al.* Stability and reactivity of copper oxo-clusters in ZSM-5 zeolite for selective methane oxidation to methanol. *J. Catal.* **338**, 305–312 (2016).
42. Guhl, H., Miller, W. & Reuter, K. Water adsorption and dissociation on SrTiO<sub>3</sub> (001) revisited: A density functional theory study. *Phys. Rev. B - Condens. Matter Mater. Phys.* **81**, 155455 (2010).
43. Khramenkova, E. V., Medvedev, M. G., Li, G. & Pidko, E. A. Unraveling the Nature of Extraframework Catalytic Ensembles in Zeolites: Flexibility and Dynamics of the Copper-Oxo Trimers in Mordenite. *J. Phys. Chem. Lett.* **12**, 10906–10913 (2021).
44. JANAF Thermochemical Tables ‘DR Stull and H. Prophet, project directors, Natl.’ in *Nat. Stand. Ref. Data Ser., Nat. Bur. Stds.(US)* vol. 1141 (1971).
45. Reuter, K. *Ab Initio* Thermodynamics and First-Principles Microkinetics for Surface Catalysis. *Catal. Letters* **146**, 541–563 (2016).
46. Vicent-Luna, J. M., Apergi, S. & Tao, S. Efficient Computation of Structural and Electronic Properties of Halide Perovskites Using Density Functional Tight Binding: GFN1-xTB Method. *J. Chem. Inf. Model.* **61**, 4415–4424 (2021).
47. Bannwarth, C. *et al.* Extended tight-binding quantum chemistry methods. *Wiley Interdiscip. Rev. Comput. Mol. Sci.* **11**, e1493 (2021).
48. Pu, X., Liu, N. W. & Shi, L. Acid properties and catalysis of USY zeolite with different extraframework aluminum concentration. *Microporous Mesoporous Mater.* **201**, 17–23 (2015).
49. Pidko, E. A., Van Santen, R. A. & Hensen, E. J. M. Multinuclear gallium-oxide cations in high-silica zeolites. *Phys. Chem. Chem. Phys.* **11**, 2893–2902 (2009).
50. Silaghi, M. C., Chizallet, C., Sauer, J. & Raybaud, P. Dealumination mechanisms of zeolites and extra-framework aluminum confinement. *J. Catal.* **339**, 242–255 (2016).

### A2.1. K-medoids clustering: silhouette score, clusters' visualization

Different zeolites' topologies have different arrangements and size pores influencing the accessibility of the extraframework species and the proximity of the BAS.<sup>1,2</sup> Therefore, it is important to evaluate the structural features of each topology used in this study. A structure of a MOR has a one-dimensional pore system including the main channel with a diameter of 6.7 x 7.0 Å and a compressed channel with a diameter of 2.6 x 5.7 Å. It was found to be efficient in catalyzing cracking, hydroisomerization, hydrocracking and alkylation.<sup>3</sup> As a one-dimensional zeolite, it might experience diffusion constraints and deactivation by pore blockage. A structure of a ZSM-5 framework has an MFI topology, with intersecting straight and sinusoidal 10-membered ring channels, with a channel of diameter 5.1 x 5.5 Å. This topology is extensively employed in synthesizing hydrocarbons from methanol (MTH), nitrous oxide decomposition and oxidation of benzene to phenol.<sup>4</sup>

### A2.2. The choice of the portion of the low-energy structures extracted from GA for the DFT refinement

To define the required portion of the GA population pool for finding the low-energy structure, we have performed a test study on the  $[\text{AlOH}]^{2+}$  and  $[\text{AlO}_2\text{H}_3]^{2+}$  stoichiometries, where 9 and 17 structures from the population pool were used respectively. The lowest-lying cluster structures obtained from the GA search were optimized at the PBE-D3(BJ) level of theory to see if the increase in theory level causes changes in energy trends and geometries. These cluster DFT calculations were carried out using CP2K software package with the orbital transformation and Quickstep module for faster convergence.<sup>5</sup> The Goedecker-Teter-Hutter pseudopotentials and DZVP-MOLOPT-SR-GTH basis sets were used.<sup>6,7</sup>

The changes in the relative electronic energies when the level of the theory increases are summarized in **Figures A2.1** and **A2.2**. For the  $[\text{AlOH}]^{2+}$  stoichiometry, the global minimum observed in the GA search forms  $\text{AlO}^+$  and  $\text{H}^+$  species, which are both bound to different framework Al sites (structure **b** in **Figure A2.1**). The other low-lying structure observed (structure **a** in **Figure A2.1**) has the  $[\text{AlOH}]^{2+}$  site which is bound to a single framework Al embedded in the zeolite. **Figure A2.1** shows that within the 5 lowest-lying configurations found in the GA search, the global minimum can be found which is supported by the DFT-level optimization.

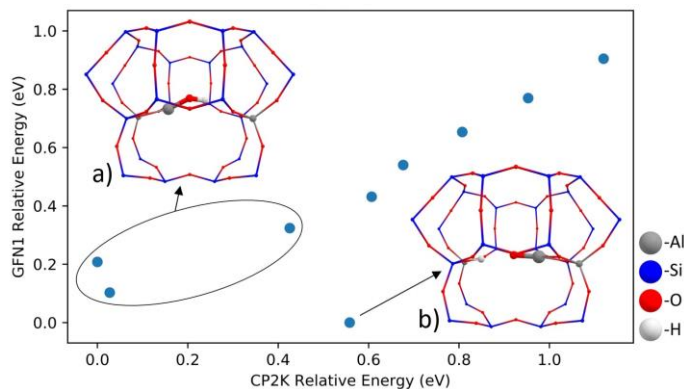


**Figure A2.1** The test study assesses the correlation between the electronic energies of the lowest-lying structures obtained from the xTB-based GA search and the electronic energies obtained from the following single-point DFT-based calculations. The comparison was conducted on  $[\text{AlOH}]^{2+}$  cluster configurations confined in the side pocket of mordenite. The level of theory employed for the xTB is GFN1, while the DFT calculations were carried out at the PBE-D3(BJ) level of theory.

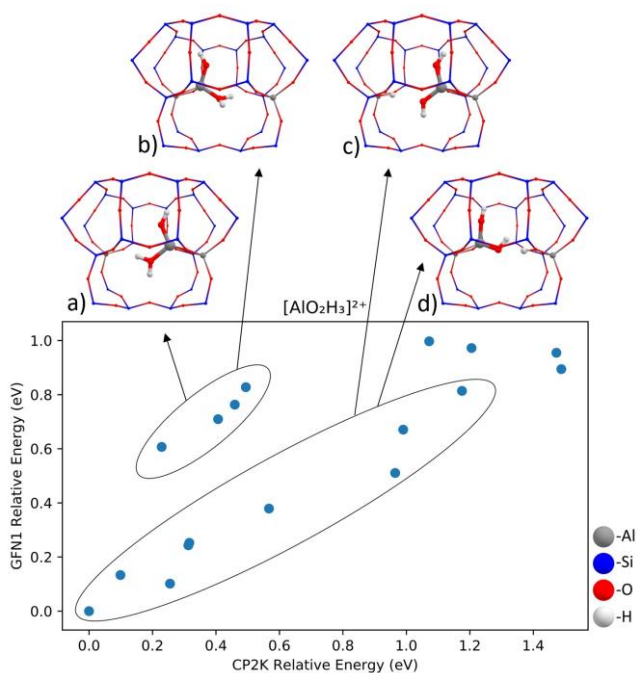


**Figure A2.2** The test study assesses the correlation between the electronic energies of the lowest-lying structures obtained from the xTB-based GA search and the electronic energies obtained from the following single-point DFT-based calculation. The comparison was conducted on  $[\text{AlO}_2\text{H}_3]^{2+}$  cluster configurations confined in the side pocket of mordenite. The level of theory employed for the xTB is GFN1, while the DFT calculations were carried out at the PBE-D3(BJ) level of theory.

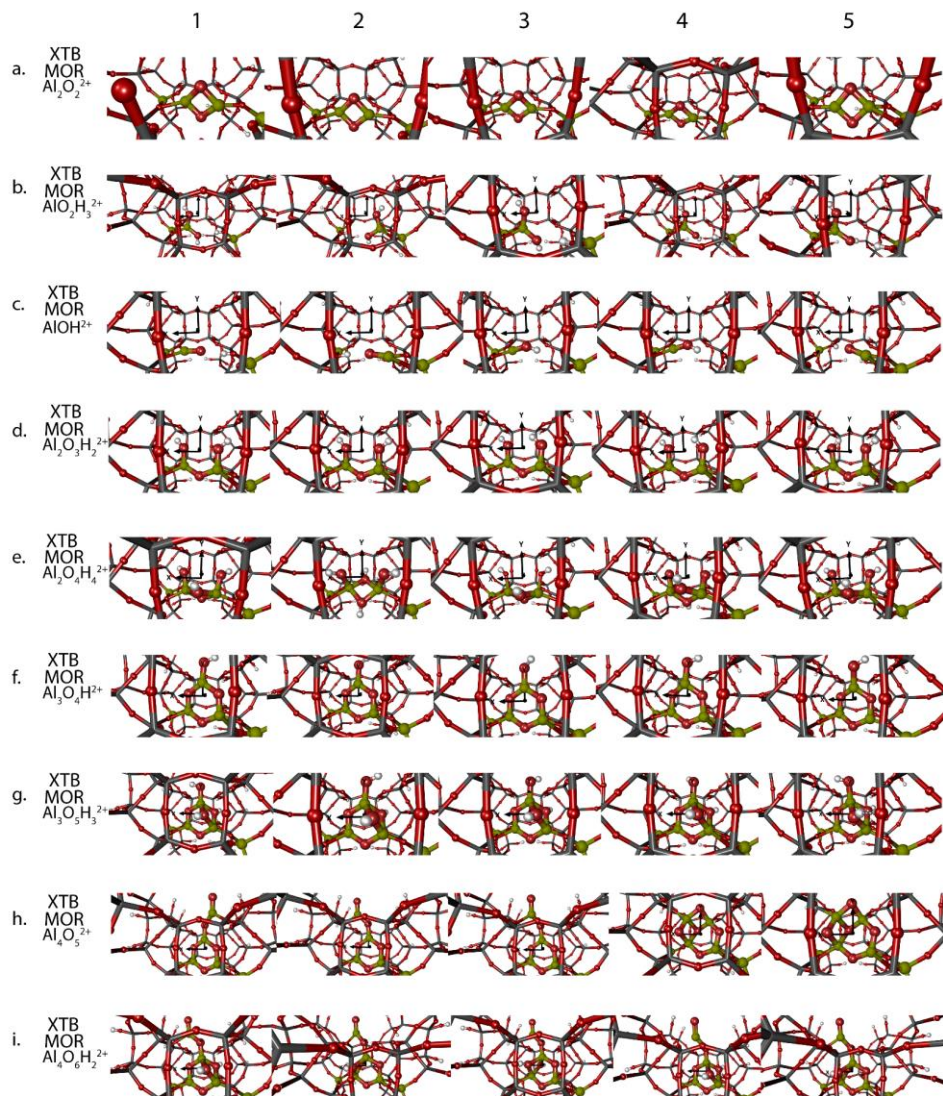


**Figure A2.3** The five lowest-lying geometries for each stoichiometry confined in the side pocket of MOR generated in the final population pool of the GA procedure.

Another stoichiometry –  $[\text{AlO}_2\text{H}_3]^{2+}$  – has shown general agreement between the  $x\text{TB}$  and PBE calculations. The best correlation has been achieved for the formation of the  $[\text{AlO}_2\text{H}_2]^+$  species over one framework Al site and  $\text{H}^+$  over the other (structures **c** and **d** in **Figure A2.2**). As for the other isomer,  $[\text{AlO}_2\text{H}_3]^{2+}$  site, which is bound to a single framework Al site, higher stability was predicted in the PBE-level optimization. Therefore, based on the inconsistencies between the energies assigned by the  $x\text{TB}$  and DFT methods to the same global minimum defined in the GA search, we have considered

a portion of the low-energy structures from the population pool instead of a single global minimum structure. The choice was made for the 5 lowest structures to capture the electronic deviations caused by the semiempirical  $xTB$  method at a reasonable computational cost.

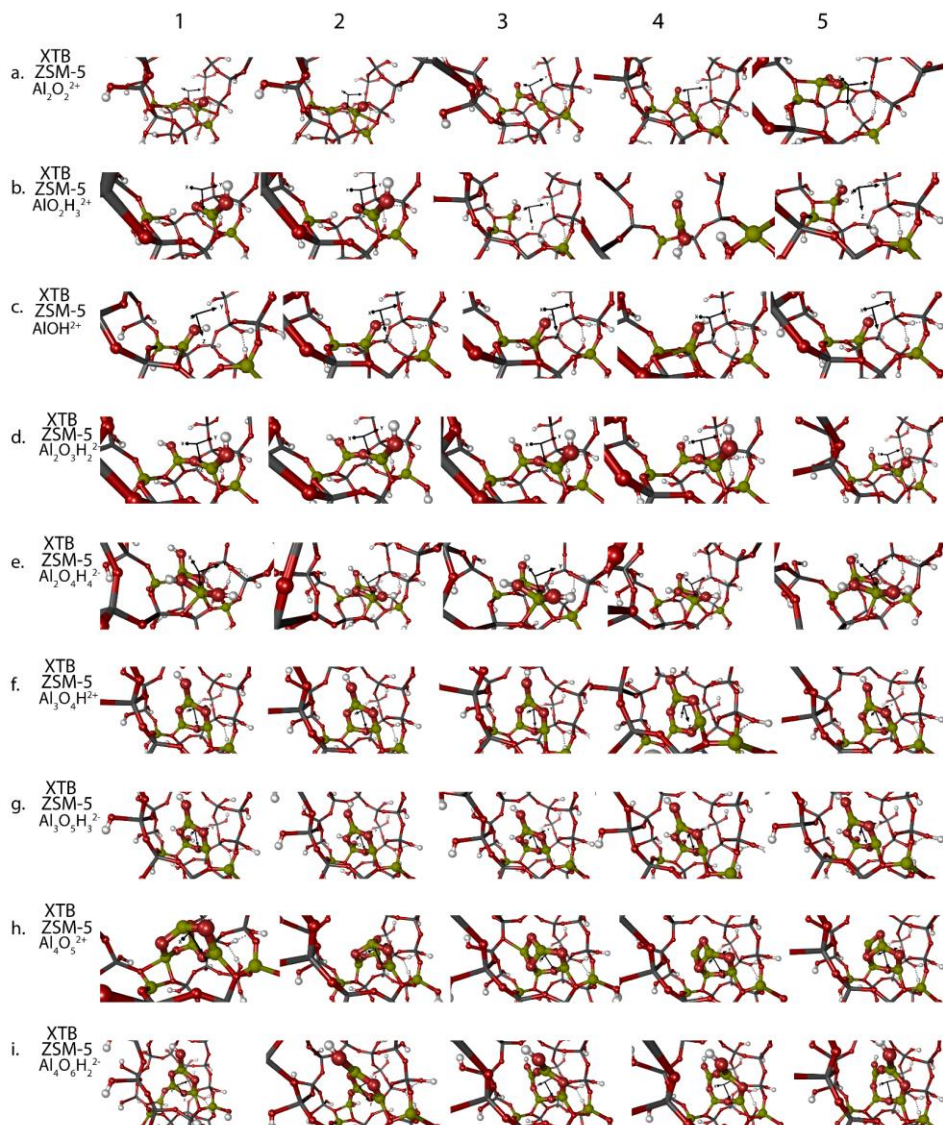


**Figure A2.4** The five lowest-lying geometries for each stoichiometry confined in the gamma site of ZSM-5 generated in the final population pool of the GA procedure.

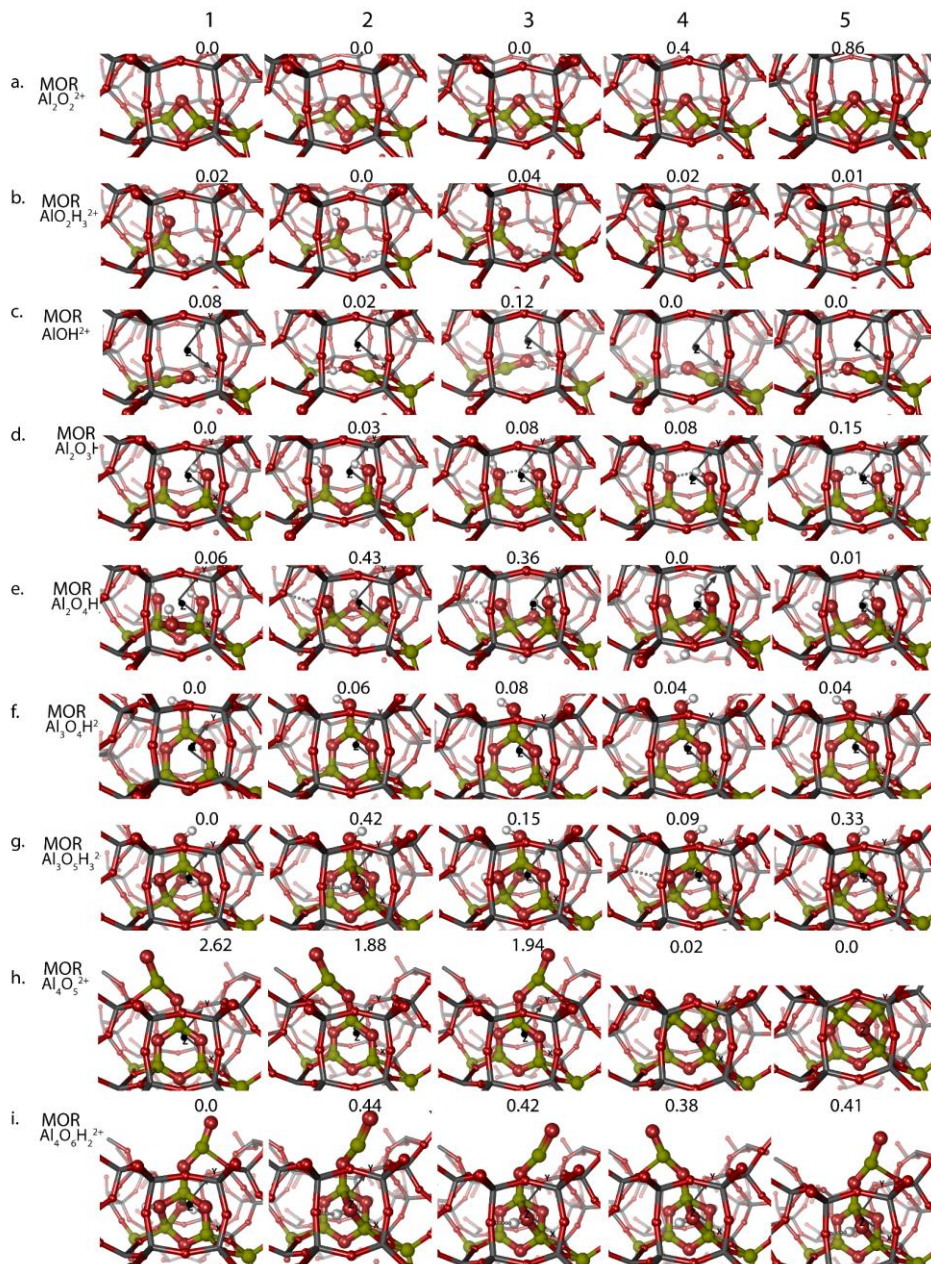


**Figure A2.5** The five lowest-lying geometries for each stoichiometry confined in the side pocket of MOR obtained from the GA final population pool and optimized in the periodic cell at the PBE-D3(BJ) level of theory. The energies are on the top of the structures in eV with respect to the lowest-lying configuration in a row.

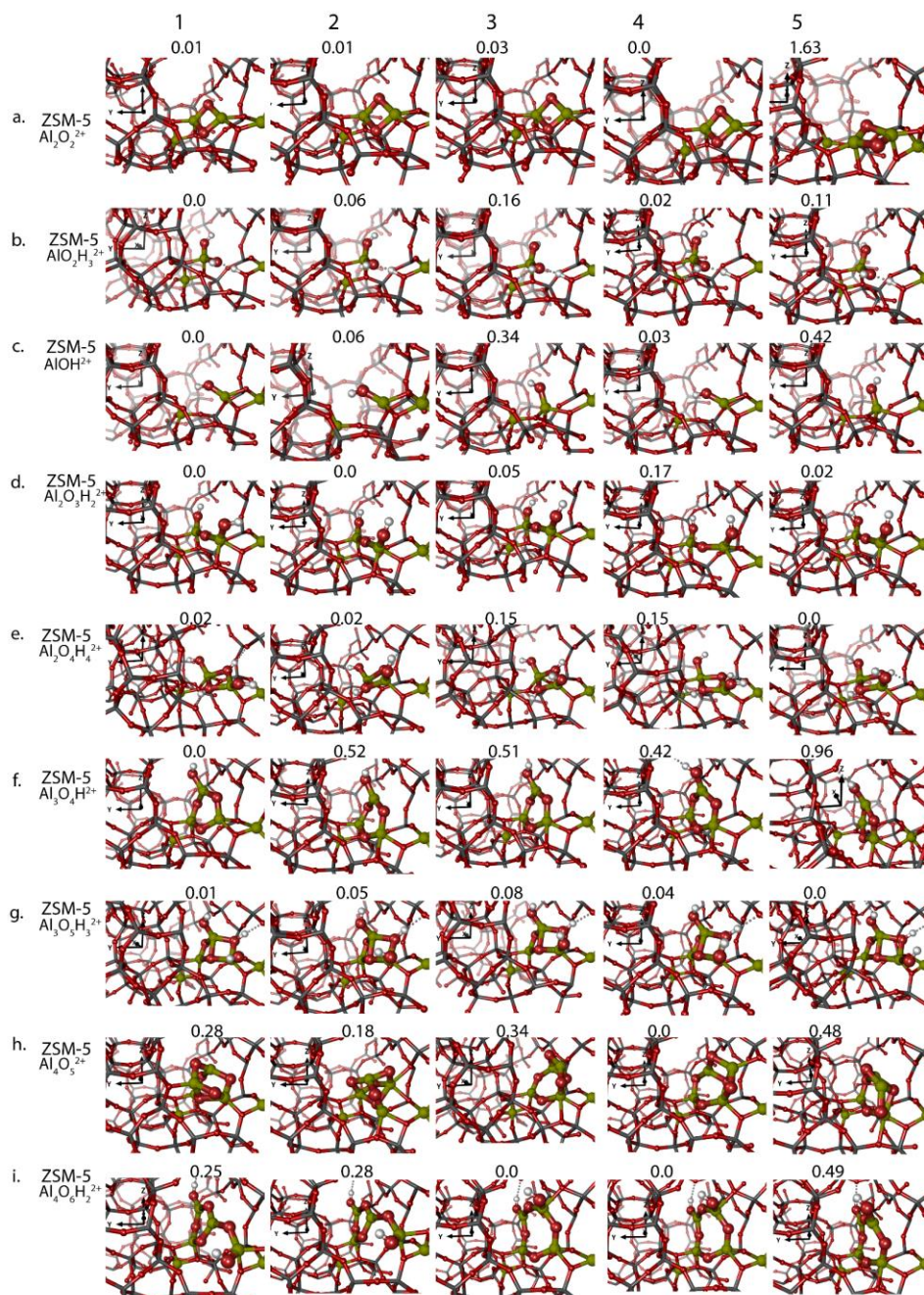


**Figure A2.6** The five lowest-lying geometries for each stoichiometry confined in the gamma site of ZSM-5 obtained from the GA final population pool and optimized in the periodic cell at the PBE-D3(BJ) level of theory. The energies are on the top of the structures in eV with respect to the lowest-lying configuration in a row.

### A2.3. Supplementary aiTA analysis with Al(OH)<sub>3</sub> as a reference system

The dealumination treatments in zeolites can lead to the formation of abundant EFAl species. To account for an alternative source of EFAl in the system – Al(OH)<sub>3</sub> – another aiTA diagram has been constructed employing Al(OH)<sub>3</sub> as a reference structure. The following equilibrium was considered for the stability assessment:

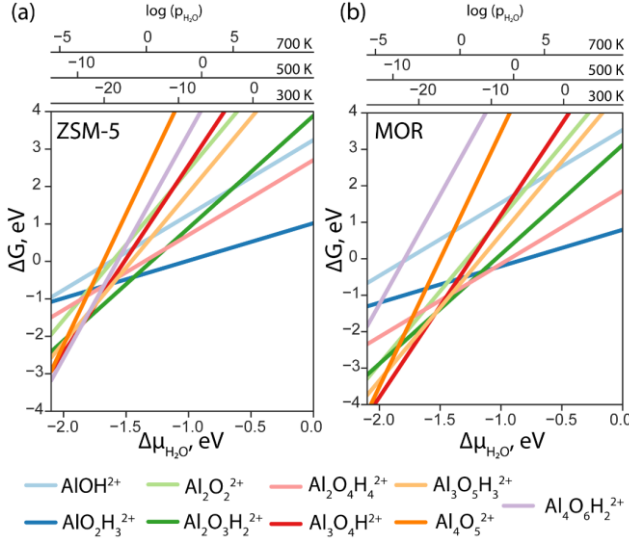
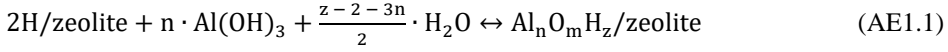


**Figure A2.7** The Gibbs free energy diagram of the EFAl species confined in ZSM-5 (a) and in MOR (b) was calculated with respect to the Al(OH)<sub>3</sub> phase as a function of water chemical potential.

The reaction free energy is defined as:

$$\Delta G_{\text{rxn}}(T, p) = G_{\text{Al}_n\text{O}_m\text{H}_z/\text{zeolite}}^{\text{S}} - n \cdot G_{\text{Al}(\text{OH})_3}^{\text{S}} - G_{2\text{H}/\text{zeolite}}^{\text{S}} - \frac{z-2-3n}{2} \cdot \mu_{\text{H}_2\text{O}}^{\text{g}} \quad (\text{AE1.2})$$

where,  $G_{\text{Al}_n\text{O}_m\text{H}_z/\text{zeolite}}^{\text{S}}$ ,  $G_{\text{Al}(\text{OH})_3}^{\text{S}}$  and  $G_{2\text{H}/\text{zeolite}}^{\text{S}}$  are the Gibbs free energies of the EFAl-containing zeolite model, bulk Al(OH)<sub>3</sub> and parent EFAl-free acidic zeolite matrix (2H/zeolite). The bulk, 2H/zeolite and Al<sub>n</sub>O<sub>m</sub>H<sub>z</sub>/zeolite are the DFT-approximated energies of the gibbsite, the respective zeolite framework with two hydrogens and the frameworks with situated EFAls. The PV-contributions entropy of the solids could be neglected and the expression for the Gibbs free energy can be written as:

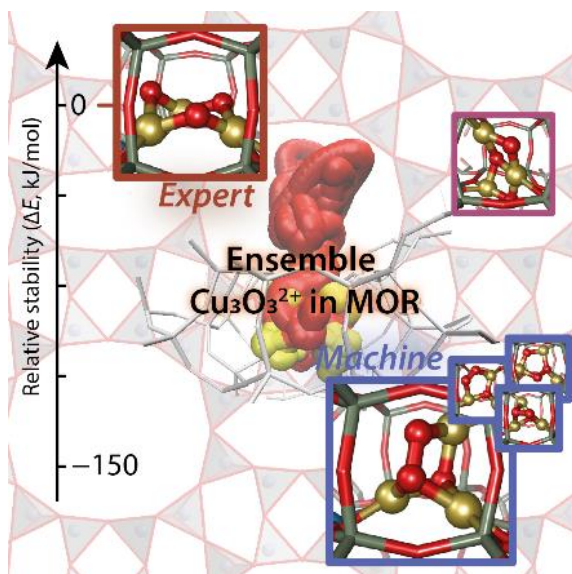
$$\Delta G_{\text{rxn}}(T, p) = E_{\text{Al}_n\text{O}_m\text{H}_z/\text{zeolite}}^{\text{S}} - n \cdot E_{\text{Al}(\text{OH})_3}^{\text{S}} - E_{2\text{H}/\text{zeolite}}^{\text{S}} - \frac{z-2-3n}{2} \cdot \mu_{\text{H}_2\text{O}}^{\text{g}} \quad (\text{AE1.3})$$

## A2.4. References (Appendix A2)

1. Xu, W., Miller, S. J., Agrawal, P. K. & Jones, C. W. Zeolite topology effects in the alkylation of phenol with propylene. *Appl. Catal. A Gen.* **459**, 114–120 (2013).
2. Van Der Graaff, W. N. P., Tempelman, C. H. L., Pidko, E. A. & Hensen, E. J. M. Influence of pore topology on synthesis and reactivity of Sn-modified zeolite catalysts for carbohydrate conversions. *Catal. Sci. Technol.* **7**, 3151–3162 (2017).
3. Aguado, J., Serrano, D. P., Escola, J. M. & Peral, A. Catalytic cracking of polyethylene over zeolite mordenite with enhanced textural properties. *J. Anal. Appl. Pyrolysis* **85**, 352–358 (2009).
4. Joyner, R. & Stockenhuber, M. Preparation, Characterization, and Performance of Fe-ZSM-5 Catalysts. *J. Phys. Chem. B* **103**, 5963–5976 (1999).
5. Kühne, T. D. *et al.* CP2K: An electronic structure and molecular dynamics software package-Quickstep: Efficient and accurate electronic structure calculations. *J. Chem. Phys.* **152**, 194103 (2020).
6. VandeVondele, J. and Hutter, J. J. Gaussian basis sets for accurate calculations on molecular systems in gas and condensed phases. *J. Chem. Phys.* **127**, 114105 (2007).
7. Krack, M. Pseudopotentials for H to Kr optimized for gradient-corrected exchange-correlation functionals. *Theor. Chem. Acc.* **114**, 145–152 (2005).



**Unraveling nature of extraframework catalytic ensembles in zeolites: flexibility and dynamics of the copper-oxo trimers in mordenite**



## Summary

---

Extraframework cations define the chemical versatility of zeolite catalysts. Addressing their structural complexity and dynamic behavior represents one of the main fundamental challenges in the field. Herein we present a computational approach for the identification and analysis of the accessible pool of intrazeolite extraframework complexes with a Cu/MOR catalyst as an industrially important model system. We employ *ab initio* molecular dynamics for capturing the ensemble of reactive isomers with the  $[\text{Cu}_3\text{O}_3]^{2+}$  stoichiometry confined in the mordenite channels. The high structural diversity of the generated isomers was ensured by concentrating the kinetic energy along the low-curvature direction of the potential energy surface (PES). Geometrically distinct  $[\text{Cu}_3\text{O}_3]^{2+}$  complexes were identified via a series of clustering procedures ensuring that one structure of each local minima is retained. The proposed procedure has resulted in a set of previously unknown peroxo-complexes, which are  $>50$  kJ/mol more stable than the recently hypothesized chair-shaped structure. Our analysis demonstrates that the most stable peroxo-containing clusters can be formed under *operando* conditions from molecular oxygen and  $\text{Cu}_3\text{O}$  unit, similar to that in methane monooxygenase (MMO) enzymes.

This chapter is based on the following publication:

Khramenkova E. V., Medvedev M. G., Li G., Pidko E. A.  
*J. Phys. Chem. Lett.* **12**, 10906–10913 (2021).

### **3.1. Introduction**

The development of advanced predictive models in heterogeneous catalysis requires a deep insight into the molecular-level structure of the active sites, the mechanism of their action and evolution under the operating conditions. There is growing evidence of the critical role of dynamic phenomena for catalytic reactivity. When exposed to the reaction conditions, the reactive ensembles may evolve and reconstruct, therefore, altering their chemical reactivity and catalytic behavior.<sup>1</sup> Understanding the dynamics of the active sites induced by the environmental variables is key to the development of a detailed molecular picture of the catalytic phenomena and thus forming the basis for the rational design of new and improved catalyst systems.<sup>2</sup>

The view of the catalytic active site as a dynamic system conflicts with the conventional theoretical approaches. It is commonly assumed that the configurations corresponding to the global minima of the active site – the intrinsically most stable dominant configuration – are maintained during the reaction. This assumption is only acceptable when the catalytic site is truly rigid.<sup>3</sup> However, a wider range of catalytic structures can emerge during the reaction in response to the exposure to the reactive environment.<sup>4,5</sup> The latter includes such parameters as an elevated temperature that induces the thermal crossing of the energy barriers, the concentration of reactants and products, electrochemical potential, pressure, solvents, etc. Therefore, active site reorganization and its dynamics have to be accounted for when building an atomistic description of the catalytic system.

The dynamics in catalytic sites was spotted by Zhang et al. who extended the description of the catalytic models by representing a dynamic evolution of the ensemble of structures occurring under realistic conditions.<sup>6</sup> In this sense, the isomerization of the catalyst introduces new reaction pathways with different mechanisms and rates. Catalyst activity, stability and reactivity can be controlled by the presence of the less populated metastable states whose catalytic role is abominably underestimated.

The growing understanding of the role of metastable states encourages studying the properties of a catalytic system as ensemble averages, with contributions of all the coexisting configurations. Such a broader picture of the catalytic active sites is crucial to construct a comprehensive mechanistic representation beyond the field of heterogeneous catalysis as demonstrated recently for uncatalyzed reactions<sup>7,8</sup> and homogeneous catalysis.<sup>9,10</sup> A representative example of dynamic heterogeneous catalysis is CO oxidation by  $\text{MnO}_x\text{-CeO}_2$  where the reaction proceeds via two parallel routes in a small temperature region of 100 – 130 °C.<sup>11</sup> Dynamic surface reconstruction and the presence of metastable reactive ensembles on the catalyst surface have been proposed as the key factors behind the unique catalytic performance of boride-based materials.<sup>12</sup> Reaction-induced reconstruction of supported Pt nanoclusters was shown to form specific reaction

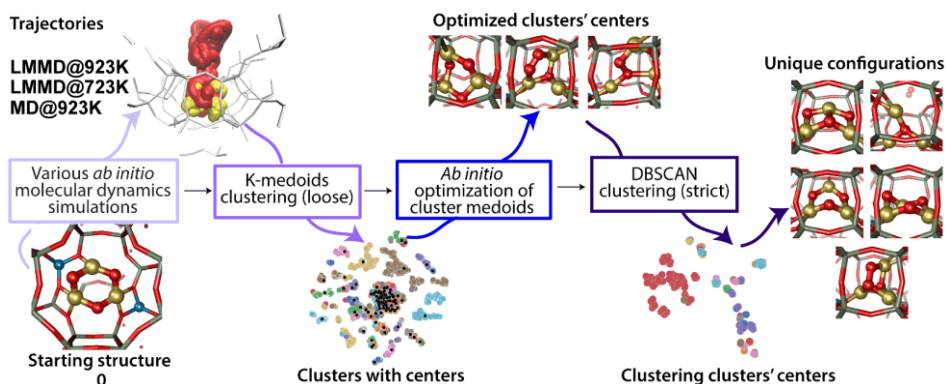
ensembles necessary for the efficient catalytic conversion of light alkanes.<sup>13</sup> In zeolite catalysis, growing evidence is presented on the critical role of reaction-induced dynamics of the extraframework complexes.<sup>14</sup> For example, the mobility of Cu ions in chabazite pores during the selective catalytic reduction was demonstrated in a combined experimental and computational study by Paolucci et al.<sup>15</sup> The mobilization of the exchangeable Cu(I) site due to the interaction with the ammonia substrate allowed for their diffusion through the zeolite channels to form the catalytically active Cu(II) dimers.

Zeolites and related materials modified with metals/non-metals are promising catalysts as they possess specific reactive and oxidative environments induced by the framework – solid ligand. Their broad applicability in many processes results from the single-site nature of the catalytic sites and their well-defined structure, stability and recyclability.<sup>16</sup> Zeolites modified with Cu are capable of hydroxylating methane at low temperatures to produce methanol.<sup>17–20</sup> Upon the activation with molecular O<sub>2</sub> extraframework oxygenated copper species are formed in the zeolite channels capable of selectively activating the strong C-H-bond in methane.<sup>21</sup> The ongoing debates on the nuclearity of the catalytically active centers have produced various hypothetical active sites, each supplied with spectroscopic and/or theoretical evidence.<sup>22</sup> The situation here closely mimics that in oxo-copper clusters in methane monooxygenases (MMOs), where various structures of active sites were “proved” over the years, including a Cu<sub>3</sub>(μ<sup>3</sup>-O)<sup>2+</sup> one.<sup>21,23–28</sup>

The speciation of Cu-oxo extraframework species relevant for methane oxofunctionalization was most extensively studied in ZSM-5 and MOR zeolites. Initial reactivity studies complemented by detailed UV-vis characterization attributed the unique methane activation activity of Cu-zeolites to the presence of bis(μ-oxo)dicopper sites.<sup>29</sup> This assignment has been later refined in a combined Raman spectroscopy and DFT study by Woertink et al, who concluded on the key role of mono(μ-oxo)dicopper in Cu/ZSM-5 zeolite for methane oxidation.<sup>30</sup> The earlier characterization studies employed catalytic materials, in which only ca. 10% of the exchangeable Cu sites contributed to the methane activation activity. Grundner et al.<sup>31</sup> reported a Cu/MOR catalyst, in which the majority of intrazeolite Cu was proposed to form the reactive ensembles. The catalysts were extensively characterized by EXAFS complemented by DFT-based *ab initio* thermodynamic analysis, which revealed the presence of a cyclic chair-shaped [Cu<sub>3</sub>(μ-O)<sub>3</sub>]<sup>2+</sup> cluster. This configuration was later also proposed as the active site in other zeolite topologies.<sup>32–35</sup> Further on, the increased stability and reactivity were shown for the clusters with higher nuclearity such as [Cu<sub>4</sub>O<sub>4</sub>]<sup>2+</sup> and [Cu<sub>5</sub>O<sub>5</sub>]<sup>2+</sup>.<sup>36</sup> The reactivity and ensemble behavior of oxygenated alumina-supported Cu<sub>4</sub>O<sub>3</sub> and Cu<sub>4</sub>O<sub>4</sub> species was investigated by Sun et al.<sup>37</sup> It was proposed the most stable configurations dominating the catalytic material are in fact inactive towards the oxidation of light alkanes. However,

their isomerization of metastable configurations under the reaction conditions may give rise to pronounced catalytic reactivity.

Because Cu/MOR system operates at ~475K, its catalytic site can be expected to show a high degree of fluxionality at the *operando* conditions, making the depiction of all its reactive conformers crucial for further mechanistic studies. Building a detailed ensemble of all the relevant structural isomers of a catalytic site is a challenging task, which, to the best of our knowledge, has not been addressed so far for zeolite catalysis.



**Scheme 3.1.** A schematic overview of the proposed computational workflow for automatic structural exploration of extraframework cations in the zeolite.

To gain molecular-level insight into the catalytic mechanism and the nature of the catalytic sites where an ensemble of states can be pictured, various experimental and theoretical methods can be utilized. However, the possibility that only a minor part of the sites are catalytically active<sup>31</sup> compromises most experimental methods which provide an averaged coarse picture of heavy atom alignment, as well as computational global-optimization approaches that aim to locate the most stable structures.<sup>38</sup> The *ab initio* molecular dynamics (aiMD), on the other hand, allow one to study the evolution of the pre-selected site under the *operando* conditions, with the drawback of being severely constrained to the starting structure.<sup>39</sup> To overcome this limitation, a set of “biased” aiMD methods including umbrella sampling,<sup>40</sup> metadynamics<sup>41</sup> or thermodynamic integration<sup>42</sup> were designed, which, however, require a choice of the structural parameters determining the evolution of the system.<sup>43</sup> For complex multi-bound systems like zeolite active sites this choice is highly non-trivial, and yet it is known that most chemical transformations proceed along the soft vibrational modes,<sup>44</sup> so it is possible to utilize a Low-Mode following aiMD (LMMD) to simulate their evolution at timescales largely exceeding those of the actual molecular dynamics. The LMMD technique improves the sampling by following the low vibrational modes only, which narrows the explored conformational

space to the physically meaningful configurations making such an approach more affordable in combination with a higher level of theory.

In this chapter, we analyze the clusters which can be formed starting from the trimeric  $[\text{Cu}_3(\mu\text{-O})_3]^{2+}$  site in MOR zeolite, for which chair conformation has been earlier proposed based on EXAFS data. To this end, we develop a new computational workflow enabling the exhaustive search of active site configurations (**Scheme 3.1**). Using this workflow we observe that while the copper triangle observed in EXAFS is indeed quite rigid, in the most stable conformations it is bound with a  $\mu^3$ -oxygen, similarly to one of the active sites hypothesized for MMO enzymes. The other two oxygens form a peroxo-unit, which, according to the thermodynamic analysis, is reversibly detachable as molecular oxygen (leaving simply  $\text{Cu}_3(\mu^3\text{-O})^{2+}$  cluster), suggesting the on-demand formation of such units at *operando* conditions.

## 3.2. Computational details

### 3.2.1. *Ab Initio* Molecular Dynamics (aiMD)

AiMD was used to sample the configurational space of the extraframework clusters confined inside the zeolite micropores. All calculations were carried out using a fully periodic zeolite structure represented by a supercell. A periodic supercell model of MOR was constructed by expanding the elementary cell by one translation along the c-axis and optimized giving the lattice parameters:  $a = b = 13.648$ ,  $c = 15.015$  Å. The two lattice Si ions in the side-pocket 8-MR channel were substituted with Al to give the Si/Al ratio of 23. The resulting framework negative charge is compensated by the  $[\text{Cu}_3(\mu\text{-O})_3]^{2+}$  cluster, for which we presumed the triplet spin state ( $s = 3/2$ ), which was found to be lower in energy than the low spin state ( $s = 1/2$ ). Previously it was shown that the energy difference between high and low spin states for this structure is small.<sup>34</sup>

AiMD simulations were carried out using CP2K software package with the Quickstep module and orbital transformation for faster convergence.<sup>45-49</sup> All calculations were carried out in the framework of density functional theory (DFT) using the gradient-corrected PBE-D3(BJ) functional<sup>50</sup> with the empirical dispersion correction by Grimme.<sup>51-53</sup> The Goedecker-Teter-Hutter pseudopotentials with a combination of periodic Poisson solver were used to calculate the electron repulsion integrals.<sup>54-56</sup> A Gaussian basis set DZVP-MOLOPT-SR-GTH was used for Si, O, Al atoms while the TZV2P-MOLOPT-SR-GTH basis set was used for Cu.<sup>57</sup> The projected augmented wave (PAW) method with a cutoff energy of 450 Ry was used.<sup>58</sup> The relative cutoff was set to 30 Ry. The SCF convergence criterion was set to  $10\text{E-}5$  a.u. Each aiMD trajectory was integrated for 4.25 ps within the canonical ensemble by solving the classical equation of motion with a time step of 0.5 fs, giving 6 MD runs of each type and 18 in total.<sup>59-61</sup> aiMD

trajectories were simulated at temperatures of 723K (**LMMD@723 K**) and 923K (**LMMD@923 K, MD@923 K**). To improve the configurational sampling, the velocity softening low mode-guided aiMD simulations were implemented as described here.<sup>7,62</sup> These trajectories were denoted as LMMD (**LMMD@923 K, LMMD@723 K**). In these simulations, the velocities were directed along the low curvatures for the first 500 steps and then the standard aiMD procedure was activated.

### 3.2.2. Clustering

A **clustering** algorithm was employed to determine the structurally distinct configurations in the aiMD trajectories. The clustering process was performed using an unsupervised machine learning algorithm – k-medoids – which is widely applied for clustering MD trajectories.<sup>63,64</sup> The algorithm is based on the procedure of minimizing a sum of pairwise dissimilarities between structures and their medoids (the centers of the cluster) as implemented in scikit-learn.<sup>65</sup> When k-medoids are generated, k-medoids algorithm refines them by computing the distance between the centers of clustering and the clusters belonging to them. Every 50<sup>th</sup> step of each trajectory was included in the clustering procedure. The silhouette index was chosen as a validation measure to establish the object's similarity to the other members of the cluster. The distance metric for both clustering method and validation measures was set to “Euclidean” distance which measures the square distance between vectors. For visualization purposes, the clusters were projected into a bidimensional Euclidean space using t-SNE algorithm.<sup>66-68</sup> We have applied clustering in the subsets of trajectories separately, but the clustering of all the trajectories together was performed but not considered further as it revealed a low silhouette score (see **Figure A3.1d** in **Appendix A3**).

Next, the geometries of the cluster's centers were optimized to local minima using the Quasi-Newton (Broyden-Fletcher-Goldfarb-Shanno) algorithm as implemented in CP2K using the same parameters for the electronic structure calculations as described above. The hybrid functional PBE0 was used to calculate the single point energy of configurations optimized at the PBE level of theory. The auxiliary density matrix method (ADMM) was utilized to reduce the costs for approximate calculations of non-local exchange energy. Vibrational analysis of the optimized structures was carried out using the finite difference method (0.02 Å atomic displacement).

To facilitate further analysis, the centers of the optimized clusters were further grouped using the density-based spatial clustering of applications with noise (DBSCAN)<sup>69,70</sup> as implemented in scikit-learn.<sup>65</sup> DBSCAN method is able to detect the core samples of high density and expand clusters from them. The optimal value of *eps* parameter, which specifies the proximity of the points to become a part of the cluster, was set to 0.4. The value was chosen based on the k-nearest neighbor of each point. The minimum number of points in a cluster equals 1.

### 3.2.3. *Ab initio* Thermodynamics Analysis (aiTA)

AiTA was used to assess the stabilities of the different active site configurations under the model conditions of the catalyst activation and catalytic reaction. aiTA enables computing the 2 – or 3 – dimensional dependencies of the Gibbs free energies on the state of the gaseous components in the catalyst's environment in terms of the T- and P-dependencies.<sup>71,72</sup> The stability of the extraframework Cu trimers was assessed with the reference to the  $\text{Cu}_3(\mu^3\text{-O})^{2+}$  in the side pocket of mordenite. Such a reference state represents the regeneration of the  $\text{Cu}_3(\mu\text{-O})_3^{2+}$  active species under  $\text{O}_2$  activation. The following equilibrium was considered:



where  $\text{Cu}_3\text{O}_3^{2+}/\text{MOR}$  is one of the configurations obtained from aiMD and  $\text{Cu}_3\text{O}^{3+}/\text{MOR}$  is a reduced isomer.  $\text{O}_2$  is the molecular oxygen. The reaction Gibbs free energy  $\Delta G_{\text{Cu}_3\text{O}_3^{2+}/\text{MOR}}$  for equilibrium (E3.1) is defined as follows:

$$\Delta G_{\text{Cu}_3\text{O}_3^{2+}/\text{MOR}} = G_{\text{Cu}_3\text{O}_3^{2+}/\text{MOR}}^{\text{S}} - G_{\text{Cu}_3\text{O}^{3+}/\text{MOR}}^{\text{S}} - 2\mu_{\text{O}}^{\text{g}} + \Delta \text{ZPE}_{\text{Cu}_3\text{O}_3^{2+}/\text{MOR}} \quad (\text{E3.2})$$

Gibbs free energies of solids are approximated as their respective electronic DFT-energies calculated at the PBE0-D3(BJ) level of theory, with the vibrational contribution  $\Delta \text{ZPE}_{\text{Cu}_3\text{O}_3^{2+}/\text{MOR}}$  calculated at the PBE level. The T- and P-condition dependencies are expressed via the chemical potential of oxygen  $\mu_{\text{O}}^{\text{g}}$  which is defined as:

$$\mu_{\text{O}}^{\text{g}}(\text{T}, \text{p}) = \frac{1}{2} E_{\text{O}_2} + \Delta \mu_{\text{O}}^{\text{g}}(\text{T}, \text{p}) \quad (\text{E3.3})$$

The  $E_{\text{O}_2}$  is the electronic energy of molecular oxygen. The change in chemical potential  $\Delta \mu_{\text{O}}^{\text{g}}(\text{T}, \text{p})$  can be expressed as:

$$\Delta \mu_{\text{O}}^{\text{g}}(\text{T}, \text{p}) = \Delta \mu_{\text{O}}(\text{T}, \text{p}^0) + \frac{1}{2} \text{RT} \ln \left( \frac{p_{\text{O}_2}}{p_{\text{O}_2}^0} \right) = \frac{1}{2} \left[ \text{H}(\text{T}, \text{p}^0, \text{O}_2) - \text{H}(\text{OK}, \text{p}^0, \text{O}_2) - \right. \\ \left. \text{T}(\text{S}(\text{T}, \text{p}^0, \text{O}_2) - \text{S}(\text{OK}, \text{p}^0, \text{O}_2)) + \text{RT} \ln \left( \frac{p_{\text{O}_2}}{p_{\text{O}_2}^0} \right) \right] \quad (\text{E3.4})$$

The zero-point energy was defined standardly. We have only considered the contributions of the extraframework Cu-oxo atoms. Combining (E3.2), (E3.3) with the ZPE we arrive at the following:

$$\Delta G_{\text{Cu}_3\text{O}_3^{2+}/\text{MOR}} = E_{\text{Cu}_3\text{O}_3^{2+}/\text{MOR}} - E_{\text{Cu}_3\text{O}^{3+}/\text{MOR}} - E_{\text{O}_2} - 2\Delta \mu_{\text{O}}^{\text{g}}(\text{T}, \text{p}) + \\ \Delta \text{ZPE}_{\text{Cu}_3\text{O}_3^{2+}/\text{MOR}} \quad (\text{E3.5})$$

where  $E_{\text{Cu}_3\text{O}_3^{2+}/\text{MOR}}$ ,  $E_{\text{Cu}_3\text{O}^{3+}/\text{MOR}}$  are electronic energies of the  $\text{Cu}_3\text{O}_3^{2+}$  structural isomer and  $\text{Cu}_3\text{O}^{2+}$  reduced isomer respectively.

### 3.3. Results and discussion

The procedure of the exhaustive structural search (**Scheme 3.1**) starts with the exploration of the available configurational space for the extraframework species inside the zeolite pores via the *ab initio* molecular dynamics (aiMD) simulations at PBE-D3(BJ) level of theory.<sup>50–53</sup> The resulting trajectories were analyzed using the loose clustering with k-medoids algorithm to identify structurally distinct frames. As some of the clusters may lay at the different slopes of the same valley, we optimize their centers and clustered them again using the DBSCAN (Density-Based Spatial Clustering of Applications with Noise) method, particularly suitable for the irregularly-shaped clusters to determine the final unique configurations of the extraframework ensembles. The details of the computational methods and procedures are provided in the **Appendix A3** of the manuscript.

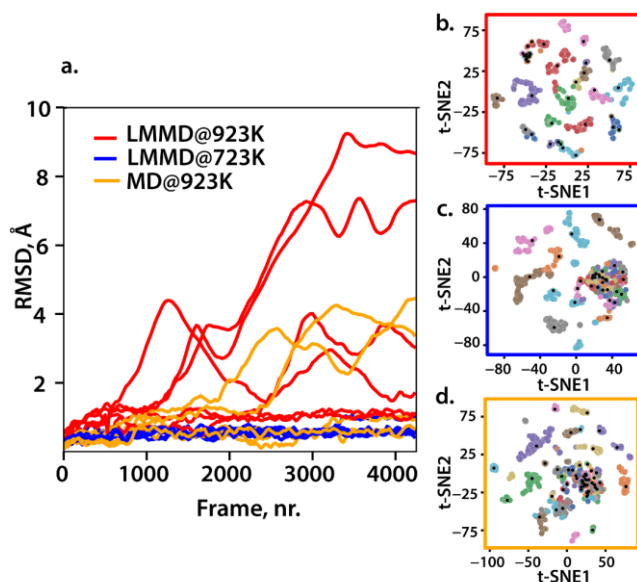


**Figure 3.1** (a) RMSD of the different simulation trajectories for  $\text{Cu}_3\text{O}_3^{2+}$  in MOR. The results of the k-medoids clustering of **LMMD@923 K** (b, the highest Silhouette score is 0.41 at 44 clusters), **LMMD@723 K** (c, the highest Silhouette score is 0.34 at 36 clusters), **MD@923 K** (d, the highest Silhouette score is 0.31 at 66 clusters), projected to 2D plane via t-SNE algorithm. Cluster centers are denoted with black dots.

The key feature for the exhaustive sampling of the configurational space is the utilization of the low-mode following (also known as velocity softening), which encourages the system's evolution along the low vibrational modes.<sup>73</sup> This approach was used in two distinct simulations carried out at high temperatures of 723 K (**LMMD@723 K**) and 923 K (**LMMD@923 K**) to improve the sampling. For comparison, the PES exploration using the conventional high-temperature aiMD simulation (**MD@923 K**) was also carried out.

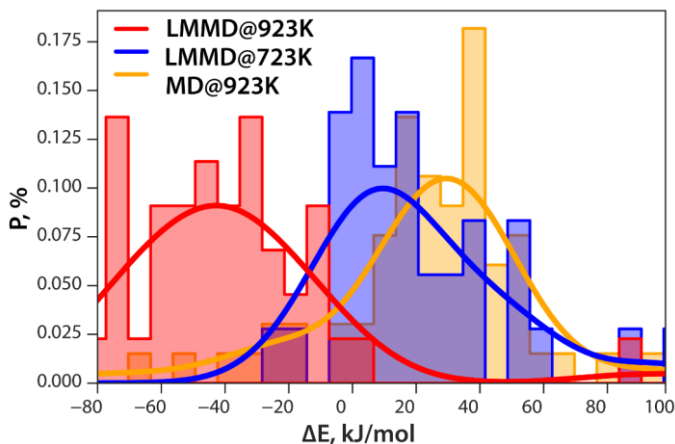


**Figure 3.2** Energy distribution of the optimized clusters' centers obtained via k-medoids clustering procedure. P stands for the probability and  $\Delta E$  is the energy difference between the isomer and the initial configuration.

Six trajectories of each simulation type were generated providing 18 trajectories in total. Analysis of the root-mean-square displacements of the  $\text{Cu}_3\text{O}_3$  fragment from the initial coordinates (RMSDs in **Figure 3.1a**) has shown that **LMMD@723 K** exhibited very limited variations in the oxo-copper cluster ( $RMSD_{MAX} = 1.1 \text{ \AA}$ ,  $RMSD_{average} = 0.5 \text{ \AA}$ ), two out of six **MD@923 K** trajectories exceeded RMSD of  $2 \text{ \AA}$  ( $RMSD_{MAX} = 4.4 \text{ \AA}$ ,  $RMSD_{average} = 1.0 \text{ \AA}$ ), and **LMMD@923 K** demonstrated the highest variation with four out of six trajectories exceeding RMSD of  $2 \text{ \AA}$  ( $RMSD_{MAX} = 9.2 \text{ \AA}$  and  $RMSD_{average} = 2.4 \text{ \AA}$ ). Thus, both elevated temperature and low-mode following approach are crucial for an extensive sampling of the atomic configurations for a zeolite-bound oxo-copper cluster; note, however, that two of the red trajectories (**LMMD@923 K**) did not exhibit large structural variations, probably because the randomly-selected low modes along which the system was dragged did not lead to the active site evolution. This result highlights the necessity of running several elevated-temperature LMMDs in order to sufficiently sample the configurational space; as we will see later, only this approach allowed us to locate the most stable  $[\text{Cu}_3\text{O}_3]^{2+}$  configurations.

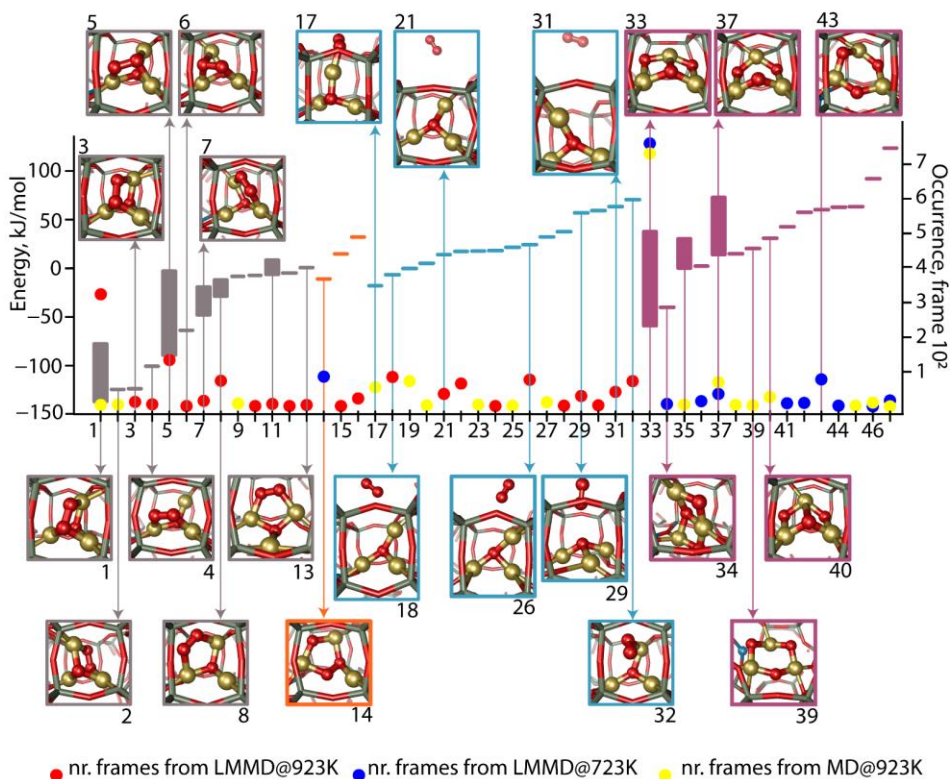


**Figure 3.3** The description of the 2nd-generation clusters obtained from the optimized 1st-generation clusters' centers. The geometries were optimized at PBE-D3(BJ) level of theory and the energies were improved with single point calculations at PBE0-D3(BJ). For each cluster, the range of energies of the residing configurations (bars of —, left axis) is given with the connected insets depicting the optimized local geometry of the lowest-lying extraframework Cu trimer structure. The occurrence of the structures (●, right axis) belonging to the cluster is shown as the number of frames from the initial aiMD trajectories with respect to the first clustering procedure. The contribution of each aiMD type into each 2nd-gen cluster is differentiated by color with red, blue and yellow circles corresponding to **LMMD@923 K**, **LMMD@723 K**, and **MD@923 K** trajectories, respectively. For a complete set of structures, we refer to **Table A3.1** in the **Appendix A3**.

**Figure 3.1b-d** illustrate the clustering of each type of trajectories to identify the unique groups of clusters using an unsupervised machine learning k-medoids algorithm with the “Silhouette” index for choosing  $k$ .<sup>74–76</sup> Clustering algorithms can capture the differences and similarities among the structures and show the relationships in the underlying properties. Among the different clustering approaches, we have chosen the k-medoids method.<sup>76</sup> This approach constructs (hyper)spherical clusters and naturally provides coordinates of the medoid points (i.e., the structures of “median catalytic sites”

for each cluster), which correspond to real data points (denoted as the “cluster centers” henceforth).

Initially, we have clustered **LMMD@723 K**, **MD@923 K** and **LMMD@923 K** sets of trajectories separately, using every 50<sup>th</sup> frame (we use a timestep of 0.5 fs, so time lags between the clustered structures are 25 fs). It gave 1020 frames for each type of trajectory. This procedure resulted in clusters illustrated in **Figure 3.1b-d** using the t-SNE (t-distributed stochastic neighbor embedding) dimensionality reduction technique, which allows projecting the high-dimensional data (6 atoms of the  $[\text{Cu}_3\text{O}_3]^{2+}$  cluster in 3D give dimensionality of 18D) onto two dimensions.<sup>66</sup> The Silhouette index reflecting the similarity of each data point with its own compared to all other clusters was used to determine the optimal number of clusters. Relatively low, yet sufficient for clustering analysis, values of the Silhouette scores for all trajectories indicate a weak separation of the individual clusters due to the high mobility and configurational freedom of the extraframework species at the simulation temperatures. More detailed information on the Silhouette score analysis is given in **Figure A3.1a-d** in **Appendix A3**. The Silhouette score assessment for **LMMD@923 K** gave 44 distinct clusters, whereas 66 and 36 clusters were obtained from **MD@923 K** and **LMMD@723 K** trajectories, respectively.

Since some of the clusters could lay at the different slopes of the same valley, we have optimized structures of all 146 located cluster centers at the same level of theory as above, now considering two possible multiplicities, triplet ( $s = 3/2$ ) and singlet ( $s = 1/2$ ), for each cluster center.<sup>34</sup> **Figure 3.2** summarizes the distribution of the relative energies ( $\Delta E$ ) of the optimized clusters' centers compared to the initial cyclic-chair  $[\text{Cu}_3(\mu\text{-O})_3]^{2+}$  configuration which was assigned relative energy of 0  $\text{kJ mol}^{-1}$ . Each subset of trajectories has been normalized independently and a Gaussian kernel density estimate was used to smoothen the distribution.<sup>77</sup> 60 out of 146 identified cluster centers are lower in energy than the initial configuration.

Notably, energy distributions show that only **LMMD@923 K** produce structures, which are *on average* more stable than the initial one. Although the **LMMD@723 K** set of trajectories has the lowest RMSD deviation from the starting configuration (**Figure 3.1a**), it still locates structurally distinct isomers with negative relative energies. A comparison of **LMMD@723 K** and **MD@923 K** energy distributions highlights the higher efficiency of the low-mode-following procedure in locating low-energy configurations relative to the brute-force temperature elevation.

Geometry optimization resulted in the convergence of the cluster centers into the corresponding minima. These were clustered again using DBSCAN<sup>78</sup> method, which is good for finding dense misshaped clusters. 146 initial cluster centers were distributed into 47 unique clusters; to evade confusion, we shall denote the initial 146 clusters “1<sup>st</sup>-gen clusters”, and the refined 47 ones as the “2<sup>nd</sup>-gen clusters”. The energetics of the “2<sup>nd</sup>-gen

clusters” was refined through single-point calculations using hybrid functional (PBE0). **Figure 3.4** shows a general consistency between the PBE0 and PBE, with lower favorability for  $\text{Cu}_3(\mu^3\text{-O})^2$  and molecular  $\text{O}_2$  bound to it at the PBE0 level of theory. Detailed properties of the 2<sup>nd</sup>-gen clusters, their relation to the 1<sup>st</sup>-gen ones and the initial structures are outlined in **Figure A3.3** and **Table A3.1**. The 2<sup>nd</sup>-gen clusters significantly vary in size. Whereas some of them are represented by single configurations (e.g. #2, 4, 6, 9 – 10, 12 – 32, 34, 36, 38 – 47), the others include multiple structures with similar local geometries but different energies (e.g., #1, 3, 5, 7 – 8, 11, 33, 35, 37).

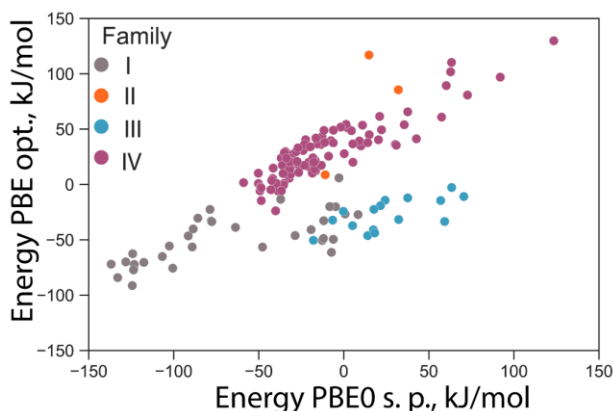


**Figure 3.4** The correlation between active sites optimization at PBE level of theory and their subsequent single point calculation at PBE0 level of theory.

Our procedure identified four distinct  $[\text{Cu}_3\text{O}_3]^{2+}$  families each forming broad ensembles of configurations. The lowest-energy family **I** (2<sup>nd</sup>-gen clusters 1 – 13, grey in **Figure 3.3**) features a  $\text{Cu}_3(\mu^3\text{-O})$  core coordinated to a peroxo ligand with two Cu ions, which adapt either a distorted square-planar or seesaw coordinational environments. These structures were predominantly found with the **LMMD@923 K** search producing 581 frames with  $[\text{Cu}_3(\mu^3\text{-O})(\text{O}-\text{O})]^{2+}$  structures, whereas the **LMMD@723 K** and the **MD@923 K** give 0 and 17 frames of this type, respectively. The second family **II** of configurations (2<sup>nd</sup> gen clusters 14 – 16, orange in **Figure 3.3**) features a peroxo-ligand linking  $\text{Cu}_2\text{O}$  and Cu moieties. These configurations are on average less stable than the peroxo-species of family **I**. They are observed in just 24 and 86 frames of the **LMMD@923 K** and **LMMD@723 K** trajectories, respectively. The third family **III** of structures (2<sup>nd</sup>-gen clusters 17 – 32, blue in **Figure 3.3**) represents formally reduced Cu trimers  $[\text{Cu}_3(\mu^3\text{-O})]^{2+}$  in MOR side-pocket with molecular  $\text{O}_2$  physisorbed within the main channel of MOR or weakly bound to one of the Cu centers. Such configurations were found only in the high-temperature runs with 415 and 150 frames, respectively, in **LMMD@923 K** and **MD@923 K** trajectories. The fourth family **IV** (2<sup>nd</sup>-gen clusters 33 – 47, magenta in **Figure 3.3**) encompasses Cu-oxo trimers corresponding to (**IVa**)

$[\text{Cu}_3(\mu^2\text{-O})_3]^{2+}$  isomers similar to the starting configuration and **(IVb)**  $[\text{Cu}_3(\mu^2\text{-O})_2(\mu^3\text{-O})]^{2+}$  species in an “envelope” configuration with two Cu ions in a distorted planar coordination and one Cu ion in a T-shaped coordination. Type **IV** structures were only found in **LMMD@723 K** and **MD@923 K** trajectories. The  $\text{Cu}_3(\mu^2\text{-O})_3^{2+}$  clusters **(IVa)** predominantly discussed in the prior literature were found in 152 and 93 frames, of the respective simulations. The alternative **IVb** configurations dominated the **LMMD@723 K** and **MD@923 K** trajectories giving 782 and 760 frames, respectively. Note, that these configurations are at least  $50 \text{ kJ mol}^{-1}$  less stable than those belonging to type **I** structures.

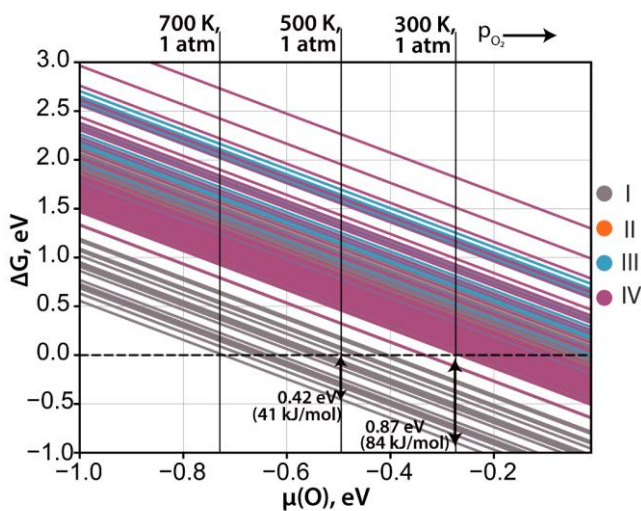


**Figure 3.5** Free energies of formation of  $\text{Cu}_3\text{O}_3^{2+}$  isomers from the partially reduced  $\text{Cu}_3\text{O}_2^{2+}$  cation in MOR as a function of oxygen chemical potential. The color code is used to differentiate the different cluster families.

Therefore, our analysis shows that a single stoichiometry of an oxygenated copper cluster can form a wide variety of low-lying configurations that were not proposed earlier. The low-mode following approach introduced in this chapter uniquely allows identifying such configurations. For Cu/MOR, the **LMMD@923 K** search of the configurational space predominantly gave the structures featuring an adsorbed O-O peroxy or molecular  $\text{O}_2$  on a stable  $[\text{Cu}_3(\mu^3\text{-O})]^{2+}$  core, resembling the trinuclear copper active site proposed for methane monooxygenases.<sup>28</sup>

Next, we carried out an *ab initio* thermodynamics analysis (aiTA) to investigate the relative stabilities of the obtained isomers under reactive conditions. The results are summarized in **Figure 3.5** presenting the Gibbs free energies of optimized  $[\text{Cu}_3\text{O}_3]^{2+}$  isomers, calculated from their reduced counterpart  $[\text{Cu}_3\text{O}]^{2+}$ , as a function of oxygen chemical potential,  $\mu(\text{O})$  (for further information see **Appendix A3**). The electronic

structures of all optimized clusters were analyzed in terms of Hirshfeld charges and spin densities, which did not reveal any correlation with the relative stability (**Figure A3.4, A3.5**).

The lowest-energy structure of  $[\text{Cu}_3\text{O}_3]^{2+}$  contains a  $\text{Cu}_3(\mu^3\text{-O})$  moiety similar to that found in the methane monooxygenase<sup>28</sup> with an  $\text{O}_2$  molecule chemisorbed on it. Notably, a deoxygenated  $\text{Cu}_3(\mu^3\text{-O})/\text{MOR}$  system appears to be very stable during **LMMD@923 K** and does not change its structure during the ~5 ps run. This behavior drastically differs from that of its  $\text{Cu}_3\text{O}_3$  counterpart indicating that the oxidation strongly increases the flexibility of the extraframework multinuclear cation.

On the basis of our calculations,  $\text{Cu}_3(\mu^3\text{-O})$  can be expected to coexist with the most stable found  $\text{Cu}_3(\mu^3\text{-O})(\eta\text{-O}_2)$  cluster at  $\mu(\text{O}) \approx -0.71$  eV, corresponding to approx. 700 K at 1 atm of  $\text{O}_2$  (catalyst activation). At lower  $\mu(\text{O})$ , that is at higher temperatures and/or lower oxygen pressure, the autoreduction of the extraframework cluster to  $\text{Cu}_3(\mu^3\text{-O})$  should take place. However, under the conditions of the catalyst activation,<sup>19</sup> the  $\text{Cu}_3(\mu^3\text{-O})(\eta\text{-O}_2)$  configurations become more energetically accessible. Specifically, we find that the  $\text{Cu}_3(\mu^3\text{-O})(\eta\text{-O}_2)$  is 40-80 kJ/mol more thermodynamically stable than its reduced counterpart in the temperature range of 500 – 300 K corresponding to the temperatures of the catalytic methane oxidation or steaming (**Figure 3.5**).

### 3.4. Conclusions

In this chapter, we analyzed the clusters which can be formed starting from the trimeric  $[\text{Cu}_3(\mu\text{-O})_3]^{2+}$  site in MOR zeolite, for which chair conformation has been earlier proposed based on EXAFS data. To this end, we develop a new computational workflow enabling the exhaustive search of active site configurations (**Scheme 3.1**). Our analysis explores the structural complexity and the highly dynamic nature of oxygenated multinuclear extraframework species in zeolite pores and emphasizes the need for new expert bias-free computational approaches to address the structural problem of zeolite catalysis.

The proposed approach for the exhaustive configurational search addresses the structural problem associated with the identification of the extraframework ensembles in zeolite catalysis in several steps. First, we sample the neighboring regions of the PES around a reference structure - the cyclic chair-shaped  $[\text{Cu}_3(\mu\text{-O})_3]^{2+}$  cluster confined in the side pocket of mordenite in this work - by dragging the system along the low modes in the LMMD simulations. This promotes an enhanced sampling that gives the atomic configurations reflecting the surrounding basins. These can be viewed as an ensemble of structures occurring under reactive conditions. Then, we cluster the LMMD trajectories using k-medoids to find distinguishable clouds of points corresponding to different

clusters. Since some of the clusters can belong to the same energy valley, an additional step of geometry optimization of the cluster centers following by the second clustering using DBSCAN is introduced.

For  $\text{Cu}_3\text{O}_3^{2+}$  cation in MOR, this procedure identified 47 distinct sites corresponding to four archetypes, among which highly stable new configurations previously not considered in experimental or computational studies were found. Finally, the thermodynamics favorability of the obtained conformations under reactive conditions indicated a link between the oxygen chemical potential and the occurrence of structures belonging to different families.

### 3.5. References

- Shetty, M. *et al.* The Catalytic Mechanics of Dynamic Surfaces: Stimulating Methods for Promoting Catalytic Resonance. *ACS Catal.* **10**, 12666–12695 (2020).
- Bruix, A., Margraf, J. T., Andersen, M. & Reuter, K. First-principles-based multiscale modelling of heterogeneous catalysis. *Nat. Catal.* **2**, 659–670 (2019).
- Warshel, A. & Bora, R. P. Perspective: Defining and quantifying the role of dynamics in enzyme catalysis. *J. Chem. Phys.* **144**, (2016).
- Ananikov, V. P. & Beletskaya, I. P. Toward the ideal catalyst: From atomic centers to a ‘cocktail’ of catalysts. *Organometallics* **31**, 1595–1604 (2012).
- Galushko, A. S., Gordeev, E. G., Kashin, A. S., Zubavichus, Y. V. & Ananikov, V. P. Visualization of catalyst dynamics and development of a practical procedure to study complex ‘cocktail’-type catalytic systems. *Faraday Discuss.* **229**, 458–474 (2021).
- Zhang, Z., Zandkarimi, B. & Alexandrova, A. N. Ensembles of Metastable States Govern Heterogeneous Catalysis on Dynamic Interfaces. *Acc. Chem. Res.* **53**, 447–458 (2020).
- Medvedev, M. G. *et al.* Quantifying Possible Routes for SpnF-Catalyzed Formal Diels-Alder Cycloaddition. *J. Am. Chem. Soc.* **139**, 3942–3945 (2017).
- Yaremenko, I. A. *et al.* How to Build Rigid Oxygen-Rich Tricyclic Heterocycles from Triketones and Hydrogen Peroxide: Control of Dynamic Covalent Chemistry with Inverse  $\alpha$ -Effect. *J. Am. Chem. Soc.* **142**, 14588–14607 (2020).
- Cruchter, T. *et al.* Asymmetric Nucleophilic Catalysis with an Octahedral Chiral-at-Metal Iridium(III) Complex. *ACS Catal.* **7**, 5151–5162 (2017).
- Larionov, V. A. *et al.* The Selective N-Functionalization of Indoles via aza-Michael Addition in the Ligand Sphere of a Chiral Nickel(II) Complex: Asymmetric Synthesis of (S)-1H-Indole-Alanine Derivatives. *European J. Org. Chem.* **2019**, 3699–3703 (2019).
- Zhang, X. man *et al.* Dynamic active sites over binary oxide catalysts: In situ/*operando* spectroscopic study of low-temperature CO oxidation over  $\text{MnO}_x$ - $\text{CeO}_2$  catalysts. *Appl. Catal. B Environ.* **191**, 179–191 (2016).
- Zhang, Z., Cui, Z. H., Jimenez-Izal, E., Sautet, P. & Alexandrova, A. N. Hydrogen Evolution on Restructured B-Rich WB: Metastable Surface States and Isolated Active Sites. *ACS Catal.* **10**, 13867–13877 (2020).
- Sun, G., Fuller, J. T., Alexandrova, A. N. & Sautet, P. Global Activity Search Uncovers Reaction Induced Concomitant Catalyst Restructuring for Alkane Dissociation on Model Pt Catalysts. *ACS Catal.* **11**, 1877–1885 (2021).
- Krishna, S. H., Jones, C. B. & Gounder, R. Dynamic Interconversion of Metal Active Site Ensembles in Zeolite Catalysis. *Annu. Rev. Chem. Biomol. Eng.* **12**, 115–136 (2021).
- Paolucci, C. *et al.* Dynamic multinuclear sites formed by mobilized copper ions in  $\text{NO}_x$  selective

- catalytic reduction. *Science* **357**, 898–903 (2017).
16. Pidko, E. A., Hensen, E. J. M. & Van Santen, R. A. Self-organization of extraframework cations in zeolites. in *Proc. R. Soc. A: Mathematical, Physical and Engineering Sciences* vol. 468 2070–2086 (2012).
  17. Dinh, K. T. *et al.* Viewpoint on the Partial Oxidation of Methane to Methanol Using Cu- and Fe-Exchanged Zeolites. *ACS Catal.* **8**, 8306–8313 (2018).
  18. Mahyuddin, M. H., Shiota, Y. & Yoshizawa, K. Methane selective oxidation to methanol by metal-exchanged zeolites: A review of active sites and their reactivity. *Catal. Sci. Technol.* **9**, 1744–1768 (2019).
  19. Newton, M. A., Knorpp, A. J., Sushkevich, V. L., Palagin, D. & Van Bokhoven, J. A. Active sites and mechanisms in the direct conversion of methane to methanol using Cu in zeolitic hosts: A critical examination. *Chem. Soc. Rev.* **49**, 1449–1486 (2020).
  20. Sushkevich, V. L. & Van Bokhoven, J. A. Methane-to-Methanol: Activity Descriptors in Copper-Exchanged Zeolites for the Rational Design of Materials. *ACS Catal.* **9**, 6293–6304 (2019).
  21. Snyder, B. E. R., Bols, M. L., Schoonheydt, R. A., Sels, B. F. & Solomon, E. I. Iron and Copper Active Sites in Zeolites and Their Correlation to Metalloenzymes. *Chem. Rev.* **118**, 2718–2768 (2018).
  22. Ravi, M. *et al.* Misconceptions and challenges in methane-to-methanol over transition-metal-exchanged zeolites. *Nat. Catal.* **2**, 485–494 (2019).
  23. Chen, Y. H., Wu, C. Q., Sung, P. H., Chan, S. I. & Chen, P. P. Y. Turnover of a Methane Oxidation Tricopper Cluster Catalyst: Implications for the Mechanism of the Particulate Methane Monooxygenase (pMMO). *ChemCatChem* **12**, 3088–3096 (2020).
  24. Ross, M. O. *et al.* Particulate methane monooxygenase contains only mononuclear copper centers. *Science* **364**, 566–570 (2019).
  25. Solomon, E. I. *et al.* Copper active sites in biology. *Chem. Rev.* **114**, 3659–3853 (2014).
  26. Prieto, G., Zečević, J., Friedrich, H., De Jong, K. P. & De Jongh, P. E. Towards stable catalysts by controlling collective properties of supported metal nanoparticles. *Nat. Mater.* **12**, 34–39 (2013).
  27. Rosenzweig, A. C. The metal centres of particulate methane mono-oxygenase. *Biochem. Soc. Trans.* **36**, 1134–1137 (2008).
  28. Chan, S. I. *et al.* Redox potentiometry studies of particulate methane monooxygenase: Support for a trinuclear copper cluster active site. *Angew. Chem. Int. Ed.* **46**, 1992–1994 (2007).
  29. Groothaert, M. H., Smeets, P. J., Sels, B. F., Jacobs, P. A. & Schoonheydt, R. A. Selective oxidation of methane by the bis( $\mu$ -oxo)dicopper core stabilized on ZSM-5 and mordenite zeolites. *J. Am. Chem. Soc.* **127**, 1394–1395 (2005).
  30. Woertink, J. S. *et al.* A  $[\text{Cu}_2\text{O}]^{2+}$  core in Cu-ZSM-5, the active site in the oxidation of methane to methanol. *Proc. Natl. Acad. Sci. U. S. A.* **106**, 18908–18913 (2009).
  31. Grundner, S. *et al.* Single-site trinuclear copper oxygen clusters in mordenite for selective conversion of methane to methanol. *Nat. Commun.* **6**, 1–9 (2015).
  32. Ikuno, T. *et al.* Formation of Active Cu-oxo Clusters for Methane Oxidation in Cu-Exchanged Mordenite. *J. Phys. Chem. C* **123**, 8759–8769 (2019).
  33. Zheng, J. *et al.* Importance of Methane Chemical Potential for Its Conversion to Methanol on Cu-Exchanged Mordenite. *Chem. Eur. J.* **26**, 7563–7567 (2020).
  34. Li, G. *et al.* Stability and reactivity of copper oxo-clusters in ZSM-5 zeolite for selective methane oxidation to methanol. *J. Catal.* **338**, 305–312 (2016).
  35. Vogiatzis, K. D., Li, G., Hensen, E. J. M., Gagliardi, L. & Pidko, E. A. Electronic Structure of the  $[\text{Cu}_3(\mu\text{-O})_3]^{2+}$  Cluster in Mordenite Zeolite and Its Effects on the Methane to Methanol Oxidation. *J. Phys. Chem. C* **121**, 22295–22302 (2017).
  36. Palagin, D., Knorpp, A. J., Pinar, A. B., Ranocchiaro, M. & Van Bokhoven, J. A. Assessing the relative stability of copper oxide clusters as active sites of a CuMOR zeolite for methane to methanol conversion: Size matters? *Nanoscale* **9**, 1144–1153 (2017).
  37. Sun, G., Alexandrova, A. N. & Sautet, P. Structural Rearrangements of Subnanometer Cu Oxide

- Clusters Govern Catalytic Oxidation. *ACS Catal.* **10**, 5309–5317 (2020).
38. Zhang, Z., Jimenez-Izal, E., Hermans, I. & Alexandrova, A. N. Dynamic Phase Diagram of Catalytic Surface of Hexagonal Boron Nitride under Conditions of Oxidative Dehydrogenation of Propane. *J. Phys. Chem. Lett.* **10**, 20–25 (2019).
39. Imaoka, T., Toyonaga, T., Morita, M., Haruta, N. & Yamamoto, K. Isomerizations of a Pt<sub>4</sub> cluster revealed by spatiotemporal microscopic analysis. *Chem. Commun.* **55**, 4753–4756 (2019).
40. Kästner, J. Umbrella sampling. *Wiley Interdiscip. Rev. Comput. Mol. Sci.* **1**, 932–942 (2011).
41. Barducci, A., Bonomi, M. & Parrinello, M. Metadynamics. *Wiley Interdiscip. Rev. Comput. Mol. Sci.* **1**, 826–843 (2011).
42. Abrams, C. & Bussi, G. Enhanced sampling in molecular dynamics using metadynamics, replica-exchange, and temperature-acceleration. *Entropy* **16**, 163–199 (2014).
43. Martínez-Suárez, L., Frenzel, J., Marx, D. & Meyer, B. Tuning the reactivity of a Cu/ZnO nanocatalyst via gas phase pressure. *Phys. Rev. Lett.* **110**, 1–5 (2013).
44. Kamachi, T. & Yoshizawa, K. Low-Mode Conformational Search Method with Semiempirical Quantum Mechanical Calculations: Application to Enantioselective Organocatalysis. *J. Chem. Inf. Model.* **56**, 347–353 (2016).
45. Schütt, O., Messmer, P., Hutter, J. & Vandevondele, J. GPU-Accelerated Sparse Matrix-Matrix Multiplication for Linear Scaling Density Functional Theory. *Electronic Structure Calculations on Graphics Processing Units* 173–190 (2016).
46. Borštnik, U., Vandevondele, J., Weber, V. & Hutter, J. Sparse matrix multiplication: The distributed block-compressed sparse row library. *Parallel Comput.* **40**, 47–58 (2014).
47. Hutter, J., Iannuzzi, M., Schiffrmann, F. & Vandevondele, J. Cp2k: Atomistic simulations of condensed matter systems. *Wiley Interdiscip. Rev. Comput. Mol. Sci.* **4**, 15–25 (2014).
48. Frigo, M. & Johnson, S. G. The design and implementation of FFTW3. *Proc. IEEE* **93**, 216–231 (2005).
49. Vandevondele, J. & Hutter, J. An efficient orbital transformation method for electronic structure calculations. *J. Chem. Phys.* **118**, 4365–4369 (2003).
50. Perdew, J. P., Burke, K. & Ernzerhof, M. Generalized gradient approximation made simple. *Phys. Rev. Lett.* **77**, 3865–3868 (1996).
51. Grimme, S., Antony, J., Ehrlich, S. & Krieg, H. A consistent and accurate *ab initio* parametrization of density functional dispersion correction (DFT-D) for the 94 elements H-Pu. *J. Chem. Phys.* **132**, 154104 (2010).
52. Grimme, S., Ehrlich, S. & Goerigk, L. Effect of the damping function in dispersion corrected density functional theory. *J. Comput. Chem.* **32**, 1456–1465 (2011).
53. Vandevondele, J. *et al.* Quickstep: Fast and accurate density functional calculations using a mixed Gaussian and plane waves approach. *Comput. Phys. Commun.* **167**, 103–128 (2005).
54. Krack, M. Pseudopotentials for H to Kr optimized for gradient-corrected exchange-correlation functionals. *Theor. Chem. Acc.* **114**, 145–152 (2005).
55. Hartwigsen, C., Goedecker, S. & Hutter, J. Relativistic separable dual-space Gaussian pseudopotentials from H to Rn. *Phys. Rev. B - Condens. Matter Mater. Phys.* **58**, 3641–3662 (1998).
56. Goedecker, S. & Teter, M. Separable dual-space Gaussian pseudopotentials. *Phys. Rev. B - Condens. Matter Mater. Phys.* **54**, 1703–1710 (1996).
57. Vandevondele, J. & Hutter, J. Gaussian basis sets for accurate calculations on molecular systems in gas and condensed phases. *J. Chem. Phys.* **127**, 114105 (2007).
58. Lippert, G., Hutter, J. & Parrinello, M. A hybrid Gaussian and plane wave density functional scheme. *Mol. Phys.* **92**, 477–488 (1997).
59. Kolafa, J. Time-Reversible Always Stable Predictor-Corrector Method for Molecular Dynamics of Polarizable Molecules. *J. Comput. Chem.* **25**, 335–342 (2004).
60. Nosé, S. A unified formulation of the constant temperature molecular dynamics methods. *J. Chem. Phys.* **81**, 511–519 (1984).

61. NosÉ, S. A molecular dynamics method for simulations in the canonical ensemble. *Mol. Phys.* **100**, 191–198 (2002).
62. Medvedev, M. G. *et al.* Exhaustive conformational search for transition states: the case of catechol O-methyltransferase active site. *Mendeleev Commun.* **27**, 224–227 (2017).
63. Park, H. S. & Jun, C. H. A simple and fast algorithm for K-medoids clustering. *Expert Syst. Appl.* **36**, 3336–3341 (2009).
64. Maranzana, F. E. On the Location of Supply Points to Minimize Transport Costs. *J. Oper. Res. Soc.* **15**, 261 (1964).
65. Blondel, M. *et al.* Scikit-learn: Machine Learning in Python. *J. Mach. Learn. Res.* **12**, 2825–2830 (2011).
66. Van Der Maaten, L. & Hinton, G. Visualizing data using t-SNE. *J. Mach. Learn. Res.* **9**, 2579–2625 (2008).
67. Krijthe, J. H. Rtsne:T-distributed stochastic neighbor embedding using barneshut implementation. Rpackageversion0.15. *R Packag. version 0.13*, URL <https://github.com/jkrijthe/Rtsne> (2015).
68. Van Der Maaten, L. Accelerating t-SNE using tree-based algorithms. *J. Mach. Learn. Res.* **15**, 3221–3245 (2014).
69. Ester, M., Kriegel, H.-P., Sander, J. & Xu, X. A Density-Based Algorithm for Discovering Clusters in Large Spatial Databases with Noise. in *Proceedings of the 2nd International Conference on Knowledge Discovery and Data Mining* vol. 96 226–231 (1996).
70. Schubert, E., Sander, J., Ester, M., Kriegel, H. P. & Xu, X. DBSCAN revisited, revisited: Why and how you should (still) use DBSCAN. *ACM Trans. Database Syst.* **42**, 1–21 (2017).
71. Grajciar, L. *et al.* Towards *operando* computational modeling in heterogeneous catalysis. *Chem. Soc. Rev.* **47**, 8307–8348 (2018).
72. Reuter, K., Stampf, C. & Scheffler, M. *Ab Initio* Atomistic Thermodynamics and Statistical Mechanics of Surface Properties and Functions. in *Handbook of Materials Modeling* 149–194 (Springer Netherlands, 2005).
73. Labute, P. LowModeMD - Implicit low-mode velocity filtering applied to conformational search of macrocycles and protein loops. *J. Chem. Inf. Model.* **50**, 792–800 (2010).
74. Shao, J., Tanner, S. W., Thompson, N. & Cheatham, T. E. Clustering molecular dynamics trajectories: 1. Characterizing the performance of different clustering algorithms. *J. Chem. Theory Comput.* **3**, 2312–2334 (2007).
75. De Paris, R., Quevedo, C. V., Ruiz, D. D., Norberto De Souza, O. & Barros, R. C. Clustering molecular dynamics trajectories for optimizing docking experiments. *Comput. Intell. Neurosci.* **2015**, 916240 (2015).
76. Mannor, S. *et al.* K-Medoids Clustering. in *Encyclopedia of Machine Learning* (eds. Sammut, C. & Webb, G. I.) 564–565 (Springer US, 2011).
77. Rosenblatt, M. Remarks on Some Nonparametric Estimates of a Density Function. in *The Annals of Mathematical Statistics* vol. 27 832–837 (Springer, 1956).
78. Van Eemeren, F. H. & Dunbar, N. R. *Proceedings of the Second International Conference on Argumentation. Philosophy and Rhetoric* vol. 27 (1991).

### A3.1. K-medoids clustering: silhouette score, clusters' visualization

To determine the optimal number of clusters for each set of trajectories, we have used the silhouette score. The number of tested clusters varied between 20 and 100. The value of the silhouette score for each number of clusters is shown in **Figure A3.1**, where **LMMD@723 K**, **LMMD@923 K**, **MD@923 K** set of trajectories are clustered separately and together and have their own number of desirable k-medoids.

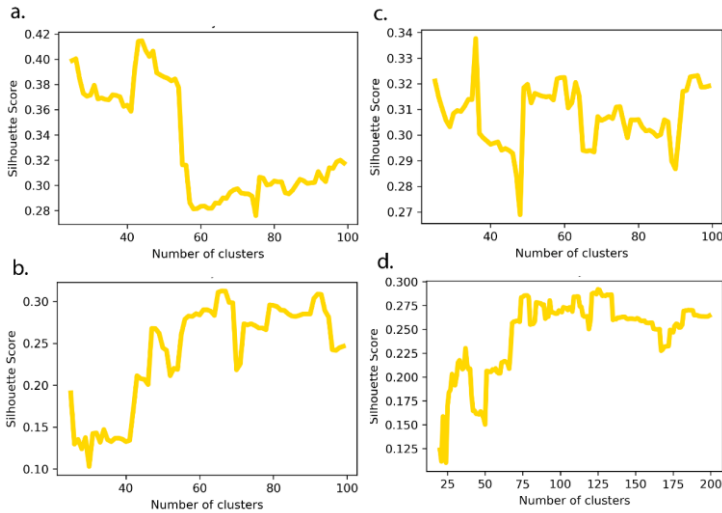


**Figure A3.1** The silhouette score for the number of clusters varied between 20 and 100 obtained for a different set of trajectories. **(a)** The silhouette score for **LMMD@923 K**. The maximum value of the silhouette score is 0.41 and corresponds to 44 clusters. **(b)** The silhouette score for **MD@923 K** set of trajectories. The maximum value of the silhouette score is 0.31 and corresponds to 66 clusters. **(c)** The silhouette score for **LMMD@723 K** set of trajectories. The maximum value of the silhouette score is 0.34 and corresponds to 36 clusters. **(d)** The silhouette score for all sets of trajectories clustered together. The maximum value of the silhouette score is 0.29 and corresponds to 125 clusters.

Clustering was carried out using k-medoids algorithm. It starts with selecting the number of centers using the value of the highest silhouette score. As the optimal clustering for the defined number of clusters is performed (**Figure A3.1**), dimensionality reduction algorithms are applied for visualization purposes. We have performed both PCA (Principal component analysis) and t-SNE (t-distributed stochastic neighbor embedding) dimensionality reduction methods. However, for all sets of trajectories, t-SNE distinguishes the data in a better way compared to PCA.

*Unraveling nature of extraframework catalytic ensembles in zeolites: flexibility and dynamics of the copper-oxo trimers in mordenite*

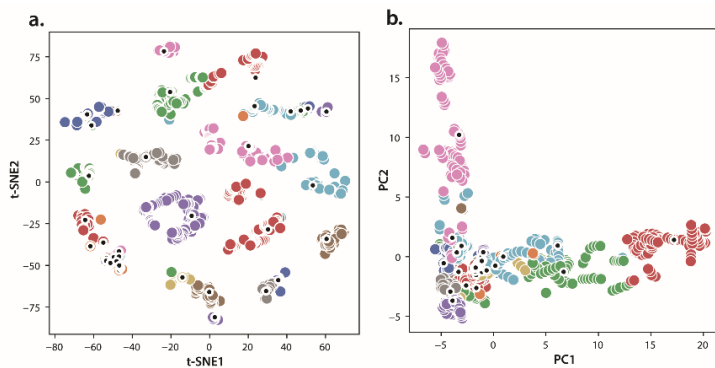


**Figure A3.2a** Visualizing 44 clusters in LMMD@923 K trajectory using dimensionality reduction methods such as (a) t-SNE and (b) PCA.

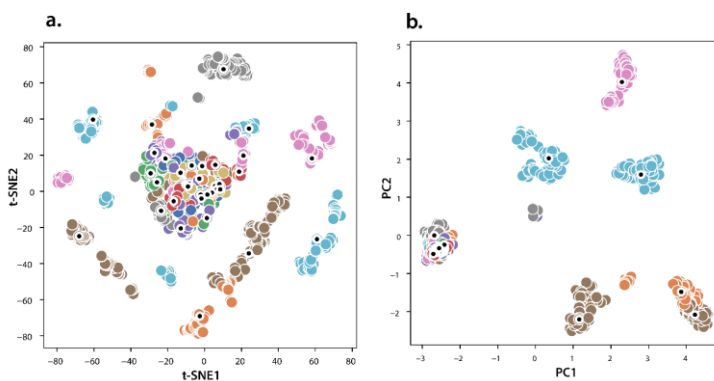


**Figure A3.2b** Visualizing 36 clusters in LMMD@723 K trajectory using dimensionality reduction methods such as (a) t-SNE and (b) PCA.

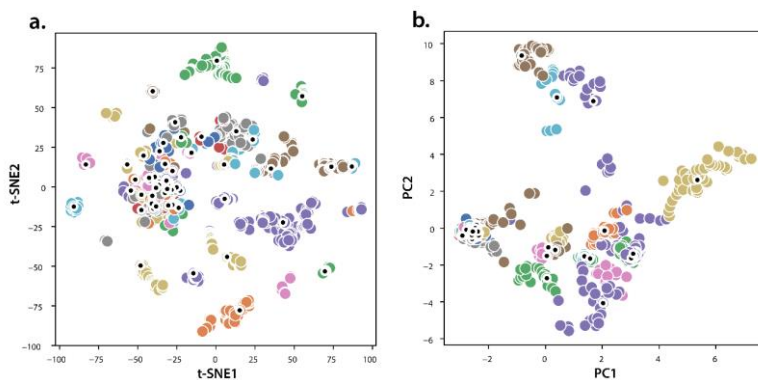


**Figure A3.2c** Visualizing 66 clusters in MD@923 K trajectory using dimensionality reduction methods such as (a) t-SNE and (b) PCA.

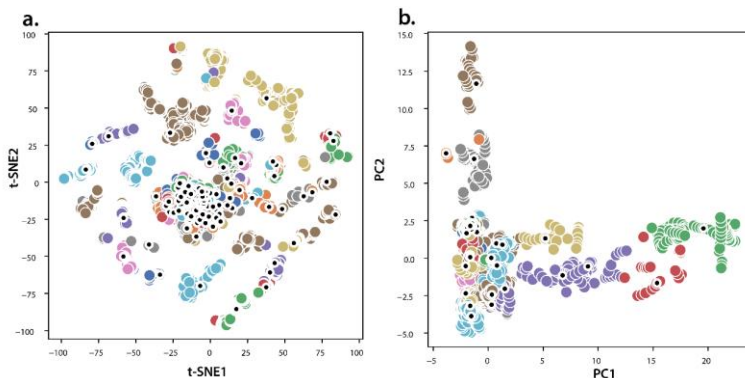


**Figure A3.2d** Visualizing 125 clusters of combined sets of trajectories using dimensionality reduction methods such as (a) t-SNE and (b) PCA.

### A3.2. DBSCAN clustering

After optimization as the PBE-D3(BJ) level of theory, the centres of the clusters (first-gen clusters) were clustered using the DBSCAN method. The change in the clustering algorithm was motivated by the low silhouette score value for the k-medoids method and better cluster separation in the DBSCAN algorithm.

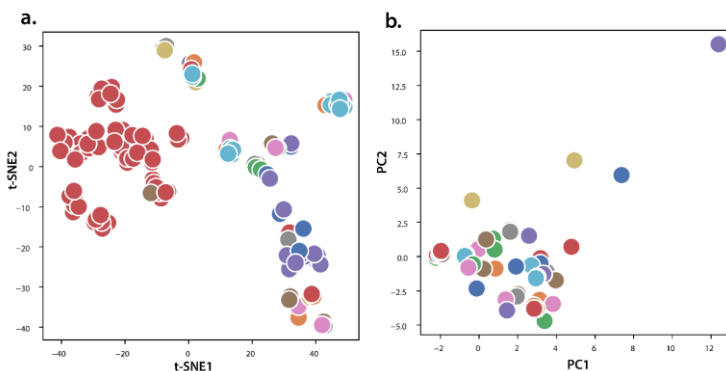


**Figure A3.3** Visualizing 47 clusters using dimensionality reduction methods: (a) t-SNE and (b) PCA.

### A3.3. Second generation clusters

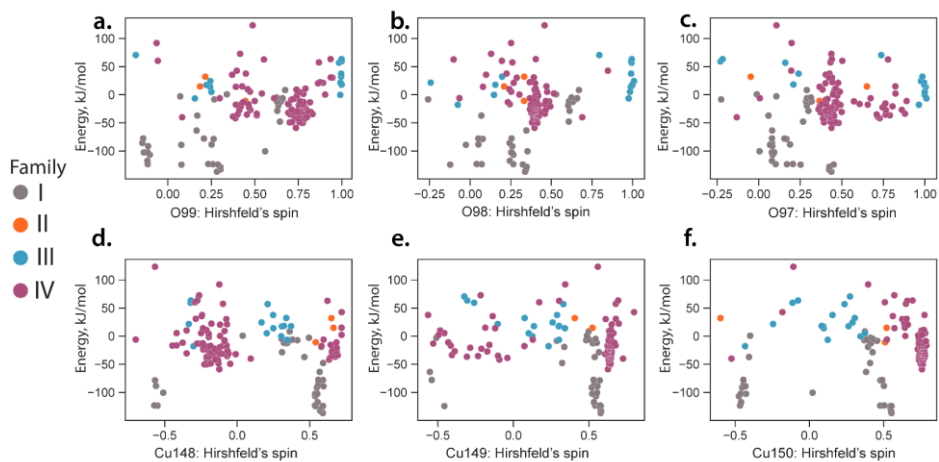
Their numbers, geometrical configurations of the lowest-lying structure optimized at the PBE level of theory, energies range (relative to the initial structure) obtained at the PBE0 level of theory, and the number of frames from each type of MD which were attributed to each cluster.

Table A3.1 Second-gen clusters.

No	Low. energy geom.	Energy conf.; Energy range (kJ/mol)	Conf. from LMMD @923K: LMMD @723K: MD@923K	No	Low. energy geom.	Energy conf.; Energy range (kJ/mol)	Conf. from LMMD @923K: LMMD @723K: MD@923K	No	Low. energy geom.	Energy conf.; Energy range (kJ/mol)	Conf. from LMMD @923K: LMMD @723K: MD@923K
1		[-137; -78]	324:0:4	17		-18	0:0:55	33		[-59; 38]	0:760:731
2		-124	0:0:5	18		-7	85:0:0	34		-40	0:7:0
3		[-124; -123]	13:0:0	19		0	0:0:73	35		[0; 30]	0:0:5
4		-101	6:0:0	20		5	0:0:3	36		2	0:15:0
5		[-89; 3]	134:0:0	21		14	36:0:0	37		[14; 73]	0:36:70
6		-64	1:0:0	22		17	66:0:0	38		15	0:0:4
7		[-48; -19]	16:0:0	23		18	0:0:5	39		20	0:0:3
8		[-29; -12]	74:0:0	24		18	1:0:0	40		31	0:0:27
9		-8	0:0:8	25		22	0:0:2	41		43	0:9:0
10		-7	1:0:0	26		24	77:0:0	42		57	0:10:0
11		[-6; 8]	7:0:0	27		32	0:0:12	43		60	0:78:0

12		-5	1:0:0	28		38	2:0:0	44		63	0:2:0
13		1	4:0:0	29		57	30:0:0	45		63	0:0:2
14		-11	0:86:0	30		59	3:0:0	46		92	0:0:11
15		15	1:0:0	31		63	42:0:0	47		123	0:17:0
16		32	23:0:0	32		71	73:0:0				

### A3.4. Hirshfeld analysis



**Figure A3.4** The correlation of the individual Hirshfeld spin on O (a-c) and Cu (d-f) atoms in  $\text{Cu}_3\text{O}_3^{2+}$  configurations calculated at the PBE-D3(BJ) level of theory with their respective energy calculated at the PBE0-D3(BJ) level of theory.

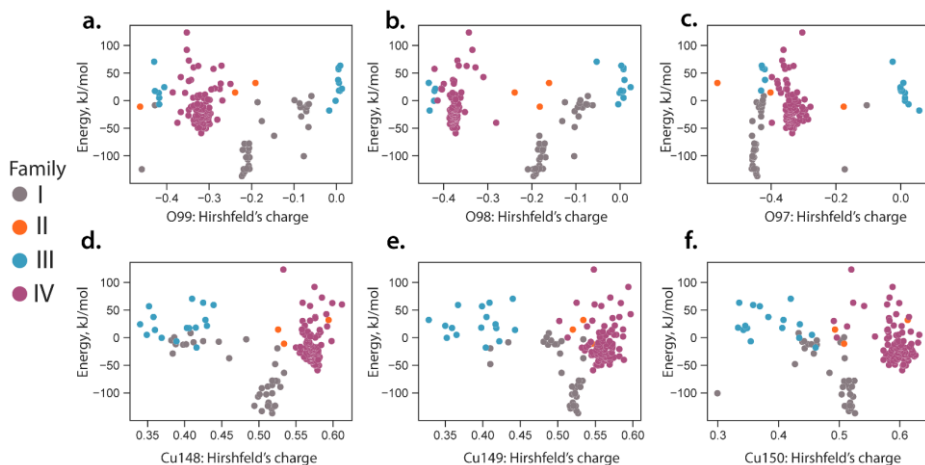


**Figure A3.5** The correlation of the individual Hirshfeld charges on O (a-c) and Cu (d-f) atoms in  $\text{Cu}_3\text{O}_3^{2+}$  configurations calculated at the PBE-D3(BJ) level of theory with their respective energy calculated at the PBE0-D3(BJ) level of theory.

To identify the difference in the electronic structure properties of generated isomers, we have calculated the Hirshfeld spin states and charges on oxygens and copper atoms for every  $\text{Cu}_3\text{O}_3^{2+}$  configuration obtained from the second-gen clusters. The energies are calculated with respect to the energy of the starting configuration. The colors correspond to the families of the active sites described in the paper.

### A3.5. LMMD simulations of $\text{Cu}_3\text{O}^{2+}$

The energies are calculated with respect to the energy of the starting configuration. The colors correspond to the families of the active sites described in the paper.

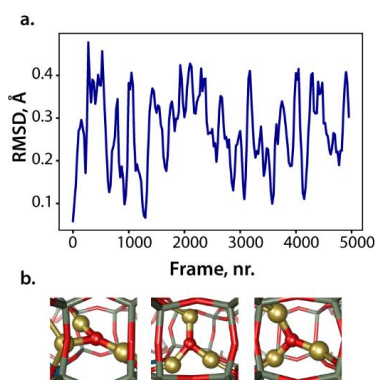


**Figure A3.6** (a) RMSD of the  $\text{Cu}_3\text{O}^{2+}$  in MOR. (b) The active site configurations corresponding to the highest RMSD deviation.

### A3.6. Methane activation

To investigate the reactivity of the active sites with a peroxo-ligand in the process of methane activation, we have calculated the reaction pathways for the activation of a single methane molecule over the lowest-lying site with a peroxo-ligand (**Figure A3.7**). It consists of the rearrangement of the active site and includes the cleavage of the O-O-bond and the activation of the C-H-bond in methane. In **Figure A3.8**, the presence of methane leads to the reorganization of the structure. It starts with the barrierless cleavage of the O-O-bond, forming the adduct that is 129 kJ/mol less stable than the initial configuration (FS). The subsequent activation of methane over structure (TS) proceeds with a low barrier of 27 kJ/mol and directly forms methanol coordinated to one of the Cu atoms.

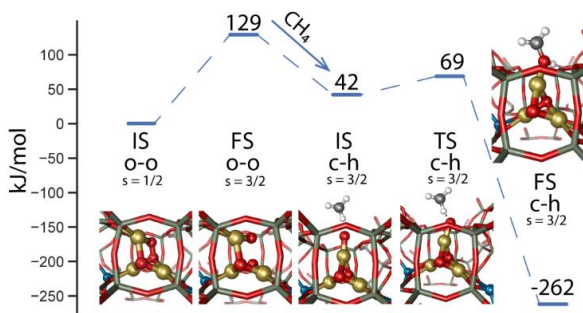


**Figure A3.7** The reaction pathway of the methane activation over one of the lowest lying active sites from family I.

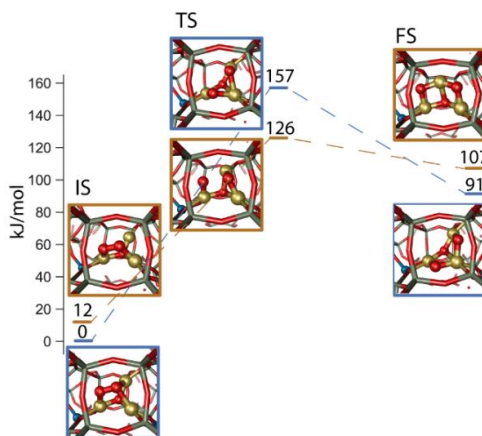


**Figure A3.8** The reaction pathways representing the rearrangements from one type of configuration (family I) to another type of configuration (family IV)

---

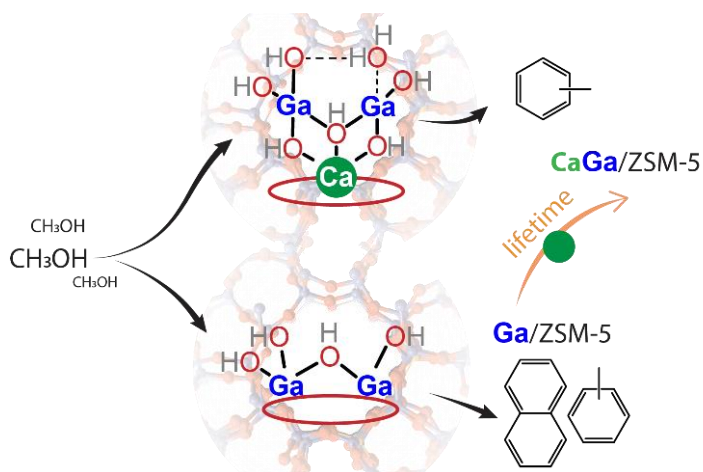
---

## Chapter 4

---

---

### High stability of methanol to aromatic conversion over bimetallic Ca,Ga-modified ZSM-5



## Summary

---

The aromatization reactions catalyzed by zeolites can be hindered by the rapid catalyst deactivation due to the coking. This joined experiment – theory chapter demonstrates that the addition of the small Ca quantities to Ga/ZSM-5 catalyst can decouple these two processes by producing bimetallic CaGa extraframework species. For this bimetallic catalyst, a higher selectivity to light aromatics and an extended lifetime in the methanol-to-aromatics (MTA) process have been achieved. The molecular nature of the structures resulting from the Ga-LAS – Ca interactions has been studied by employing a global optimization technique. Here we used a genetic algorithm (GA) for elucidating the possible configurations of the bimetallic CaGa species confined in ZSM-5. To identify the most stable configurations under the reactive conditions of the MTA process, a bias-free GA configurational search has been complemented by the *ab initio* thermodynamics analysis. Finally, a Ca-concentration dependency on the stability of the formed CaGa stoichiometries has been assessed. The results of these calculations have been found in line with the experimentally observed promotion effect of minute amounts of Ca, attributed to the stabilization of the intrazeolite extraframework Ga complexes.

This chapter is based on the following publication:

Liu C., Uslamin E. A., Khramenkova E. V., Sireci E., Ouwehand L.T., Ganapathy S., Kapteijn F., Pidko E.A. *ACS Catal.* **12**, 3189–3200 (2022).

The experimental part of this book has been carried out by Chuncheng Liu.

## **4.1. Introduction**

Aromatic compounds, especially benzene, toluene and ethylbenzene, and xylenes (BTEX) are important basic compounds for the production of polymers, solvents, coatings and other materials. Nowadays, more than 90% of these compounds are obtained in the reforming process of different petroleum fractions complemented by the subsequent modification procedures. In the last decade, a promising route for the methanol-to-aromatics from the readily available methanol has received a great attention.<sup>1-3</sup>

Zeolites are promising catalysts for the aromatization process based on their hydrothermal stability, shape-selectivity and well-defined crystallinity. The conversion of methanol over zeolites proceeds through complex transformations, which include the cooperation between the Brønsted acid sites (BAS) and confined hydrocarbon intermediates. In this route, also called hydrocarbon pool, formed C-C-bond species act as the catalytic platform for combining the reactants and products and producing the final products.<sup>4,5</sup> A proposed dual-cycle in the HP route differentiates the alkenes and aromatics production. In this cycle, the conversion of methanol to light olefins proceeds via methylation/cracking of longer olefins, whereas the formation of BTEX and ethylene originates from the alkylation/dealkylation process of the methylated aromatic species.<sup>6</sup>

To tune the selectivity to aromatics in the methanol conversion process, zeolites get modified with various metals, such as Au, Ga, Ni, Cu, Mo et.<sup>7-9</sup> The following boost in the aromatics cycle is attributed to the formation of the Lewis acid sites (LAS) that are capable of catalysing the direct dehydrogenation reactions. However, it has been reported that the increased selectivity to aromatics intermediates results in rapid catalyst deactivation due to the formation of polycyclic aromatics.<sup>10,11</sup> Among the approaches to extend the lifetime are post-synthetic modifications and Ca introduction.<sup>12</sup> The effect of the latter involves the reduction of the aromatic selectivity and an increase in the catalyst lifetime.

The inclusion of one or several metals can lead to the formation of the unique LAS with a distinct structure and acidic strength, affecting the stability and reactivity of the catalyst in the methanol-to-aromatics process. To unravel the chemical nature of these extraframework species in ZSM-5 and their reactivity in the hydrocarbon pool mechanism, a computational chemistry toolbox can be employed to supplement experimental findings. One of the ways to explore the configurational space is by applying global optimization methods, such as a genetic algorithm (GA). It allows to mitigate the user's input on the nature of the structural elements in the extraframework species and predict the global minima structures for the stoichiometries of various complexity.

In this chapter, we present the investigation of the structural nature of the bimetallic [Ca, Ga]/H-ZSM-5 catalyst, which has revealed increased stability and high yield of BTEX in the MTA process. Following the experimental lead on the formation of bimetallic CaGa complexes in the ZSM-5 intersection channel, we have computationally discovered the mechanistic basis for the catalytic effect of Ca addition. First, a bias-free configurational search of the global minima structures of various stoichiometries has been carried out. As a result of this procedure, the configurations of the complex clusters have been discovered, that were previously unknown. To assess the stability of different configurations under reactive conditions and the effect of the Ca concentration, the *ab initio* thermodynamics analysis was conducted. Lastly, the reactivity of the bimetallic species in the process of ethane dehydrogenation has been modelled.

## 4.2. Experimental and computational details

### 4.2.1. Catalyst preparation

Protonic H-ZSM-5 (CBV5020E) with Si/Al ratio of 25 was purchased from Zeolyst Int. and denoted as H-ZSM-5. Ga-modified ZSM-5 sample was prepared via incipient wetness impregnation with an aqueous solution of  $\text{Ga}(\text{NO}_3)_3$  [gallium(III) nitrate hydrate, Sigma Aldrich, 99.9% trace metals basis]. After the impregnation, the sample was first dried at 80 °C overnight and then calcined at 550 °C (ramp rate 2°C/min) under static air for 6 h. To increase the dispersion of Ga species in the zeolite micropores, the calcined Ga/H-ZSM-5 sample was further reduced at 500 °C (2 °C/min) in a 30 vol%  $\text{H}_2$  in Ar flow for 7 h. After that, the sample was cooled to 150 °C and re-oxidized in a flow of air for 1 h.<sup>13</sup> Samples containing 1, 2 and 3 wt% Ga were prepared, denoted as  $\text{Ga}(x)$  ( $x = 1, 2, \text{ or } 3$ ) where the value in the bracket represents the weight loading of the metal.  $\text{Ca}(0.02)$  and  $\text{Ca}(1)$  samples, containing 0.02 wt% and 1 wt% Ca, respectively, were prepared via the same incipient wetness impregnation procedure with calcium nitrate tetrahydrate solutions, followed by calcination at 550 C (ramp rate 2°C/min) under static air for 6 h without the final reduction-oxidation step.

A second incipient wetness impregnation was carried out with prepared  $\text{Ga}(2)$  to obtain the bimetallic catalyst. Aqueous solutions with different concentrations of  $\text{Ca}(\text{NO}_3)_2$  [calcium nitrate tetrahydrate, Sigma Aldrich, ACS reagent, 99%] were used. After impregnation, the as-prepared sample went through drying and calcination steps under the same conditions as described above. The notation is  $\text{Ca}(x)\text{Ga}(2)$  where  $x$  represents the wt% loading of Ca. To check the relevance of the addition order, one sample was prepared according to the above procedures in which the Ca was added first and then the Ga. This sample is denoted as  $\text{Ga}(2)\text{Ca}(0.02)$ .

### 4.2.2. Catalytic tests

MTA catalytic runs were performed at 450 °C using a fixed-bed reactor setup. In a typical experiment, a 4 mm (ID) quartz reactor tube was filled with 40 mg sieved zeolite fraction (particle size 150–212 μm). MeOH was fed into the reactor through a thermostatted saturator with liquid MeOH (Sigma Aldrich, for HPLC, ≥99.9%) using N<sub>2</sub> as a carrier gas. The reaction products were analyzed with an online Thermo Trace GC (Trace 1300 Ultra, ThermoFisher) equipped with a thermal conductivity detector (TCD) coupled with a Poraplot Q pre-column (2 m; i.d. 0.32 mm; film thickness 20 μm) and Molsieve 5 Å column (10 m; i.d. 0.32 mm) for the analysis of permanent gases, a flame ionization detector (FID) equipped with RTX-1 column (2 m; i.d. 0.32 mm; film thickness 5 μm) and Al<sub>2</sub>O<sub>3</sub>/KCl column (15 m; i.d. 0.32 mm; film thickness 10 μm) for the analysis of C<sub>1</sub> to C<sub>4</sub> hydrocarbons and another FID equipped with RTX-VMS column (30 m; i.d. 0.33 mm; film thickness 3 μm) for C<sub>5+</sub> hydrocarbons.

Prior to reaction, the catalyst was activated in 50 mL/min air up to 550 °C (5 °C/min) for 1 h and then cooled down to the reaction temperature of 450 °C. The initial partial pressure of MeOH in the feed flow was set at 5.2 kPa. The corresponding WHSV amounted 5.3 g<sub>MeOH</sub>g<sub>cat</sub><sup>-1</sup> h<sup>-1</sup>. The MeOH conversion (excluding DME), reaction selectivity, and yield were calculated on a carbon molar basis as follows:

$$X = \frac{\phi_{C,MeOH_{in}} - \phi_{C,MeOH_{out}} - 2\phi_{C,DME_{out}}}{\phi_{C,MeOH_{in}}} \cdot 100\% \quad (E4.1)$$

$$S_{C_n} = \frac{n \cdot \phi_{C_n}}{\phi_{C,MeOH_{in}} - \phi_{C,MeOH_{out}} - 2\phi_{C,DME_{out}}} \cdot 100\% \quad (E4.2)$$

$$Y_{C_n} = \frac{X \cdot S_{C_n}}{100} \% \quad (E4.3)$$

where X, S<sub>C<sub>n</sub></sub>, and Y<sub>C<sub>n</sub></sub> represent the conversion of MeOH and dimethyl ether (DME), carbon selectivity of certain hydrocarbon products and the corresponding carbon yield in the exhaust with carbon number equal to n, respectively.

For additional details on the experimental data and catalysts' characterization, please refer to publication ref (14).

### 4.2.3. Genetic Algorithm

The stability and reactivity of extraframework cations in cation-modified ZSM-5 were computationally studied using the cluster modelling approach. 22T cluster models representing the different environments of the alpha-, beta-, and gamma sites of ZSM-5 were constructed to accommodate the cationic ensembles. For each ZSM-5 cluster model, two Si<sup>4+</sup> atoms were substituted with two Al<sup>3+</sup> generating a negative charge in the system, which was compensated by extraframework oxygenated Ga or Ca-Ga cationic clusters. Ga/Al ratio of 1 was assumed for all models. The -OH dangling bonds were used to

terminate the cluster models. Varied chemical compositions of the cluster models were considered and the preferred structures were determined by using a fully automated genetic algorithm optimization strategy. The relative stabilities of the extraframework species with different stoichiometries under the catalytically relevant conditions were evaluated using the *ab initio* thermodynamic analysis.

A genetic algorithm (GA) applies the principles from evolutionary biology by learning the structural features of a “good” solution throughout the operations of fitness assignment, crossover, mutation, and selection.<sup>15,16</sup> In this chapter, the GA was executed and controlled using the Atomic Simulation Environment (ASE) employing the semiempirical tight-binding calculator GFN1-xTB.<sup>17–20</sup> A GA developed by Vilhelmsen and Hammer was utilized.<sup>20</sup> The whole zeolitic framework was kept fixed during the GA runs. The workflow of GA starts by initializing a population consisting of 20 structures in random arrangements. The operation of selection uses an energy-based fitness function to rank the candidates and the crossover operator picks the candidates as parents for new structures generation. The mutation probability was set to a 30% rate with equal probabilities for mirror and rattle mutations. The candidates were found to be converged as the maximum energy difference, the maximum interatomic distances and the maximum difference in interatomic difference reached 0.02 eV, 0.015 Å and 0.7 Å respectively. In each run, the maximum number of cycles given to the algorithm to converge was 120. The calculation was considered to have converged if no significant change was recorded in the last 5 generations. The structures generated within the GA runs are provided in **Appendix A4**.

The global minima obtained from the GA runs were further optimized using the PBE-D3(BJ)<sup>21–25</sup> level of theory implementing a modified version of the mixed Gaussian and plane-wave code CP2K/Quickstep.<sup>26–29</sup> Using this method, the electronic charge density is calculated using plane waves, while the Kohn-Sham orbitals get extended in contracted Gaussians. A Gaussian basis set DZVP-MOLOPT-GTH basis was used,<sup>30</sup> and the density cutoff of 280 Ry was employed. The Goedecker-Teter-Hutter pseudopotentials<sup>31</sup> with a combination of non-periodic wavelet-based Poisson solver<sup>32</sup> were employed to calculate the electron repulsion integrals. During the DFT-level optimization, only the positions of the dangling H atoms of the cluster models were kept fixed to their original positions, while the atoms of the zeolite framework and extraframework ensemble were fully relaxed.

#### 4.2.4. *Ab initio* thermodynamics analysis

The energies of the lowest-lying structures after the optimization at the DFT level of theory were further employed for *ab initio* thermodynamics analysis. *Ab initio* thermodynamics analysis (aiTA) was conducted to account for the temperature and pressure effects in the presence of water on the stability of the extraframework species. The relative energies were computed with the reference to water, pure Ca-ZSM-5, H-ZSM-5 and bulk  $\beta$ -

Ga<sub>2</sub>O<sub>3</sub> structures, which are provided in the publication<sup>14</sup>. The equilibria between species were established to have the following general form for the formation of the Ca-Ga and Ga-only structures:

$$\frac{2p-2m-3n-q+2}{4} \cdot O_2 + \frac{q+2m-2}{2} \cdot H_2O + \frac{n}{2} \cdot Ga_2O_3\text{bulk} + (1-m) \cdot 2H/\text{zeolite} + m \cdot \text{Ca/zeolite} \rightleftharpoons Ca_mGa_nO_pH_q \quad (\text{E4.4})$$

where the  $Ca_mGa_nO_pH_q$  is the total electronic energy of one of the global minima,  $2H/\text{zeolite}$  is the energy of the H-form of ZSM-5 structure with two framework Al atoms,  $\text{Ca/zeolite}$  is the total energy of ZSM-5 structure with two framework Al atoms compensated by an exchangeable Ca<sup>2+</sup> cation. The O<sub>2</sub>, H<sub>2</sub>O, and Ga<sub>2</sub>O<sub>3</sub> bulk are the total energies of gaseous O<sub>2</sub>, H<sub>2</sub>O and bulk Ga<sub>2</sub>O<sub>3</sub>, respectively. The vibrational and pressure-volume contributions of solids were neglected and their Gibbs free energies are approximated as their respective electronic energies. The chemical potentials of gaseous water and oxygen species were calculated with respect to the reference state at 0 K and 1 bar using tabulated thermodynamic tables.<sup>33</sup>

The reaction Gibbs free energy  $\Delta G(T, p)$  equals to:

$$\Delta G(T, p) = \Delta E - \frac{2p-2m-3n-q+2}{2} \cdot \Delta\mu_{O_2} - \frac{q+2m-2}{2} \cdot \Delta\mu_{H_2O} \quad (\text{E4.5})$$

where the reaction energy  $\Delta E$  and the chemical potential of water  $\mu_{H_2O}(T, p)$  at arbitrary temperature  $T$  and pressure  $p$  are defined as follows:

$$\Delta E = Ca_mGa_nO_pH_q - \frac{2p-2m-3n-q+2}{4} \cdot O_2 - \frac{q+2m-2}{2} \cdot H_2O - \frac{n}{2} \cdot Ga_2O_3\text{bulk} - (1-m) \cdot 2H/\text{zeolite} - m \cdot \text{Ca/zeolite} \quad (\text{E4.6})$$

$$\mu_{H_2O}(T, p) = E_{H_2O} + \Delta\mu_{H_2O}(T, p) \quad (\text{E4.7})$$

The expression for the chemical potential change includes the temperature- and pressure-dependent free energy contributions as follows:

$$\Delta\mu_{H_2O}(T, p) = \Delta\mu_{H_2O}(T, p^0) + RT \ln \left( \frac{p_{H_2O}}{p_{H_2O}^0} \right) = H(T, p^0, H_2O) - H(0 \text{ K}, p^0, H_2O) - T(S(T, p^0, H_2O) - S(0 \text{ K}, p^0, H_2O)) + RT \ln \left( \frac{p_{H_2O}}{p_{H_2O}^0} \right) \quad (\text{E4.8})$$

#### 4.2.5. Ca-concentration dependencies

The investigate how the Ca concentration influences the stability of the formation of pure Ga-oxo and CaGa species, a new thermodynamic model has been introduced. Here we assume that the extraframework complexes can be described as defects in the zeolite matrix.<sup>34</sup> To calculate the change in Gibbs free energy associated with the formation of  $n$  vacancies in the crystal, the following expression has been used:

$$\Delta G(T, p) = (n \cdot \Delta G_f(T, p) - TS^{\text{conf}})/N \quad (\text{E4.9})$$

The  $\Delta G_f(T, p)$  includes all entropic contributions (vibrational, electronic, etc) except the configurational entropy, and, therefore, accounts for the formation/consumption of gaseous species computed with the ideal gas approximation. In equation E4.9, the configurational entropy  $S^{\text{conf}}$  results from the disorder in the parent material due to the introduction of extraframework species. It was shown to stabilize the defects with positive formation energy and to be the largest contribution to the overall entropy. The value of the configurational entropy  $S^{\text{conf}}$  can be defined as follows:

$$S^{\text{conf}} = k_b \ln \frac{(N+n)!}{N!n!} \quad (\text{E4.10})$$

Applying the Stirling formula for  $n, N$  values  $\gg 1$ , ( $\ln N! = N \ln N - N$ ) a good differentiable approximation of a factorial can be written as the following:

$$S^{\text{conf}} = k_b N \left[ \ln \left( 1 + \frac{n}{N} \right) + \frac{n}{N} \ln \left( 1 + \frac{N}{n} \right) \right] \quad (\text{E4.11})$$

$\Delta G_f(T, p)$  is the Gibbs free energy of a single defect formation in originally BAS-containing ZSM-5. It can be defined as follows:

$$\Delta G_f(T, p) = \Delta E - \sum \Delta \mu_i(T, p) \quad (\text{E4.12})$$

where the  $\Delta \mu_i(T, p)$  are the chemical potentials of gaseous species defined in E4.7 and E4.8. In the models with pure Ga-oxo species, the number of defects is defined as  $n = \frac{1}{2} c^{\text{Ga}} N_a$  for 1 gram of catalyst, where  $c^{\text{Ga}}$  is the concentration of Ga from the experiment. As all analyzed samples have been prepared with the same Ga concentration, it was constant and equal to  $2.87 \cdot 10^{-4}$  mol/g. The  $N$  value is the number of the unit cell calculated for 1 gram of catalyst of a respective zeolite model:  $N = 1 \cdot N_a / M(\text{unit cell})$ . The final expression for the Gibbs free energy change for the formation of  $n$  pure Ga-oxo defects in ZSM-5 at the operational conditions of 700 K and 1 atm is defined as follows:

$$\Delta G_{\text{Ga-oxo}} = \left( \left( \Delta E_{\text{Ga-oxo}} - \frac{2p-2m-3n-q+2}{2} \cdot \Delta \mu_{\text{O}_2}^{700 \text{ K}} - \frac{q+2m-2}{2} \cdot \Delta \mu_{\text{H}_2\text{O}}^{700 \text{ K}} \right) \frac{1}{2} c^{\text{Ga}} N_a - T \left( k_b N \left[ \ln \left( 1 + \frac{\frac{1}{2} c^{\text{Ga}} N_a}{N} \right) + \frac{\frac{1}{2} c^{\text{Ga}} N_a}{N} \ln \left( 1 + \frac{N}{\frac{1}{2} c^{\text{Ga}} N_a} \right) \right] \right) \right) / N \quad (\text{E4.13})$$

The Gibbs free energy change for the formation of CaGa-oxo defects in ZSM-5 also includes the concentration of Ca in the catalyst. According to the experiment, Ca concentration  $c^{\text{Ca}}$  was in the range  $[2.5 \cdot 10^{-6}; 125 \cdot 10^{-6}]$  mol/g. The number of defects per gram of catalysts can be defined as  $n = \frac{1}{2} c^{\text{Ga}} N_a - c^{\text{Ca}} N_a$ . The final expression for the Gibbs free energy change for the formation of CaGa-oxo complexes in ZSM-5 at the operational conditions of 700 K and 1 atm is defined as follows:

$$\Delta G_{\text{CaGa-oxo}} = \left( \left( \Delta E_{\text{CaGa-oxo}} - \frac{2p-2m-3n-q+2}{2} \cdot \Delta \mu_{\text{O}_2}^{700 \text{ K}} - \frac{q+2m-2}{2} \cdot \Delta \mu_{\text{H}_2\text{O}}^{700 \text{ K}} \right) \cdot \left( \frac{1}{2} c^{\text{Ga}} N_a - c^{\text{Ca}} N_a \right) - T \left( k_b N \left[ \ln \left( 1 + \frac{\frac{1}{2} c^{\text{Ga}} N_a - c^{\text{Ca}} N_a}{N} \right) + \frac{\frac{1}{2} c^{\text{Ga}} N_a - c^{\text{Ca}} N_a}{N} \ln \left( 1 + \frac{N}{\frac{1}{2} c^{\text{Ga}} N_a - c^{\text{Ca}} N_a} \right) \right] \right) \right) / N \quad (\text{E4.14})$$

#### 4.2.6. Reaction mechanisms calculations

Ethane dehydrogenation was chosen as the representative model reaction to computationally assess the dehydrogenation reactivity of the extraframework LAS. The Lewis acidic cationic clusters were stabilized within the periodic ZSM-5 model with the optimized unit cell lattice parameters of  $a = 20.2 \text{ \AA}$ ,  $b = 20.0 \text{ \AA}$ ,  $c = 13.4 \text{ \AA}$ ,  $\alpha = \beta = \gamma = 90^\circ$ , which were kept fixed throughout the calculations. Periodic density functional theory (DFT) calculations were carried out at the PBE-D3(BJ) level of theory<sup>25,35</sup> using the Vienna *Ab Initio* Simulation Package (VASP 5.3.5).<sup>36,37</sup> The plane wave basis set with an energy cutoff of 450 eV and the projector augmented wave (PAW)<sup>38</sup> method were used. Brillouin zone sampling was restricted to the  $\Gamma$  point. The convergence was considered to be reached when the forces acting on each atom were below  $0.05 \text{ eV \AA}^{-1}$ . The minimum reaction energy path and the transition states search were performed by employing the nudged-elastic band (CI-NEB) method.<sup>39</sup> The geometry corresponding to the maximum energy structure along the reaction path was further optimized via a quasi-Newton algorithm, where only the relevant atoms of the extraframework species were relaxed. The finite difference method was used to calculate the vibrational frequencies ( $0.02 \text{ \AA}$  atomic displacements). The energy barrier for the  $\beta$ -H elimination was disregarded on the grounds of earlier reports that indicate that this elementary step depends only slightly on the coordination environment of the Ga atom<sup>40</sup> and therefore cannot give rise to the diverging dehydrogenation activity.

### 4.3. Results and discussion

#### 4.3.1. Catalyst characterization and testing

A series of Ga- and Ca-Ga-modified ZSM-5 zeolites was synthesized using the incipient wetness impregnation technique. A reduction-oxidation activation procedure was employed to ensure good dispersion of Ga throughout the zeolite pores. The catalysts were extensively characterized using Ar physisorption, X-ray diffraction and FTIR of adsorbed pyridine and acetonitrile as molecular probes. The detailed characterization and catalytic results are summarized in **Appendix A4**. Below we will briefly discuss the main findings, while the main part of this chapter will be devoted to the computational

elucidation of the structure and catalytic role of Ca-promoted Ga extraframework ensembles in ZSM-5 zeolite.

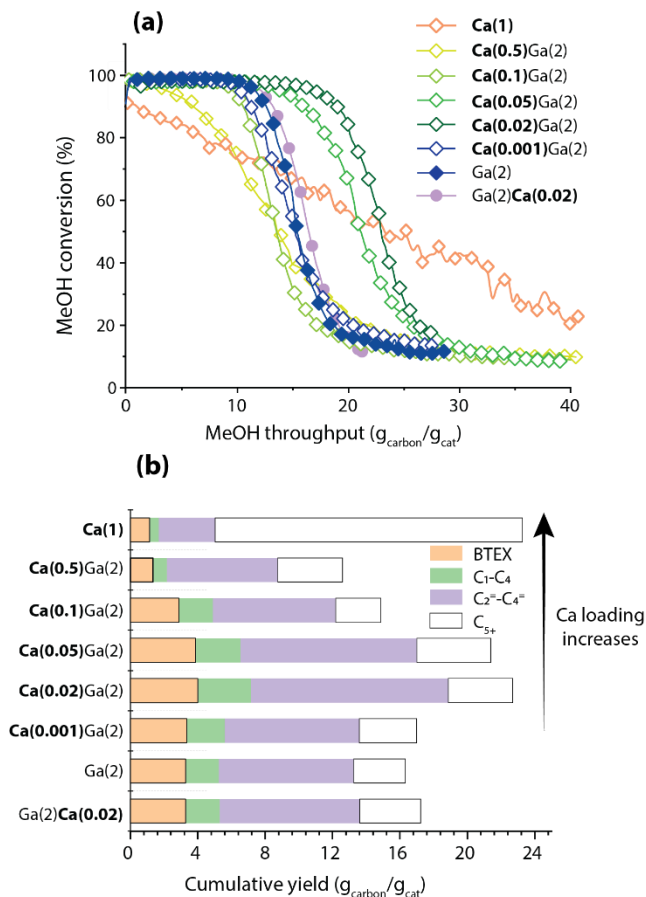


**Figure 4.1** Summary of the catalytic results of MTA over Ca,Ga-modified catalysts: **(a)** MeOH conversion as a function of MeOH conversion per gram of catalyst; **(b)** Integral yields of the main groups of MTA products before MeOH conversion drops below 20%. MTA reaction conditions:  $T = 450\text{ }^{\circ}\text{C}$ ,  $m_{\text{cat}} = 40\text{ mg}$  (150–212  $\mu\text{m}$ ),  $P_{\text{reactor}} = 1\text{ bar}$ ,  $\text{WHSV} = 5.3\text{ g}_{\text{MeOH}}\text{ g}_{\text{cat}}^{-1}\text{ h}^{-1}$ , carrier gas  $\text{N}_2 = 50\text{ mL min}^{-1}$ . C<sub>5+</sub>: aliphatics with the carbon number higher than 4; C<sub>1</sub>-C<sub>4</sub>: C<sub>1</sub> to C<sub>4</sub> alkanes; C<sub>2</sub>-C<sub>4</sub>: C<sub>2</sub> to C<sub>4</sub> olefins.

**Figure 4.1** shows the MTA results obtained for bimetallic CaGa-modified H-ZSM-5 with 2 wt% Ga and Ca loadings ranging from 0.02 to 0.05 wt%. The results indicate that upon the addition of only 0.02 wt % Ca to Ga(2), the total MeOH throughput increases from 16 to 23  $g_{\text{carbon}}/g_{\text{cat}}$  for Ga(2) and Ca(0.02)Ga(2), respectively. Accordingly, the integral yield of BTEX increases from 3 to 4  $g_{\text{carbon}}/g_{\text{cat}}$  and that of light olefins increases from 8 to 12  $g_{\text{carbon}}/g_{\text{cat}}$  for Ga(2) and Ca(0.02)Ga(2), demonstrating a strong effect of low Ca loadings on the catalytic performance of Ga-modified zeolites.

The lifetime extension impact gradually diminishes with a further increase in Ca loading to 0.05 and 0.1wt%. Upon 0.5 wt% addition to Ga(2), the MeOH conversion rapidly drops, resulting in a total MeOH throughput and integral BTEX yield of only 12 and 2 g<sub>carbon</sub>/g<sub>cat</sub>, respectively. On the basis of these data and additional characterizations in <sup>14</sup> and **Appendix A4**, we propose that Ca first interacts with extraframework Ga species and the synergy of Ca and Ga moderates the dehydrogenation rate. This leads to lower hydrogen formation and eventually reduces the deactivation rate in MTA at small Ca loadings. At higher Ca loadings (> 0.05 wt %) on Ga(2), the dehydrogenation-aromatization rate is further suppressed. However, more Ca atoms inevitable interact with BAS, forming Ca-LAS (**Figure A4.1b-c**). Newly formed Ca-LAS forces the MeOH transformations into C<sub>5+</sub> aliphatics rather than olefins (cracking) or BTEX (dehydrogenation), causing the fast deactivation of Ca(1) or Ca(0.5)Ga(2) as presented in **Figure 4.1** For more detailed experimental procedures and catalyst characterization, please refer to ref.(14).

### 4.3.2. Configurational search employing GA

In an attempt to provide a molecular proposal for the observed reactivity changes upon Ca modification of Ga/H-ZSM-5, model DFT calculations were carried out. Following the hypothesis on Ca-mediated reactivity changes in extraframework Ga sites, a fully automated analysis of the interaction modes<sup>18</sup> between Ca<sup>2+</sup> and representative binuclear Ga<sub>2</sub>O<sub>x</sub>H<sub>y</sub> moiety was carried out. The calculations were expanded into the *operando* regime through the *ab initio* thermodynamics (aiTA) analysis to find out the extraframework complexes potentially formed under the MTA conditions.<sup>41</sup>

Following on earlier works on Ga-modified H-ZSM-5 materials, we have considered the model of the active site consisting of a binuclear Ga cluster stabilized by two negatively charged aluminum, incorporated in the MFI framework with a different environment such as alpha-, beta-, gamma sites.<sup>42-44</sup> The alpha and beta sites are the six-membered rings along the straight channel, whereas the gamma site is the eight-membered ring on the wall of the sinusoidal channel.<sup>45</sup> The effect of Ca addition was studied by introducing one Ca<sup>2+</sup> cation. The overall charge neutrality of the pure Ga or CaGa bimetallic species was achieved by introducing the O<sup>2-</sup> and OH<sup>-</sup> ligands, whose quantity varied to represent different water content. This resulted in the structures containing a water content of 0–5 H<sub>2</sub>O molecules, giving six stoichiometries for pure Ga and six for CaGa structures.

To find the global minima structures corresponding to these stoichiometries, a genetic algorithm optimization process was carried out, with the electronic structure evaluation calculated by an accelerated *x*TB semiempirical method.<sup>17,46</sup> As the exhaustive computational search of the 96 T periodic atom-system is currently prohibitively demanding, the cluster models representing the Ga pure and CaGa bimetallic active sites confined in the sites of the ZSM-5 were utilized.<sup>18</sup> The outcome of each genetic algorithm

procedure was 20 lowest-lying configurations of the corresponding stoichiometry, with indicated structural diversity, whose geometries were further refined at the PBE-D3(BJ) level of theory with Gaussian DZVP-MOLOPT-GTH basis set as implemented in CP2K 6.1.<sup>21,22,24,26–31,47</sup> The stability of the lowest high-level refined structures of each stoichiometry was further assessed at experimentally relevant conditions employing aiTA (E4.4 – E4.8).<sup>48</sup>

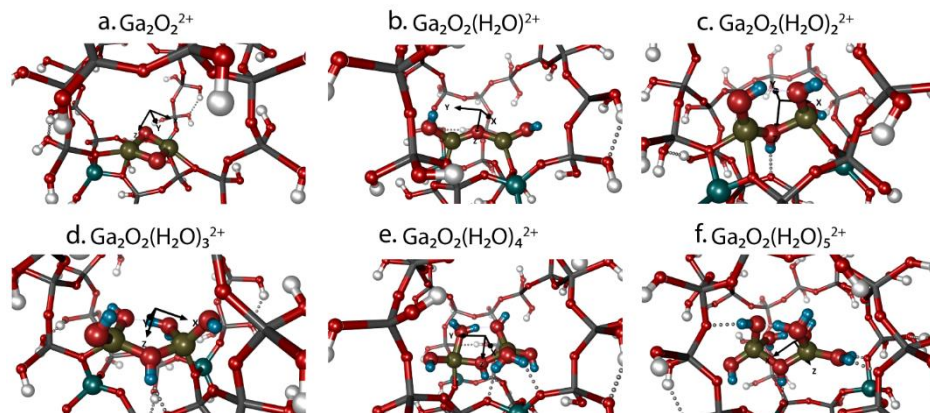


**Figure 4.2** Global minima of  $\text{Ga}_2\text{O}_2(\text{H}_2\text{O})_x^{2+}$  confined in the alpha site of the ZSM-5 and optimized at PBE-D3(BJ) level of theory, where  $x = 0$  (a), 1 (b), 2 (c), 3 (d), 4 (e), 5 (f). Aluminum is aquamarine, oxygen is red, gallium is dark green, silicon is grey, and hydrogen of the cluster is blue.

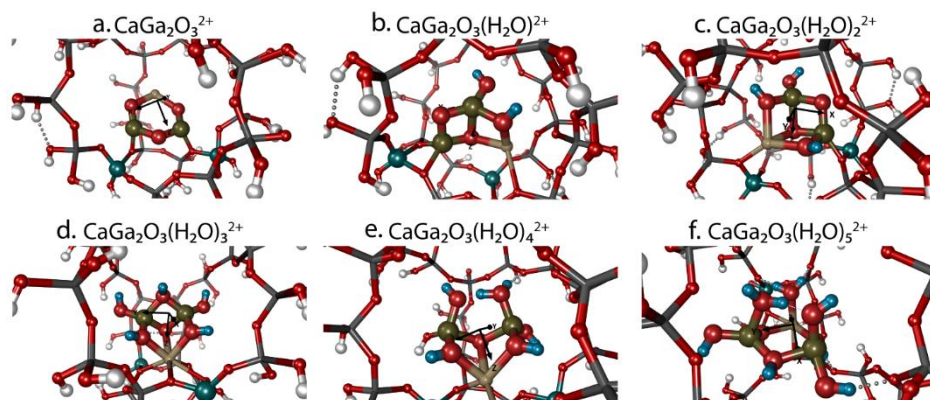


**Figure 4.3** Global minima of  $\text{CaGa}_2\text{O}_3(\text{H}_2\text{O})_x^{2+}$  confined in the alpha site of the ZSM-5 and optimized at PBE-D3(BJ) level of theory, where  $x = 0$  (a), 1 (b), 2 (c), 3 (d), 4 (e), 5 (f). Aluminum is aquamarine, oxygen is red, gallium is dark green, silicon is grey, calcium is beige and hydrogen of the cluster is blue.

The cluster models of the global minima for all pure Ga and bimetallic CaGa stoichiometries are shown in **Figures 4.2** and **4.3**, respectively. For the  $\text{Ga}_2\text{O}_2^{2+}$  species,

in the absence of water, a symmetrical diamond-shaped binuclear  $\text{Ga}(\mu\text{-O})_2\text{Ga}^{2+}$  configuration is formed (**Figure 4.2a**). A linear isomer  $\text{HOGa}(\mu\text{-O})\text{GaOH}^{2+}$  with one bridging oxygen and two hydroxyl groups is observed in **Figure 4.2b**, whereas the addition of another water molecule in **4.2c**, leads to the accommodation of another hydroxyl group and a hydrogen atom on bridging oxygen. With increasing  $\text{H}_2\text{O}$  contents, the Ga atoms increase their coordination numbers, coordinating more water molecules or hydroxyl groups. Finally, for the clusters  $\text{Ga}_2\text{O}_2(\text{H}_2\text{O})_4^{2+}$  and  $\text{Ga}_2\text{O}_2(\text{H}_2\text{O})_5^{2+}$ , the bonds between Ga and oxygens of the framework get hydrolyzed leading to the cluster's detachment from the framework. The inclusion of the Ca atom in the GA procedure influences the geometries of the obtained configurations. In **Figure 4.3a**, a six-membered ring is formed, where gallium atoms are coordinated to the framework aluminum. Adding a single water molecule in **4.3b** results in the formation of the envelope-like  $\text{CaGa}_2\text{O}_3$  with hydrogen and OH-group coordinated to the cluster. The inclusion of the other water molecules (**4.3c – 4.3f**), leads to Ga atoms accommodating water molecules and hydroxyl groups in a tetrahedral coordinational environment. Starting from the addition of the third molecule, the Ca atoms get anchored between two aluminum embedded in the framework. This produces the structures where extraframework  $\text{CaGa}_2\text{O}_3(\text{H}_2\text{O})_x^{2+}$  species ( $x=3 - 5$ ) are connected to the ZSM-5 framework through the Ca atoms.

The comparison of the optimized geometries reveals that at all hydration levels Ga ions in both Ga pure and CaGa extraframework clusters tend to adapt a distorted tetrahedral coordination environment. The only observed exception is the trigonal bipyramidal coordination formed around one of the gallium centers in the  $\text{Ga}_2\text{O}_2(\text{H}_2\text{O})_4^{2+}$  model (**Figure 4.2e**). The coordination of the Ca ions in the bimetallic clusters depends more strongly on the water content. In the presence of 1 or 2 water molecules (**Figure 4.3b-c**), the coordination of the  $\text{Ca}^{2+}$  center in the CaGa clusters is best described as the square pyramidal, whereas at a higher solvation level (with 3, 4 or 5 added  $\text{H}_2\text{O}$  molecules), distorted pentagonal bipyramidal or octahedral coordinations of the Ca centres are realized in the extraframework clusters (**Figure 4.2d-f**).

To evaluate the relative stabilities of the most stable pure Ga and bimetallic CaGa configurations as a function of reaction conditions, aiTA has been carried out. In **Figure 4.4**, the optimized geometries of the most thermodynamically favorable phases expressed as a function of water chemical potential  $\mu(\text{H}_2\text{O})$  are depicted. Accordingly, at the low values of the water chemical potential ( $-2.0 \text{ eV} < \Delta\mu < -1.2 \text{ eV}$ ), pure Ga-oxo species tend to coordinate one or two water molecules, whereas bimetallic CaGa species favor the hydration with up to 4 water molecules. At intermediate and high values of  $\Delta\mu$  ( $> -1.2 \text{ eV}$ ), pure Ga species can coexist with configurations having various degrees of hydration ( $\Delta\mu \sim -1 \text{ eV}$ ) and eventually get hydrolysed ( $\Delta\mu > -1 \text{ eV}$ ). At high water chemical potential, the coordination of 5 water molecules to the pure Ga species leads to the hydrolysis of Si-O-Ga bonds resulting in the detachment of the species from the framework, as in structure  $\text{Ga}_2\text{O}_2(\text{H}_2\text{O})_5^{2+}$  in **Figure 4.4a**. However, the bimetallic cations

remain effectively attached to the cation site at all  $\Delta\mu$  through coordinating Ca to the framework Al sites. This effect is illustrated with the most stable bimetallic  $\text{CaGa}_2\text{O}_3(\text{H}_2\text{O})_4^{2+}$  and  $\text{CaGa}_2\text{O}_3(\text{H}_2\text{O})_5^{2+}$  configurations (**Figure 4.4b**) suggesting that Ca acts as an anchor, preventing the highly hydrated extraframework species from washing away from the cation site and agglomerate. The aiTA diagrams indicate that Ca addition stabilizes the bimetallic species with a higher degree of hydration (containing more water molecules) rather than pure Ga configurations under the same conditions.

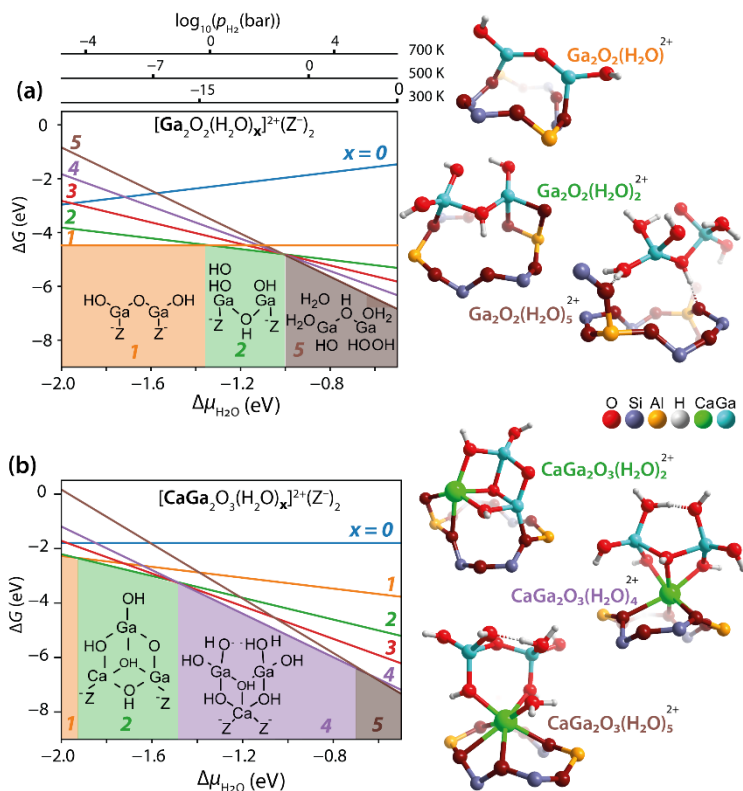


**Figure 4.4** Stability and geometries of cationic extraframework species in ZSM-5 zeolite with different water contents (up to five water molecules). **(a)** The aiTA analysis on the pure Ga complexes. The geometries of the most stable configurations amongst the following stoichiometries:  $\text{Ga}_2\text{O}_2(\text{H}_2\text{O})^{2+}$ ,  $\text{Ga}_2\text{O}_2(\text{H}_2\text{O})_2^{2+}$ ,  $\text{Ga}_2\text{O}_2(\text{H}_2\text{O})_5^{2+}$  are displayed. The geometry of the  $\text{Ga}_2\text{O}_2(\text{H}_2\text{O})_5^{2+}$  illustrates the detaching from the framework. **(b)** The aiTA analysis on the bimetallic CaGa complexes. The geometries of the most stable configurations amongst the following stoichiometries:  $\text{CaGa}_2\text{O}_3(\text{H}_2\text{O})_2^{2+}$ ,  $\text{CaGa}_2\text{O}_3(\text{H}_2\text{O})_4^{2+}$ ,  $\text{CaGa}_2\text{O}_3(\text{H}_2\text{O})_5^{2+}$  are displayed.

### 4.3.3. Ca-concentration dependency and dehydrogenation activity

To analyze how the stability of the formed complexes in the zeolites depends on the Ca concentration and explain the experimental observations, we have modified the aiTA

approach by considering these cationic species as defects in the zeolite matrix. This approximation assumes that the Gibbs free energies for the pure Ga and CaGa site formation are concentration-dependent (equations E4.13 and E4.14).

The thermodynamical analysis of the stabilities as a function of Ca concentration in **Figure 4.5** shows that the formation of the separate pure Ga-oxo cations and exchangeable  $\text{Ca}^{2+}$  ions of the various hydration level is generally more favorable than the formation of the CaGa-oxo species. However, at the low Ca loadings (up to  $2 \cdot 10^{-5}$  mol/g), the formation of the CaGa complexes becomes more thermodynamically favorable if compared to the  $\text{Ga}_2\text{O}_2^{2+}$ ,  $\text{Ga}_2\text{O}_2(\text{H}_2\text{O})_5^{2+}$  and  $\text{Ga}_2\text{O}_2(\text{H}_2\text{O})_4^{2+}$  species. If compared to the  $\text{Ga}_2\text{O}_2^{2+}$  cluster, the formation of the CaGa clusters of various hydration becomes advantageous at concentrations up to  $6 \cdot 10^{-5}$  mol/g.

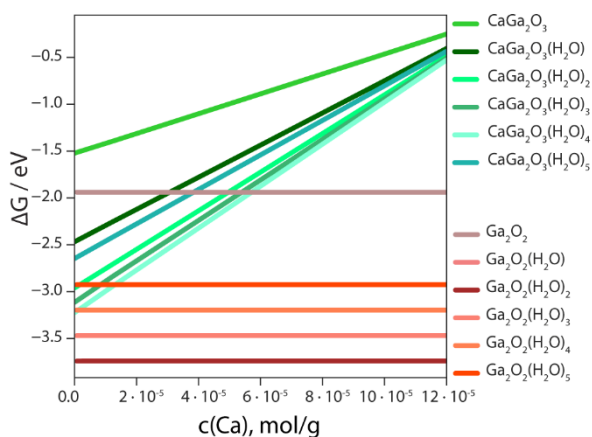


**Figure 4.5** The thermodynamic stability of the  $\text{Ga}_2\text{O}_2(\text{H}_2\text{O})_x^{2+}$  and  $\text{CaGa}_2\text{O}_3(\text{H}_2\text{O})_x^{2+}$  ( $x$  lies in a range between 0 and 5) complexes formed from  $\text{Ga}_2\text{O}_3$  bulk structure and Ca ion stabilized in zeolite as a function of Ca concentration in the system.

Furthermore, the dehydrogenation activity of the pure Ga and CaGa complexes, stabilized at intermediate water chemical potentials (mimicking the MTA conditions), was assessed by using ethane dehydrogenation as a model test reaction.<sup>40,49–51</sup> Specifically, the reactivity of  $\text{Ga}_2\text{O}_2(\text{H}_2\text{O})^{2+}$ ,  $\text{Ga}_2\text{O}_2(\text{H}_2\text{O})_2^{2+}$  and their Ca-containing counterparts  $\text{CaGa}_2\text{O}_3(\text{H}_2\text{O})_2^{2+}$ ,  $\text{CaGa}_2\text{O}_3(\text{H}_2\text{O})_4^{2+}$  were computationally investigated. **Figure 4.6** and **4.7a** summarize the DFT-computed reaction pathways for the ethane dehydrogenation reaction, namely, the heterolytic C–H bond cleavage,  $\beta$ -elimination, and  $\text{H}_2$  recombination steps over pure Ga and bimetallic CaGa species. The reaction energies and activation barriers of the respective steps are summarized in **Table A4.1**.

DFT calculations indicate that the Lewis acidity and the dehydrogenation activity of the intrazeolite clusters decrease with the increasing hydration levels, which are more favored for the bimetallic CaGa clusters. In **Figure 4.6**, the most thermodynamically

stable stoichiometries from the low water chemical potential region ( $-2.0 \text{ eV} < \Delta\mu_{\text{H}_2\text{O}} < -1.2 \text{ eV}$ , **Figure 4.4**) are explored for the ethane dehydrogenation process. The C–H bond activation step is 24 kJ/mol higher over the  $\text{CaGa}_2\text{O}_3(\text{H}_2\text{O})_2^{2+}$  when compared to its pure Ga-oxo counterpart  $\text{Ga}_2\text{O}_2(\text{H}_2\text{O})_2^{2+}$ . Under the conditions relevant for the MTA reaction ( $\Delta\mu_{\text{H}_2\text{O}} > -1.2 \text{ eV}$ , **Figure 4.4**), the dominant bimetallic  $\text{CaGa}_2\text{O}_3(\text{H}_2\text{O})_4^{2+}$  cluster exhibits computed barriers for the C–H activation and  $\text{H}_2$  recombination that are 32 and 10 kJ/mol, respectively, higher compared to its Ga-only counterpart  $\text{Ga}_2\text{O}_2(\text{H}_2\text{O})_2^{2+}$  (**Figure 4.7**).

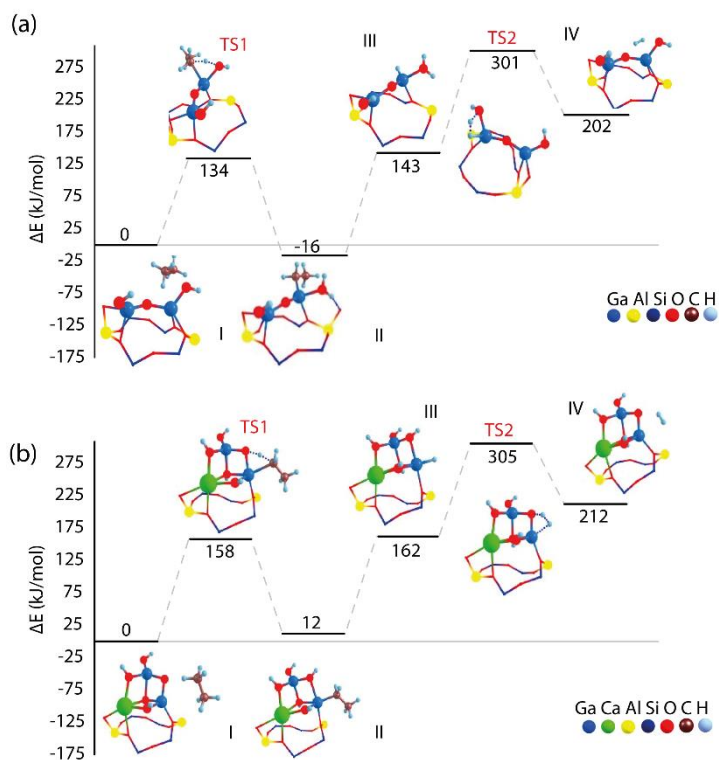


**Figure 4.6** DFT-computed reaction energy diagrams and local optimized structures of the key intermediates and transition states for ethane dehydrogenation over (a)  $\text{Ga}_2\text{O}_2(\text{H}_2\text{O})_2^{2+}$  (b) and  $\text{CaGa}_2\text{O}_3(\text{H}_2\text{O})_2^{2+}$  clusters in ZSM-5 zeolite thermodynamically favored at low  $\text{H}_2\text{O}$  partial pressures ( $-2.0 \text{ eV} < \Delta\mu_{\text{H}_2\text{O}} < -1.2 \text{ eV}$ ).

The current reactivity assessment specifically focused on the impact of the change of the properties of the Lewis acidic Ga center on the dehydrogenation activity. We anticipate that similar to other intrazeolite active complexes, the reactivity of the Ga-containing multinuclear clusters depends on a wide variety of secondary effects such as the presence of multiple reaction channels,<sup>52</sup> active site dynamics,<sup>53</sup> and the variation of the local zeolite environment.<sup>54</sup> The detailed investigation of these factors is beyond the scope of this chapter and is a focus of the ongoing computational efforts in our group.

Therefore, we propose that the addition of Ca allows to sustain the catalytic CaGa complexes in a more hydrated state during the MTA reaction. The higher degree of hydration for the CaGa system results in a higher barrier for the C–H bond cleavage, moderating thus effectively the rate of the dehydrogenation paths of the MTA reaction.

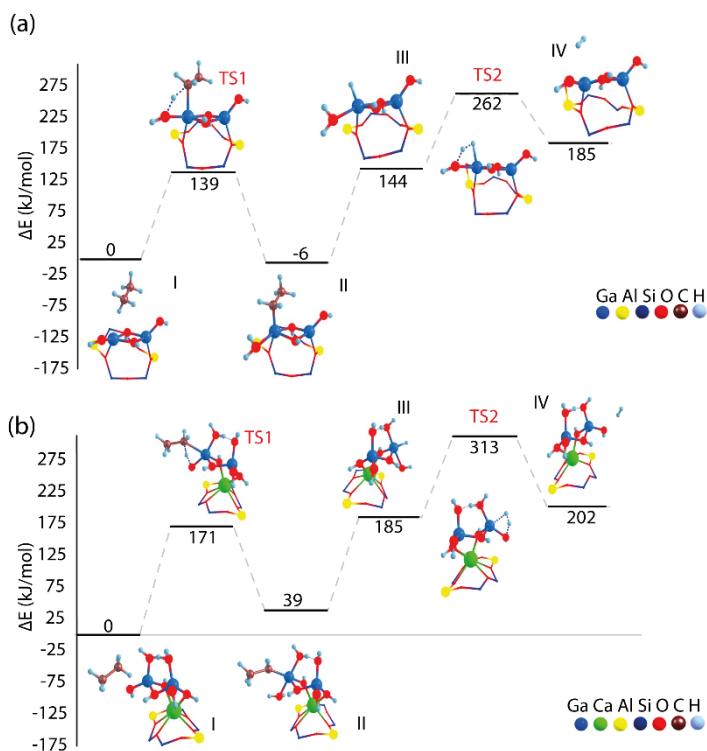


**Figure 4.7** DFT-computed reaction energy diagrams and local optimized structures of the key intermediates and transition states for ethane dehydrogenation over (a)  $\text{Ga}_2\text{O}_2(\text{H}_2\text{O})_2^{2+}$  and (b)  $\text{CaGa}_2\text{O}_3(\text{H}_2\text{O})_4^{2+}$  clusters in ZSM-5 zeolite thermodynamically favored at  $\text{H}_2\text{O}$  partial pressures relevant to the MTA process ( $\Delta\mu_{\text{H}_2\text{O}} > -1.2$  eV).

#### 4.4. Conclusions

MTA over Ga-modified zeolites offers a sustainable route for the production of important commodities such as benzene, ethylbenzene, toluene and xylenes. The increase in the selectivity towards the aromatics is accompanied by issues of enhanced coke deposition and subsequent early deactivation of the catalyst. The addition of minute amounts of Ca (0.02 wt%) prolongs the lifetime of the catalyst while maintaining a high selectivity toward aromatics. The Ca(0.02)Ga(2) converted 43% more MeOH and gave 33% higher yield of BTEX than Ga/H-ZSM-5 before the catalyst was fully deactivated.

Higher Ca loadings (>0.05 wt%) not only gives rise to Ca-LAS formation but also diminishes the impact of lifetime extension in MTA.

The mechanistic basis of the catalytic impact of Ca in the MTA process depending on Ca loading is still unclear. The interaction of Ca and Ga results in a moderated dehydrogenation rate evidenced by the lower hydrogen formation over Ca(0.02)Ga(2) than Ga(2) in the MeOH aromatization process. Using GA for global minima structures prediction, we were able to find the stable configurations of the pure Ga-oxo and CaGa-oxo stoichiometries with various water content. The thermodynamical stability of these configurations has been assessed in the aiTA as a function of water chemical potential. It has been shown that under the reactive conditions of the MTA process, the Ca<sup>2+</sup> cation added to the Ga extraframework structure allows to accommodate more water molecules. This results in a lower Lewis acidity of the Ca-containing sites and their higher stability in the presence of water. Accordingly, the higher C–H bond activation energy barrier over CaGa clusters leads to reduced dehydrogenation activity and a slower deactivation process, which is in line with the experimental results. Moreover, a Ca-concentration dependency analysis has been carried out to correlate the experimental Ca and Ga concentrations with thermodynamical favorability of the formation of the respective Ca-oxo and CaGa-oxo complexes. A theoretically established preference for the formation of the bimetallic CaGa-oxo clusters only at low Ca loadings has illustrated a good agreement with the experiment.

The targeted modification of Ga extraframework species with small quantities of Ca is demonstrated as a promising approach for further optimization and practical implementation of the MTA process.

## 4.5. References

1. Sheldon, R. A. Green and sustainable manufacture of chemicals from biomass: State of the art. *Green Chem.* **16**, 950–963 (2014).
2. Wei, J. *et al.* Directly converting CO<sub>2</sub> into a gasoline fuel. *Nat. Commun.* **8**, 15174 (2017).
3. Tian, P., Wei, Y., Ye, M. & Liu, Z. Methanol to olefins (MTO): From fundamentals to commercialization. *ACS Catal.* **5**, 1922–1938 (2015).
4. Zhong, J., Han, J., Wei, Y. & Liu, Z. Catalysts and shape selective catalysis in the methanol-to-olefin (MTO) reaction. *J. Catal.* **396**, 23–31 (2021).
5. Haw, J. F., Song, W., Marcus, D. M. & Nicholas, J. B. The mechanism of methanol to hydrocarbon catalysis. *Acc. Chem. Res.* **36**, 317–326 (2003).
6. Svelle, S. *et al.* Conversion of methanol into hydrocarbons over zeolite H-ZSM-5: Ethene formation is mechanistically separated from the formation of higher alkenes. *J. Am. Chem. Soc.* **128**, 14770–14771 (2006).
7. Conte, M. *et al.* Modified zeolite ZSM-5 for the methanol to aromatics reaction. *Catal. Sci. Technol.* **2**, 105–112 (2012).
8. Gao, P. *et al.* A Mechanistic Study of Methanol-to-Aromatics Reaction over Ga-Modified ZSM-5 Zeolites: Understanding the Dehydrogenation Process. *ACS Catal.* **8**, 9809–9820 (2018).
9. Zhu, X. *et al.* Synergistic co-conversion of pentane and methanol to aromatics over bifunctional

- metal/ZSM-5 zeolite catalysts. *Microporous Mesoporous Mater.* **320**, 111107 (2021).
10. Song, W., Fu, H. & Haw, J. F. Selective synthesis of methylnaphthalenes in HSAPO-34 cages and their function as reaction centers in methanol-to-olefin catalysis. *J. Phys. Chem. B* **105**, 12839–12843 (2001).
  11. Fu, H., Song, W. & Haw, J. F. Polycyclic aromatics formation in HSAPO-34 during methanol-to-olefin catalysis: Ex situ characterization after cryogenic grinding. *Catal. Lett* **76**, 89–94 (2001).
  12. Yarulina, I. *et al.* Structure–performance descriptors and the role of Lewis acidity in the methanol-to-propylene process. *Nat. Chem.* **10**, 804–812 (2018).
  13. Uslamin, E. A. *et al.* Gallium-promoted HZSM-5 zeolites as efficient catalysts for the aromatization of biomass-derived furans. *Chem. Eng. Sci.* **198**, 305–316 (2019).
  14. Liu, C. *et al.* High Stability of Methanol to Aromatic Conversion over Bimetallic Ca,Ga-Modified ZSM-5. *ACS Catal.* **12**, 3189–3200 (2022).
  15. Hussein, H. A. & Johnston, R. L. The DFT-genetic algorithm approach for global optimization of subnanometer bimetallic clusters. in *Frontiers of Nanoscience* vol. 12 145–169 (Elsevier, 2018).
  16. Jennings, P. C., Lysgaard, S., Hummelshøj, J. S., Vegge, T. & Bligaard, T. Genetic algorithms for computational materials discovery accelerated by machine learning. *Npj Comput. Mater.* **5**, 46 (2019).
  17. Bannwarth, C. *et al.* Extended tight-binding quantum chemistry methods. *Wiley Interdiscip. Rev. Comput. Mol. Sci.* **11**, e1493 (2021).
  18. Grimme, S., Bannwarth, C. & Shushkov, P. A Robust and Accurate Tight-Binding Quantum Chemical Method for Structures, Vibrational Frequencies, and Noncovalent Interactions of Large Molecular Systems Parametrized for All spd-Block Elements ( $Z = 1-86$ ). *J. Chem. Theory Comput.* **13**, 1989–2009 (2017).
  19. Bannwarth, C., Ehlert, S. & Grimme, S. GFN2- $\alpha$ TB - An Accurate and Broadly Parametrized Self-Consistent Tight-Binding Quantum Chemical Method with Multipole Electrostatics and Density-Dependent Dispersion Contributions. *J. Chem. Theory Comput.* **15**, 1652–1671 (2019).
  20. Pracht, P., Caldeweyher, E., Ehlert, S. & Grimme, S. A Robust Non-Self-Consistent Tight-Binding Quantum Chemistry Method for large Molecules. *ChemRxiv preprint*10.26434/chemrxiv.8326202.v1 (2019).
  21. Schütt, O., Messmer, P., Hutter, J. & VandeVondele, J. GPU-Accelerated Sparse Matrix-Matrix Multiplication for Linear Scaling Density Functional Theory. in *Electronic Structure Calculations on Graphics Processing Units: From Quantum Chemistry to Condensed Matter Physics* 173–190 (Wiley Online Library, 2016).
  22. Borštnik, U., VandeVondele, J., Weber, V. & Hutter, J. Sparse matrix multiplication: The distributed block-compressed sparse row library. *Parallel Comput.* **40**, 47–58 (2014).
  23. Maintz, S., Deringer, V. L., Tchougréeff, A. L. & Dronskowski, R. LOBSTER: A tool to extract chemical bonding from plane-wave based DFT. *J. Comput. Chem.* **37**, 1030–1035 (2016).
  24. Ehrlich, S., Moellmann, J., Reckien, W., Bredow, T. & Grimme, S. System-dependent dispersion coefficients for the DFT-D3 treatment of adsorption processes on ionic surfaces. *ChemPhysChem* **12**, 3414–3420 (2011).
  25. Perdew, J. P., Burke, K. & Ernzerhof, M. Generalized gradient approximation made simple. *Phys. Rev. Lett.* **77**, 3865–3868 (1996).
  26. Frigo, M. & Johnson, S. G. The design and implementation of FFTW3. *Proc. IEEE* **93**, 216–231 (2005).
  27. Kolafa, J. Time-Reversible Always Stable Predictor-Corrector Method for Molecular Dynamics of Polarizable Molecules. *J. Comput. Chem.* **25**, 335–342 (2004).
  28. VandeVondele, J. & Hutter, J. An efficient orbital transformation method for electronic structure calculations. *J. Chem. Phys.* **118**, 4365–4369 (2003).
  29. Lippert, G., Hutter, J. & Parrinello, M. A hybrid Gaussian and plane wave density functional scheme. *Mol. Phys.* **92**, 477–488 (1997).
  30. VandeVondele, J. & Hutter, J. Gaussian basis sets for accurate calculations on molecular systems in gas and condensed phases. *J. Chem. Phys.* **127**, 114105 (2007).
  31. Goedecker, S. & Teter, M. Separable dual-space Gaussian pseudopotentials. *Phys. Rev. B - Condens.*

- Matter Mater. Phys.* **54**, 1703–1710 (1996).
32. Genovese, L., Deutsch, T. & Goedecker, S. Efficient and accurate three-dimensional Poisson solver for surface problems. *J. Chem. Phys.* **127**, 54704 (2007).
  33. JANAF Thermochemical Tables ‘DR Stull and H. Prophet, project directors, Natl.’ in *Nat. Stand. Ref. Data Ser., Nat. Bur. Stds.(US)* vol. 1141 (1971).
  34. Sutton, C. & Levchenko, S. V. First-Principles Atomistic Thermodynamics and Configurational Entropy. *Front. Chem.* **8**, 757 (2020).
  35. Grimme, S., Ehrlich, S. & Goerigk, L. Effect of the damping function in dispersion corrected density functional theory. *J. Comput. Chem.* **32**, 1456–1465 (2011).
  36. Kresse, G. & Furthmüller, J. Efficient iterative schemes for *ab initio* total-energy calculations using a plane-wave basis set. *Phys. Rev. B - Condens. Matter Mater. Phys.* **54**, 11169–11186 (1996).
  37. Joubert, D. From ultrasoft pseudopotentials to the projector augmented-wave method. *Phys. Rev. B - Condens. Matter Mater. Phys.* **59**, 1758–1775 (1999).
  38. Blöchl, P. E. Projector augmented-wave method. *Phys. Rev. B* **50**, 17953–17979 (1994).
  39. Henkelman, G., Uberuaga, B. P. & Jónsson, H. Climbing image nudged elastic band method for finding saddle points and minimum energy paths. *J. Chem. Phys.* **113**, 9901–9904 (2000).
  40. Pidko, E. A., Hensen, E. J. M. & Van Santen, R. A. Dehydrogenation of light alkanes over isolated gallium ions in Ga/ZSM-5 zeolites. *J. Phys. Chem. C* **111**, 13068–13075 (2007).
  41. Grajciar, L. *et al.* Towards *operando* computational modeling in heterogeneous catalysis. *Chem. Soc. Rev.* **47**, 8307–8348 (2018).
  42. Corbett, P. T., Sanders, J. K. M. & Otto, S. Systems chemistry: Pattern formation in random dynamic combinatorial libraries. *Angew. Chem. Int. Ed.* **46**, 8858–8861 (2007).
  43. Pidko, E. A. & Van Santen, R. A. Structure-reactivity relationship for catalytic activity of gallium oxide and sulfide clusters in zeolite. *J. Phys. Chem. C* **113**, 4246–4249 (2009).
  44. Pidko, E. A., Van Santen, R. A. & Hensen, E. J. M. Multinuclear gallium-oxide cations in high-silica zeolites. *Phys. Chem. Chem. Phys.* **11**, 2893–2902 (2009).
  45. Kim, S., Park, G., Woo, M. H., Kwak, G. & Kim, S. K. Control of Hierarchical Structure and Framework-Al Distribution of ZSM-5 via Adjusting Crystallization Temperature and Their Effects on Methanol Conversion. *ACS Catal.* **9**, 2880–2892 (2019).
  46. Vilhelmsen, L. B. & Hammer, B. A genetic algorithm for first principles global structure optimization of supported nano structures. *J. Chem. Phys.* **141**, 044711 (2014).
  47. Frisch, M. J., Trucks, G. W. & Schlegel, H. B. Gaussian 09, Revision B. 01 and Revision D. 01. *Wallingford CT: Gaussian* (2010).
  48. Reuter, K., Stampf, C. & Scheffler, M. *Ab Initio* Atomistic Thermodynamics and Statistical Mechanics of Surface Properties and Functions. in *Handbook of Materials Modeling* 149–194 (Springer Netherlands, 2005).
  49. Pidko, E. A., Kazansky, V. B., Hensen, E. J. M. & van Santen, R. A. A comprehensive density functional theory study of ethane dehydrogenation over reduced extra-framework gallium species in ZSM-5 zeolite. *J. Catal.* **240**, 73–84 (2006).
  50. Pidko, E. A. & Van Santen, R. A. Activation of light alkanes over zinc species stabilized in ZSM-5 zeolite: A comprehensive DFT study. *J. Phys. Chem. C* **111**, 2643–2655 (2007).
  51. Mansoor, E., Head-Gordon, M. & Bell, A. T. Computational Modeling of the Nature and Role of Ga Species for Light Alkane Dehydrogenation Catalyzed by Ga/H-MFI. *ACS Catal.* **8**, 6146–6162 (2018).
  52. Szécsényi, Á., Li, G., Gascon, J. & Pidko, E. A. Mechanistic Complexity of Methane Oxidation with H<sub>2</sub>O<sub>2</sub> by Single-Site Fe/ZSM-5 Catalyst. *ACS Catal.* **8**, 7961–7972 (2018).
  53. Khramenkova, E. V., Medvedev, M. G., Li, G. & Pidko, E. A. Unraveling the Nature of Extraframework Catalytic Ensembles in Zeolites: Flexibility and Dynamics of the Copper-Oxo Trimers in Mordenite. *J. Phys. Chem. Lett.* **12**, 10906–10913 (2021).
  54. Szécsényi, Á. *et al.* Breaking Linear Scaling Relationships with Secondary Interactions in Confined Space: A Case Study of Methane Oxidation by Fe/ZSM-5 Zeolite. *ACS Catal.* **9**, 9276–9284 (2019).

## A4.1. Characterization of mono- and bimetallic CaGa/H-ZSM-5

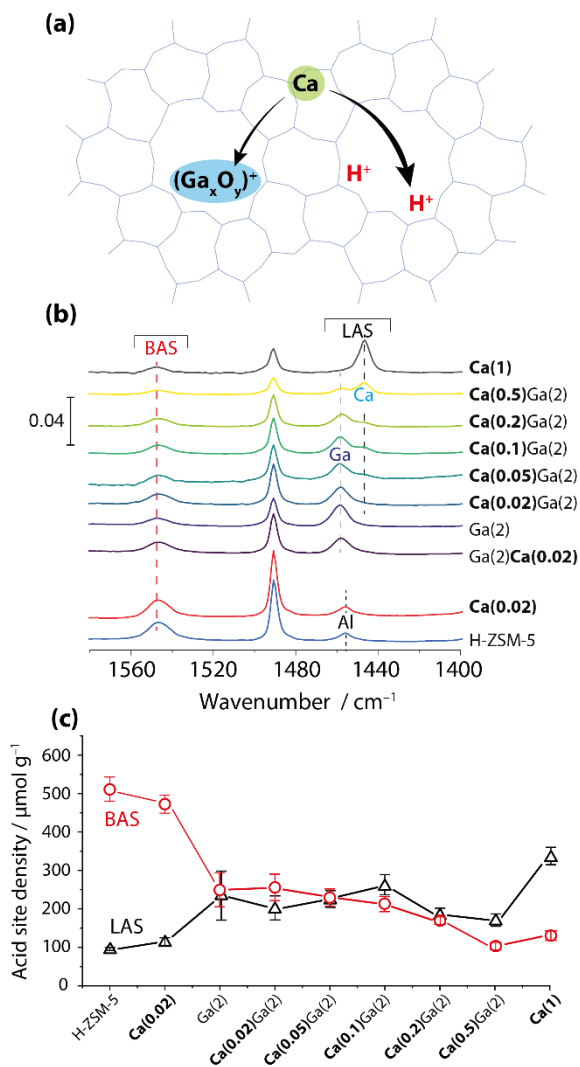


**Figure A4.1** Acidity characterization of mono- and bimetallic CaGa/H-ZSM-5 catalysts by FTIR measurements using pyridine as a probe. **(a)** Schematic illustration of Ca doping on Ga oxide species and BAS in H-ZSM-5 zeolite framework, **(b)** FTIR spectra with pyridine adsorption on zeolites with different metal loadings, and **(c)** acid site density of BAS and LAS determined by integrating bands at 1550  $\text{cm}^{-1}$  and 1460–1440  $\text{cm}^{-1}$ . The spectra with pyridine adsorption were obtained at 160  $^{\circ}\text{C}$ . Error bars represent the standard deviations of the quantitative analysis results from at least two measurements for each sample.

## A4.2. Global minima configurations

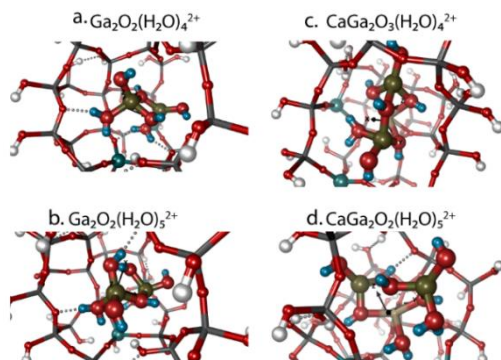


**Figure A4.2** Global minima of  $\text{Ga}_2\text{O}_2(\text{H}_2\text{O})_x^{2+}$  and  $\text{CaGa}_2\text{O}_3(\text{H}_2\text{O})_x^{2+}$  confined in the beta site of the ZSM-5 and optimized at the PBE-D3(BJ) level of theory, where  $x = 4$ (**a**, **b**), 5(**c**, **d**). Aluminum is aquamarine, oxygen is red, gallium is dark green, silicon is grey, calcium is beige and hydrogen of the cluster is blue.

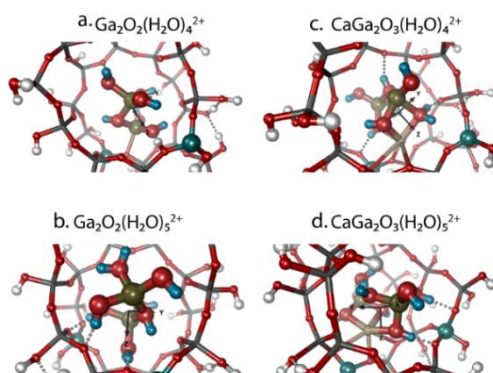
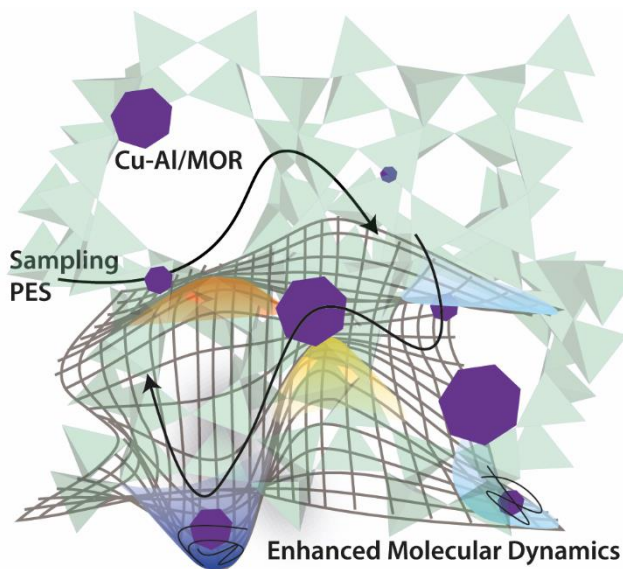


**Figure A4.3** Global minima of  $\text{Ga}_2\text{O}_2(\text{H}_2\text{O})_x^{2+}$  and  $\text{CaGa}_2\text{O}_3(\text{H}_2\text{O})_x^{2+}$  confined in the gamma site of the ZSM-5 and optimized at the PBE-D3(BJ) level of theory, where  $x = 4$ (**a**, **b**), 5(**c**, **d**). Aluminum is aquamarine, oxygen is red, gallium is dark green, calcium is beige, silicon is grey, and hydrogen of the cluster is blue.

**Table A4.1** The reaction energies ( $\Delta E$ ) and the activation barriers ( $E_{\text{act}}^\ddagger$ ) of the C–H bond activation,  $\beta$ -elimination and  $\text{H}_2$  recombination steps of ethane dehydrogenation.

Reaction step	C–H bond activation		$\beta$ -elimination		$\text{H}_2$ recombination	
	$\Delta E$	$E_{\text{act}}^\ddagger$	$\Delta E$	$E_{\text{act}}^\ddagger$	$\Delta E$	$E_{\text{act}}^\ddagger$
<b>Structures</b>						
$\text{Ga}_2\text{O}_2(\text{H}_2\text{O})_4^{2+}$	-16	134	159	/	59	158
$\text{Ga}_2\text{O}_2(\text{H}_2\text{O})_5^{2+}$	-6	139	150	/	41	118
$\text{CaGa}_2\text{O}_3(\text{H}_2\text{O})_4^{2+}$	12	158	150	/	50	143
$\text{CaGa}_2\text{O}_3(\text{H}_2\text{O})_5^{2+}$	39	171	147	/	16	128

**Impact of metal ion concentration on the formation  
of active CuAl-oxo clusters in mordenite for  
oxidative activation of methane**



## Summary

---

A comprehensive experiment-theory investigation on the role of the extraframework aluminum species (EFAl) in tailoring the reactivity of Cu-modified MOR zeolite catalysts for selective methane oxidation was carried out. The presence of the EFAl in the zeolite catalyst gave rise to a higher methanol yield achievable under ambient conditions, whereas for EFAl-free Cu/MOR a similar performance could only be observed under elevated pressures. This has been attributed to the formation of the bimetallic CuAl-oxo species at certain Cu concentrations in the catalyst. These bimetallic CuAl-oxo species were able to activate two methane molecules per cluster, while its pure Cu-oxo counterpart activated a single methane molecule per cluster. The experimental findings were also in line with the computationally derived conclusions on the enhanced reactivity of the bimetallic CuAl-oxo species. Using the low-mode molecular dynamics (LMMD) technique with enhanced sampling and the unsupervised machine learning algorithm, the possible configurations of the CuAl-oxo were generated. Considering the formation of the extraframework clusters inside zeolite cavities as the formation of defects, a thermodynamic equilibrium between the CuAl-oxo and pure Cu-oxo species as a function of Cu concentration has been found. The thermodynamical favorability of the intermediates formed in the sequential process of methane activation over MOR has been revealed, where the second methane molecule can be activated over CuAl-oxo under normal pressure.

This chapter is based on the following publications:

Zheng J., Lee I., Khramenkova E. V., Wang M., Peng B., Gutiérrez O.Y., Fulton J. L., Camaioni D. M., Khare R., Jentys A., Haller G. L., Pidko E. A., Sanchez-Sanchez M., Lercher J.A. *Chem. Eur. J.* **26**, 7563–7567 (2020).

Tao L., Khramenkova E. V., Lee I., Ikuno T., Fulton J. L., Pidko E. A., Sanchez-Sanchez M., Lercher J. A. *J. Am. Chem. Soc.*, *submitted*

The experimental part of this book has been carried out by Lei Tao, Insu Lee and Jian Zheng.

## 5.1. Introduction

The utilization of methane as a feedstock for various industrially relevant chemicals has attracted enormous attention, especially with the increasing number of discovered gas reserves around the world.<sup>1-3</sup> Among the different transformation routes, the direct conversion of methane to methanol represents one of the most enticing yet challenging pathways. Due to the rather harsh reaction conditions required to overcome the activation barrier of methane, usually, very low methanol yields are obtained, owing to its higher susceptibility to deep oxidation.<sup>4,5</sup>

Inspired by the naturally occurring particulate methane monooxygenases (pMMO),<sup>6-8</sup> copper-exchanged zeolites were found active in the selective conversion of methane to methanol through a three-stage process that can use oxygen from the air as an oxidant. Multiple zeolite topologies have been shown to accommodate active cationic Cu-oxo clusters in paired Al sites for the transformation, among which mordenite (MOR) is arguably the most widely studied zeolite. Spectroscopic characterization of these materials has led to different and at times conflicting proposals of the geometry of the active sites in zeolites. Mostly dimeric or trimeric Cu-oxo clusters are shown to be active in Cu/MOR.<sup>9-19</sup> Numerous material and synthesis parameters have been identified as relevant in directing the structure of Cu-oxo clusters, including the presence of other cations in the parent zeolite,<sup>15,20</sup> the distribution of the framework aluminum<sup>21,22</sup> and the ion exchange procedure.<sup>10,23</sup> The ability of Cu-oxo clusters to activate CH<sub>4</sub> also depends on the geometry and size of the pores as well as the local environment.<sup>12,21,24-26</sup> Understanding of the speciation of Cu ions and charged Cu-oxo clusters have been found also to be relevant for other redox catalytic applications such as NH<sub>3</sub> selective catalytic reduction of NO<sub>x</sub>.<sup>27,28</sup> All these spectroscopic, theoretical and catalytic studies of Cu-oxo clusters have opened a new field for the determination and synthesis of structures capable to stabilize active oxygen species.

Recently, the presence of extraframework Al (EFAl) has been found to increase the activity of Cu/MOR materials in methane oxidation.<sup>23,29</sup> The combination of spectroscopic and computational studies linked the origin of such activity increase to the formation of active CuAl-oxo clusters by reaction of the Cu ions with EFAl species located near the bottom of the 8-MR side pockets.<sup>29</sup> The proposed CuAl-oxo active site has a higher productivity per Cu than extraframework clusters formed with only Cu.

In this chapter, a formation of the highly reactive bimetallic CuAl-oxo species in MOR in the presence of EFAl was proposed. The origin of this reactivity of the CuAl-oxo extraframework species and their occurrence under *operando* conditions were studied by UV-Vis and X-ray absorption methods. These experimental results were complemented by the low-mode molecular dynamics (LMMD) technique, *ab initio* thermodynamic analysis (aiTA) and Cu-concentration-dependency phase diagram. Our

results indicated a dynamic equilibrium between Cu-oxo and CuAl-oxo extraframework structures, both active in methane oxidation. The relative fraction of each cluster formed depends on the concentration of Cu exchanged and the availability of EFAl, therefore justifying the increase in activity observed for Cu/MOR materials in the presence of EFAl species within the micropores.

## 5.2. Experimental and computational details

### 5.2.1. Catalyst preparation

Cu/MOR samples were prepared by aqueous ion exchange of H/MOR with copper acetate solution under controlled conditions. Typically, Cu<sup>2+</sup>-exchange was carried out by dispersing 2 g of H/MOR at ambient temperature. The pH of the solution was adjusted with an aqueous solution of nitric acid (0.2 M) and kept to 5.5 - 6.0 during the Cu exchange. After the exchange, the sample was separated from the suspension by centrifugation and rinsed four times with double deionized water followed by an intervening centrifugation step after each rinse cycle. All Cu/MOR samples were calcined in synthetic air flow at 500 °C (100 mL/min) for 2 h prior to IR and XAS measurements. The contents of Si, Al, Na and Cu were measured by atomic absorption spectroscopy.

### 5.2.2. Catalytic tests

The activity of the Cu/MOR samples for the selective oxidation of methane to methanol was tested in a three-step reaction scheme. Typically, 50 mg of Cu/MOR (250 – 400 μm) sample was packed in a stainless steel plug flow reactor with a 4-mm inner diameter. First, the sample was activated at 500 °C in O<sub>2</sub> flow for 1 h, cooled down to 200 °C and then flushed with He. In the next step, CH<sub>4</sub> was flowed over the sample at 200 °C for 3 h. Finally, the sample was flushed with He and cooled to 135 °C and subjected to steam-assisted product desorption with 20 % H<sub>2</sub>O in He. Reaction products were identified and quantified with a QMG 220 M1, PrismaPlus (Pfeiffer Vacuum) online MS (mass spectrometer) with a C-SEM detector by monitoring the m/z signals of 31, 44 and 46 for CH<sub>3</sub>OH, CO<sub>2</sub> and (CH<sub>3</sub>)<sub>2</sub>O. (CH<sub>3</sub>)<sub>2</sub>O was considered from the condensation of two CH<sub>3</sub>OH molecules and therefore the equivalent. The sum of all detected products was taken as the total yield.

For additional details on the experimental data and catalysts' characterization, please refer to **Appendix A5**.

### 5.2.3. *Ab initio* Low-mode Molecular Dynamics

The structures of the extraframework species were determined with the combination of the low-mode molecular dynamics (LMMD) configurational space exploration, automated clustering and DFT optimization of the most stable conformers following the

procedure described in ref. <sup>30</sup>. The configurational space of the extraframework CuAl-oxo bimetallic species was sampled using the LMMD approach by dragging the systems along the low curvature and enhancing the conformational alteration. The LMMD procedure was carried out employing fully periodic DFT simulations performed in the CP2K 8.2. software package with the Quickstep module and orbital transformation.<sup>31–35</sup> The parameters of the mordenite structure were set to:  $a = b = 13.648$ ,  $c = 15.015$  Å and the Si/Al ratio were set to 23 giving two Al framework species in the model. The generalized gradient approximation (PBE) was used to describe the exchange-correlation energy, with empirical correction by Grimme.<sup>36–38</sup> The periodic Poisson solver in combination with the Goedecker-Teter-Hutter pseudopotentials was used.<sup>39–41</sup> The projected augmented wave (PAW) method with a cutoff of 450 Ry and a relative cutoff of 30 Ry was employed.<sup>41</sup> A Gaussian basis set TZV2P-MOLOPT-SR-GTH was used for describing Cu atoms and a DZVP-MOLOPT-SR-GTH basis set was used for describing Si, Al, O and H atoms.<sup>42</sup> Two configurations were selected as initial configurations for conducting the LMMD (**Figure 5.1**). Each trajectory was integrated for 4.25 ps within the canonical ensemble employing the time step of 0.5 fs. The convergence criterion was set to  $10^{-5}$  a.u. During the simulations, the temperature was set to 723 and 923 K and the velocity softening low mode-guided algorithm was employed, providing a sampling enhancement.<sup>30</sup> For each type of initial configuration, four trajectories were simulated, giving eight trajectories in total.

#### 5.2.4. Clustering procedure

A clustering algorithm was used to extract the structurally distinct configurations from the eight LMMD trajectories.<sup>43</sup> The clustering was utilized based on an unsupervised machine learning algorithm – k-medoids as implemented in the scikit-learn.<sup>44</sup> This method minimizes a sum of pairwise dissimilarities between structures and centers of the cluster. Every 50<sup>th</sup> step of each trajectory was included in the clustering procedure and the silhouette index was used for determining the optimal number of clusters, where each cluster represents a structurally distinct set of configurations. The distance metric for both clustering method and validation measures was defined as ‘Euclidean’ which measures the square distance between vectors. In **Figure 5.1**, the components **a** and **b** show visualized clusters for the trajectories simulated from two different initial configuration. The visualization was done by projecting clusters and their respective centers into a bidimensional Euclidean space using t-SNE algorithm.<sup>45–47</sup> The geometries of centers of the clusters that are indicated as black dots in **Figure 5.1** were extracted and optimized to local minima using the Quasi-Newton algorithm. These optimized geometries capture the essential geometrical features of the clusters and are clusters’ centers.

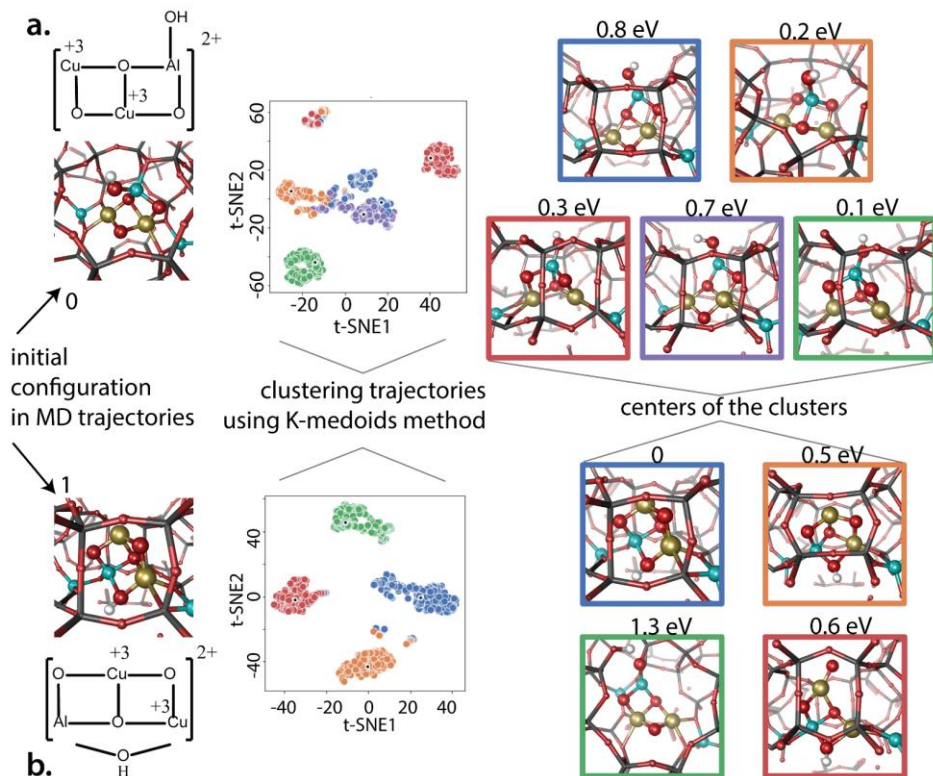


**Figure 5.1** The workflow of conducting the LMMD simulations utilizing two possible initial isomers  $[\text{Cu}_2\text{AlO}_4\text{H}]^{2+}$  (**a**) and (**b**), followed by the clustering procedure of the respective trajectories and optimizing centers of the clusters for both isomers. The energies of the optimized complexes are depicted with respect to the lowest-lying configuration. Clustering of the trajectories initiated by (**a**) gives the highest Silhouette score of 0.27 at 5 clusters. Clustering of the trajectories initiated by (**b**) gives the highest Silhouette score of 0.48 at 4 clusters.

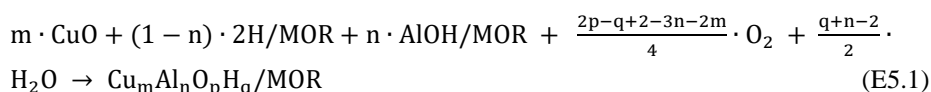
### 5.2.5. Extraframework aluminum species

The structural versatility of aluminum results in a plurality of the potential extraframework aluminum (EFAl) species in zeolites. The mononuclear charged  $\text{Al}^{3+}$ ,  $\text{AlO}^+$ ,  $\text{AlOH}^{2+}$  and  $\text{Al}(\text{OH})_2$  and neutral  $\text{Al}(\text{OH})_3$ ,  $\text{AlOOH}$  complexes have been previously found in dealuminated HY zeolites using a  $^1\text{H}$  double-quantum magic-angle-spinning NMR technique.<sup>48,49</sup> The model of the mononuclear  $\text{AlOH}^{2+}$  configuration was used as an extraframework Al species in this study. This choice is also motivated by the results in **Chapter 2**, where the mononuclear EFAl species were found to be the most stable ones for the ZSM-5. The dehydrated EFAl complex was selected to reduce the configurational uncertainty of the model.

### 5.2.6. *Ab initio* thermodynamics analysis: the stabilities of $\text{Cu}_2\text{AlO}_3$ and $\text{Cu}_2\text{AlO}_4\text{H}$ complexes

The non-hydroxylated  $[\text{Cu}_2\text{AlO}_3]^{2+}$  has been proposed earlier.<sup>29</sup> In the current analysis, we however consider an alternative stoichiometry  $[\text{Cu}_2\text{AlO}_4\text{H}]^{2+}$  of the bimetallic cluster that potentially allows for the 2-electron oxidation of multiple methane molecules. Indeed, the oxidation of 2 methane molecules by  $[\text{Cu}_2\text{AlO}_3]^{2+}$  would result in the formal reduction of the Cu sites to 0 and +1 states, whereas the respective reaction over the  $[\text{Cu}_2\text{AlO}_4\text{H}]^{2+}$  species reduces both sites to +1 oxidation state. Furthermore, the thermodynamic analysis reveals substantially higher stability of the  $[\text{Cu}_2\text{AlO}_4\text{H}]^{2+}$  species (see **Figure A5.3**).

The thermodynamic analysis was conducted to account for the influence of temperature and pressure effects on the stabilities of the  $[\text{Cu}_2\text{AlO}_3]^{2+}$  and  $[\text{Cu}_2\text{AlO}_4\text{H}]^{2+}$  configurations. A general form of the equilibria representing the formation of both complexes is defined as follows:



where CuO, 2H/MOR, AlOH/MOR,  $\text{O}_2$  and  $\text{H}_2\text{O}$  are the reference structures of the bulk copper oxide, H-form of the parent zeolite, EF aluminum species in the side pocket of mordenite and energies of the oxygen and water molecules respectively. The reaction Gibbs free energy  $\Delta G$  for equilibrium (E5.1) is defined as:

$$\Delta G = \Delta E - \frac{2p-q+2-3n-2m}{2} \cdot \Delta\mu(\text{O}_2) - \frac{q+n-2}{2} \cdot \Delta\mu(\text{H}_2\text{O}) \quad (\text{E5.2})$$

where  $\Delta E$  is the reaction energy and  $\Delta\mu(\text{O}_2)$  and  $\Delta\mu(\text{H}_2\text{O})$  are the chemical potential change of oxygen and water respectively. The reaction energy  $\Delta E$  is defined as the following:

$$\Delta E = E_{\text{Cu}_m\text{Al}_n\text{O}_p\text{H}_q/\text{MOR}} - m \cdot E_{\text{CuO}} - (1 - n) \cdot E_{2\text{H}/\text{MOR}} - n \cdot E_{\text{AlOH}/\text{MOR}} - \frac{2p-q+2-3n-2m}{4} \cdot E_{\text{O}_2} - \frac{q+n-2}{2} \cdot E_{\text{H}_2\text{O}} \quad (\text{E5.3})$$

where  $E_{\text{Cu}_m\text{Al}_n\text{O}_p\text{H}_q/\text{MOR}}$  is the total electronic energy of a CuAl-oxo complex, the  $E_{\text{CuO}}$  is the total energy of the bulk CuO,  $E_{2\text{H}/\text{MOR}}$  is the energy of the H-form of the mordenite structure,  $E_{\text{AlOH}/\text{MOR}}$ ,  $E_{\text{O}_2}$  and  $E_{\text{H}_2\text{O}}$  are the electronic energies of the mononuclear EF aluminum, gaseous  $\text{O}_2$  and  $\text{H}_2\text{O}$ . In this approach, the vibrational and PV contributions of solids are neglected and the Gibbs free energies of solids (H-form and modified zeolites) are computed as their respective DFT electronic energies. The chemical potentials of the gas phase at arbitrary conditions were calculated with respect to the

reference state at 0 K. To reflect the dependency of the chemical potential on the temperature and pressure, the chemical potential of water can be defined as:

$$\mu_{\text{H}_2\text{O}}(T, p) = E_{\text{H}_2\text{O}} + \Delta\mu_{\text{H}_2\text{O}}(T, p) \quad (\text{E5.4})$$

where  $\Delta\mu_{\text{H}_2\text{O}}(T, p)$  is defined as the following:

$$\begin{aligned} \Delta\mu_{\text{H}_2\text{O}}(T, p) &= \Delta\mu_{\text{H}_2\text{O}}(T, p^0) + RT \ln \left( \frac{p_{\text{H}_2\text{O}}}{p_{\text{H}_2\text{O}}^0} \right) = H(T, p^0, \text{H}_2\text{O}) - H(0 \text{ K}, p^0, \text{H}_2\text{O}) - \\ &T(S(T, p^0, \text{H}_2\text{O}) - S(0 \text{ K}, p^0, \text{H}_2\text{O})) + RT \ln \left( \frac{p_{\text{H}_2\text{O}}}{p_{\text{H}_2\text{O}}^0} \right) \end{aligned} \quad (\text{E5.5})$$

Similarly, the chemical potential of oxygen can be defined in the following way:

$$\mu_{\text{O}}(T, p) = \frac{1}{2} E_{\text{O}_2} + \Delta\mu_{\text{O}}(T, p) \quad (\text{E5.6})$$

where  $\Delta\mu_{\text{O}}(T, p)$  is defined as follows:

$$\begin{aligned} \Delta\mu_{\text{O}}(T, p) &= \Delta\mu_{\text{O}}(T, p^0) + \frac{1}{2} RT \ln \left( \frac{p_{\text{O}_2}}{p_{\text{O}_2}^0} \right) = \frac{1}{2} \left[ H(T, p^0, \text{O}_2) - H(0 \text{ K}, p^0, \text{O}_2) - \right. \\ &T(S(T, p^0, \text{O}_2) - S(0 \text{ K}, p^0, \text{O}_2)) \left. + RT \ln \left( \frac{p_{\text{O}_2}}{p_{\text{O}_2}^0} \right) \right] \end{aligned} \quad (\text{E5.7})$$

The standard values of the enthalpy and entropy used in eq (E5.5) and (E5.7) were taken from the respective tabulated thermodynamic data.<sup>50</sup> This approach has been previously employed on a range of solids.<sup>51,52</sup>

### 5.2.7. The concentration dependency of the CuAl- and Cu-oxo complexes formation

To get an insight into the concentration-dependent probability of forming mono- and bimetallic CuAl-oxo, Cu-oxo and EFAl species within the zeolite materials, a new methodology based on the aiTA analysis and defect representation of the extraframework species in zeolites has been developed and employed herein. To investigate the difference in stability of the pure Cu-oxo and CuAl-oxo clusters at different Cu concentrations, we have studied the formation of both types of complexes as point defects in a model crystal representing a zeolite with isolated EFAl species and Brønsted acid sites.<sup>53-55</sup> The theory of defects in solids was used here as the key approximation to derive the concentration-dependent free energy change in the zeolite materials with varied Cu contents. At the fixed (T, p) conditions, the Gibbs free energy change is defined by the value of the formation energy of the extraframework species and the associated configurational entropy stabilizing the effect. The change in Gibbs free energy associated with the formation of n vacancies in the crystal can be written as follows:

$$\Delta G(T, p) = (n \cdot \Delta G_f(T, p) - TS^{\text{conf}})/N \quad (\text{E5.8})$$

where  $\Delta G_f$  is the Gibbs free energy of a single defect formation and can be defined as the following:

$$\Delta G_f(T, p) = \Delta E - \sum \Delta \mu_i(T, p) \quad (E5.9)$$

where  $\Delta G_f(T, p)$  is the formation of Gibbs free energy of the extraframework (EF) clusters ( $[\text{Cu}_2\text{AlO}_3]^{2+}$ ,  $[\text{Cu}_2\text{AlO}_4\text{H}]^{2+}$  or  $[\text{Cu}_3\text{O}_3]^{2+}$ ) in an originally EFAl- and BAS-containing zeolite. The  $\Delta \mu_i(T, p)$  is the chemical potential of gaseous species which is defined in equations E5.5 and E5.7. The  $\Delta G_f(T, p)$  includes all entropic contributions (vibrational, electronic, etc) except the configurational entropy, and, therefore, accounts for the formation/consumption of gaseous species computed with the ideal gas approximation. In E5.9, the configurational entropy  $S^{\text{conf}}$  results from the disorder in the parent material due to the introduction of extraframework species. It was shown to stabilize the defects with positive formation energy and to be the largest contribution to the overall entropy.<sup>56</sup>

The value of the configurational entropy  $S^{\text{conf}}$  can be defined as follows:

$$S^{\text{conf}} = k_b \ln \frac{(N+n)!}{N!n!} \quad (E5.10)$$

Applying the Stirling formula for  $n, N$  values  $\gg 1$ , ( $\ln N! = N \ln N - N$ ) a good differentiable approximation of factorial can be written as the following:

$$S^{\text{conf}} = k_b N \left[ \ln \left( 1 + \frac{n}{N} \right) + \frac{n}{N} \ln \left( 1 + \frac{N}{n} \right) \right] \quad (E5.11)$$

For the pure Cu-oxo model, the number of defects  $n$  is defined as  $n = c^{\text{Cu}} N_a$  for 1 gram of catalyst, where  $c^{\text{Cu}}$  is the experimental concentration of Cu in a range of [0, 500] ( $\mu\text{mol/g}$ ). The value  $N$  is the number of the unit cells calculated for 1 gram of catalyst considering the molar weight of the used computational model:  $N = 1 \cdot N_a / M(\text{unit cell})$ . The final expression for the Gibbs free energy change in the process of formation  $n$  number of  $[\text{Cu}_3\text{O}_3]^{2+}$  defects in mordenite at the reactive conditions corresponding to the 700 K and 1 atm is defined as the following:

$$\Delta G_{\text{Cu}_3\text{O}_3} = \left( (\Delta E_{\text{Cu}_3\text{O}_3} - \Delta \mu_{\text{O}_2}^{700\text{K}} - \Delta \mu_{\text{H}_2\text{O}}^{700\text{K}}) c^{\text{Cu}} N_a - T \left( k_b N \left[ \ln \left( 1 + \frac{c^{\text{Cu}} N_a}{N} \right) + \frac{c^{\text{Cu}} N_a}{N} \ln \left( 1 + \frac{N}{c^{\text{Cu}} N_a} \right) \right] \right) \right) / N \quad (E5.12)$$

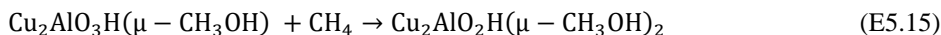
For the CuAl-oxo complexes, the Gibbs free energy of formation depends not only on the concentration of Cu ions but also on the concentration of EF aluminum species in the material. The number of defects per gram of catalysts can be defined as  $n = c^{\text{Al}} N_a - c^{\text{Cu}} N_a$ . The concentration of the EFAl ( $c^{\text{Al}}$ ) was taken from the experimental characterization analysis of the <sup>27</sup>Al MAS NMR and IR with pyridine adsorption of the

H-MOR parent sample, indicating 260  $\mu\text{mol/g}$  of EF aluminum. The final expression for the Gibbs free energy of the formation of  $[\text{Cu}_2\text{Al}_3\text{O}_4\text{H}]^2$  is expressed as:

$$\Delta G_{\text{Cu}_2\text{AlO}_4\text{H}} = \left( (\Delta E_{\text{Cu}_2\text{AlO}_4\text{H}} - \Delta\mu_{\text{O}_2}^{700\text{K}} - \Delta\mu_{\text{H}_2\text{O}}^{700\text{K}}) (c^{\text{Al}}N_{\text{a}} - c^{\text{Cu}}N_{\text{a}}) - T \left( k_{\text{b}}N \left[ \ln \left( 1 + \frac{c^{\text{Al}}N_{\text{a}} - c^{\text{Cu}}N_{\text{a}}}{N} \right) + \frac{c^{\text{Al}}N_{\text{a}} - c^{\text{Cu}}N_{\text{a}}}{N} \ln \left( 1 + \frac{N}{c^{\text{Al}}N_{\text{a}} - c^{\text{Cu}}N_{\text{a}}} \right) \right] \right) \right) / N \quad (\text{E5.13})$$

### 5.2.8. The sequential activation of methane molecules over $[\text{Cu}_3\text{O}_3]^{2+}$ and $[\text{Cu}_2\text{AlO}_4\text{H}]^{2+}$

The thermodynamic and kinetic investigation of the process of methane activation over Cu-oxo and CuAl-oxo complexes has been carried out. By comparing the stabilities of the different surface intermediates, the thermodynamic favorability of oxidizing methane over the catalytically active Cu- and CuAl-oxo species confined in mordenite was evaluated. The following equilibria representing the formation of the products of methane oxidation over  $[\text{Cu}_2\text{AlO}_4\text{H}]^{2+}$  were considered:



Equilibrium E5.14 illustrates the activation of the first methane molecules over  $[\text{Cu}_2\text{AlO}_4\text{H}]^{2+}$ , while the equilibrium E5.15 shows the activation of the second methane molecule over the final product from the E5.14. Hence, the configurations  $\text{Cu}_2\text{AlO}_3\text{H}(\mu - \text{CH}_3\text{OH})$  and  $\text{Cu}_2\text{AlO}_2\text{H}(\mu - \text{CH}_3\text{OH})_2$  are the surface intermediates formed as a result of the reaction with one or two methane molecules, respectively. These two structures result from the static calculations that underwent the annealing procedure to find nearby lying energy basins. The initial temperature in the annealing was set to 1000 K and the rescaling factor was set to 0.999. The configurations resulting from the annealing were optimized at the DFT level of theory and utilized for further analysis.

To account for the influence of the temperature and pressure of gaseous  $\text{CH}_4$  on the stability of the formed surface intermediates, the same approach has been carried out as described in 5.2.6. The energies of the  $\text{Cu}_2\text{AlO}_4\text{H}$ ,  $\text{Cu}_2\text{AlO}_3\text{H}(\mu - \text{CH}_3\text{OH})$  and  $\text{Cu}_2\text{AlO}_2\text{H}(\mu - \text{CH}_3\text{OH})_2$  were approximated as their respective electronic energies computed by DFT. The chemical potential of methane at arbitrary conditions can be defined as the following:

$$\mu_{\text{CH}_4}(T, p) = E_{\text{CH}_4} + \Delta\mu_{\text{CH}_4}(T, p) \quad (\text{E5.16})$$

where methane chemical potential is defined as the following:

$$\Delta\mu_{\text{CH}_4}(T, p) = \Delta\mu_{\text{CH}_4}(T, p^0) + RT\ln\left(\frac{p_{\text{CH}_4}}{p_{\text{CH}_4}^0}\right) = H(T, p^0, \text{H}_2\text{O}) - H(0 \text{ K}, p^0, \text{H}_2\text{O}) - T(S(T, p^0, \text{H}_2\text{O}) - S(0 \text{ K}, p^0, \text{H}_2\text{O})) + RT\ln\left(\frac{p_{\text{CH}_4}}{p_{\text{CH}_4}^0}\right) \quad (\text{E5.17})$$

Combining the equations above, we arrive at the final expression for the Gibbs free energy change for the formation of the first surface intermediate from E5.14:

$$\Delta G^{1\text{CH}_4} = \Delta E^{1\text{CH}_4} - \Delta\mu(\text{CH}_4) \quad (\text{E5.18})$$

$$\text{where } \Delta E^{1\text{CH}_4} = E_{\text{Cu}_2\text{AlO}_3\text{H}(\mu\text{-CH}_3\text{OH})} - E_{\text{Cu}_2\text{AlO}_4\text{H}} - E_{\text{CH}_4}$$

The Gibbs free energy change for the oxidation of the second methane molecule was defined as follows:

$$\Delta G^{2\text{CH}_4} = \Delta E^{2\text{CH}_4} - \Delta\mu(\text{CH}_4) \quad (\text{E5.19})$$

$$\text{where } \Delta E^{2\text{CH}_4} = E_{\text{Cu}_2\text{AlO}_2\text{H}(\mu\text{-CH}_3\text{OH})_2} - E_{\text{Cu}_2\text{AlO}_3\text{H}(\mu\text{-CH}_3\text{OH})} - E_{\text{CH}_4}$$

To compare the thermodynamical favorability of methane activation over the pure Cu-oxo complex with the bimetallic CuAl-oxo structure, the aiTA diagram has been built for the activation of methane over  $[\text{Cu}_3\text{O}_3]^{2+}$ , utilizing the same approach.

### 5.3. Results and discussion

#### 5.3.1. Oxidative conversion of CH<sub>4</sub> over CuAl-oxo clusters hosted in MOR

A series of Cu/MOR materials were prepared and extensively characterized using a wide range of physical-chemical methods, which results have been reported in refs.<sup>17,29</sup> The catalytic tests have revealed that these materials show the capacity to activate ca 0.6 molecules of CH<sub>4</sub> per Cu in a typical three-stage process of methane oxidation at 1 bar. The selectivity to methanol was in all cases in the range of 65 to 85%. This unusually high Cu efficiency ( $\text{Cu}_{\text{eff}}$ , defined as the molar ratio of converted methane to the total Cu content) was attributed to the formation of highly active Al-containing clusters by the reaction of exchanged Cu ions with EFAl species entrained in the zeolite pores.<sup>29</sup> On the other hand, it has been shown that Cu/MOR materials can reach significantly higher  $\text{Cu}_{\text{eff}}$  under high methane pressures (ca. 40 bar).<sup>13,17,57</sup> In order to determine whether the reactivity of CuAl-oxo clusters could be increased at high CH<sub>4</sub> chemical potentials, the activity of an EFAl-containing Cu/MOR series was tested at 40 bar and compared to activity at 1 bar. The results are shown in **Figure 5.2**, where total yields achieved at 40 bar of methane pressure increased by at least 10%. However, this increase in EFAl-containing samples was significantly smaller than the ca. 100% activity increase we previously achieved for Cu/MOR materials containing solely  $[\text{Cu}_3\text{O}_3]^{2+}$  clusters.<sup>17,58</sup> This

shows that the response to CH<sub>4</sub> chemical potential of CuAl-oxo clusters is different from pure Cu-oxo clusters. It should be noted that this is true for samples in the Cu/MOR series with low to medium Cu concentrations. However, for Cu loadings above 400 μmol/g, we observed an increase in methanol yields of nearly 100 % when increasing pressure from 1 to 40 bars, similar to Cu/MOR series containing Cu-oxo species. This is the first indication of a complex Cu speciation in presence of EFAl, with likely different Cu-oxo structures depending on the Cu concentration available during ion exchange.

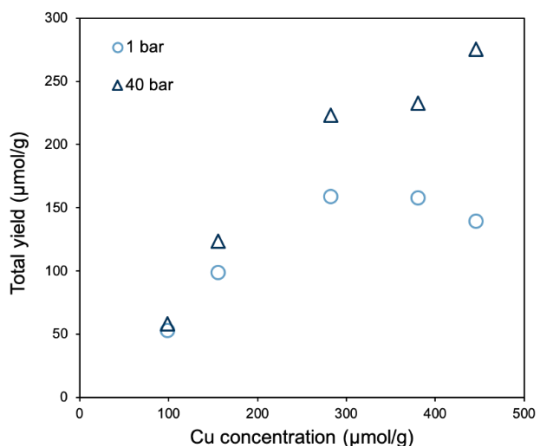


**Figure 5.2** Total yields achieved on Cu/MOR series after activation in O<sub>2</sub> at 500 °C for 1 h, followed by reaction in CH<sub>4</sub> flow at 200 °C (at 1 or 40 bar) for 3 h and subsequent treatment in 20% H<sub>2</sub>O/He flow at 200 °C.

Based on the previous studies on Cu clusters in MOR,<sup>17,29</sup> we can hypothesize that EFAl-containing MOR materials can accommodate both CuAl-oxo and Cu-oxo clusters. Hence, the activity of Cu/MOR materials is the function of the CuAl-oxo bimetallic<sup>29</sup> and pure Cu-oxo species<sup>58</sup> clusters' concentrations. The availability of the Cu ions and EFAl species in MOR affects these clusters' concentrations differently. A mild increase of activity with CH<sub>4</sub> pressure, as seen for low Cu loading samples in **Figure 5.2**, could be indeed explained by a larger proportion of an Al-containing cluster like the previously proposed CuAl-oxo site. These clusters might have already reached their activity upper limit at 1 bar, with the ability to activate two CH<sub>4</sub> molecules per cluster.<sup>29</sup> Conversely, it is known that [Cu<sub>3</sub>O<sub>3</sub>]<sup>2+</sup> clusters activate ca. 1 CH<sub>4</sub> molecule at 1 bar<sup>58</sup> and 2 CH<sub>4</sub> molecules at 40 bar.<sup>17</sup>

Based on these CH<sub>4</sub>-to-cluster stoichiometries, and assuming that only these two types of clusters participate in the reaction, the concentrations of each of the two clusters can be calculated from the Cu concentration and the total yields at 1 bar. As shown in **Figure 5.3**, materials with Cu concentrations below 300 μmol/g contain approximately

50 % of each type of cluster, while the proportion of the Cu-oxo cluster significantly increases at higher Cu concentrations, at the expense of the CuAl-oxo cluster.

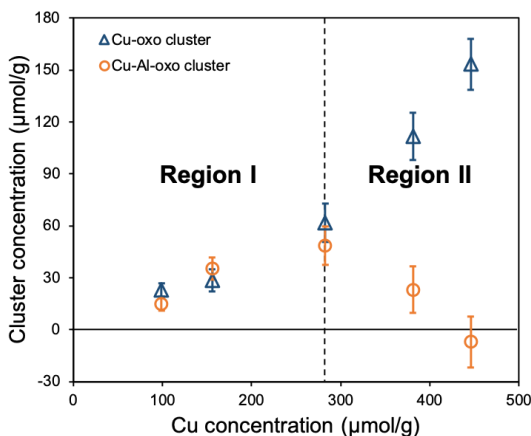


**Figure 5.3** The distribution of Cu-oxo and CuAl-oxo clusters in EFAl-containing Cu/MOR materials, calculated based on the assumption of 1 CH<sub>4</sub> activated per Cu-oxo cluster containing 3 Cu and 1 CH<sub>4</sub> activated per CuAl-oxo cluster containing 2 Cu, and the experimental yields obtained for selective methane oxidation at 1 bar.

### 5.3.2. Configurational search with LMMD

To rationalize and theoretically support the experimentally induced concentration of each type of cluster, we studied the thermodynamic stability of the Cu-oxo and CuAl-oxo clusters at different Cu concentrations with DFT-based aiTA. The stability of the respective models and their potential reactivity towards the sequential activation of several methane molecules were studied utilizing the periodic spin-polarized calculations at the PBE-D3(BJ) level of theory, where active sites were stabilized by the negative charges of framework Al T-sites located in the side pocket of mordenite.

The Cu-oxo species was represented by the [Cu<sub>3</sub>O<sub>3</sub>]<sup>2+</sup> trimeric cluster configuration determined with a recently developed expert bias-free computational procedure.<sup>30</sup> The structure of the CuAl-oxo cluster, on the other hand, has been constructed assuming a Cu<sub>2</sub>Al core and overall +2 charge, based on the stoichiometry of the Cu-EFAl interactions and the concentration of BAS exchanged with Cu.<sup>29</sup> Here, we consider a [Cu<sub>2</sub>AlO<sub>4</sub>H]<sup>2+</sup> stoichiometry capable of sequential 2-electron oxidation of CH<sub>4</sub> to methanol and at the same time, more stable thermodynamically than the previously proposed [Cu<sub>2</sub>AlO<sub>3</sub>]<sup>2+</sup> cluster (see **Figure A5.3** in **Appendix A5**). To determine the most stable geometries of [Cu<sub>2</sub>AlO<sub>4</sub>H]<sup>2+</sup> cationic complex, an exhaustive configurational search was carried out using the combination of the low-mode molecular dynamics (LMMD) and machine-learning clustering algorithm k-medoids approach<sup>30,59,60</sup> (see **5.2.3.** and **5.2.4.** in **Experimental and computational details**). The employed molecular dynamics

procedure provides an enhancement in the configurational search by dragging the system along the low-mode frequency mode. Linking the results of the LMMD with the clustering algorithm allows us to efficiently analyze the trajectories by grouping them based on the similar structural features they possess. The results of this post-processing analysis are depicted in **Figure 5.4**, where the extracted centers of the formed clusters are shown. As the geometries divided from the clustering of the trajectories have uncompensated forces acting on atoms, they have been optimized to local minima and their respective energies have been compared to the most stable configuration identified. A general workflow of analyzing the LMMD trajectories simulated with two distinct  $[\text{Cu}_2\text{AlO}_4\text{H}]^{2+}$  starting geometries is illustrated in **Figure 5.1**.

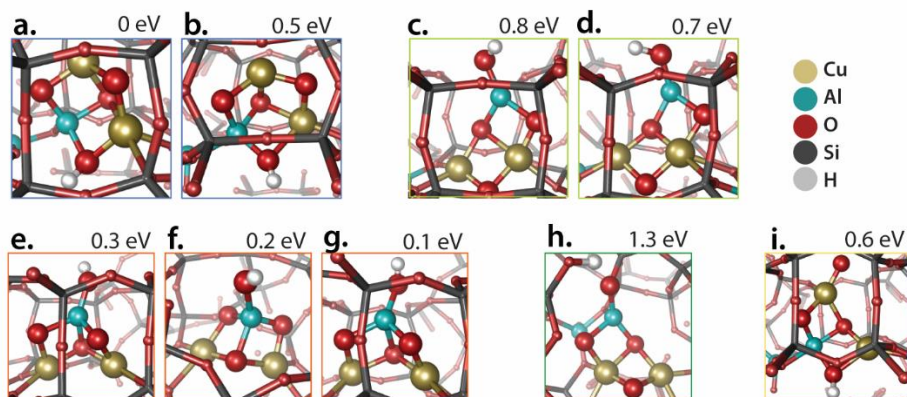


**Figure 5.4** The centers of the clusters resulting from the k-medoids clustering of  $[\text{Cu}_2\text{AlO}_4\text{H}]^{2+}$  LMMD trajectories analysis, grouped and colored based on the similarities in their structural features. The energies of the extracted geometries are evaluated and displayed in eV relative to the lowest-lying configuration (**a**).

In all geometries shown in **Figure 5.4**, a  $\text{Cu}_2\text{AlO}_3$  core can be identified. We also observe a few similar structures displayed within a single clustering procedure (**Figure 5.1**). This can be justified by a relatively low value of the Silhouette score – the separation quality metrics – for a portion of trajectories causing an overlap of the clusters in clustering procedures. Nevertheless, there is substantial structural diversity in the extracted isomers. Taking into account the similarities, we have displayed structures as colored groups featuring the same structural identity within the group.

Among the isomers identified in **Figure 5.4**, the most stable configuration **a** reveals a  $\text{Cu}_2\text{AlO}_3$  core augmented by an additional bridging  $\mu\text{-OH}$  ligand coordinated to Cu and Al centers featuring distorted tetrahedral environments. Additional distortion of the Cu coordination environment gives rise to a similar but 0.5 eV less stable configuration **b**. Structures **c** and **d** that are 0.7 – 0.8 eV less stable than **a**, feature trigonal coordination of the EF Al ion bearing a terminal OH-group. Structures **e** – **g** in **Figure 5.4** contain the

OH-ligand in the terminal coordination to the tetrahedral EF Al center resulting in only slightly lower stability of the respective isomers ( $\Delta E = 0.1 - 0.3$  eV). Our procedure also identified less stable configurations containing a terminal oxyl ligand in **h** and **i** structures, at the EF Al ( $\Delta E = 1.3$  eV) and Cu ( $\Delta E = 0.6$  eV), respectively. Our sampling results indicate substantial configurational flexibility of the extraframework clusters with the most stable structures all featuring the experimentally-observed  $\text{Cu}_2\text{AlO}_3$  core.

### **5.3.3. The stability of Cu-oxo and CuAl-oxo clusters as a function of Cu-concentration**

To theoretically describe the experimentally observed change in the Cu-oxo and CuAl-oxo speciation as a function of Cu concentration (**Figure 5.3**), a new thermodynamic model has been developed and integrated within the aiTA framework. We propose to treat the extraframework cations as defects in the zeolite matrix.<sup>53-55</sup> The Gibbs free energy change for the formation of an EF ensemble with a given stoichiometry includes the intrinsic free energy of the formation of a single EF species, the concentration of the EF species, as well as the associated configurational entropy terms (E5.8).

Here we consider the formation of the Cu-oxo or CuAl-oxo cationic complexes as ‘defects’ in a mordenite material with a given concentration of isolated EFAl species and Brønsted acid sites (BAS) at the reaction conditions of 1 atm and 700 K. The reaction of CuO as the reference copper source with either the BAS or EFAl species yields Cu-oxo or CuAl-oxo complexes, respectively. For the Cu-oxo extraframework species, the number of defects is proportional to the experimental concentration of Cu defined in a range of [0; 500]  $\mu\text{mol/g}$ , whereas the number of defects of the CuAl-oxo species depends on both – concentration of the EFAl species and Cu. The concentration of the EF aluminum species in the parent MOR model was set as 260  $\mu\text{mol/g}$ , according to <sup>27</sup>Al MAS NMR and pyridine-FTIR characterization. The key approximations for the concentration-dependent Gibbs free energy expressions for the  $[\text{Cu}_3\text{O}_3]^{2+}$  and  $[\text{Cu}_2\text{AlO}_4\text{H}]^{2+}$  defects (E5.12 and E5.13) are based on earlier computational studies.<sup>53,61</sup>

**Figure 5.5** reveals that at low loadings, copper preferentially binds with the EFAl sites to form the bimetallic species. However, with increasing Cu contents, the separation of the cationic EFAl and Cu species becomes thermodynamically more favorable. Our model predicts the transition point at ca. 200  $\mu\text{mol/g}$  in excellent agreement with the experimental results (**Figure 5.3**). Note, however, that the free energies computed in the presented scheme depend on the choice of the EFAl structure and the initial assumption of the zeolite composition (BAS and EFAl concentration).

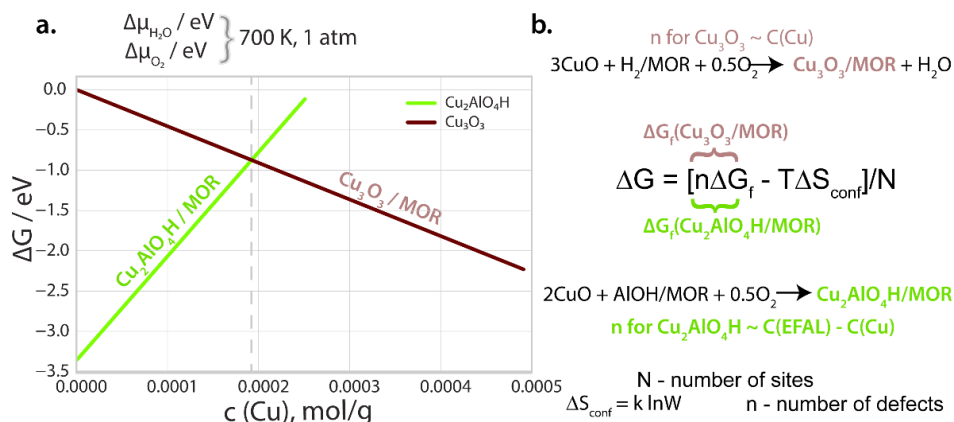


**Figure 5.5 (a)** Thermodynamic stability of the  $[\text{Cu}_2\text{AlO}_4\text{H}]^{2+}$  and  $[\text{Cu}_3\text{O}_3]^{2+}$  complexes in EFAL-containing MOR zeolite model as a function of Cu contents computed under reactive conditions of 700 K and 1 atm **(b)** the defect model approximation and accounting for concentration-dependencies and configurational entropy terms.

### 5.3.4. The reactivity of Cu-oxo and CuAl-oxo clusters in the methane oxidation process

Furthermore, periodic DFT calculations were carried out to evaluate the reactivity of the most stable  $[\text{Cu}_2\text{AlO}_4\text{H}]^{2+}$  in MOR towards the activation of multiple methane molecules. **Figure 5.6** presents the computed reaction energy diagrams for the sequential methane activation by the bimetallic cation.

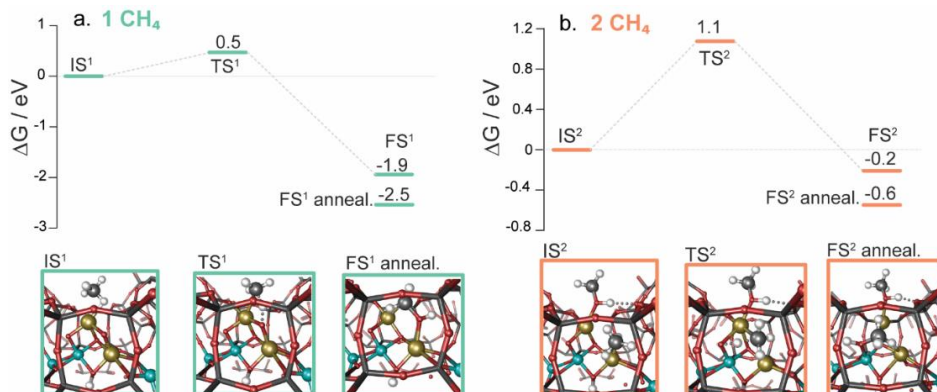


**Figure 5.6** The reaction energy diagrams for **(a)** the first and **(b)** second methanol molecule oxidation by the  $[\text{Cu}_2\text{AlO}_4\text{H}]^{2+}$  cation in MOR. The annealing procedure revealed the possibility of an additional stabilization of the surface oxidation products ( $\text{FS} \rightarrow \text{FS}_{\text{anneal}}$ ) via a facile isomerization process. The final states undergo the procedure of annealing to converge to the near-lying energy basin on the potential energy surface.

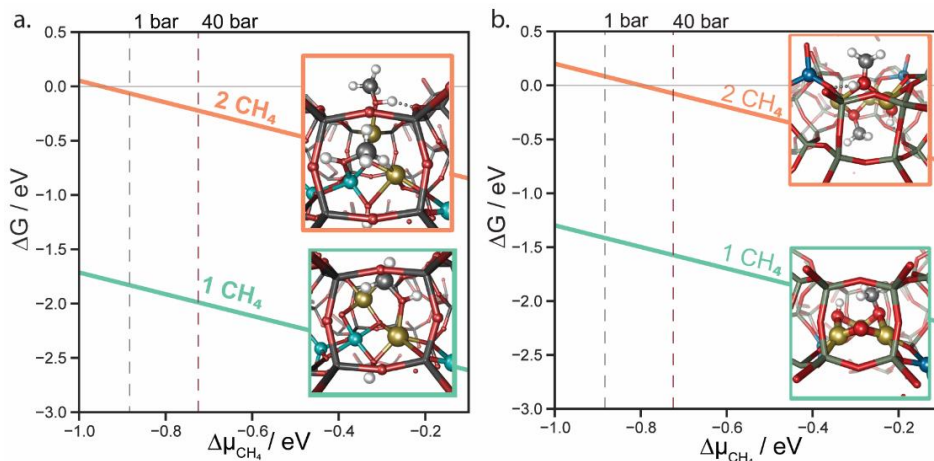


**Figure 5.7 (a)** The computed Gibbs free energies of sequential activation of methane by  $[\text{Cu}_2\text{AlO}_4\text{H}]^{2+}$  active site situated in the side pocket of mordenite as a function of  $\Delta\mu_{\text{CH}_4}$ . **(b)** The computed Gibbs free energies of sequential activation of methane by  $[\text{Cu}_3\text{O}_3]^{2+}$  active site situated in the side pocket of mordenite as a function of  $\Delta\mu_{\text{CH}_4}$ . The geometries of the corresponding intermediate surface products are displayed. The dashed lines correspond to the reactive conditions at the temperature of 500 K and pressure of 1 bar (left) and 40 bar (right).

In both steps, C–H bond activation follows a homolytic dissociation mechanism followed by a facile radical rebound to form  $\text{CH}_3\text{OH}$  (1<sup>st</sup>  $\text{CH}_4$  activation, FS<sup>1</sup>) or  $\text{CH}_3\text{O}$ - and  $\text{OH}$ - species (2<sup>nd</sup>  $\text{CH}_4$  activation, FS<sup>2</sup>) adsorbed to the cationic cluster. An additional annealing procedure on the final reaction intermediate formed via the elementary C–H activation processes revealed that a facile isomerization process can give rise to an additional stabilization of the surface intermediates by 0.4 – 0.6 eV. Both steps proceed with relatively low activation barriers. The oxidation of the first  $\text{CH}_4$  molecule proceeds with a barrier of about 0.5 eV, whereas the subsequent C–H activation by the thus formed partially reduced dual-metal cation faces a much higher barrier of 1.1 eV.

To further assess the thermodynamics of methane activation over the Cu-oxo and bimetallic CuAl-oxo complexes under the experimentally-relevant conditions, an aiTA has been carried out. **Figure 5.7** shows the thermodynamical favorability of the intermediates formed in the sequential process of methane activation over  $[\text{Cu}_2\text{AlO}_4\text{H}]^{2+}$  **(a)** and  $[\text{Cu}_3\text{O}_3]^{2+}$  **(b)**. The green line corresponds to the activation of the first methane molecule, while the orange line indicates the thermodynamical favorability of the formation of the intermediate resulting from the methane oxidation over the product of the previous step. The geometries of the respective  $\text{CH}_4$  oxidation intermediates are displayed. The diagram in **Figure 5.7a** shows that the hydroxylated  $[\text{Cu}_2\text{AlO}_4\text{H}]^{2+}$  cluster proposed here, despite its high intrinsic thermodynamic stability, is capable of favorably oxidizing up to two methane molecules per complex under ambient pressure. However,

the activation of methane over  $[\text{Cu}_3\text{O}_3]^{2+}$  is strongly exergonic at all methane chemical potentials while an elevated pressure is required for favorable thermodynamics to oxidize a second  $\text{CH}_4$  molecule. Therefore, the activation of the second methane molecule by the pure Cu-oxo species  $[\text{Cu}_3\text{O}_3]^{2+}$  is only feasible at elevated pressures, which is in line with the experimental findings.

## 5.4. Conclusions

A series of highly active Cu/MOR samples containing EFAl were tested for  $\text{CH}_4$  oxidation at ambient and elevated  $\text{CH}_4$  pressure. These materials have shown significantly higher yields to methanol, attributed to the formation of CuAl-oxo species, more efficient than the Cu-oxo counterparts. The aiTA combined with MD calculations allowed us to identify the stoichiometry and geometry of the stable  $[\text{Cu}_2\text{AlO}_4\text{H}]^{2+}$  clusters as active sites in  $\text{CH}_4$  oxidation. Contrary to the previously described  $[\text{Cu}_3\text{O}_3]^{2+}$  cluster, the  $[\text{Cu}_2\text{AlO}_4\text{H}]^{2+}$  cluster can readily activate two  $\text{CH}_4$  molecules per cluster at 200 °C and 1 bar of  $\text{CH}_4$  pressure. Thermodynamic equilibrium has been found between the formation of  $[\text{Cu}_2\text{AlO}_4\text{H}]^{2+}$  and  $[\text{Cu}_3\text{O}_3]^{2+}$  clusters as a function of the Cu concentration available during the ion exchange synthesis protocol on MOR zeolite. Based on the  $\text{CH}_4$  oxidation activity at different pressures, we have calculated the concentration of each type of CuAl-oxo cluster formed in MOR. Spectroscopic characterization supported the presence of the two clusters and the change in relative proportions with Cu loading.

In this chapter, the positive impact of EFAl on the activity of Cu/MOR materials has been fully described, paving the way for the synthesis of novel Cu-based catalysts with highly active and selective oxygen species for the conversion of light alkanes. Overall, understanding the speciation of Cu ions and oxo-clusters in zeolites has enabled the geometric description of active structures and the results shed light on metal-oxo ensembles capable to stabilize oxygen species with exceptional catalytic properties.

## 5.5. References

1. Malakoff, D. The gas surge. *Science* **344**, 1464–1467 (2014).
2. Kerr, R. A. Natural gas from shale bursts onto the scene. *Science* **328**, 1624–1626 (2010).
3. Caballero, A. & Pérez, P. J. Methane as raw material in synthetic chemistry: The final frontier. *Chem. Soc. Rev.* **42**, 8809–8820 (2013).
4. Periana, R. A. *et al.* Platinum catalysts for the high-yield oxidation of methane to a methanol derivative. *Science* **280**, 560–564 (1998).
5. Schwarz, H. Chemistry with methane: Concepts rather than recipes. *Angew. Chem. Int. Ed.* **50**, 10096–10115 (2011).
6. Ross, M. O. & Rosenzweig, A. C. A tale of two methane monooxygenases. *J. Biol. Inorg. Chem.* **22**, 307–319 (2017).
7. Sazinsky, M. H. & Lippard, S. J. Methane monooxygenase: Functionalizing methane at iron and

- copper. *Met. Ions Life Sci.* **15**, 205–256 (2015).
8. Solomon, E. I. *et al.* Copper active sites in biology. *Chem. Rev.* **114**, 3659–3853 (2014).
  9. Mahyuddin, M. H., Tanaka, T., Shiota, Y., Staykov, A. & Yoshizawa, K. Methane Partial Oxidation over  $[\text{Cu}_2(\mu\text{-O})]^{2+}$  and  $[\text{Cu}_3(\mu\text{-O})_3]^{2+}$  Active Species in Large-Pore Zeolites. *ACS Catal.* **8**, 1500–1509 (2018).
  10. Le, H. V. *et al.* Solid-State Ion-Exchanged Cu/Mordenite Catalysts for the Direct Conversion of Methane to Methanol. *ACS Catal.* **7**, 1403–1412 (2017).
  11. Sushkevich, V. L., Palagin, D., Ranocchiaro, M. & Van Bokhoven, J. A. Selective anaerobic oxidation of methane enables direct synthesis of methanol. *Science* **356**, 523–527 (2017).
  12. Snyder, B. E. R., Vanelderen, P., Schoonheydt, R. A., Sels, B. F. & Solomon, E. I. Second-Sphere Effects on Methane Hydroxylation in Cu-Zeolites. *J. Am. Chem. Soc.* **140**, 9236–9243 (2018).
  13. Brezicki, G., Kammert, J. D., Gunnoe, T. B., Paolucci, C. & Davis, R. J. Insights into the Speciation of Cu in the Cu-H-Mordenite Catalyst for the Oxidation of Methane to Methanol. *ACS Catal.* **9**, 5308–5319 (2019).
  14. Pappas, D. K. *et al.* The Nuclearity of the Active Site for Methane to Methanol Conversion in Cu-Mordenite: A Quantitative Assessment. *J. Am. Chem. Soc.* **140**, 15270–15278 (2018).
  15. Grundner, S., Luo, W., Sanchez-Sanchez, M. & Lercher, J. A. Synthesis of single-site copper catalysts for methane partial oxidation. *Chem. Commun.* **52**, 2553–2556 (2016).
  16. Grundner, S. *et al.* Single-site trinuclear copper oxygen clusters in mordenite for selective conversion of methane to methanol. *Nat. Commun.* **6**, 7546 (2015).
  17. Zheng, J. *et al.* Importance of Methane Chemical Potential for Its Conversion to Methanol on Cu-Exchanged Mordenite. *Chem. Eur. J.* **26**, 7563–7567 (2020).
  18. Vogiatzis, K. D., Li, G., Hensen, E. J. M., Gagliardi, L. & Pidko, E. A. Electronic Structure of the  $[\text{Cu}_3(\mu\text{-O})_3]^{2+}$  Cluster in Mordenite Zeolite and Its Effects on the Methane to Methanol Oxidation. *J. Phys. Chem. C* **121**, 22295–22302 (2017).
  19. Dandu, N. K., Reed, J. A. & Odoh, S. O. Performance of Density Functional Theory for Predicting Methane-to-Methanol Conversion by a Tri-Copper Complex. *J. Phys. Chem. C* **122**, 1024–1036 (2018).
  20. Sushkevich, V. L. & Van Bokhoven, J. A. Effect of Brønsted acid sites on the direct conversion of methane into methanol over copper-exchanged mordenite. *Catal. Sci. Technol.* **8**, 4141–4150 (2018).
  21. Markovits, M. A. C., Jentys, A., Tromp, M., Sanchez-Sanchez, M. & Lercher, J. A. Effect of Location and Distribution of Al Sites in ZSM-5 on the Formation of Cu-Oxo Clusters Active for Direct Conversion of Methane to Methanol. *Top. Catal.* **59**, 1554–1563 (2016).
  22. Pappas, D. K. *et al.* Methane to Methanol: Structure-Activity Relationships for Cu-CHA. *J. Am. Chem. Soc.* **139**, 14961–14975 (2017).
  23. Dyballa, M. *et al.* On How Copper Mordenite Properties Govern the Framework Stability and Activity in the Methane-to-Methanol Conversion. *ACS Catal.* **9**, 365–375 (2019).
  24. Tao, L., Lee, I. & Sanchez-Sanchez, M. Cu oxo nanoclusters for direct oxidation of methane to methanol: Formation, structure and catalytic performance. *Catal. Sci. Technol.* **10**, 7124–7141 (2020).
  25. Mahyuddin, M. H., Staykov, A., Shiota, Y., Miyanishi, M. & Yoshizawa, K. Roles of Zeolite Confinement and Cu-O-Cu Angle on the Direct Conversion of Methane to Methanol by  $[\text{Cu}_2(\mu\text{-O})]^{2+}$ -Exchanged AEI, CHA, AFX, and MFI Zeolites. *ACS Catal.* **7**, 3741–3751 (2017).
  26. Newton, M. A., Knorpp, A. J., Sushkevich, V. L., Palagin, D. & Van Bokhoven, J. A. Active sites and mechanisms in the direct conversion of methane to methanol using Cu in zeolitic hosts: A critical examination. *Chem. Soc. Rev.* **49**, 1449–1486 (2020).
  27. Mohan, S., Dinesha, P. & Kumar, S.  $\text{NO}_x$  reduction behaviour in copper zeolite catalysts for ammonia SCR systems: A review. *Chem. Eng. J.* **384**, 123253 (2020).
  28. Han, L. *et al.* Selective Catalytic Reduction of  $\text{NO}_x$  with  $\text{NH}_3$  by Using Novel Catalysts: State of the Art and Future Prospects. *Chem. Rev.* **119**, 10916–10976 (2019).
  29. Lee, I. *et al.* Activity of Cu–Al–Oxo Extra-Framework Clusters for Selective Methane Oxidation on Cu-Exchanged Zeolites. *JACS Au* **1**, 1412–1421 (2021).

30. Khramenkova, E. V., Medvedev, M. G., Li, G. & Pidko, E. A. Unraveling the Nature of Extraframework Catalytic Ensembles in Zeolites: Flexibility and Dynamics of the Copper-Oxo Trimers in Mordenite. *J. Phys. Chem. Lett.* **12**, 10906–10913 (2021).
31. Schütt, O., Messmer, P., Hutter, J. & VandeVondele, J. GPU-Accelerated Sparse Matrix-Matrix Multiplication for Linear Scaling Density Functional Theory. in *Electronic Structure Calculations on Graphics Processing Units: From Quantum Chemistry to Condensed Matter Physics* 173–190 (Wiley Online Library, 2016).
32. Borštnik, U., VandeVondele, J., Weber, V. & Hutter, J. Sparse matrix multiplication: The distributed block-compressed sparse row library. *Parallel Comput.* **40**, 47–58 (2014).
33. Hutter, J., Iannuzzi, M., Schiffmann, F. & VandeVondele, J. Cp2k: Atomistic simulations of condensed matter systems. *Wiley Interdiscip. Rev. Comput. Mol. Sci.* **4**, 15–25 (2014).
34. Frigo, M. & Johnson, S. G. The design and implementation of FFTW3. *Proc. IEEE* **93**, 216–231 (2005).
35. VandeVondele, J. & Hutter, J. An efficient orbital transformation method for electronic structure calculations. *J. Chem. Phys.* **118**, 4365–4369 (2003).
36. Grimme, S., Antony, J., Ehrlich, S. & Krieg, H. A consistent and accurate *ab initio* parametrization of density functional dispersion correction (DFT-D) for the 94 elements H-Pu. *J. Chem. Phys.* **132**, 154104 (2010).
37. Grimme, S., Ehrlich, S. & Goerigk, L. Effect of the damping function in dispersion corrected density functional theory. *J. Comput. Chem.* **32**, 1456–1465 (2011).
38. VandeVondele, J. *et al.* Quickstep: Fast and accurate density functional calculations using a mixed Gaussian and plane waves approach. *Comput. Phys. Commun.* **167**, 103–128 (2005).
39. Krack, M. Pseudopotentials for H to Kr optimized for gradient-corrected exchange-correlation functionals. *Theor. Chem. Acc.* **114**, 145–152 (2005).
40. Sharma, S. Ā. *et al.* Improved tetrahedron. *J. Appl. Phys.* **7**, 16223–16233 (2009).
41. Goedecker, S. & Teter, M. Separable dual-space Gaussian pseudopotentials. *Phys. Rev. B - Condens. Matter Mater. Phys.* **54**, 1703–1710 (1996).
42. VandeVondele, J. & Hutter, J. Gaussian basis sets for accurate calculations on molecular systems in gas and condensed phases. *J. Chem. Phys.* **127**, 114105 (2007).
43. Park, H. S. & Jun, C. H. A simple and fast algorithm for K-medoids clustering. *Expert Syst. Appl.* **36**, 3336–3341 (2009).
44. Blondel, M. *et al.* Scikit-learn: Machine Learning in Python. *J. Mach. Learn. Res.* **12**, 2825–2830 (2011).
45. Van Der Maaten, L. & Hinton, G. Visualizing data using t-SNE. *J. Mach. Learn. Res.* **9**, 2579–2625 (2008).
46. Krijthe, J. H. Rtsne:T-distributed stochastic neighbor embedding using barneshut implementation. *R package version 0.13*, URL: <https://github.com/jkrijthe/Rtsne> (2015).
47. Van Der Maaten, L. Accelerating t-SNE using tree-based algorithms. *J. Mach. Learn. Res.* **15**, 3221–3245 (2014).
48. Brown, S. P. & Spiess, H. W. Advanced solid-state NMR methods for the elucidation of structure and dynamics of molecular, macromolecular, and supramolecular systems. *Chem. Rev.* **101**, 4125–4155 (2001).
49. Liu, C., Li, G., Hensen, E. J. M. & Pidko, E. A. Nature and Catalytic Role of Extraframework Aluminum in Faujasite Zeolite: A Theoretical Perspective. *ACS Catal.* **5**, 7024–7033 (2015).
50. JANAF Thermochemical Tables ‘DR Stull and H. Prophet, project directors, Natl.’ in *Nat. Stand. Ref. Data Ser., Nat. Bur. Stds.(US)* vol. 1141 (1971).
51. Li, G. *et al.* Stability and reactivity of copper oxo-clusters in ZSM-5 zeolite for selective methane oxidation to methanol. *J. Catal.* **338**, 305–312 (2016).
52. Guhl, H., Miller, W. & Reuter, K. Water adsorption and dissociation on SrTiO<sub>3</sub> (001) revisited: A density functional theory study. *Phys. Rev. B - Condens. Matter Mater. Phys.* **81**, 155455 (2010).

53. Sutton, C. & Levchenko, S. V. First-Principles Atomistic Thermodynamics and Configurational Entropy. *Front. Chem.* **8**, 757 (2020).
54. Bukonte, L., Ahlgren, T. & Heinola, K. Thermodynamics of impurity-enhanced vacancy formation in metals. *J. Appl. Phys.* **121**, 45102 (2017).
55. Web Page: <https://refubium.fu-berlin.de> (Date Accessed: 2022-11-21) (2022).
56. Estreicher, S. K., Sanati, M., West, D. & Ruymgaart, F. Thermodynamics of impurities in semiconductors. *Phys. Rev. B - Condens. Matter Mater. Phys.* **70**, 125209 (2004).
57. Tomkins, P. *et al.* Isothermal Cyclic Conversion of Methane into Methanol over Copper-Exchanged Zeolite at Low Temperature. *Angew. Chem. Int. Ed.* **55**, 5467–5471 (2016).
58. Grundner, S. *et al.* Single-site trinuclear copper oxygen clusters in mordenite for selective conversion of methane to methanol. *Nat. Commun.* **6**, 1–9 (2015).
59. Medvedev, M. G. *et al.* Exhaustive conformational search for transition states: the case of catechol O-methyltransferase active site. *Mendeleev Commun.* **27**, 224–227 (2017).
60. Medvedev, M. G. *et al.* Quantifying Possible Routes for SpnF-Catalyzed Formal Diels-Alder Cycloaddition. *J. Am. Chem. Soc.* **139**, 3942–3945 (2017).
61. Zhang, X., Grabowski, B., Hickel, T. & Neugebauer, J. Calculating free energies of point defects from *ab initio*. *Comput. Mater. Sci.* **148**, 249–259 (2018).
62. Wulfers, M. J., Teketel, S., Ipek, B. & Lobo, R. F. Conversion of methane to methanol on copper-containing small-pore zeolites and zeotypes. *Chem. Commun.* **51**, 4447–4450 (2015).
63. Giordanino, F. *et al.* Characterization of Cu-exchanged SSZ-13: A comparative FTIR, UV-Vis, and EPR study with Cu-ZSM-5 and Cu- $\beta$  with similar Si/Al and Cu/Al ratios. *Dalt. Trans.* **42**, 12741–12761 (2013).
64. Brezicki, G., Zheng, J., Paolucci, C., Schlögl, R. & Davis, R. J. Effect of the Co-cation on Cu Speciation in Cu-exchanged mordenite and ZSM-5 catalysts for the oxidation of methane to methanol. *ACS Catal.* **11**, 4973–4987 (2021).
65. Qayyum, M. F. *et al.* L-edge X-ray absorption spectroscopy and DFT calculations on Cu<sub>2</sub>O<sub>2</sub> species: Direct electrophilic aromatic attack by side-on peroxo bridged dicopper(II) complexes. *J. Am. Chem. Soc.* **135**, 17417–17431 (2013).
66. Sarangi, R. *et al.* X-ray absorption edge spectroscopy and computational studies on LCuO<sub>2</sub> species: Superoxide-Cu<sup>II</sup> versus peroxide-Cu<sup>III</sup> bonding. *J. Am. Chem. Soc.* **128**, 8286–8296 (2006).

### A5.1. In-situ ultraviolet-visible (UV-Vis) spectroscopy

The UV-vis spectra were measured on an Avantes AvaSpec 2048 spectrometer equipped with a high-temperature optical fiber (Avantes FCR-7UV400-2ME-HTX). The sample (250 - 400  $\mu\text{m}$ ) was placed in a quartz tube with square optical-grade quartz windows. The intensity of the diffuse reflectance UV-vis is shown as the Kubelka-Munk function, defined as  $F(R) = (1 - R)^2 / 2R$ , where  $R = R_s/R_r$ ,  $R_s$  and  $R_r$  refer to the signal intensity of the sample and reference, respectively. The reference spectra were taken on the parent H-MOR sample. The samples were first activated in synthetic air (16 mL/min) at 450  $^\circ\text{C}$  with a heating rate of 10 K/min for 1 h. Then the samples were cooled down to 200  $^\circ\text{C}$  and flushed with He (10 mL/min) for 0.5 h, followed by contact with  $\text{CH}_4$  flow (16 mL/min) for 1 h. The spectra were recorded periodically with a certain time interval to monitor the changes through time.

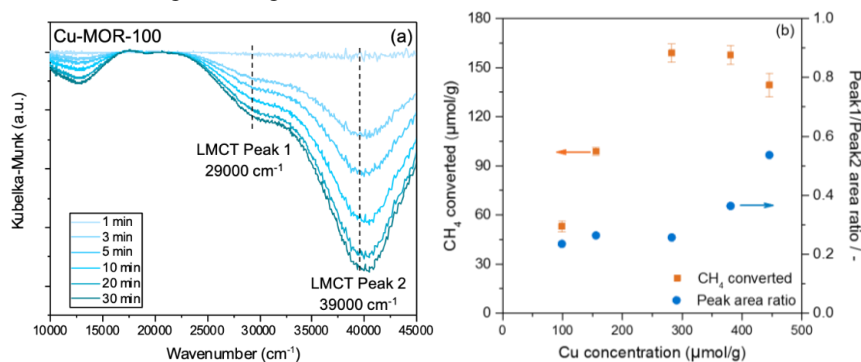


**Figure A5.1** (a) In-situ UV-Vis difference spectra of oxygen activated Cu-MOR-100 after  $\text{CH}_4$  exposure at 200  $^\circ\text{C}$  for 30 min, (b) the peak area ratio of the decrease of two LMCT bands from UV-Vis absorption spectra upon activation of methane at 1 bar as a function of Cu concentration in MOR.

The differential spectra, obtained by subtracting the spectra after  $\text{CH}_4$  exposure for 30 min from those of the  $\text{O}_2$ -activated samples, show decreases in the absorption bands centered at 29000 and 39000  $\text{cm}^{-1}$  (**Figure A5.1**), which are attributed to the intensity change of the charge transfer bands of extraframework<sup>10,58,62</sup> and framework oxygen atoms<sup>63,64</sup>, respectively, to Cu species during  $\text{CH}_4$  reaction. The relative ratios of these two features stay roughly between 0.2 and 0.3 for samples with Cu concentrations lower than 300  $\mu\text{mol/g}$ , while they gradually increase up to 0.54, which matches very well with the value observed on a conventional Cu-MOR sample containing exclusively  $[\text{Cu}_3\text{O}_3]^{2+}$  clusters. These results are also in good agreement with our proposal of the cluster distribution in **Figure 5.3** based on  $\text{CH}_4$  oxidation activity at 1 bar and theoretical calculations, because a relatively higher extraframework oxygen to Cu ratio in  $[\text{Cu}_3\text{O}_3]^{2+}$  than in  $[\text{Cu}_2\text{AlO}_4\text{H}]^{2+}$  should contribute to greater Peak 1/Peak 2 values.

## **A5.2. In-situ X-ray absorption spectroscopy**

X-ray absorption spectra at Cu L-edge were measured at the Swiss Light Source (SLS) of the Paul Scherrer Institut (Villigen, Swiss) on PHOENIX II. The photon source is an elliptical undulator and monochromatic light was generated by a planar grating monochromator. Energy calibration was achieved by setting an inflection point of a measured Al-foil to 1559.6 eV. The samples were pressed into self-supporting pellets with a thickness of ca. 0.5 mm and placed into a multi-pellet holder. The samples were first activated in 1 % O<sub>2</sub> in Ar at 800 mbar at 450°C with a heating rate of 10 K/min for 1 h and then cooled down to room temperature. The measurements were performed before and after thermal activation in vacuum ( $1.0 \cdot 10^{-4}$  mbar). All measurements were carried out in fluorescence mode and the incoming I<sub>0</sub> was measured as a total electron yield signal taken from a 0.5 μm thin polyester foil coated with 50 nm of Ni. The described I<sub>0</sub> detector was held 1 m upstream of the sample in the beamline vacuum of ca. 10<sup>-6</sup> mbar. The X-ray fluorescence signal was detected by a one-element energy dispersive Silicon drift diode (DSS, manufacturer Ketek, Germany). The introduced gases were further dried by using Supelco 5A Moisture trap. ATHENA software was used during the background processing.

## **A5.3. Spectroscopic evidence on the cluster distributions**

First, the differences observed in the Cu L<sub>3</sub>-edge X-ray absorption near edge structure (XANES) of O<sub>2</sub>-activated Cu-MOR samples with different Cu loadings were investigated. The main peak appearing at 929 eV corresponds to 2p to 3d dipole transitions of Cu(II) species. The position of the satellite feature that arises from the mixing of Cu 3d orbitals with 2p orbitals from the oxygen ligands generally reveals more information on the local chemical environment of the Cu species hosted in each material.<sup>65,66</sup> While the Cu-MOR-160 and Cu-MOR-280 both show a satellite peak at a ΔE value of 3.5 eV, the satellite feature for Cu-MOR-450 appears at a ΔE value of 3.2 eV (**Figure A5.2**). In our previous work, the satellite peak for the simulated spectra of both [Cu<sub>2</sub>AlO<sub>3</sub>]<sup>2+</sup> homologue and [Cu<sub>3</sub>O<sub>3</sub>]<sup>2+</sup> appears at a ΔE value of 3.3 eV, while [Cu<sub>3</sub>O<sub>3</sub>]<sup>2+</sup> cluster has shown an additional satellite feature at ca. ΔE 2.0 eV.<sup>29</sup> Therefore, we propose that the shift towards lower energies of the satellite peak with increasing Cu loading is indicative of a larger contribution of [Cu<sub>3</sub>O<sub>3</sub>]<sup>2+</sup> clusters, in good agreement with the relative concentrations calculated in **Figure 5.3**.

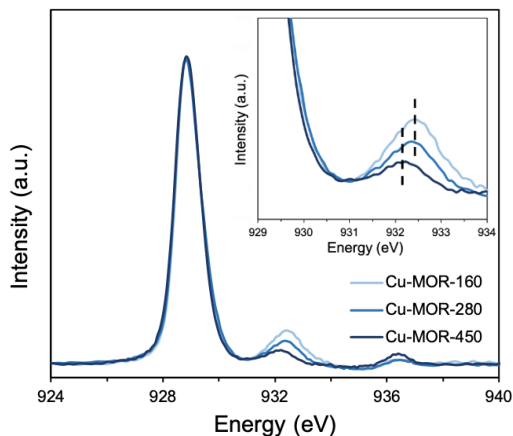


**Figure A5.2** Cu  $L_3$ -edge XANES of Cu-MOR samples activated in  $O_2$  at 450 °C for 1 h (Intensities of the main edge were made the same for better visualization.)

**Table A5.1** Physicochemical properties of Cu/FER samples

Sample	Cu conc. ( $\mu\text{mol/g}$ )	Si/Al after Cu exchange (-)	Cu conc. after Na back-exchange ( $\mu\text{mol/g}$ )	Not back-exchanged Cu (%)
Cu-FER-100	99	9.6	6.3	6.4
Cu-FER-150	155	9.4	10	6.4
Cu-FER-280	283	9.3	20	7.0
Cu-FER-380	381	10.2	25	6.6
Cu-FER-450	446	9.4	32	7.1

#### A5.4. The concentration dependency of the Cu-Al- and Cu-oxo complexes formation

**Table A5.2** The  $\Delta G$  values of the  $\text{Cu}_3\text{O}_3$  and  $\text{Cu}_2\text{AlO}_4\text{H}$  formation according to the equations (E5.12) and (E5.13) respectively.

Concentration Cu, $\mu\text{mol/g}$	$\Delta G_{\text{Cu}_3\text{O}_3}$ , eV	$\Delta G_{\text{Cu}_2\text{AlO}_4\text{H}}$ , eV
1e-6	-0.45e-2	-3.35
100e-6	-0.46	-2.06
200e-6	-0.91	-0.76
300e-6	-1.37	-
400e-6	-1.82	-
450e-6	-2.05	-

### A5.5. *Ab initio* thermodynamics analysis on the stabilities of $\text{Cu}_2\text{AlO}_3$ and $\text{Cu}_2\text{AlO}_4\text{H}$ complexes

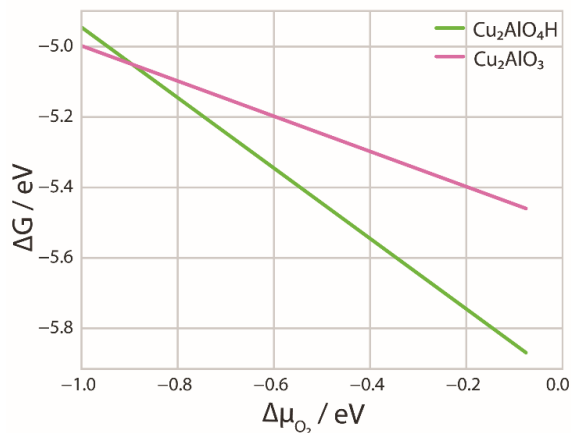
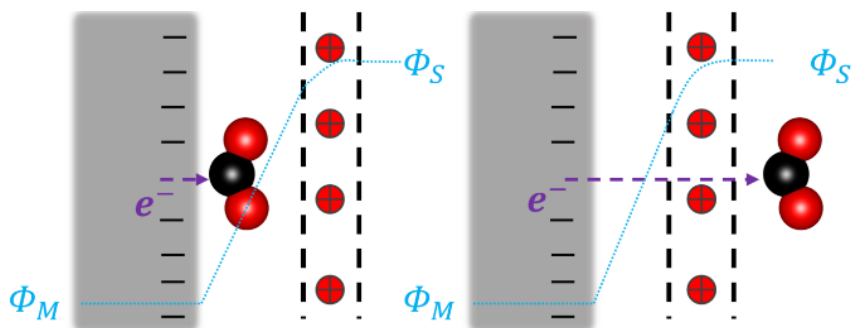


**Figure A5.3** The phase diagram reflecting the thermodynamic stability  $[\text{Cu}_2\text{AlO}_4\text{H}]^{2+}$  and  $[\text{Cu}_2\text{AlO}_3]^{2+}$  as a function of  $\Delta\mu_{\text{O}_2}$  defined at a fixed value of water chemical potential  $\Delta\mu_{\text{H}_2\text{O}}$ . The value of the  $\Delta\mu_{\text{H}_2\text{O}}$  corresponds to the reactive conditions of the extraframework species formation at the temperature of 700 K and 1 atm. The diagram indicates that under the reactive conditions of high-temperature CuAl/MOR activation processes, that lies in the range of  $\Delta\mu_{\text{O}_2}$  between 0 and -1 eV, the  $[\text{Cu}_2\text{AlO}_4\text{H}]^{2+}$  is more thermodynamically favorable compared to the  $[\text{Cu}_2\text{AlO}_3]^{2+}$ .



**Solvent-mediated outer-sphere  $\text{CO}_2$   
electroreduction mechanism over Ag111 surface**



## Summary

---

Electrocatalytic CO<sub>2</sub> reduction reaction (CO<sub>2</sub>RR) is one of the key technologies of the clean energy economy. Molecular-level understanding of the CO<sub>2</sub>RR process is instrumental for the better design of electrodes operable at low overpotentials with high current density. The catalytic mechanism underlying the turnover and selectivity of CO<sub>2</sub>RR is modulated by the nature of the electrocatalyst, as well as the electrolyte liquid, and its ionic components that form the electrical double layer (EDL). Herein we demonstrate the critical non-innocent role of the EDL for the activation and conversion of CO<sub>2</sub> at a high cathodic bias for the electrocatalytic conversion over the silver surface as a representative low-cost model cathode. By using a multiscale modelling approach we demonstrate that under such conditions a dense EDL is formed, which hinders the diffusion of CO<sub>2</sub> towards the Ag111 electrocatalyst surface. By combining DFT calculations and *ab initio* molecular dynamics simulations we identify favorable pathways for CO<sub>2</sub> reduction directly over the EDL without the need for adsorption to the catalyst surface. The dense EDL promotes homogeneous phase reduction of CO<sub>2</sub> via electron transfer from the surface to the electrolyte. Such an outer-sphere mechanism favors the formation of formate as the CO<sub>2</sub>RR product. The formate can undergo dehydration to CO via a transition state stabilized by the solvated alkali cations in the EDL.

This chapter is based on the following publication:

Sinha V., Khramenkova E. V., Pidko E. A.  
*Chemical Science* **13**, 3803–3803 (2022).

The DFT calculations and *ab initio* molecules dynamics have been carried out by Vivek Sinha.

## 6.1. Introduction

Electrochemical conversion of CO<sub>2</sub> holds the promise to help mitigate the carbon footprint of the production of fuels and chemicals.<sup>1</sup> The abundant CO<sub>2</sub> greenhouse waste gas is an attractive substrate to stabilize excess “electrons” generated from renewable energy via the CO<sub>2</sub> reduction reaction (CO<sub>2</sub>RR).<sup>2</sup> A wide range of electrocatalysts has been described so far for the CO<sub>2</sub>RR.<sup>3,4</sup> Depending on the catalyst employed the primary CO<sub>2</sub>RR product can be either the formate or CO resulting from a 2e<sup>-</sup> reduction, or multielectron transfer products such as alcohols and hydrocarbons. The electrocatalytic reduction of CO<sub>2</sub> to CO opens a path for carbon recycling within the established syngas chemistry infrastructure to produce fuels and chemicals.<sup>1</sup>

In an electrocatalytic cell, CO<sub>2</sub>RR proceeds on the cathode side. The cathode material, its morphology and the electrolyte properties collectively influence the electrocatalytic activity and selectivity at the solid-liquid interface.<sup>5,6</sup> Gold-based electrocatalysts have been reported to reduce CO<sub>2</sub> to CO with high activity and selectivity. Hori and co-workers used bulk Au to reduce CO<sub>2</sub> to CO with 87.1% Faradaic efficiency (FE) at -1.14 V (NHE) with a partial CO current of 5 mA cm<sup>-2</sup>.<sup>7</sup> At the same partial current, Ag showed a FE of 81.5% towards CO at -1.37 V (NHE).<sup>7</sup> The lower cost, and comparable selectivity and activity to Au make Ag an attractive electrocatalyst for CO<sub>2</sub>RR.

The selectivity and activity of an electrocatalyst for the CO<sub>2</sub>RR are strongly influenced by the electrolyte and the local environment close to the cathode.<sup>5,6,8-11</sup> At potentials ( $\Phi_M$ ) below the potential of zero charge (pzc) ( $\Phi_M < \Phi_{pzc}$ ) the negative charge density on the cathode surface increases attracting more cations resulting in the formation of an electrical double layer (EDL). The EDL influences the local electrochemical environment close to the cathode surface such as the interfacial pH and the structure of water at the interface.<sup>11-13</sup> The cations in the EDL also interact with the surface intermediates and tune the stabilization of transition states and adsorbates on the electrocatalyst surface.<sup>14,15</sup> However, at a higher cathodic bias, the EDL becomes very dense and compact hampering thus strongly the mass transport of CO<sub>2</sub> to the electrocatalyst surface.<sup>16-18</sup>

The electron transfer (ET) from the cathode to the reagent is the key mechanistic step of any electrocatalytic conversion. ET can in principle proceed via two alternative mechanisms: the inner- and outer-sphere ET (**Figure 6.1**). The inner-sphere mechanism starts with the chemisorption of the reagent (CO<sub>2</sub>) to the catalyst surface that enables the direct ET via overlapping orbitals (**Figure 6.1a**). In the outer-sphere mechanism, the indirect ET from the catalyst surface to CO<sub>2</sub> takes place through the electrolyte without the direct chemical interaction between the reagent and the electrocatalyst (**Figure 6.1b**).

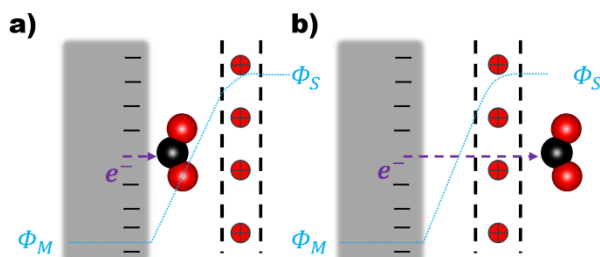


**Figure 6.1** (a) Inner-sphere and (b) outer-sphere electron transfer from cathode to  $\text{CO}_2$ . The red positive charges within the black dotted lines denote the EDL.  $\Phi_M$  and  $\Phi_S$  are surface and bulk solution phase potentials respectively.

The inner-sphere mechanisms describing the electrocatalytic conversions in the framework of surface adsorbed species dominate the current literature.<sup>5,19–25</sup> Investigating the selectivity of  $\text{CO}_2\text{RR}$  on various Ag facets, Bohra and co-workers proposed that the formation of formate species is self-inhibited on Ag surfaces resulting in improved selectivity to CO at low to moderate potentials, and  $\text{H}_2$  at higher potentials.<sup>26</sup> Their work did not consider the effects of the EDL and the electrolyte explicitly. Realistic description of the reaction medium and conditions in modelling studies has been currently emphasized across the fields of catalysis.<sup>27–39</sup> The importance of including an explicit representation of the EDL and accounting for the reaction conditions in mechanistic studies of electrocatalytic  $\text{CO}_2\text{RR}$  has been emphasized in recent literature.<sup>14,15,40</sup>

However, most mechanistic studies assume facile mass transport of  $\text{CO}_2$  from the bulk phase to the surface *via* the EDL. Such an assumption is reasonable for hydrodynamic transport through a low concentration electrolyte but under the *operando*  $\text{CO}_2\text{RR}$  potentials, the EDL can get more condensed and strongly impact the mass transport of  $\text{CO}_2$ .<sup>17,41</sup> Under such conditions an outer-sphere ET in the homogeneous phase over the EDL is a plausible mechanism for the  $\text{CO}_2\text{RR}$ .

Herein, we have taken a multiscale *operando* modelling approach to investigate the possibility and the impact of the homogeneous ET on  $\text{CO}_2\text{RR}$  under realistic electrocatalytic conditions. The combination of classical molecular dynamics (CMD), and *ab initio* molecular dynamics (aiMD) simulations show that  $\text{CO}_2$  can be favorably reduced to formate anion via the outer-sphere ET over the dense EDL. The formate species can then convert to CO via a thermally activated dehydration reaction facilitated by the solvated cations within the EDL.

## 6.2. Computational details

### 6.2.1. CMD model

CMD simulations were performed using the Large-scale Atomic/Molecular Massively Parallel Simulator (LAMMPS) (version from 22Aug 2018).<sup>42</sup> An aqueous solution of KCl, which is a standard electrolyte in electrocatalytic studies, was confined between two charged Ag walls that represented the cathodic and anodic surfaces. The silver slabs with an electrolyte bulk, that consisted of K<sup>+</sup>, Cl<sup>-</sup> ions and CO<sub>2</sub> and H<sub>2</sub>O molecules were constructed using Atomic Simulation Environment (ASE). The concentrations were set to correspond to the experimentally relevant conditions, namely, 0.86M for K<sup>+</sup>, 0.86M for Cl<sup>-</sup> and 0.06M for CO<sub>2</sub>. The simulations were carried out using a supercell of 33.1 x 37.2 x 265.5 Å. The supercell was set to be periodic in the x and y directions and non-periodic in the z-direction. A vacuum spacing of 1.7 Å was set behind the silver slabs. The charging of the electrode surfaces due to externally applied potential was mimicked by introducing negative and positive ghost charges behind the Ag slabs. The calculated magnitudes of the electric field on the cathodic surface due to polarization induced by the ghost charges were 0 V/nm (no ghost charges), 0.05 V/nm, and 0.5 V/nm. The interatomic interactions between the components of the medium were modelled via Lennard-Jones (LJ) potential with the cutoff of 9.0 Å. The cross-terms were obtained using the Lorentz-Berthelot mixing rules. Water was modelled using the parameters of the SPC/E model,<sup>43 44-46</sup> which is widely used in simulations of the ions in aqueous solutions.<sup>43 44-46</sup> The LJ parameters for CO<sub>2</sub>, K<sup>+</sup>, and Cl<sup>-</sup> were taken from the literature.<sup>47,48</sup> The long-range interactions were calculated with the particle-particle-mesh (PPPM) method. The O-H bonds and H-O-H angles were kept rigid within the SHAKE algorithm, whereas the C-O bonds and O-C-O angles were kept rigid via harmonic bond approximation. The temperature of the simulations was maintained using the Nose-Hoover thermostat at the value of 300 K.<sup>47,48</sup> We used a time step of 1 fs. The production runs were 90 ns long, excluding 10 ps of equilibration time in the beginning. The snapshots of trajectory for further analysis were taken every 10 ps. The post-processing analysis was conducted using the MDAnalysis<sup>49</sup> and maicos\_delft<sup>50</sup> packages. For all the simulations, the system was initially equilibrated in the isothermal regime with different integration time steps (10<sup>-5</sup>, 10<sup>-4</sup>, 10<sup>-3</sup>, 10<sup>-2</sup>, 10<sup>-1</sup> and 1) for 10<sup>3</sup> steps within each time step. However, the snapshots of atom quantities in the final dcd trajectory were included every 10 ps timesteps, giving the first 10 ps as equilibration time. **Figure A6.1** (left) shows that the energy of the production runs starting from the 10 ps is stabilized, with some small fluctuations present.

### 6.2.2. DFT calculations

In this chapter, we constructed a smaller molecular model of the electrocatalyst system consisting of a 4 x 4 x 5 Ag111 slab and performed density functional theory

(DFT) calculations for the reactive events. The EDL was composed of 4 Na<sup>+</sup> cations per supercell which corresponds to  $\sim -1.0$  V vs pzc (*vide infra*). The supercell was charge neutral. We performed geometry optimizations using periodic DFT calculations using the PBE<sup>51</sup> functional and projector augmented wave (PAW) potentials<sup>52,53</sup> with the valence electrons expanded as plane waves (cutoff 450 eV) using VASP 5.4.4 software package.<sup>54</sup> In all DFT-based geometry optimizations, the fcc supercell of dimensions 11.5 Å, 11.5 Å, and 30.0 Å was selected. The unit cell was constructed in the following manner: the first 5 layers of the 1 x 1 fcc cell of Ag111 were created with a lattice constant of 4.079 Å<sup>18</sup> and lattice vectors: (0.70710678, 0.0000000, 0.0000000), (-0.35355339, 0.6123724, 0.0000000), and (0.0000000, 0.0000000, 5.1961524). This 1 x 1 supercell was extended to create the 4 x 4 x 5 slab by changing the Bravais Matrix and adding additional atoms. The 4 x 4 x 5 Ag111 slab was fully optimized using DFT, and so were “4 x 4 x 5 Ag111 slab+water molecules”, “4x4x5 Ag111 slab+water molecules + Na ions”, “4x4x5 Ag111 slab+water molecules + Na ions + CO<sub>2</sub>”, “4 x 4 x 5 Ag111 slab+water molecules + CO<sub>2</sub>”. Grimme’s D3 method with Becke–Johnson damping (D3(BJ)) was adopted for the van der Waals correction.<sup>55,56</sup> In the DFT-based geometry optimizations we considered 24 water molecules for the solvation of the 4Na<sup>+</sup> cations over the 4 x 4 x 5 Ag111 slab. We further placed a CO<sub>2</sub> molecule at the EDL-vacuum interface and performed geometry optimizations. Calculations without Na<sup>+</sup> cations, that is Ag111-(H<sub>2</sub>O)<sub>24</sub>-CO<sub>2</sub> system were also performed where CO<sub>2</sub> was found to adopt a linear configuration upon geometry optimization. For the Ag111-(Na<sup>+</sup>)<sub>4</sub>-(H<sub>2</sub>O)<sub>24</sub>-CO<sub>2</sub> system, DFT-based geometry optimizations resulted in CO<sub>2</sub> adapting to a bent configuration and involved in hydrogen bonding with protons from H<sub>2</sub>O moieties.

### 6.2.3. *Ab initio* molecular dynamics simulations (aiMD)

We further added 37 additional water molecules to solvate the entire supercell optimized *via* DFT. This system comprising Ag111-4Na<sup>+</sup>-(H<sub>2</sub>O)<sub>61</sub>-CO<sub>2</sub> was used for aiMD simulations in an NVT ensemble at 360 K using the Nose-Hoover thermostat. The BLYP exchange-correlation (XC) functional was used for aiMD simulations. This combination of the XC functional and simulation temperature provides a better description of the structure and dynamics of water and a lower computational cost.<sup>33,57–61</sup> We reran a part of the constrained aiMD simulations using the PBE functional which resulted in a similar barrier as obtained with the BLYP functional. Grimme’s D3 method with Becke–Johnson damping (D3(BJ)) was used for the van der Waals correction.<sup>55,56</sup> To generate a first guess of the Gibbs free energy profile slow-growth approach (SGA) simulations were performed to traverse the Gibbs free energy surface from the reactant to the product state via the transition state using a reaction coordinate (Q) defined via a collective variable (bond lengths; bond angle etc.).<sup>62–64</sup> To further refine the Gibbs free energy profile, several intermediate values of Q were chosen and subjected to long (> 10 ps) constrained (fixed value of Q) aiMD simulations. In all aiMD simulations, constrained and unconstrained, we used an integrator time step of 1 fs. The average force (F) required

to maintain the constraint was computed on an equilibrated trajectory via the bluemoon sampling method. The convergence of the force required to maintain the constraint was visually checked by plotting the force profiles for the last 5 ps of the simulation trajectory for each constrained aiMD run. The average force calculated on the last 1 ps of the equilibrated trajectory was integrated from the reactant (Q<sub>i</sub>) to product (Q<sub>f</sub>) state to obtain the corresponding Gibbs free energy change ( $\Delta G$ ):

$$\Delta G_{Q_i \rightarrow Q_f} = \int_{Q_i}^{Q_f} F \cdot dQ. \quad (\text{E6.1})$$

### 6.3. Results and discussion

#### 6.3.1. Molecular structure of the EDL

To rationally construct an atomistic operando model of the cathode-electrolyte interface under the reaction conditions, the formation and structure of the EDL at the Ag111 surface were first investigated by classical molecular dynamics (CMD) simulations. The electrocatalytic system was modelled as an aqueous electrolyte containing 0.86 M KCl and 0.06 M CO<sub>2</sub>, confined between two Ag111 slabs (model cathode and the anode) in a supercell of dimensions 33.1 x 37.2 x 265.5 Å<sup>3</sup> periodic in the x and y direction (**Figure 6.2a**). These simulations aimed to probe the formation of the EDL at the electrodes under different polarization conditions. The polarization conditions were mimicked by placing uniform distributions of point charges behind the Ag111 slabs resulting in negative (cathode) and positive (anode) surface charge densities on the electrolyte-facing surfaces.

The CMD simulations of the extended electrocatalyst system representing the electrochemical cell revealed the formation of a dense EDL at the cathode as the polarization was increased (**Figure 6.2**). The density of water oscillates within 1 nm of the cathode surface indicating the formation of ordered layers of solvation, while it was found to be constant at 1 kg m<sup>-3</sup> in the bulk phase. Simulations show a deeper penetration of water molecules into the outer Helmholtz plane (OHP; indicated by the dashed line at 1 Å from the electrode) of the cathode compared to the anode. K<sup>+</sup> ions accumulated near the cathode while Cl<sup>-</sup> anions accumulated at the anode and their respective concentrations in the EDL region increased with increasing surface polarization. This effectively resulted in compacting of the EDL and the associated depletion of the CO<sub>2</sub> near the electrocatalyst surface. The latter is fully covered by solvated alkali cations, which can be further considered as the reactive sites for CO<sub>2</sub> activation instead of the bare metal surface.

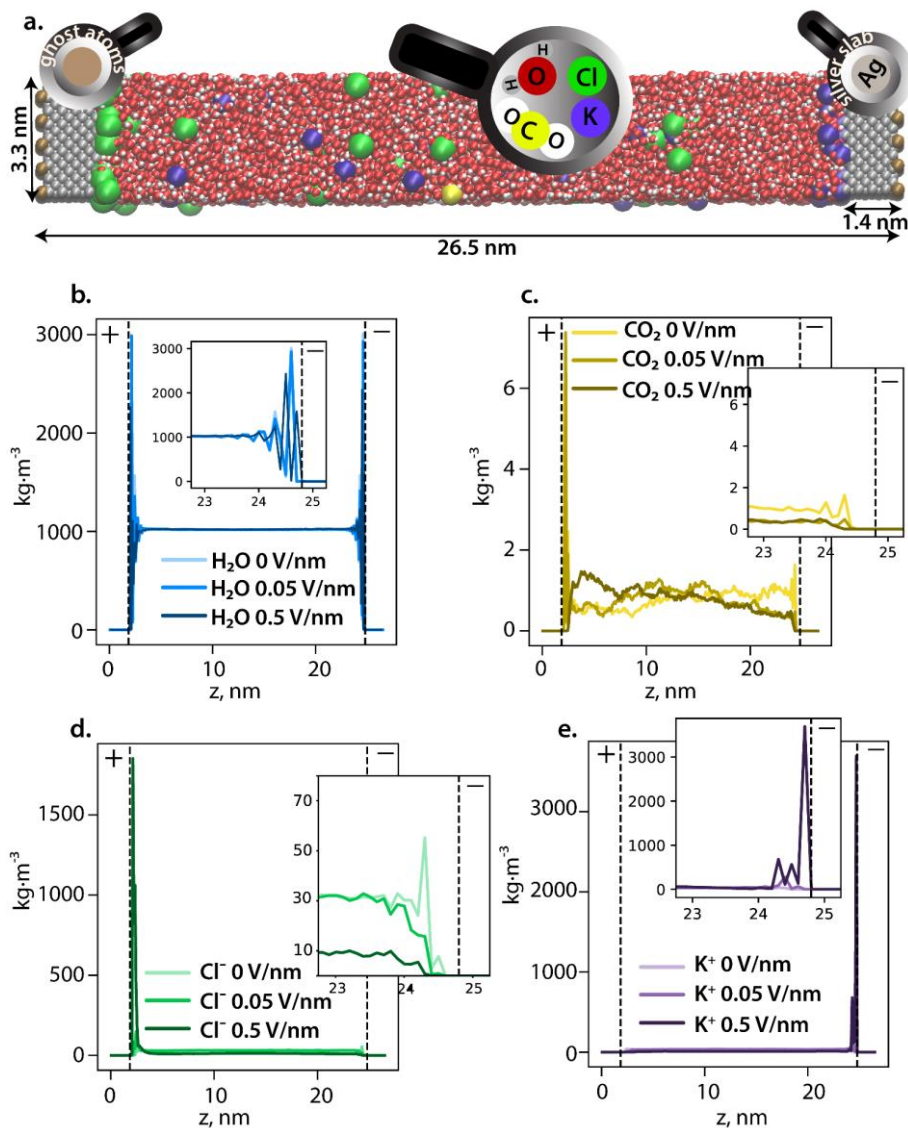


**Figure 6.2** (a) A snapshot of the model of the KCl electrolyte with CO<sub>2</sub> confined between two silver slabs simulated at 0.5 V/nm. The surface on the left represents the anode, with positive ghost charges imposed behind the wall, while the right surface represents the cathode, with negative ghost charges imposed behind the wall. The color code is as follows: silver is grey, oxygen is red, hydrogen is white, potassium is violet, chlorine is green, carbon of CO<sub>2</sub> is yellow, and the ghost atoms are light brown. b-e. Density profile of H<sub>2</sub>O (b), CO<sub>2</sub> (c), Cl<sup>-</sup> (d), K<sup>+</sup> (e), and under increasing polarization conditions represented by the electric field at the surface of the electrode. At low or zero polarization most of the ions are present in the bulk phase. With increasing polarization, the respective densities of K<sup>+</sup> at the cathode and Cl<sup>-</sup> at the anode show a sharp increase leading to the formation of compact EDLs at the respective electrodes.

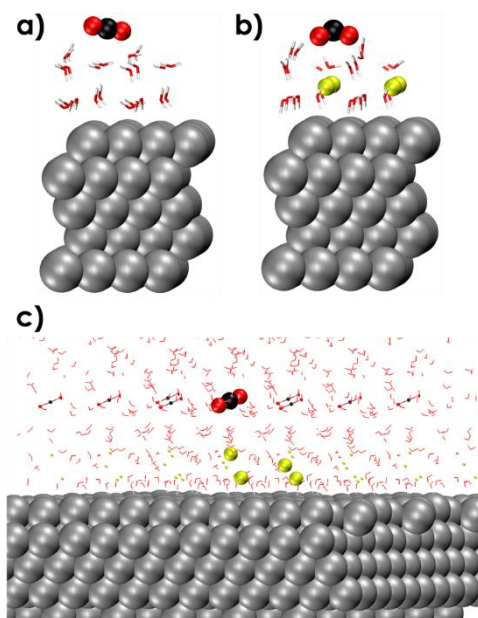


**Figure 6.3** DFT optimized molecular models of 4x4x5 Ag111 slab with one CO<sub>2</sub> molecule in vacuum over (a) Ag111-water interface (b) Ag111-EDL interface (EDL = (Na<sup>+</sup>)<sub>4</sub>(H<sub>2</sub>O)<sub>24</sub>) (c) fully solvated and periodic (in x, y and z directions) system used for aiMD simulations composed of 4 x 4 x 5 Ag111 slab, 4Na<sup>+</sup> cations and 61 water molecules. Periodic images have also been shown. The CO<sub>2</sub> and Na<sup>+</sup> species in the original simulation cell are shown as larger VdW spheres. Color code: C (black), Ag (silver), O (red), Na (Yellow), and H (white).

### 6.3.2. Modelling the outer-sphere CO<sub>2</sub>RR

The outer-sphere reduction of CO<sub>2</sub> over the solvated Ag111 surface was next investigated with periodic density functional theory (DFT) calculations. The reactive events were simulated using a smaller molecular model representing the reaction environment near the Ag111 cathode (4 x 4 x 5 slab model). The initial static DFT calculations on the simplified models revealed the critical role of the EDL for the outer-sphere charge transfer elicited indirect reduction of CO<sub>2</sub>. Indeed, the interaction of CO<sub>2</sub> with an aqueous solvation layer on Ag111 is very weak and does not lead to notable perturbations of the adsorbed molecules (Ag111-(H<sub>2</sub>O)<sub>24</sub>-CO<sub>2</sub>, **Figure 6.3a**). The situation drastically changes upon the introduction of sodium ions and the formation of the EDL (Ag111-(Na<sup>+</sup>)<sub>4</sub>-(H<sub>2</sub>O)<sub>24</sub>-CO<sub>2</sub>, **Figure 6.3b**), which facilitates the reduction of CO<sub>2</sub>. The CO<sub>2</sub> molecule in this case adopts a bent configuration due to the partial charge transfer from the silver slab. The bent anionic CO<sub>2</sub> moiety is stabilized by hydrogen bonding with the neighboring H<sub>2</sub>O molecules.

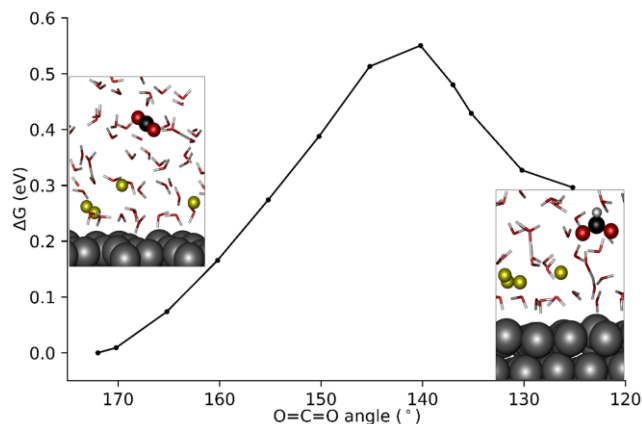


**Figure 6.4** Computed Gibbs free energy profile for homogeneous reduction of  $\text{CO}_2$  to formate using  $\angle\text{O}=\text{C}=\text{O}$  angle as the reaction coordinate.

To better investigate the outer-sphere ET and the subsequent conversions of  $\text{CO}_2$  over the EDL, an extended fully solvated model was employed containing ( $\text{Ag111-4Na}^+(\text{H}_2\text{O})_{61}\text{-CO}_2$ , **Figure 6.3c**) in combination with aiMD simulations. The reactive environment was simulated with a 19 ps long aiMD simulation of  $\text{CO}_2$  in the solvated phase over the Ag111-EDL interface.  $\text{CO}_2$  was found to preferentially stay in the 3<sup>rd</sup> and 4<sup>th</sup> water layers of solvation at about 10 Å from the Ag111 surface. The average  $\text{O}=\text{C}=\text{O}$  angle was  $\sim 172^\circ$  during the runs. Two of the four  $\text{Na}^+$  cations forming the EDL were found at about  $\sim 3$  Å from the surface while the other two  $\text{Na}^+$  cations were located further away at  $\sim 5$  Å and on the Ag111 surface (**Figure 6.3c**).<sup>11</sup> The water molecules within the EDL close to the surface facet were found to show limited mobility. They pointed their protons towards the metal surface during the simulations. In the absence of the EDL, the water molecules preferentially oriented with O moieties pointed towards the Ag111 surface (**Figure 6.3a**). Next, constrained aiMD simulations were carried out on 11 intermediate states representing different stages of the outer-sphere ET  $\text{CO}_2\text{RR}$ . The  $\text{O}=\text{C}=\text{O}$  angle was chosen as the reaction coordinate (Q), and it was varied from  $172^\circ$  to  $125^\circ$ . The resulting Gibbs free energy profile along with the representative snapshots of the relevant reactant and product configurations are presented in **Figure 6.4**.

The constrained aiMD simulations revealed that upon bending, the  $\text{CO}_2$  moiety diffused closer to the EDL. The transition state was located between  $\text{O}=\text{C}=\text{O}$  angles of  $140^\circ$  -  $145^\circ$  (**Figure 6.4**). Releasing the constraint at  $\angle\text{O}=\text{C}=\text{O} = 140^\circ$  directly results in the formation of formate product. The activation free energy barrier for the outer-sphere  $\text{CO}_2\text{RR}$  is 0.55 eV with reference to the linear  $\text{CO}_2$  molecule.

Bader charge analysis at  $Q = 140^\circ$  (equilibrated supercell at  $\sim 18$  ps) revealed a net atomic charge of -0.80 on the  $\text{CO}_2$  moiety. This is comparable to the Bader net atomic

charge of -0.74 units computed for the 1e<sup>-</sup> reduced CO<sub>2</sub> radical in water (see **Appendix A6** and ref 65). Therefore, the bent CO<sub>2</sub> moiety at 140° represents a 1e<sup>-</sup> reduced CO<sub>2</sub> radical. Upon further bending the transient radical species accepts an H<sup>+</sup> by the C site from the solvent simultaneously with the second ET to yield the formate product. A snapshot of proton transfer at ∠O=C=O = 137° is shown in section in **Appendix A6**. Three water molecules coordinated to a Na<sup>+</sup> in the EDL are actively involved during the proton transfer via H-bonding interactions. The bent CO<sub>2</sub> moiety is strongly solvated forming 5 H-bonds.

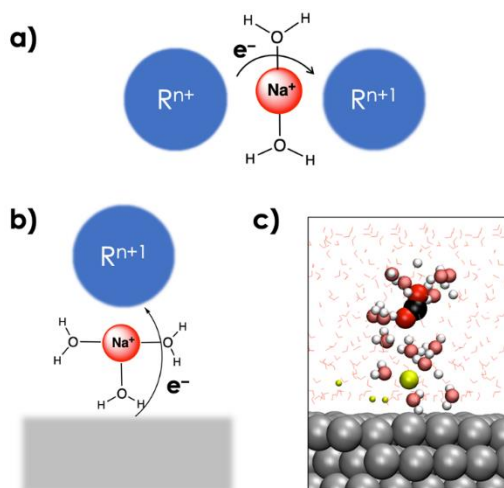


**Figure 6.5** (a) Schematic representation of alkali cation promoted outer-sphere ET between two species in the homogenous phase. (b) Proposed schematic representation of alkali cation mediated outer-sphere ET from a cathode surface to a species in the homogeneous phase. (c) Snapshot of an aiMD trajectory with O=C=O angle constrained at 140° showing the interaction between a solvated cation in the EDL and the solvated CO<sub>2</sub> moiety analogous to the schematic depiction in b). VdW representation is used for the CO<sub>2</sub> moiety interacting with a solvated Na<sup>+</sup> cation along with their first solvation shells which are shown in brushed metal colors. Other Na<sup>+</sup> cations are shown as smaller spheres, and water molecules are shown via line representation. Periodic images have also been included.

The interaction with the EDL is critical for the reduction of CO<sub>2</sub> and can be compared with cation-mediated outer-sphere ET among species in the homogeneous phase (**Figure 6.5a**).<sup>66</sup> In the homogeneous phase solvated alkali cations have been reported to mediate outer-sphere ET between two species.<sup>66</sup> AiMD simulations show that the solvated cations in the EDL can facilitate a similar outer-sphere ET between the cathode surface and CO<sub>2</sub> (**Figure 6.5b,c**). The critical role of the EDL in facilitating the CO<sub>2</sub>RR was further highlighted by the slow-growth approach (SGA) simulations that slowly bent the CO<sub>2</sub> moiety when it was located far away from the EDL. In the absence of interaction of CO<sub>2</sub> with the EDL, bending the CO<sub>2</sub> moiety resulted in the formation of the HCO<sub>3</sub><sup>-</sup> species by

nucleophilic attack of water suggesting the importance of the EDL in facilitating the electroreduction (see **Appendix A6**).

The formate species formed via the outer sphere ET mechanism can undergo dehydration to form CO, which is expected to be favored by low pH conditions near the EDL.<sup>67</sup> Dehydration of formic acid/formate in acidic conditions is well-established chemistry. Consistently, aiMD simulations revealed similar free energy barriers for dehydration of formate in the solvated phase to CO in the presence of EDL (Ag111-4Na<sup>+</sup>-(H<sub>2</sub>O)<sub>61</sub>-CO<sub>2</sub> system; 1.19 eV), and without the EDL (Ag111-(H<sub>2</sub>O)<sub>61</sub>-CO<sub>2</sub> system; 1.26 eV) (see **Appendix A6**). The presence of EDL attributes a small stabilization (0.07 eV) to the dehydration TS. The dehydration of formate to CO is expected to be more favorable with larger cations such as K<sup>+</sup> and Cs<sup>+</sup> where the pH near the EDL is lower.<sup>67</sup>

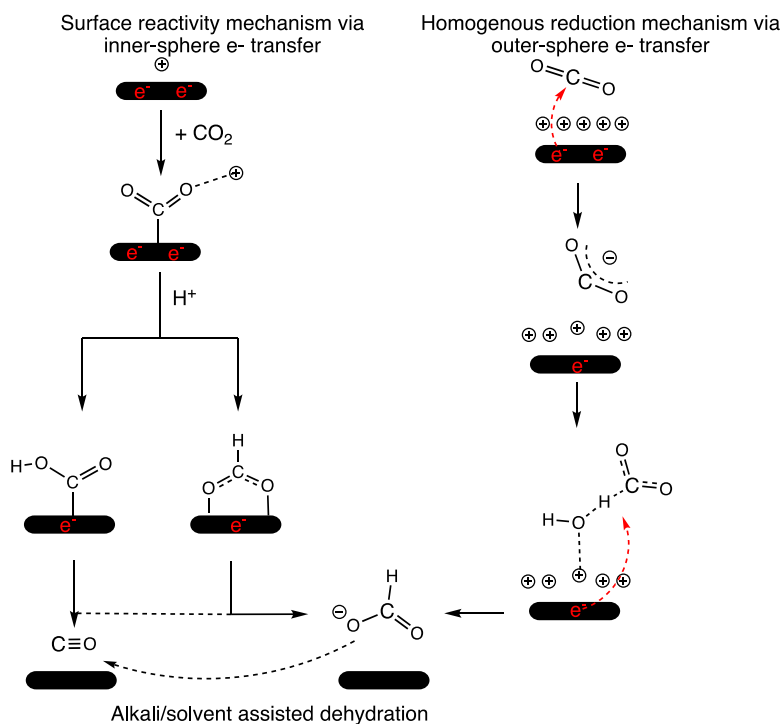
Experimental results for CO<sub>2</sub>RR over Ag show that at high cathodic bias the hydrogen evolution reaction outcompetes the formation of CO. Jaramillo and co-workers showed that the partial current density for the formation of H<sub>2</sub> exceeds that of CO at cathodic potentials below -1.3 V (RHE).<sup>68</sup> The rate of formation of CO peaks around -1.1 V (RHE) and then decreases as the potential is lowered. Further analysis revealed that the decrease in CO formation was due to mass transport limitations. Both formate and CO require CO<sub>2</sub> to reach the cathode surface for the CO<sub>2</sub>RR to proceed via an inner-sphere ET mechanism. Therefore, the rate of formate production is also expected to decrease around the same potential where CO production dips due to mass transport limitations. Contrastingly, the partial current density of formate, although always lower than CO and H<sub>2</sub> kept growing as the cathodic bias was decreased.

An outer-sphere ET mechanism, which does not require mass transport of CO<sub>2</sub> to the surface, can explain the increasing partial formate current density. At moderate to low cathodic bias, CO<sub>2</sub> can reach the surface, and its adsorption is stabilized by the EDL<sup>14,15</sup> leading to the production of CO (kinetically favored) and HCOO<sup>-</sup> (less favored). Thus, the current density for CO and HCOO<sup>-</sup> both increase as the applied voltage is lowered. At high cathodic bias the current density switches from kinetic control to mass transport limitations leading to decreased CO production. We suggest the mass transport limitations (at least partially) result from a condensed EDL rather than only solubility and diffusion of CO<sub>2</sub> in the electrolyte. CO<sub>2</sub> is therefore available in the region close to the EDL and gets reduced to formate via an outer-sphere ET mechanism, which explains the increasing formate current density.

To gain further insight into HCOO<sup>-</sup> versus CO production we compare the free energy barriers for CO formation (inner-sphere ET) reported in the literature versus HCOO<sup>-</sup> formation (outer-sphere ET) as computed by us. Based on the results reported by Chen and co-workers for CO<sub>2</sub>RR over Ag111 surface in the presence of a model EDL, a free energy barrier of 0.52 eV can be estimated for the surface-mediated CO formation at

an applied external potential of -1 V (SHE) at pH = 7.<sup>14</sup> The current aiMD-computed free energy barrier of 0.55 eV at -1.45 V (SHE) (~ 1 V versus the PZC)<sup>69</sup> reflects a relatively higher barrier for the CO<sub>2</sub>RR via the outer sphere ET, explaining the lower partial current density for formate.

Therefore, we propose that the mechanism of 2e<sup>-</sup> reduction of CO<sub>2</sub> is dependent on the applied bias. **Scheme 6.1** summarizes the outer- and inner- sphere 2e<sup>-</sup> mechanisms to produce CO and formate via CO<sub>2</sub>RR. Jaramillo and co-workers also demonstrated the formation of >2e<sup>-</sup> reduction products of CO<sub>2</sub>RR over Ag at high overpotentials<sup>68</sup> and an outer-sphere ET could potentially be involved in those mechanistic steps as well.



**Scheme 6.1** Mechanism of CO<sub>2</sub>RR over a cathode surface via Inner- and outer-sphere electron transfer. 2e<sup>-</sup> that originate from the cathode surface and reduce the CO<sub>2</sub> moiety are shown in red for a representative purpose. The cathode surface is maintained at a constant potential in the electrolyzer.

## 6.4. Conclusions

In this chapter, we have explored the CO<sub>2</sub>RR over the Ag111 surface via an outer-sphere ET mechanism. Following a multiscale *operando* modelling strategy, we first simulated the multi-component electrolyte-cathode interface under various applied

potentials. Investigation of density profiles of water, ions and CO<sub>2</sub> revealed the formation of a condensed EDL within 1 nm of the cathode surface composed of cations and ordered layers of solvation at high overpotentials. This finding motivated the development of a smaller periodic model of the cathode-electrolyte interface which was used to investigate the reactive events during CO<sub>2</sub>RR at high cathodic potentials via aiMD simulations. AiMD simulations showed that an outer-sphere ET mechanism resulted in the formation of formate species over the EDL. The formate species was further shown to undergo alkali-promoted dehydration to CO with a moderate free energy barrier of 1.19 eV. The presence of EDL was found to be the key to promote an outer-sphere ET CO<sub>2</sub>RR mechanism.

The outer-sphere ET CO<sub>2</sub>RR is a plausible mechanism to produce formate and CO under high cathodic bias. Surface-based, alkali-promoted CO<sub>2</sub>RR is likely still the dominant mechanism for the formation of CO. Our calculations show that an alternative reaction channel to reduce CO<sub>2</sub> is accessible in the presence of a dense EDL, and the reaction mechanism is a complex network of voltage-dependent inner- and outer-sphere ET steps. Outer-sphere mechanisms should be further explored for heterogeneous electrocatalytic systems and can be especially relevant for electrocatalytic reduction of organic substrates which occur under high voltage conditions.

## 6.5. References

1. van Bavel, S., Verma, S., Negro, E. & Bracht, M. Integrating CO<sub>2</sub> electrolysis into the gas-to-liquids–power-to-liquids process. *ACS Energy Lett.* **5**, 2597–2601 (2020).
2. Olah, G. A., Goepfert, A. & Prakash, G. K. S. Beyond Oil and Gas: The Methanol Economy: Second Edition. *Beyond Oil Gas Methanol Econ. Second Ed.* **44**, 1–334 (2009).
3. Zhang, S., Fan, Q., Xia, R. & Meyer, T. J. CO<sub>2</sub> Reduction: From Homogeneous to Heterogeneous Electrocatalysis. *Acc. Chem. Res.* **53**, 255–264 (2020).
4. Quan, Y., Zhu, J. & Zheng, G. Electrocatalytic Reactions for Converting CO<sub>2</sub> to Value-Added Products. *Small Sci.* **1**, 2100043 (2021).
5. Pei, Y., Zhong, H. & Jin, F. A brief review of electrocatalytic reduction of CO<sub>2</sub>—Materials, reaction conditions, and devices. *Energy Sci. Eng.* **9**, 1012–1032 (2021).
6. Mahyoub, S. A. *et al.* An overview on the recent developments of Ag-based electrodes in the electrochemical reduction of CO<sub>2</sub> to CO. *Sustain. Energy Fuels* **4**, 50–67 (2019).
7. Hori, Y., Wakebe, H., Tsukamoto, T. & Koga, O. Electrocatalytic process of CO selectivity in electrochemical reduction of CO<sub>2</sub> at metal electrodes in aqueous media. *Electrochim. Acta* **39**, 1833–1839 (1994).
8. Xi, C. *et al.* Distribution of alkali cations near the Cu (111) surface in aqueous solution. *J. Mater. Chem. A* **8**, 24428–24437 (2020).
9. Resasco, J. *et al.* Promoter Effects of Alkali Metal Cations on the Electrochemical Reduction of Carbon Dioxide. *J. Am. Chem. Soc.* **139**, 11277–11287 (2017).
10. Gu, J. *et al.* Modulating electric field distribution by alkali cations for CO<sub>2</sub> electroreduction in strongly acidic medium. *Nat. Catal.* **5**, 268–276 (2022).
11. Waegle, M. M., Gunathunge, C. M., Li, J. & Li, X. How cations affect the electric double layer and the rates and selectivity of electrocatalytic processes. *J. Chem. Phys.* **151**, 1DUMMT (2019).
12. Ringe, S. *et al.* Understanding cation effects in electrochemical CO<sub>2</sub> reduction. *Energy Environ. Sci.*

- 12**, 3001–3014 (2019).
13. Briega-Martos, V., Sarabia, F. J., Climent, V., Herrero, E. & Feliu, J. M. Cation Effects on Interfacial Water Structure and Hydrogen Peroxide Reduction on Pt(111). *ACS Meas. Sci. Au* **1**, 48–55 (2021).
  14. Chen, L. D., Urushihara, M., Chan, K. & Nørskov, J. K. Electric Field Effects in Electrochemical CO<sub>2</sub> Reduction. *ACS Catal.* **6**, 7133–7139 (2016).
  15. Monteiro, M. C. O. *et al.* Absence of CO<sub>2</sub> electroreduction on copper, gold and silver electrodes without metal cations in solution. *Nat. Catal.* **4**, 654–662 (2021).
  16. Zhong, J., Han, J., Wei, Y. & Liu, Z. Catalysts and shape selective catalysis in the methanol-to-olefin (MTO) reaction. *J. Catal.* **396**, 23–31 (2021).
  17. Bohra, D., Chaudhry, J. H., Burdyny, T., Pidko, E. A. & Smith, W. A. Correction: Modeling the electrical double layer to understand the reaction environment in a CO<sub>2</sub> electrocatalytic system. *Energy Environ. Sci.* **12**, 3608 (2019).
  18. Goyal, A., Marcandalli, G., Mints, V. A. & Koper, M. T. M. Competition between CO<sub>2</sub> Reduction and Hydrogen Evolution on a Gold Electrode under Well-Defined Mass Transport Conditions. *J. Am. Chem. Soc.* **142**, 4154–4161 (2020).
  19. Ješić, D., Lašić Jurković, D., Pohar, A., Suhadolnik, L. & Likozar, B. Engineering photocatalytic and photoelectrocatalytic CO<sub>2</sub> reduction reactions: Mechanisms, intrinsic kinetics, mass transfer resistances, reactors and multi-scale modelling simulations. *Chem. Eng. J.* **407**, 126799 (2021).
  20. Wang, Y., Liu, J., Wang, Y., Al-Enizi, A. M. & Zheng, G. Tuning of CO<sub>2</sub> Reduction Selectivity on Metal Electrocatalysts. *Small* **13**, 1701809 (2017).
  21. Cave, E. R. *et al.* Electrochemical CO<sub>2</sub> reduction on Au surfaces: Mechanistic aspects regarding the formation of major and minor products. *Phys. Chem. Chem. Phys.* **19**, 15856–15863 (2017).
  22. Nitopi, S. *et al.* Progress and Perspectives of Electrochemical CO<sub>2</sub> Reduction on Copper in Aqueous Electrolyte. *Chem. Rev.* **119**, 7610–7672 (2019).
  23. Sun, Z., Ma, T., Tao, H., Fan, Q. & Han, B. Fundamentals and Challenges of Electrochemical CO<sub>2</sub> Reduction Using Two-Dimensional Materials. *Chem* **3**, 560–587 (2017).
  24. Saeidi, S. *et al.* Mechanisms and kinetics of CO<sub>2</sub> hydrogenation to value-added products: A detailed review on current status and future trends. *Renew. Sustain. Energy Rev.* **80**, 1292–1311 (2017).
  25. Xu, S. & Carter, E. A. Theoretical Insights into Heterogeneous (Photo)electrochemical CO<sub>2</sub> Reduction. *Chem. Rev.* **119**, 6631–6669 (2019).
  26. Bohra, D. *et al.* Lateral Adsorbate Interactions Inhibit HCOO<sup>-</sup> while Promoting CO Selectivity for CO<sub>2</sub> Electrocatalysis on Silver. *Angew. Chem.* **131**, 1359–1363 (2019).
  27. Fey, N. & Lynam, J. M. Computational mechanistic study in organometallic catalysis: Why prediction is still a challenge. *Wiley Interdiscip. Rev. Comput. Mol. Sci.* **12**, e1590 (2022).
  28. Gauthier, J. A. *et al.* Challenges in Modeling Electrochemical Reaction Energetics with Polarizable Continuum Models. *ACS Catal.* **9**, 920–931 (2019).
  29. Varghese, J. J. & Mushrif, S. H. Origins of complex solvent effects on chemical reactivity and computational tools to investigate them: A review. *React. Chem. Eng.* **4**, 165–206 (2019).
  30. Saleheen, M. & Heyden, A. Liquid-Phase Modeling in Heterogeneous Catalysis. *ACS Catal.* **8**, 2188–2194 (2018).
  31. Harvey, J. N., Himo, F., Maseras, F. & Perrin, L. Scope and Challenge of Computational Methods for Studying Mechanism and Reactivity in Homogeneous Catalysis. *ACS Catal.* **9**, 6803–6813 (2019).
  32. Govindarajan, N. *et al.* An In-Depth Mechanistic Study of Ru-Catalysed Aqueous Methanol Dehydrogenation and Prospects for Future Catalyst Design. *ChemCatChem* **12**, 2610–2621 (2020).
  33. Sinha, V., Sun, D., Meijer, E. J., Vlucht, T. J. H. & Bieberle-Hutter, A. A multiscale modelling approach to elucidate the mechanism of the oxygen evolution reaction at the hematite-water interface. *Faraday Discuss.* **229**, 89–107 (2021).
  34. Weitzner, S. E. *et al.* Toward Engineering of Solution Microenvironments for the CO<sub>2</sub> Reduction Reaction: Unraveling pH and Voltage Effects from a Combined Density-Functional-Continuum Theory. *J. Phys. Chem. Lett.* **11**, 4113–4118 (2020).
  35. Krieger, A. M., Kuliaev, P., Armstrong Hall, F. Q., Sun, D. & Pidko, E. A. Composition- A nd

- Condition-Dependent Kinetics of Homogeneous Ester Hydrogenation by a Mn-Based Catalyst. *J. Phys. Chem. C* **124**, 26990–26998 (2020).
36. Meeprasert, J., Li, G. & Pidko, E. A. Mechanistic investigation of benzene esterification by  $K_2CO_3/TiO_2$ : The catalytic role of the multifunctional interface. *Chem. Commun.* **57**, 7890–7893 (2021).
  37. Krieger, A. M. & Pidko, E. A. The Impact of Computational Uncertainties on the Enantioselectivity Predictions: A Microkinetic Modeling of Ketone Transfer Hydrogenation with a Noyori-type Mn-diamine Catalyst. *ChemCatChem* **13**, 3517–3524 (2021).
  38. van Schendel, R. K. A., Yang, W., Uslamin, E. A. & Pidko, E. A. Utilizing Design of Experiments Approach to Assess Kinetic Parameters for a Mn Homogeneous Hydrogenation Catalyst. *ChemCatChem* **13**, 4886–4896 (2021).
  39. Kovalenko, A. & Neburchilov, V. Density functional theory and 3D-RISM-KH molecular theory of solvation studies of  $CO_2$  reduction on Cu-,  $Cu_2O$ -, Fe-, and  $Fe_3O_4$ -based nanocatalysts. *J. Mol. Model.* **26**, 267 (2020).
  40. Gauthier, J. A. *et al.* Facile Electron Transfer to  $CO_2$  during Adsorption at the Metal|Solution Interface. *J. Phys. Chem. C* **123**, 29278–29283 (2019).
  41. Zhong, H., Fujii, K. & Nakano, Y. Effect of  $KHCO_3$  Concentration on Electrochemical Reduction of  $CO_2$  on Copper Electrode. *J. Electrochem. Soc.* **164**, F923–F927 (2017).
  42. Tranchida, J., Plimpton, S. J., Thibaudeau, P. & Thompson, A. P. Massively parallel symplectic algorithm for coupled magnetic spin dynamics and molecular dynamics. *J. Comput. Phys.* **372**, 406–425 (2018).
  43. Berendsen, H. J. C., Grigera, J. R. & Straatsma, T. P. The missing term in effective pair potentials. *J. Phys. Chem.* **91**, 6269–6271 (1987).
  44. Dezfoli, A. A., Mehrabian, M. A. & Hashemipour, H. Molecular Dynamics Simulation of Heavy Metal Ions in Aqueous Solution Using Lennard-Jones 12-6 Potential. *Chem. Eng. Commun.* **202**, 1685–1692 (2015).
  45. Mester, Z. & Panagiotopoulos, A. Z. Temperature-dependent solubilities and mean ionic activity coefficients of alkali halides in water from molecular dynamics simulations. *J. Chem. Phys.* **143**, 44505 (2015).
  46. Heinz, H., Vaia, R. A., Farmer, B. L. & Naik, R. R. Accurate simulation of surfaces and interfaces of face-centered cubic metals using 12-6 and 9-6 Lennard-Jones potentials. *J. Phys. Chem. C* **112**, 17281–17290 (2008).
  47. Chowdhuri, S. & Chandra, A. Molecular dynamics simulations of aqueous NaCl and KCl solutions: Effects of ion concentration on the single-particle, pair, and collective dynamical properties of ions and water molecules. *J. Chem. Phys.* **115**, 3732–3741 (2001).
  48. Nielsen, L. C., Bourg, I. C. & Sposito, G. Predicting  $CO_2$ -water interfacial tension under pressure and temperature conditions of geologic  $CO_2$  storage. *Geochim. Cosmochim. Acta* **81**, 28–38 (2012).
  49. Michaud-Agrawal, N., Denning, E. J., Woolf, T. B. & Beckstein, O. MDAAnalysis: A toolkit for the analysis of molecular dynamics simulations. *J. Comput. Chem.* **32**, 2319–2327 (2011).
  50. Döpke, M. F. maicos\_delft [https://gitlab.com/mdopke/maicos\\_delft](https://gitlab.com/mdopke/maicos_delft). (2022).
  51. Perdew, J. P., Burke, K. & Ernzerhof, M. Generalized gradient approximation made simple. *Phys. Rev. Lett.* **77**, 3865–3868 (1996).
  52. Blöchl, P. E. Projector augmented-wave method. *Phys. Rev. B* **50**, 17953–17979 (1994).
  53. Joubert, D. From ultrasoft pseudopotentials to the projector augmented-wave method. *Phys. Rev. B - Condens. Matter Mater. Phys.* **59**, 1758–1775 (1999).
  54. Kresse, G. & Furthmüller, J. Efficient iterative schemes for *ab initio* total-energy calculations using a plane-wave basis set. *Phys. Rev. B - Condens. Matter Mater. Phys.* **54**, 11169–11186 (1996).
  55. Grimme, S., Antony, J., Ehrlich, S. & Krieg, H. A consistent and accurate *ab initio* parametrization of density functional dispersion correction (DFT-D) for the 94 elements H-Pu. *J. Chem. Phys.* **132**, 154104 (2010).
  56. Grimme, S., Ehrlich, S. & Goerigk, L. Effect of the damping function in dispersion corrected density functional theory. *J. Comput. Chem.* **32**, 1456–1465 (2011).

57. Sprik, M., Hutter, J. & Parrinello, M. *Ab initio* molecular dynamics simulation of liquid water: Comparison of three gradient-corrected density functionals. *J. Chem. Phys.* **105**, 1142–1152 (1996).
58. VandeVondele, J. *et al.* The influence of temperature and density functional models in *ab initio* molecular dynamics simulation of liquid water. *J. Chem. Phys.* **122**, 14515 (2005).
59. Johnson, B. G., Gill, P. M. W. & Pople, J. A. The performance of a family of density functional methods. *J. Chem. Phys.* **98**, 5612–5626 (1993).
60. Lee, C., Yang, W. & Parr, R. G. Development of the Colle-Salvetti correlation-energy formula into a functional of the electron density. *Phys. Rev. B* **37**, 785–789 (1988).
61. Becke, A. D. Density-functional exchange-energy approximation with correct asymptotic behavior. *Phys. Rev. A* **38**, 3098–3100 (1988).
62. Oberhofer, H., Dellago, C. & Geissler, P. L. Biased sampling of nonequilibrium trajectories: Can fast switching simulations outperform conventional free energy calculation methods? *J. Phys. Chem. B* **109**, 6902–6915 (2005).
63. Woo, T. K., Margl, P. M., Blöchl, P. E. & Ziegler, T. A combined Car-Parrinello QM/MM implementation for *ab initio* molecular dynamics simulations of extended systems: Application to transition metal catalysis. *J. Phys. Chem. B* **101**, 7877–7880 (1997).
64. Jarzynski, C. Nonequilibrium equality for free energy differences. *Phys. Rev. Lett.* **78**, 2690–2693 (1997).
65. Sinha, V., Khramenkova, E. & Pidko, E. A. Solvent-mediated outer-sphere CO<sub>2</sub> electro-reduction mechanism over the Ag111 surface. *Chem. Sci.* **13**, 3803–3808 (2022).
66. Metelski, P. D. & Swaddle, T. W. Cation catalysis of anion-anion electron transfer in aqueous solution: Self-exchange reaction kinetics of some hexa- and octacyanometalate couples at variable pressure. *Inorg. Chem.* **38**, 301–307 (1999).
67. Zhang, F. & Co, A. C. Direct Evidence of Local pH Change and the Role of Alkali Cation during CO<sub>2</sub> Electroreduction in Aqueous Media. *Angew. Chem. Int. Ed.* **59**, 1674–1681 (2020).
68. Hatsukade, T., Kuhl, K. P., Cave, E. R., Abram, D. N. & Jaramillo, T. F. Insights into the electrocatalytic reduction of CO<sub>2</sub> on metallic silver surfaces. *Phys. Chem. Chem. Phys.* **16**, 13814–13819 (2014).
69. Valette, G. Double layer on silver single crystal electrodes in contact with electrolytes having anions which are slightly specifically adsorbed: Part III. The (111) face. *J. Electroanal. Chem.* **269**, 191–203 (1989).
70. Krynicki, K., Green, C. D. & Sawyer, D. W. Pressure and temperature dependence of self-diffusion in water. *Faraday Discuss. Chem. Soc.* **66**, 199–208 (1978).
71. Moulτος, O. A., Tsimpanogiannis, I. N., Panagiotopoulos, A. Z. & Economou, I. G. Atomistic molecular dynamics simulations of CO<sub>2</sub> diffusivity in H<sub>2</sub>O for a wide range of temperatures and pressures. *J. Phys. Chem. B* **118**, 5532–5541 (2014).
72. Braun, D., Borech, S. & Steinhauser, O. Transport and dielectric properties of water and the influence of coarse-graining: Comparing BMW, SPC/E, and TIP3P models. *J. Chem. Phys.* **140**, 64107 (2014).

## A.6.1. Molecular dynamics simulations in LAMMPS

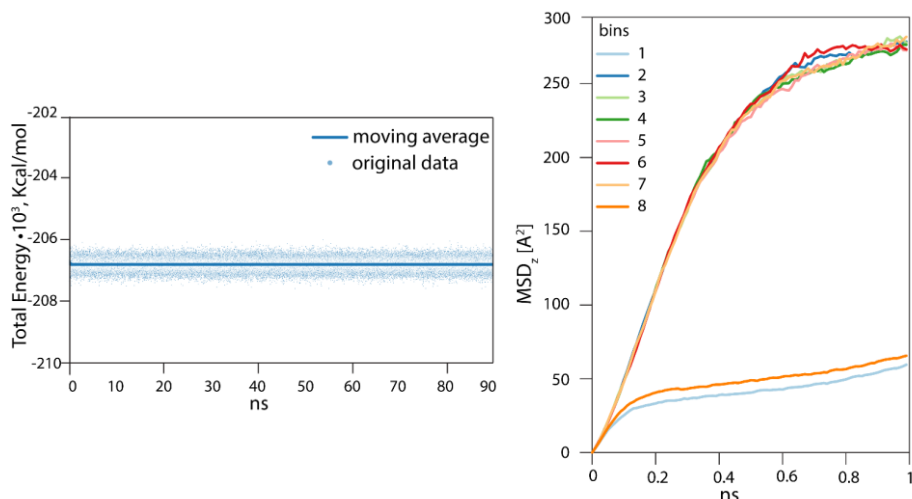


**Figure A6.1** Left: the total energy of the system with no electric field applied during the production run (original data in the scatter plot and the moving average is reflected in the line plot to account for the fluctuations). Right: mean-squared displacement (MSD) of water in 8 bins along the z-direction in the system with no electric field applied. The first and the last bins (1 and 8) represent the area next to electrodes, whereas the other bins represent bulk diffusivity.

To calculate the self-diffusion coefficient of water, we have calculated the mean-squared displacement (MSD). The slope of the linear regression fit of MSD versus simulation time is proportional to the diffusion coefficient. For calculating the ensemble average, we have considered all the water molecules and multiple time origins. To indicate the difference in self-diffusivity in the bulk and next to the anode/cathode, the model was divided into 8 bins.

In **Figure A6.1** (right), we show the MSD versus time plot of water molecules along the z dimension – the longest in the model. The time frame between 20 – 400 ps was used for linear regression of the  $MSD_z$  versus time. As the first and the last bins were located near the electrodes (1 and 8), the self-diffusion coefficient was calculated for the central bins (2 – 7) which represent the bulk diffusivity of water. The calculated diffusion coefficient based on the linear regressions resulted in a mean value of  $2.78 \cdot 10^{-9} \text{ m}^2/\text{s}$  with the standard error of the mean equal to  $0.01 \cdot 10^{-9} \text{ m}^2/\text{s}$  which compares well with the experimental value of  $2.3 \cdot 10^{-9} \text{ m}^2/\text{s}$ ,<sup>70</sup> and CMD simulations of pure water using the SPC/E model at 298 K (in the range of  $2.6 - 3.1 \cdot 10^{-9} \text{ m}^2/\text{s}$  depending on the integrator time-step).<sup>71,72</sup>

**Table A6.1** Short-range pair interaction potentials used in the molecular dynamics simulations.

		$\epsilon$	$\sigma$			$\epsilon$	$\sigma$
Ag	Ag	4.56076	2.6325	Cl	H	0.0	2.2
Ag	C	0.50352	2.69475	Cl	K	0.1	3.8655
Ag	Cl	0.67533	3.51625	Cl	O	0.12464	3.783
Ag	H	0.00000	1.31625	Cl	Oc	0.12645	3.7165
Ag	K	0.67533	2.98175	H	H	0.0	0.0
Ag	O	0.84173	2.89925	H	K	0.0	1.6655
Ag	Oc	0.85394	2.83275	H	O	0.0	1.58300
C	C	0.05593	2.757	H	Oc	0.0	1.5165
C	Cl	0.07479	3.5785	K	K	0.1	3.331
C	H	0.00000	1.3785	K	O	0.12464	3.2485
C	K	0.07479	3.044	K	Oc	0.12645	3.182
C	O	0.09321	2.9615	O	O	0.15535	3.16600
C	Oc	0.09457	2.895	O	Oc	0.15760	3.0995
Cl	Cl	0.1	4.40	Oc	Oc	0.15989	3.033

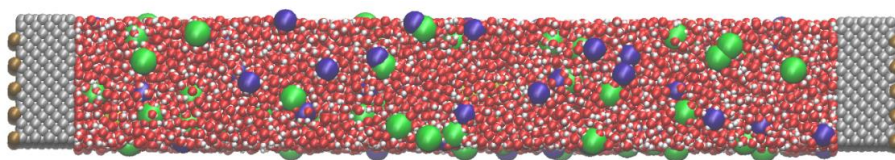


**Figure A6.2** The snapshot of the KCl electrolyte with CO<sub>2</sub> confined between two silver slabs simulated at zero potential. The surface on the left represents the anode, with positive ghost charges imposed behind the wall, while the right surface represents the cathode, with negative ghost charges imposed behind the wall. The color code is the following: silver is grey, oxygen is red, hydrogen is white, potassium is violet, chlorine is green, carbon of CO<sub>2</sub> is yellow, and the ghost atoms are light brown.

The electric field above the silver cathode was imposed by adding the ghost atoms behind the cathode and anode and was calculated according to Gauss's law which relates the distribution of the electric charge to the resulting electric field. The electric flux can be expressed as:

$\Phi_E = \frac{\Theta}{\epsilon_{\text{water}} \cdot \epsilon_{\text{vacuum}}}$ , where  $\Theta$  is the electric charge enclosed and  $\epsilon_{\text{water}}$  is the dielectric constant of water and  $\epsilon_{\text{vacuum}}$  is the dielectric constant of the vacuum. The values of the total induced charge were calculated according to the following:

$$\Theta = 25 \cdot e \cdot q \quad (\text{AE6.1})$$

where  $q$  is the charge assigned to each ghost atom in LAMMPS simulation (for units style real),  $e$  is the electron charge equal to  $1.6 \cdot 10^{-19}$  C and 25 is the number of ghost atoms imposed behind each surface. We have assumed that Ag is a perfect conductor and there

is no charge density trapped in the bulk volume of Ag. We have also assumed that the dielectric constant of water does not change in the EDL.

The magnitude of the electric field passing through the cathode:  $E = \Phi_E/S$ , where  $S$  is the surface area of the cathode, which is assumed to be a rectangular prism.

### A6.2. Analysis of Bader net atomic charges

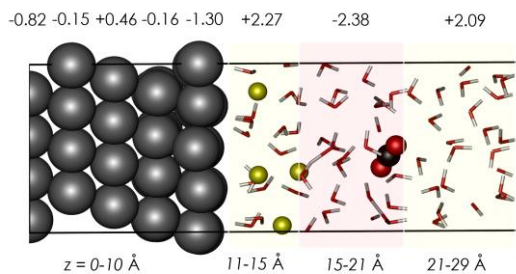


**Figure A6.3** Analysis of Bader net atomic charges for a well equilibrated (19 ps) frame of CO<sub>2</sub> in the solvated phase over EDL-Ag111. The Bader net atomic charges for the five layers of Ag have been shown. The total Bader net atomic charges for various sections in the electrolyte phase have also been shown. The z-coordinate runs from 0 – 30 Å along the length of the simulation cell with 0-10 Å being the Ag111 slab.

### A6.3. Estimation of potential at the cathode

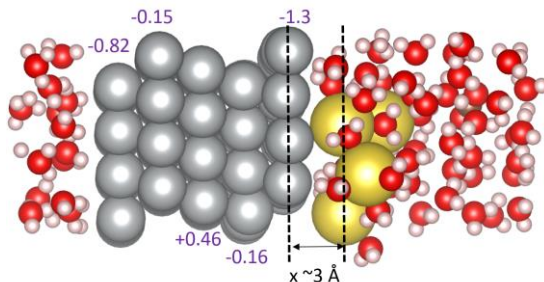


**Figure A6.4** Ag111-EDL system. Total Bader net atomic charges are mentioned for each Ag layer.

The estimated surface potentials are tabulated in **Table A6.2**.

**Table A6.2** Calculated cathode potential at different value of  $q$  and  $C_H$ .

$q$	$\phi - \phi_{pzc}$ (V (SHE)) with $C_H = 18 \mu\text{F cm}^{-2}$	$\phi - \phi_{pzc}$ (V (SHE)) with $C_H = 25 \mu\text{F cm}^{-2}$	$\phi - \phi_{pzc}$ (V (SHE)) with $C_H = 50 \mu\text{F cm}^{-2}$
-1.3	1.0	0.7	0.36
-1.46	1.1	0.8	0.41

#### A6.4. Bicarbonate formation

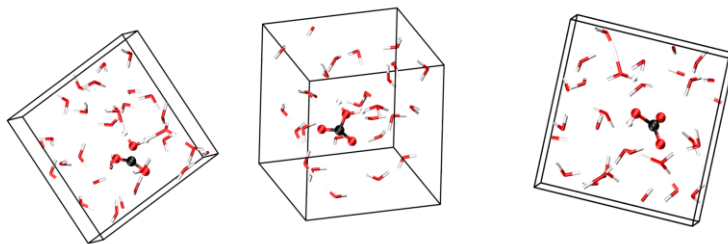


**Figure A6.5** Snapshots from slow-growth approach simulations for the formation of bicarbonate species from CO<sub>2</sub> solvated in a cubic cell with water. The O=C=O angle was used as the reaction coordinate.

#### A6.5. Formate formation during homogeneous CO<sub>2</sub> reduction

An outer-sphere ET would reduce CO<sub>2</sub> in the homogeneous phase. To gain insight into this homogeneous CO<sub>2</sub> reduction we carried out aiMD simulations of CO<sub>2</sub> in water (23 H<sub>2</sub>O and 1 CO<sub>2</sub> per supercell). We performed three simulations: neutral, anionic, and dianionic. The neutral simulation consisted of a solvated CO<sub>2</sub> molecule in a neutral supercell. The introduction of 1e<sup>-</sup> in the neutral simulation resulted in the *anionic* system where the CO<sub>2</sub> molecule was found to bend ( $\langle \angle \text{O}=\text{C}=\text{O} \rangle = 134.3^\circ \pm 3.1^\circ$ ). Both O moieties formed hydrogen bonds with water, and the C moiety was found to have a strong H-bonding interaction but did not get protonated during the simulations (**Figure A6.6a**). The introduction of a second electron led to a doubly negatively charged *dianionic* system where formic acid quickly (within 50 fs of simulation time) formed (**Figure A6.6b,c**). From the aiMD simulations of solvated CO<sub>2</sub>, we conclude that an outer-sphere 2e<sup>-</sup> transfer to CO<sub>2</sub> would drive the formation of formic acid/formate.

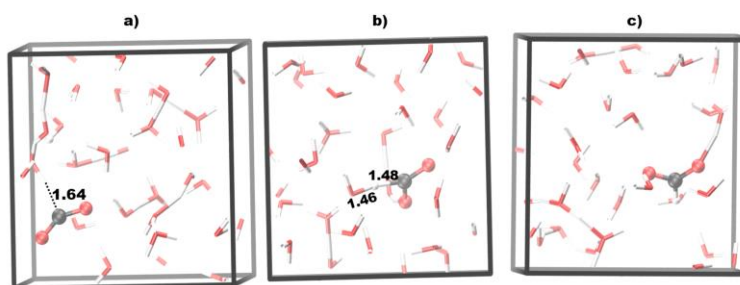


**Figure A6.6** Snapshots of aiMD trajectories: **(a)** the anionic system where CO<sub>2</sub> adopts a bent configuration and is involved in H-bonding with water, **(b)** proton being transferred from water to doubly reduced CO<sub>2</sub> in the dianionic system, and **(c)** formate species formed in the dianionic system. All bond distances are shown in Å units.

### A6.6. Bicarbonate formation in the presence of EDL

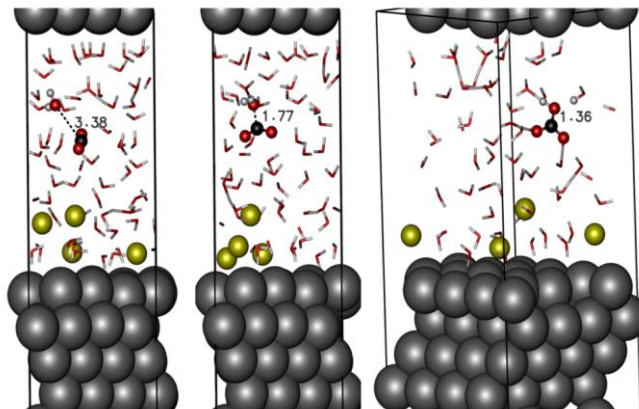


**Figure A6.7** Snapshots from slow-growth approach simulations showing the formation of  $\text{HCO}_3^-$  in Ag111-EDL supercell. The  $\text{O}=\text{C}=\text{O}$  bond angle was used as the reaction coordinate.

### A6.7. Snapshot of proton transfer forming $\text{HCOO}^-$

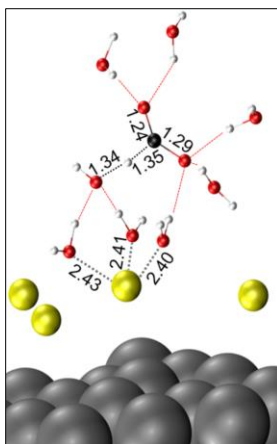


**Figure A6.8** Snapshot from constrained aiMD simulations with  $\text{O}=\text{C}=\text{O}$  angle constrained at  $137^\circ$  showing proton transfer from water to a bent  $\text{CO}_2$  moiety over the EDL. Only the most relevant water molecules have been shown. Bonds involved in the proton transfer are highlighted in dashed black and red (H bonds) lines. Color code: Na: Yellow; Ag: Silver; H: White; O: Red; C: Black.

## A6.8. PBE versus BLYP

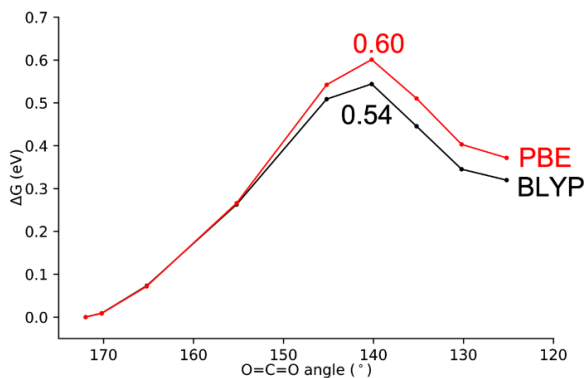
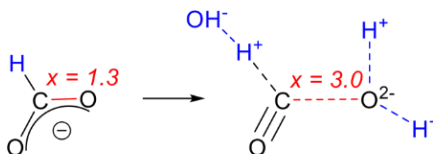


**Figure A6.9** BLYP (black) and PBE (red) computed Gibbs free energy for the reduction of CO<sub>2</sub> to formate via constrained aiMD simulations. The respective free energy barriers are also mentioned. Fewer values of the reaction coordinate (Q) were used here compared to **Figure 6.4** in the main text.

## 6.6.9. Reaction coordinate

### Reaction Coordinate and Gibbs Free Energy: formate dehydration



- Generate several configurations with different values of  $x$
- Run simulations with constrained value of  $x$  until equilibration
- Force ( $F$ ) is required to maintain the constrain, averaged ( $\langle F \rangle$ ) over trajectory for each  $x$
- Compute  $\Delta G = \int_{x=x_i}^{x=x_f} \langle F \rangle dx$

**Figure A6.10** Schematic description of the reaction coordinate and steps involved in the constrained aiMD simulations for dehydration of formate to CO.

## 6.6.10. Gibbs free energy profile

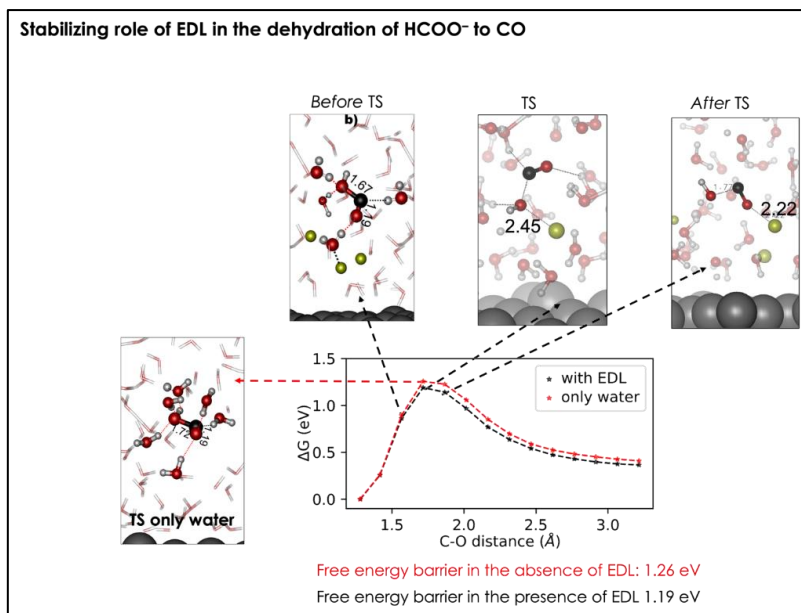


**Figure A6.11** Computed Gibbs free energy profiles for the dehydration of formate assisted by the EDL (black) and unassisted (red). Snapshots of intermediates and TS have been included.

---

---

## Summary

---

---

In this thesis, we have presented and investigated the possible strategies for modelling complex heterogeneous catalytic systems in *operando* regimes. By introducing modern computational approaches to sample the potential energy surface of the catalytic active site, we have attempted to account for the reactive conditions, solvent presence, additives inclusion, and structural dynamics of the active site. There is growing spectroscopic and theoretical evidence of the critical role of the active site dynamics for the catalytic performance, advocating for the active site representation as an ensemble of possible isomers. Challenged by the complexity of the reactive environment and common heterogeneous catalysts, we strongly believe that addressing these factors and incorporating them explicitly into the model description will contribute to a more realistic representation of the catalytic system.

In **Chapter 1**, we present the latest developments in the field of computational modelling that aim to capture the diversity and multivariable nature of the active sites in catalysis. Illustrated spectroscopic findings emphasize the fluxionality of the catalytic systems and the ability of the active sites to rearrange and evolve under the conditions of the catalytic reactions, that is in the *operando* regime. Special attention was devoted to the computational approaches to address the structural complexity of the active sites in heterogeneous catalysis. The computational techniques discussed in this chapter were divided into two groups, namely, the individually- and population-based methods. In the former, the choice of the starting configuration impacts the outcome of the structural search, while the population-based methods have no regard for the starting model and explore the potential energy surface exhaustively. The latter approaches thus provide the means to battle the possible expert bias that may impact the structural proposals in catalysis. The possibility of connecting the oversimplified 0 K-in vacuo models with the more realistic catalytically-relevant conditions is enabled by the *ab initio* thermodynamics analysis (aiTA) approach, which is extensively employed in this thesis. **Chapter 1** also provides a brief overview of possible strategies for connecting the model results with the realistic catalyst systems, which is not complete due to the fast-growing computational chemistry field. In the next chapters, we have used these strategies complementary or separately, choosing a preferred computational strategy based on the specific research question pursued.

In this thesis, we explored the use of both individual and population-based methods for elucidating the structures of multicomponent reactive ensembles in zeolite-based catalysts. The genetic algorithm (GA)-based search, belonging to the former class of methods, was explored in **Chapters 2** and **4**, whereas the ensemble-based advanced

molecular dynamic sampling methods were the main methods employed in **Chapters 3** and **5**. The influence of the reactive environment on the nature and stability of the active sites in the zeolite catalysts was investigated by considering the presence of the reactive atmosphere in an implicit model. The impact of a more complex representation of the reaction environment on the nature of the catalytic sites is discussed in **Chapter 6** reporting a multiscale modelling study of the electrochemical CO<sub>2</sub> reduction.

**Chapter 2** utilizes the power of the GA to predict the nature of the EFAl species in high-silica ZSM-5 and MOR zeolites, which are known to greatly influence the activity, selectivity and stability of zeolite-based catalysts. To realize the superior catalyst design, factors such as the confinement effect imposed by the zeolitic frameworks, spatial limitations, and the locations of the extraframework species have to be accounted for in the model description. Furthermore, bridging the vacuo-0 K DFT results with the stability patterns under the reactive conditions brings the outlook on the EFAl structures formed under the experimentally-relevant conditions. The use of the fast semiempirical  $x$ TB method, appropriate for the closed-shell TM-free species, enabled an efficient GA-based exhaustive configurational search of various EFAl stoichiometries confined in MOR and ZSM-5 zeolite pores. Our automated procedure combining the accelerated global minima search with periodic DFT energy refinement allowed identifying and predicting relative stabilities of different extraframework aluminum configurations containing up to 4 Al centers and featuring different levels of hydration. The subsequent aiTA allowed prediction of how the conditions of the catalyst activation or the catalytic reaction may affect the preferred speciation of the EFAl species in high-silica zeolites. Our results predict that in contrast to low-silica faujasites dominated by multinuclear cationic EFAl species, high-silica MOR and ZSM-5 zeolites preferably host mono- and binuclear EFAl cations or bulk Al<sub>2</sub>O<sub>3</sub> species, depending on the preparation. The aiTA approach has outlined the most stable EFAl configurations in terms of Al concentration and water content under the zeolite-catalyzed reaction conditions.

The GA-based structure exploration methodology has been employed in **Chapter 4** to address the active site speciation in the new highly active and stable Ca-promoted Ga-ZSM-5 catalyst for the conversion of methanol to aromatics. Here, the automated expert bias-free  $x$ TB-based PES exploration has been complemented with the DFT-refinement and aiTA analysis to investigate the structures and stability of CaGa bimetallic ensembles inside the zeolite pores. In this chapter, we describe the experimental findings on the rapid deactivation of Ga-modified ZSM-5 catalyst during methanol aromatization reaction due to cooking. The addition of the small Ca quantities promotes a higher selectivity to the light aromatics and an extended lifetime in the methanol-to-aromatics process. The catalytic tests and spectroscopic characterization suggest that this effect may be due to the formation of the bimetallic CaGa extraframework species, whose molecular nature has been established using our expert-bias-free computational methodology. We computationally analyzed various stoichiometries of Ga-only and CaGa

oxide/hydroxide/hydrate species inside the ZSM-5 pores and analyzed their reactivity by using ethane dehydrogenation as a model reaction. The experimentally observed effects of minute amounts of Ca were assessed and attributed to the stabilization of the intrazeolite extraframework Ga clusters and moderating their dehydrogenation activity, which favorably affects the lifetime of the catalysts during the conversion of methanol to aromatics.

Exploring the geometries of the active sites with more advanced electronic configurations often represents a challenge for the accelerated/semiempirical methodologies that are necessary for the exhaustive GA configurational search of complex heterogeneous catalytic ensembles. Molecular dynamics and its enhanced variations can carry out the sampling of the PES at a lower computational cost with higher-level full DFT electronic structure methods. **Chapter 3** presents such a methodology for the expert-bias-free analysis of active site structures and their dynamics using a representative example of Cu-modified mordenite zeolite – a promising catalyst for the direct oxidation of methane to methanol. To access the pool of the Cu-oxo structural isomers possible to occur under the *operando* conditions, low-mode molecular dynamics (LMMD) has been employed, which enables the exhaustive structural search by concentrating the kinetic energy along the low-curvature direction of the PES. Using the cyclic chair-shaped  $[\text{Cu}_3\text{O}_3]^{2+}$  stoichiometry in the side pocket of mordenite as a representative and widely studied example of the Cu-oxo structure, a continuum of geometrically diverse isomers with varied stabilities has been generated in the LMMD procedure. Next, a representative pool of unique configurations was identified using the unsupervised machine learning clustering procedure based on similar structural features. Our procedure gives revealed several previously unknown peroxo-complexes that are >100 kJ/mol more stable than the widely-discussed chair-shaped structure. This chapter emphasizes the importance of eliminating expert bias in computational and mechanistic studies in catalysis.

In **Chapter 5** we employ this new methodology to resolve the debate around the nature and structure of Cu cations establishing a synergistic interaction with EFAl species in MOR zeolites. Our experimental collaborators from PNNL and TU Munich have discovered the cooperation between Cu and EFAl species enhances the methane oxidation activity of the zeolite catalyst. The EFAl-containing samples provide a higher methanol yield per Cu center already under the ambient conditions, whereas the same performance for the EFAl-free catalysts is only achievable at elevated pressures. This is attributed to the formation of CuAl-oxo species in a narrow range of Cu concentrations. With the use of the LMMD technique and clustering algorithm, stable configurations of the CuAl-oxo species have been identified. Their reactivity towards  $\text{CH}_4$  oxidation has been evaluated by DFT calculations complemented by aiTA, which results are in full accord with the experimental observations. A new model describing the concentration-dependent speciation of bimetallic extraframework ensembles in zeolites based on solid-state defect

## Summary

theory is introduced, which explains the experimental activity changes across catalysts with different compositions.

In **Chapter 6**, a multiscale *operando* modelling strategy was employed to simulate a multicomponent electrolyte-cathode interface under various applied potentials. As a target reaction, the process of CO<sub>2</sub> electroreduction over the Ag111 surface was studied. Investigating the density profiles of water, components of the electrolyte and CO<sub>2</sub>, the formation of a condensed EDL next to the cathode surface consisting of cations and ordered layers of solvation at high overpotentials was revealed. The following aiMD simulations showed that the outer-sphere electron transfer mechanism is promoted to produce formate and CO under high cathodic bias.

The results described in this thesis emphasize the critical importance of the reaction conditions and the adequate representation of the reaction environment – the *operando* regime – for constructing representative models of the active sites in heterogeneous catalytic systems. The computational methodologies that I have developed here will help reduce the expert bias in mechanistic studies that is critical for the development of truly predictive models in catalysis.

---

---

## Samenvatting

---

---

Dit proefschrift presenteert de mogelijke strategieën voor het modelleren van complexe heterogene katalytische systemen in *operando*-regimes. Dit wordt gedaan door het introduceren van de moderne computationele benaderingen om het potentiële energieoppervlak van de katalytische actieve sites te testen rekening houdend met de reactieve omstandigheden, de aanwezigheid van oplosmiddelen, de opname van additieven en de structurele dynamiek van de actieve sites. Er is groeiend spectroscopisch en theoretisch bewijs van de cruciale rol van de dynamiek van de actieve sites in de katalytische processen. Er wordt gepleit voor de representatie van de actieve sites als een ensemble van mogelijke isomeren. Uitgedaagd door de complexiteit van de reactieve omgeving en veelvoorkomende heterogene katalysatoren, geloven wij dat het aanpakken van deze factoren en het expliciet opnemen in de modelbeschrijving zal bijdragen aan een meer realistische representatie van het katalytische systeem.

In **Hoofdstuk 1** beschrijven we de nieuwste ontwikkelingen op het gebied van computationele modellering die de diversiteit en multivariabele aard van de actieve sites in katalyse willen vastleggen. Geïllustreerde spectroscopische bevindingen benadrukken de fluxionaliteit van de katalytische systemen en het vermogen van de actieve sites om te evolueren onder de omstandigheden van de katalytische reacties in het *operando*-regime. Speciale aandacht werd besteed aan de computationele benaderingen om de structurele complexiteit van de actieve sites in heterogene katalyse te behandelen. De computationele technieken die in dit hoofdstuk worden besproken, zijn verdeeld in twee groepen, namelijk de individueel- en populatiegebaseerde methoden. Het eerste wordt beïnvloed door de keuze van de startconfiguratie, terwijl de populatiegebaseerde methoden geen rekening houden met de startconfiguratie en een potentiële energieoppervlak uitputtend doorzoeken. De laatste benadering biedt dus de middelen om de mogelijke bias van experts te bestrijden die van invloed kunnen zijn op de voorstellen van katalysatorstructuren. De mogelijkheid om de te vereenvoudigde 0 K vacuomodellen te verbinden met de meer realistische katalytisch relevante omstandigheden wordt mogelijk gemaakt door de *ab initio* thermodynamische analyse (aiTA) benadering, die uitgebreid wordt gebruikt in dit proefschrift. **Hoofdstuk 1** geeft ook een kort overzicht van de mogelijke strategieën om de modelresultaten te verbinden met de realistische katalysatorsystemen, wat niet compleet is vanwege het snelgroeiende computationele gebied. In de volgende hoofdstukken hebben we deze strategieën complementair of afzonderlijk gebruikt, deze werden gekozen op basis van de specifieke onderzoeksvragen die worden nagestreefd.

In dit proefschrift hebben we het gebruik van zowel individuele- als populatiegebaseerde methoden onderzocht voor het ophelderen van de structuren van multicomponent reactieve ensembles in zeoliet-gebaseerde katalysatoren. Het op genetische algoritme (GA) gebaseerde zoeken, dat tot de eerste klasse van methoden behoort, werd onderzocht in de **Hoofdstukken 2 en 4**, terwijl de op ensembles gebaseerde geavanceerde moleculair dynamische bemonsteringsmethoden de belangrijkste methoden waren die in de **Hoofdstukken 3 en 5** werden gebruikt. De invloed van de reactieve omgeving op de aard en stabiliteit van de actieve sites in de zeolietkatalysatoren werd onderzocht in de reactieve atmosfeer in een impliciet model. De impact van de een complexere weergave van de reactieomgeving op de aard van de katalytische sites wordt besproken in **Hoofdstuk 6**, waarin een multischaalmodelstudie van de elektrochemische CO<sub>2</sub>-reductie wordt gerapporteerd.

**Hoofdstuk 2** gebruikt de kracht van het GA om de aard van de EFAl-soorten in ZSM-5 en MOR-zeolieten te voorspellen, waarvan bekend is dat ze de activiteit, selectiviteit en stabiliteit van op zeoliet gebaseerde katalysatoren sterk beïnvloeden. Om het superieure katalysatorontwerp te realiseren, moet rekening worden gehouden met factoren zoals het opsluitingseffect, ruimtelijke beperkingen en de locaties van de extraframeworks soorten in de modelbeschrijving. Bovendien brengt het verbinden van de vacuo-0 K DFT-resultaten en stabiliteitspatronen meer duidelijkheid over de stabiliteit van de EFAl-structuren gevormd onder de experimenteel relevante omstandigheden. De snelle semiempirische  $\chi$ TB methode is geschikt voor de TM-vrije soorten met gesloten elektronische schaal. Het maakte een efficiënte, op GA gebaseerde, uitputtende configuratieonderzoek mogelijk van verschillende EFAl-stoichiometrieën in MOR en ZSM-5-zeolietporiën. Onze geautomatiseerde procedure, die de versnelde minima-zoekopdracht combineert met periodieke DFT-energieverfijning, maakte het mogelijk om de relatieve stabiliteit van verschillende EFAl met maximaal 4 Al-centra en hydratatie niveaus te identificeren en voorspellen. De daaropvolgende aiTA maakte het mogelijk te voorspellen hoe de omstandigheden van de katalysatoren of de katalytische reactie de voorkeursspeciatie van de EFAl kunnen beïnvloeden. Onze resultaten voorspellen dat, in tegenstelling tot faujasieten met een laag siliciumgehalte, gedomineerd door multinucleaire kationische EFAl, zeolieten met een hoog siliciumgehalte bij voorkeur mono- en binucleaire EFAl-kationen of bulk Al<sub>2</sub>O<sub>3</sub> herbergen. De aiTA benadering heeft de meest stabiele EFAl-configuraties geschetst in termen van Al-concentratie en watergehalte onder de zeoliet gekatalyseerde reactieomstandigheden.

**Hoofdstuk 4** gebruikt de GA gebaseerde structuurverkenningmethodologie om de speciatie van actieve sites in de nieuwe Ca-gepromote Ga-ZSM-5-katalysator voor de omzetting van methanol in aromaten aan te pakken. De geautomatiseerde bias-vrije  $\chi$ TB-gebaseerde PES-exploratie is aangevuld met de DFT-verfijning en aiTA-analyse om de structuren en stabiliteit van CaGa ensembles te onderzoeken. In dit hoofdstuk beschrijven we de experimentele bevindingen over de snelle deactivering van Ga-gemodificeerde

ZSM-5-katalysator tijdens de aromatiseringsreactie van methanol. De toevoeging van de kleine Ca hoeveelheden bevordert een hogere selectiviteit naar de lichte aromaten en een langere levensduur in het methanol-naar-aromaten proces. De katalytische tests en spectroscopische karakterisering voorstellen dat dit effect kan komen door de vorming van de bimetallische CaGa extraframework soorten, waarvan de moleculaire aard is vastgesteld met behulp van onze expert-bias-vrij computationele methodologie. We analyseerden verschillende stoichiometrieën van Ga en CaGa-oxide/hydroxide/hydraatsoorten in de ZSM-5-poriën en analyseerden hun reactiviteit in ethaandehydrogenering. Experimenteel werden de effecten van minieme hoeveelheden Ca vastgesteld en toegeschreven aan de stabilisatie van de intrazeoliet extraframework Ga en het matigen van hun dehydrogeneringsactiviteit. Dit heeft positief invloed op de levensduur van de katalysatoren tijdens de omzetting van methanol in aromaten.

Het verkennen van de geometrieën van de actieve sites met meer complexe elektronische configuraties vormt vaak een uitdaging voor de versnelde methodologieën die nodig zijn voor het GA-configuratie onderzoek. Moleculaire dynamica en zijn verbeterde variaties kunnen de bemonstering van de PES uitvoeren tegen lagere computationele kosten met volledige DFT methoden op een hoger niveau. **Hoofdstuk 3** presenteert een methodologie voor de expert-bias-vrij analyse van actieve structuren en hun dynamiek met behulp van een representatief voorbeeld van Cu-gemodificeerde mordeniet. Om toegang te krijgen tot de poel van de structurele Cu-oxo isomeren die mogelijk kunnen optreden onder de *operando*-omstandigheden, is low-mode moleculaire dynamica (LMMD) gebruikt. Deze methode maakt uitputtend structuuronderzoek mogelijk door het concentreren van de kinetische energie langs de lage krommingsrichting van de PES. De cyclische stoelvormige  $[\text{Cu}_3\text{O}_3]^{2+}$  stoichiometrie in het zijvak van mordeniet werd gebruikt als een representatief en veel bestudeerd voorbeeld van de Cu-oxo structuur. De LMMD-procedure werd gebruikt om een continuüm van geometrisch diverse isomeren met verschillende stabiliteiten te genereren. Vervolgens werd een representatieve poel van unieke configuraties geïdentificeerd met behulp van de niet-gesuperviseerde machine learning-clusteringsprocedure. Onze procedure brengt een aantal onbekende peroxo-complexen aan het licht die  $> 100$  kJ/mol stabiel zijn dan de veelbesproken cyclische stoelvormige  $[\text{Cu}_3\text{O}_3]^{2+}$ . Dit hoofdstuk benadrukt het belang van het elimineren van expert bias in computationele en mechanistische studies in katalyse.

**Hoofdstuk 5** gebruikt deze nieuwe methodologie om de aard en structuur van Cu-kationen op te lossen en synergetische interactie met EFAl-soorten in MOR zeolieten tot stand te brengen. Onze experimentele collega's van PNNL en TU München hebben ontdekt dat de samenwerking tussen Cu- en EFAl-soorten de  $\text{CH}_4$  oxidatie-activiteit verbetert. De EFAl-bevattende monsters zorgen zelfs al onder de omgevingsomstandigheden voor een hogere methanolopbrengst per Cu-centrum. Tegelijkertijd is dezelfde prestatie voor de EFAl-vrije katalysatoren alleen haalbaar bij

verhoogde druk. Dit effect wordt toegeschreven aan de vorming CuAl-oxo-soorten in een smal bereik van Cu-concentraties. Met behulp van de LMMD-techniek en het clusteralgorithme zijn stabiele configuraties van de CuAl-oxo-soorten geïdentificeerd. Hun reactiviteit voor CH<sub>4</sub>-oxidaties is geëvalueerd door DFT-berekeningen aangevuld met aiTA. Deze resultaten zijn volledig in overeenstemming met de experimentele waarnemingen. Een nieuw model, gebaseerd op de theorie van vastestofdefecten, wordt geïntroduceerd. In dit model wordt de concentratie-afhankelijke soortvorming van bimetalen extraframework-ensembles in zeolieten beschreven, wat de veranderingen van experimentele activiteit tussen katalysatoren met verschillende samenstellingen verklaart.

Een multischaal *operando* modelleringsstrategie wordt gebruikt in **Hoofdstuk 6**, waar een multicomponent elektrolyt-kathode interface onder verschillende toegepaste potentialen wordt gesimuleerd. Als doelreactie werd het proces van CO<sub>2</sub>-elektroreductie over het Ag111-oppervlak bestudeerd. Tijdens onderzoek naar de dichtheidsprofielen van water, componenten van de elektrolyt en CO<sub>2</sub> werd de vorming van een gecondenseerde EDL naast het kathodeoppervlak bestaande uit kationen en geordende solvatatielagen bij hoge overpotentialen onthuld. De daaropvolgende aiMD-simulaties toonden aan dat het elektronenoverdracht in de buiten-bol mechanisme wordt bevorderd waardoor formaat en CO worden geproduceerd onder hoge kathodische bias.

De resultaten beschreven in dit proefschrift benadrukken het kritische belang van de reactieomstandigheden en de adequate representatie van de reactieomgeving. Het *operando* regime wordt gebruikt voor het construeren van representatieve modellen van de actieve sites in heterogene katalytische systemen. De computationele methodologieën die ik hier heb ontwikkeld, zullen de expert bias in mechanistische studies helpen verminderen. Dit is essentieel voor de ontwikkeling van écht voorspellende modellen in katalyse.

---

---

## Acknowledgements

---

---

I want to thank my supervisor Evgeny Pidko for the opportunities and challenges I was facing since the day we met. During my Master's degree at ITMO University, you introduced me to a completely new world of theoretical chemistry, modelling and ... grants managing. I was very happy every step of the journey as I was working in a dynamic environment on various scientific tasks and I always felt supported, inspired, and guided by you along the way. Thank you for letting me grow as a theoretical chemistry researcher while doing a PhD in the ISE group, where I always felt welcomed, valued, and never alone. I wish for you many talented and enthusiastic people around and get a Nobel prize one day without too much sacrificing on life's pleasures. I also want to say thank you to Agi, who let me smoothly dive into the world of quantum chemical calculations and gave me a lot of excruciatingly honest feedback. In the first years of my PhD, I was receiving a lot of help from the researchers I was closely working with. Dear Guanna, Dapeng and Divya, thank you very much for always helping me out, giving me such great ideas, and being so easy to talk to. I want to thank Michael Medvedev for his patience and punctilious attitude and for letting me learn new approaches from him. I would also like to express my gratitude to Vivek, who was always very understanding and patient with me and was always able to answer my silly and not so silly questions. Dear collaborators Maricruz Sanchez-Sanchez, Lei Tao, Insu Lee and Johannes Lercher from TU Munich, I want to say thank you for the time you put into our joined projects and all the fruitful scientific discussions that we had. Dear Els and Karin, thank you for taking care of all bureaucratic matters and being so helpful!

The aspirations of starting a PhD have been rooted in my visit to the TU/e, where, apart from the learning, I have met fun and cool people of the Chem. Eng. department. I want to thank Roderigh for letting me learn a lot from you and Elizabeth and Robbert for being so kind to me and making my stay so enjoyable. When I came to Delft, I quickly got along with the outnumbered female part of the group, where we supported, encouraged each other and also stay sportive together. Specifically, I want to express my love to gorgeous Annika and Liliana for all the clubbing, talking, gossiping, waking together and crying on your shoulders. I hope you will stay in my life and we have many other adventures ahead of us. I would also like to thank Christophe for taking so patiently my attempts to speak Dutch to you and thank you for all the nice talks that we managed to convey in Dutch during our coffee breaks. Adarsh and Ali, thank you for being such cool roommates in Lyon. Adarsh, I wish you a lot of success with your PhD, your optimistic and confident attitude will make everything possible. Ali again and Robbert, thank you for contributing to making my current apartment a livable place. I would not have made it without your help. Chuncheng, thank you for being willing to explain and

### *Acknowledgements*

show me the lab work and, of course, delicious samples of Chinese food. Jenechka, thank you for being so helpful with everything and for your beautiful and slightly dark jokes. I hope that CyberHydra will rock. Wenjun, thank you for giving exceptional presentations and for your help with my thesis cover. Dear Gosha, thank you for providing an interesting, unique perspective on life and being always fun and full of beautiful allegories. I want to thank my current and former team members: Robert for inspiring me to cook sometimes, Ina for being an example of an energetic and strong character, Jittima and Nithya for being always nice, helpful and approachable. I would also like to say thank you to the Master's students whom I have worked with. Dear Harshini, Enrico, Victor, Sumant, Maria and Marijke, thank you for being so talented and awesome! This book would not be completed without your input.

I thank my parents, sister and my little nephew for their unconditional love, support and motivation to go forward. Я так же хочу сказать спасибо моим родителям, сестре и Арсению за их любовь, воодушевление и поддержку во всем. Я вас очень люблю! Finally, I would like to express my love and gratitude to Jeroentje for dragging me from the laptop, believing in me and giving me so much support and care.

---

---

## List of publications

---

---

### Publications within the scope of this thesis

Zheng J., Lee I., **Khramenkova E. V.**, Wang M., Peng B., Gutiérrez O. Y., Fulton J. L., Camaioni D. M., Khare R., Jentys A., Haller G. L., Pidko E. A., Sanchez-Sanchez M., Lercher J. A. Importance of methane chemical potential for its conversion to methanol on Cu-exchanged mordenite. *Chem. Eur. J.* **26**, 7515–7515 (2020).

**Khramenkova E. V.**, Medvedev M. G., Li G., Pidko E. A. Unraveling nature of extraframework catalytic ensembles in zeolites: flexibility and dynamics of the copper-oxo trimers in mordenite. *J. Phys. Chem. Lett.* **12**, 10906–10913 (2021).

Liu C., Uslamin E. A., **Khramenkova E. V.**, Sireci E., Ouwehand L. T., Ganapathy S., Kapteijn F., Pidko E. A. High Stability of Methanol to Aromatic Conversion over Bimetallic Ca,Ga-Modified ZSM-5. *ACS Catal.* **12**, 3189–3200 (2022).

Sinha V., **Khramenkova E. V.**, Pidko E. A. Solvent-mediated outer-sphere CO<sub>2</sub> electroreduction mechanism over Ag111 surface. *Chemical Science* **13**, 3803–3803 (2022).

**Khramenkova E. V.**, Venkatraman H., Soethout V., Pidko E. A. Global optimization of extraframework ensembles in zeolites: structural analysis of extraframework aluminum species in MOR and MFI zeolites. *Phys. Chem. Chem. Phys.* **24**, 27047–27054 (2022).

**Khramenkova E. V.**, Meeprasert J., Uslamin E. A., Pidko E. A. *Operando* computational characterization and modelling in heterogeneous catalysis. (Wiley-VCH Verlag), *submitted*.

Tao L., **Khramenkova E. V.**, Lee I., Ikuno T., Fulton J. L., Pidko E. A., Sanchez-Sanchez M., Lercher J. A. Impact of metal ion concentration on the formation of active Cu-Al-oxo clusters in mordenite for oxidative activation of methane. *J. Am. Chem. Soc.*, *submitted*.

### Publications outside the scope of this thesis

Kozlova M. A., Poezhaev A. I., **Khramenkova E. V.**, Korzhikov V. A., Osmolovskaya O. M., Osmolovskii M. G. Glycine. biocompatible growth regulator for preparation of inorganic nanomaterials for medicine. *Russ. J. Gen. Chem.* **84**, 2047–2048 (2014).

Perovskiy I. A., **Khramenkova E. V.**, Pidko E. A., Krivoschapkin P. V., Vinogradov A. V., Krivoschapkina E. F. Efficient extraction of multivalent cations from aqueous solutions into sitinakite-based sorbents. *Chem. Eng. J.* **354**, 727–739 (2018).

Vrubel I. I., Senkevich N. Y., **Khramenkova E. V.**, Polozkov R. G., Shelykh I. A. Electronic Structure and Optical Response of Zn-Based Metal–Organic Frameworks. *Adv. Theory Simulations* **9**, 1800049 (2018).

**Khramenkova E. V.**, Polynski M. V., Vinogradov A. V., Pidko E. A. Degradation paths of manganese-based MOF materials in a model oxidative environment: a computational study. *Phys. Chem. Chem. Phys.* **20**, 20785–20795 (2018).

Keller K., **Khramenkova E. V.**, Slabov V., Musin A., Kalashnikov A., Vinogradov A. V., Pidko E. A. Inkjet printing of Sc-Doped TiO<sub>2</sub> with enhanced photoactivity. *Coatings* **9**, 78 (2019).

Szécsényi Á., **Khramenkova E. V.**, Chernyshov I. Y., Li G., Gascon J., Pidko E. A. Breaking Linear Scaling Relationships with Secondary Interactions in Confined Space: A Case Study of Methane Oxidation by Fe/ZSM-5 Zeolite. *ACS Catal.* **9**, 9276–9284 (2019).

---

---

## Presentations

---

---

**Khramenkova E. V.**, Izatulina A. R., Osmolovskaya O. M., Korzhikov V. A., Frank-Kamenetskaya O. V., Osmolovskii M. G. Synthesis and characterization of hydroxyapatite and nanocomposites based thereon. *V International Symposium: Biogenic–abiogenic interactions in natural and anthropogenic systems*. October 20–22, **2014**. Saint Petersburg, Russia. (poster)

**Khramenkova E. V.**, Osmolovskaya O. M., Averyanov I. V., Korzhikov V. A. The hydroxyapatite nanoparticle with different morphology and nanocomposites based on. *X Russian symposium with international participation: Thermodynamics and Materials*. April 7–11, **2015**. Saint Petersburg, Russia. (poster)

**Khramenkova E. V.**, Osmolovskaya O. M., Korzhikov V. A., Osmolovskii M. G. The hydroxyapatite nanoparticle with different morphology and nanocomposites based on. *IX International conference of young scientists on chemistry Mendeleev 2015*. April 7–10, **2015**. Saint Petersburg, Russia. (poster)

**Khramenkova E. V.**, Osmolovskaya O. M., Averyanov I. V., Korzhikov V. A. The hydroxyapatite nanoparticle with different morphology and nanocomposites based on.

*XVIII International research conference: Fundamental sciences and clinical medicine – man and health.* April 18, **2015**. Saint Petersburg, Russia. (oral)

**Khramenkova E. V.**, Vinogradov A. V., Pidko E. A. A complementary theoretical and experimental approach to the development of metal-organic frameworks as a novel platform for targeted drug delivery. *Science and Progress-2016.* October 17–21, **2016**. Saint Petersburg, Russia. (oral)

**Khramenkova E. V.**, Szécsényi Á., Pidko E. A. The role of confinement on the reactivity of Fe-ZSM-5 zeolite in the selective methane oxidation. *5th International School-Conference on Catalysis for Young Scientists “Catalyst Design: From Molecular to Industrial Level.* May 20–23, **2018**. Moscow, Russia. (poster)

**Khramenkova E. V.**, Szecsenyi A., Pidko E. A. The role of confinement for the reactivity of Fe-ZSM-5 zeolite in the selective methane oxidation. *The Netherlands' Catalysis and Chemistry Conference.* May 5–7, **2018**. Noordwijkerhout, The Netherlands. (poster)

**Khramenkova E. V.**, Li G., Medvedev M. G., Pidko E. A. Local dynamics of the active centers in zeolite in partial methane oxidation. *KNCV-division Computational and Theoretical Chemistry.* 26 March, **2019**. Amsterdam, The Netherlands. (poster)

**Khramenkova E. V.**, Szecsenyi A., Pidko E. A. Mapping the reaction landscape for methane oxidation by copper-exchanged zeolites. *The Netherlands' Catalysis and Chemistry Conference.* March 4–6, **2019**. Noordwijkerhout, The Netherlands. (poster)

**Khramenkova E. V.**, Medvedev M. G., Pidko E. A. Mapping the reaction landscape for partial methane activation by Cu-modified zeolites. *The 8<sup>th</sup> Federal European Zeolite Association – FEZA 2021.* July 5–9, **2021**. Virtual. (poster)

**Khramenkova E. V.**, Medvedev M. G., Li G., Pidko E. A. The flexibility and dynamics of the extraframework oxygenated Cu species in mordenite: a computational study. *The Netherlands' Catalysis and Chemistry Conference.* May 9–11, **2022**. Noordwijkerhout, The Netherlands. (oral)

**Khramenkova E. V.**, Medvedev M. G., Li G., Pidko E. A. Scanning the reaction energy landscape in Cu/MOR zeolites. *International Conference on Theoretical Aspects of Catalysis.* June 13–11, **2022**. Lyon, France. (poster)

**Khramenkova E. V.**, Medvedev M. G., Li G., Pidko E. A. An automated expert-bias free strategy for unraveling nature of extraframework catalytic ensembles in zeolites: a case study of Cu/MOR methane oxidation catalyst. *The 9<sup>th</sup> Tokyo Conference on Advanced Catalytic Science and Technology.* July 24–29, **2022**. Fukuoka, Japan. (oral)

---

---

## Curriculum Vitae

---

---

Elena Khramenkova was born on the 21<sup>st</sup> of June in 1994 in Bratsk, Russia. After finishing elementary school, she transferred to physico-mathematical lyceum 1 in Bratsk. At the age of 18, she moved to Saint Petersburg to pursue her Bachelor's degree in (Analytical) Chemistry at Saint Petersburg State University. During her Bachelor's degree, she was actively working in the lab on projects involving hydroxyapatite synthesis of different morphology for bone tissue engineering. Under the supervision of Olga Osmolovskaya, she carried out her thesis project on hydrothermal and precipitation nanoparticle synthesis with antibacterial properties for water purification. After that, she started her Master's degree at ITMO University and a research project at the laboratory of Solution Chemistry of Advanced Materials and Technologies. During these years, she developed a passion for computational chemistry and modelling under the guidance of prof. dr. Evgeny Pidko. This emerged in various projects that involved studies on the degradation of the metal-organic frameworks in an oxidation environment, prediction of the enhanced photosensitivity of the Sc-doped TiO<sub>2</sub> and confinement effect in zeolites for the methane oxidation process. After graduating, she received an exciting opportunity to continue working in the computational catalysis field with prof. dr. Evgeny Pidko at the TU Delft. In 2018, she started her PhD in the Inorganic Systems Engineering group at the Chemical Engineering department. In these four years, new computational strategies for investigating various catalytic systems have been developed along with the prediction and justification of the experimental results.



Currently, she is open to a new exciting turn where life will take her.